

**Investigation of boundary layer transition  
at high Reynolds numbers using  
time-resolved temperature-sensitive paint**

**Dissertation**

for the award of the degree

“Doctor rerum naturalium” (Dr. rer. nat.)  
of the Georg-August-Universität Göttingen

within the doctoral program physics  
of the Georg-August University School of Science (GAUSS)

submitted by

**Benjamin Daniel Dimond**

from Mosbach

Göttingen, 2023

## Thesis Committee

### **Prof. Dr. Martin Rein**

Georg-August-Universität Göttingen, Institute for the Dynamics of Complex Systems and  
Institute of Aerodynamics and Flow Technology, German Aerospace Center (DLR)

### **Prof. Dr. Dr. Andreas Dillmann**

Georg-August-Universität Göttingen, Institute for the Dynamics of Complex Systems and  
Institute of Aerodynamics and Flow Technology, German Aerospace Center (DLR)

### **Dr. Marco Costantini**

Institute of Aerodynamics and Flow Technology, German Aerospace Center (DLR)

## Members of the Examination Board

### **Reviewer: Prof. Dr. Martin Rein**

Georg-August-Universität Göttingen, Institute for the Dynamics of Complex Systems and  
Institute of Aerodynamics and Flow Technology, German Aerospace Center (DLR)

### **Second Reviewer: Prof. Dr. Dr. Andreas Dillmann**

Georg-August-Universität Göttingen, Institute for the Dynamics of Complex Systems and  
Institute of Aerodynamics and Flow Technology, German Aerospace Center (DLR)

## Further members of the Examination Board

### **Prof. Dr. Andreas Tilgner**

Georg-August-Universität Göttingen, Institute of Geophysics

### **Prof. Dr. Ulrich Parlitz**

Georg-August-Universität Göttingen, Institute for the Dynamics of Complex Systems and  
Max Planck Institute for Dynamics and Self-Organization (MPI-DS)

### **Prof. Dr. Stefan Klumpp**

Georg-August-Universität Göttingen, Institute for the Dynamics of Complex Systems

### **Dr. Marco Costantini**

Institute of Aerodynamics and Flow Technology, German Aerospace Center (DLR)

Day of the oral examination: 05.12.2023

## Acknowledgements

This thesis is the result of research I conducted at the Institute of Aerodynamics and Flow Technology at DLR Göttingen. First of all, I would like to thank Prof. Dr. Martin Rein, reviewer, and Prof. Dr. Dr. Andreas Dillmann, reviewer and head of the institute, for refereeing this thesis and for valuable scientific discussion and advice over the last years. I would also like to thank Prof. Dr. Andreas Tilgner, Prof. Dr. Ulrich Parlitz, and Prof. Dr. Stefan Klumpp for their participation in the Examination Board.

Special thanks go to my supervisor and member of the Examination Board Dr. Marco Costantini. Over the last years he has constantly motivated, encouraged, helped and advised me and kept me on track to focus on the important parts of my research.

I am thankful to Dr. Christian Klein as the research group coordinator of the pressure- and temperature-sensitive paint group, for all his support and encouragement, as well as keeping me on track and providing fruitful inspiration for this work. I would like to thank both Dr. Klein and Dr. Lars Koop, Head of the Department, for the possibility of conducting this research at the Institute. Further, I am grateful to Jonathan Lemarechal, Dr. Michael Hilfer, and Dr. Ulrich Henne for the countless fruitful and fun discussions and support, as well as the other members of the group: Dr. Daisuke Yorita and Dr. Nils van Hinsberg.

Dr. Daniel Ernst, Dr. Massimo Miozzi and Dr. Stefan Hein are acknowledged for valuable discussions of the results.

Furthermore, I would like to thank the people involved in the experimental setup and realisation: Carsten Fuchs, Tobias Kleindienst and Tobias Herrmann for model preparation and support with the experimental setup, Sebastian Roth, Heiko Böhlken and Dr. Stefan Koch for hot-film installation and data acquisition, and Sebastian Weiss, Martin Aschoff and Rainer Kahle for wind tunnel operation. I would like to thank the people involved in developing the iTSP paint in our group and the colleagues from the Spacecraft department, especially Dr. Jan Martinez Schramm for collaboration and support with the iTSP.

I would like to thank the people who proofread parts or all of this thesis: Dr. Marco Costantini, Dr. Walter Beck, Dr. Christian Klein, Dr. Michael Hilfer, Dr. Ulrich Henne, Dr. Nils van Hinsberg and my father. A big thank you goes to my family and friends for their unconditional support and love and to my study colleagues who motivated me to persevere throughout my studies: Wieland, Nick, Heike, Lotta, and Ole.

Most of all I would like to thank my wife Natascha. I cannot write in words what your love and support mean to me. You have kept my back free, motivated me and supported me throughout this period and it would not have been possible without you.

*Men became scientific because they expected Law in nature, and they expected Law in nature because they believed in a Legislator*

C. S. LEWIS



## Abstract

Understanding the fundamental principles of the processes that lead to laminar-turbulent transition on aerodynamic surfaces is of significant importance to correctly describe, model and perhaps ultimately influence the transition region. The understanding is still limited for many relevant flow conditions due to the challenges involved in both experimental and numerical studies. This thesis studies the phenomena and processes (i.e. specifically turbulent spots, intermittency distribution and turbulent wedges) of laminar-turbulent transition of a quasi-two-dimensional boundary layer over a flat plate in a compressible subsonic flow at high Reynolds numbers for which experimental data is scarce, and uses the specially developed time-resolved temperature-sensitive paint (iTSP) measurement technique. Experiments were conducted in the Cryogenic Ludwig-Tube Göttingen at ambient temperatures with various streamwise pressure gradients, freestream Mach numbers ranging  $0.3 \leq M \leq 0.8$ , and local Reynolds numbers  $1 \cdot 10^6 \leq Re_x \leq 6.5 \cdot 10^6$  with high temporal (20 kHz to 100 kHz) and spatial (17 px/mm) resolution. A Ru(phen)-based iTSP was investigated for its suitability, characterised to enable a quantitative surface temperature and heat flux determination, and applied for the first time under these investigated flow conditions. The emphasis was laid on systematically investigating turbulent spots for independently varied test conditions. The characteristic streamwise pointing triangle shape of the turbulent spot with its rounded wing tip region could be identified for all flow conditions. Additionally, the leading and trailing edge celerities, spreading and opening angles, and resulting turbulent spot propagation parameters were determined. While turbulent spots were observed to grow unaffected when merging laterally with other turbulent spots or turbulent wedges, the leading edge celerities of trailing spots were found to be considerably slower if trailing within about one spot length of another spot. A direct intermittency determination was possible when considering the surface heat flux computed from the time-resolved iTSP data. There was good agreement between transition location, defined at 50% intermittency, with commonly used definitions for stationary surface temperature measurements and the intermittency distribution in the transition region with models from literature. Turbulent wedges were found to consist of a fully turbulent core and intermittent outer region, although the latter was smaller than those found in other investigations. Intermittent turbulent wedges could be resolved and were shown to be a series of individual turbulent spots. For the first time, unsteady laminar-turbulent transition phenomena could be temporally resolved and characterised with an image based thermographic surface measurement technique under the investigated flow conditions. These findings are an essential aid to understanding and modelling the transition region for compressible high Reynolds number flow conditions and to demonstrate the capabilities of this new time-resolved iTSP technique to help gain a new understanding of instationary boundary layer transition phenomena.

## Kurzbeschreibung

Das Verständnis der grundlegenden Prozesse, die zum laminar-turbulenten Grenzschichtumschlag (Transition) auf aerodynamischen Oberflächen führen, ist von großer Bedeutung um den Transitionsbereich korrekt zu beschreiben, zu modellieren oder gar zu beeinflussen. Für viele relevante Strömungsbedingungen ist das Verständnis aufgrund der Herausforderungen von sowohl experimentellen als auch numerischen Studien, begrenzt. In dieser Arbeit werden die Phänomene und Prozesse (insbesondere Turbulenzflecken, Intermittenzverteilung und Turbulenzkeile) des laminar-turbulenten Übergangs einer quasi-zweidimensionalen Grenzschicht über einer ebenen Platte in einer kompressiblen Unterschallströmung bei hohen Reynoldszahlen untersucht, für die nur wenige experimentelle Daten verfügbar sind. Dafür wird die speziell entwickelte und charakterisierte Methode der zeitaufgelösten temperatursensitiven Farbe (iTSP) verwendet. Durchgeführt wurden die Experimente im kryogenen Ludwieg-Rohrwindkanal Göttingen bei Umgebungstemperaturen mit verschiedenen Druckgradienten, Machzahlen im Bereich von  $0,3 \leq M \leq 0,8$  und lokalen Reynoldszahlen  $1 \cdot 10^6 \leq Re_x \leq 6,5 \cdot 10^6$  mit hoher zeitlicher (20 kHz bis 100 kHz) und räumlicher (17 px/mm) Auflösung. Eine Ru(phen)-basierte iTSP wurde bezüglich seiner Eignung untersucht und charakterisiert, um die Oberflächentemperatur und Wärmestromdichten quantitativ zu untersuchen. Dabei wurde die Farbe erstmals unter diesen untersuchten Strömungsbedingungen eingesetzt. Der Schwerpunkt der Arbeit lag dabei auf der systematischen Untersuchung von Turbulenzflecken für verschiedene, voneinander unabhängig variierten Strömungsbedingungen. Die charakteristische stromabwärts gerichtete Dreiecksform der Turbulenzflecken mit den abgerundeten Randbereichen konnte für alle Strömungsbedingungen identifiziert werden. Zusätzlich wurden die Konvektionsgeschwindigkeiten der Vorder- und Hinterkante, Ausbreitungs- und Öffnungswinkel sowie die daraus resultierenden Ausbreitungsparameter bestimmt. Es wurde beobachtet, dass sich Turbulenzflecken spannungsweitig unabhängig voneinander ausbreiten, bis sie sich mit anderen Turbulenzflecken oder Turbulenzkeilen vereinen. Die Konvektionsgeschwindigkeiten der Vorderkante nachfolgender Flecken hingegen ist erheblich verlangsamt, wenn sie sich ungefähr innerhalb einer Länge des vorhergehenden Turbulenzflecks ausbreitet. Mit den aus den zeitaufgelösten iTSP-Daten berechneten Wärmestromdichten war eine direkte Bestimmung der Intermittenzverteilung möglich. Dabei wurde eine gute Übereinstimmung des Umschlagpunkts, definiert als 50% Intermittenz, mit den üblicherweise verwendeten Definitionen für stationäre Oberflächentemperaturmessungen sowie der Intermittenzverteilung im Transitionsbereich mit Modellen aus der Literatur beobachtet. Es konnte gezeigt werden, dass Turbulenzkeile aus einem vollturbulenten Kern und einem intermittierenden Außenbereich bestehen, obwohl letzterer kleiner war als in anderen Untersuchungen beobachtet. Intermittierende Turbulenzkeile konnten zeitlich aufgelöst werden und erwiesen sich als eine Reihe einzelner Turbulenzflecken. Zum ersten Mal konnten instationäre laminar-turbulente Transitionsphänomene für die untersuchten Strömungsbedingungen mit einer thermographischen Oberflächenmesstechnik zeitlich aufgelöst und charakterisiert werden. Die Ergebnisse tragen wesentlich zum Verständnis und zur Modellierung des Transitionsbereichs bei kompressiblen Strömungsbedingungen mit hoher Reynoldszahl bei. Es konnten die Möglichkeiten und Vorzüge dieser neuen zeitaufgelösten iTSP Messtechnik dargestellt werden, um ein neues Verständnis der instationären Transitionsphänomene zu gewinnen.

# Contents

<b>1</b>	<b>Introduction</b>	<b>1</b>
1.1	Motivation . . . . .	2
1.2	Scope of this work . . . . .	3
1.3	Outline . . . . .	5
<b>2</b>	<b>Theory and Literature Review</b>	<b>7</b>
2.1	Laminar-turbulent transition process . . . . .	7
2.2	Turbulent wedges . . . . .	9
2.3	Turbulent spots . . . . .	10
2.3.1	General features of turbulent spots . . . . .	10
2.3.2	General remarks on the quantification of turbulent spots . . . . .	13
2.3.3	Properties of turbulent spots . . . . .	14
2.4	Intermittency distribution . . . . .	18
<b>3</b>	<b>Experimental Methods</b>	<b>21</b>
3.1	Cryogenic Ludwig-Tube Göttingen KRG . . . . .	21
3.2	Principle of Temperature-Sensitive Paint (TSP) . . . . .	23
3.3	Wind tunnel model . . . . .	25
3.3.1	Design and model cross-section . . . . .	25
3.3.2	Conventional instrumentation . . . . .	26
3.3.3	TSP instrumentation . . . . .	29
3.4	iTSP setup in KRG . . . . .	29

3.4.1	iTSP properties . . . . .	29
3.4.2	Coating . . . . .	32
3.4.3	LEDs and filters . . . . .	34
3.4.4	Camera . . . . .	36
3.4.5	Wind tunnel implementation . . . . .	36
3.4.6	Limitations . . . . .	37
<b>4</b>	<b>Evaluation Techniques</b>	<b>39</b>
4.1	Calibration . . . . .	39
4.2	Image processing . . . . .	43
4.2.1	Marker detection and image alignment . . . . .	43
4.2.2	Mapping to model coordinates . . . . .	46
4.2.3	Image filtering . . . . .	46
4.3	Numerical methods . . . . .	47
4.3.1	Boundary layer parameters . . . . .	47
4.3.2	Linear stability analysis . . . . .	48
4.4	Heat flux determination . . . . .	48
4.5	Turbulent spot celerities . . . . .	51
4.5.1	Techniques discussed in the literature . . . . .	52
4.5.2	Trailing edge celerity . . . . .	52
4.5.3	Leading edge celerity . . . . .	56
4.5.4	Manual detection of leading edge celerity . . . . .	59
4.5.5	Comparison of leading and trailing edge interfaces with heat flux levels	61
4.6	Spreading and opening angles of turbulent spots . . . . .	62
4.7	High-frequency iTSP evaluation . . . . .	63
4.8	Hot-film anemometry . . . . .	63

<b>5</b>	<b>Results and Discussion</b>	<b>65</b>
5.1	Turbulent spots . . . . .	65
5.1.1	General features of turbulent spots . . . . .	65
5.1.2	Turbulent spot celerities . . . . .	71
5.1.3	Spreading and opening angles . . . . .	80
5.1.4	Comparison with hot-film data . . . . .	83
5.1.5	Spot propagation parameter . . . . .	87
5.1.6	Merging turbulent spots . . . . .	88
5.2	Laminar turbulent transition . . . . .	93
5.2.1	Standard deviation of iTSP temperature distributions . . . . .	95
5.2.2	Surface temperature distribution . . . . .	96
5.3	Turbulent wedges . . . . .	100
5.3.1	Fully turbulent core wedges . . . . .	100
5.3.2	Intermittent turbulent wedges . . . . .	103
5.4	Tollmien-Schlichting waves . . . . .	109
5.4.1	Hot-film analysis . . . . .	109
5.4.2	iTSP analysis . . . . .	110
<b>6</b>	<b>Conclusions</b>	<b>115</b>
6.1	Overview and summary . . . . .	115
6.2	Outlook and further suggested work . . . . .	117
	<b>Appendices</b>	<b>119</b>
<b>A</b>	<b>Remarks on Evaluation Techniques</b>	<b>121</b>
A.1	Further remarks on the heat flux calculations . . . . .	121
A.2	Other possible methods and comparisons determining celerities . . . . .	123
A.3	Remarks on the temperature correction procedure of hot-films . . . . .	124
A.4	Error analysis for the laminar-turbulent transition measurements . . . . .	125

CONTENTS

---

A.5 Remarks on visibility of markers in the result images . . . . . 128

**B Additional results 129**

B.1 Additional turbulent spot celerities . . . . . 129

B.2 Further remarks on the high Mach number cases . . . . . 133

**Nomenclature 135**

**Bibliography 139**

# Chapter 1

## Introduction

In 1883, Osborne Reynolds discovered random “flashes” in a pipe flow that occurred under certain flow conditions [132]. He was investigating the flow resistance in a pipe and why, in some cases, it was proportional to the mean velocity, while in others it was proportional to the square mean velocity. Using a thin filament of dye, he noticed two different states of flow - “direct” and “sinuos” - which would later be described as laminar and turbulent, respectively. In the laminar case, fluid particles move along orderly paths, whereas in the turbulent case, the filament of dye flutters and random cross movements are superimposed on the mean particle flow, associated with strong intermixing. It is nowadays known that the “flashes” he observed were patches of turbulent flow developing as the flow transitioned from laminar to turbulent. This observation marks the beginning of a long history of research [13, 16, 79] devoted to investigating the process known as laminar-turbulent transition.

The basic concept of a laminar and turbulent state also holds true for a boundary layer, the thin layer of fluid close to a bounding surface. This was investigated after Reynolds’ pioneering work and first described by Ludwig Prandtl [126] at the beginning of the twentieth century. Special attention was paid to a flat plate boundary layer, which still serves as a representative model flow [146]. Understanding the properties of this model flow is vital since it significantly influences skin friction drag and heat transfer in many applications. Examples include boundary layers on airfoils [32, 36], turbomachinery blades [25, 89] or hypersonic vehicles [10, 86].

As mentioned above, transition is a process that cannot be generally assumed to occur at a singular “transition location”. The transition region is spread out in space, with some parts being laminar and others turbulent at different times. The prevailing physical model for the transitional region is attributed to Emmons [49]: A random formation of turbulent “spots” (patches of turbulent flow with properties similar to those of a fully turbulent boundary layer) in an otherwise laminar boundary layer that grow in space and time as they convect downstream, eventually merging until the whole flow is considered turbulent. The formation and growth of these turbulent spots therefore characterises the transition region. Figure 1.1 shows one such turbulent spot visualised using a suspension of aluminium flakes in a low-speed water flow. The illustrated downstream-pointing arrowhead shape is a common characteristic of turbulent spots at various flow conditions.



**Figure 1.1:** Visualisation of sublayer streaks of a turbulent spot in water illustrated with the use of aluminium flakes at  $U_\infty = 0.23$  m/s. Adapted from Cantwell et al. [17]. No scale was given by the original authors, but based on the description of the experimental setup, the spanwise extent of the turbulent spot is in the range of several centimetres.

## 1.1 Motivation

A global pandemic had a dramatic impact on aviation in 2020, with passenger numbers decreasing by around 60% [45] compared to 2019 and with a revenue loss of 118.5 billion USD for global commercial airlines [71]. Despite this crisis, current projections estimate that the total civil passenger numbers will recover to pre-pandemic levels by the end of 2023 or early 2024, there being only a small impact on the long-term development [45]. With the increased number of flights needed to cater for these greater passenger numbers, reaching the goal of net-zero global carbon dioxide emissions set by the aviation industry and various governments presents a huge challenge. Such required reductions in emissions for the aviation sector are difficult to achieve since they must occur even as new energy-dense liquid fuels are being developed. Even the possible widespread introduction of sustainable aviation fuel, which would require involved manufacturing and concomitant investment in sustainable feedstock to meet the demand, would still be insufficient to attain the goals [8, 157]. Therefore, substantial efforts are necessary to decrease fuel consumption by increasing the efficiency of jet engines and reducing the overall drag of aircraft.

In the case of airfoils, the boundary layer flow can transition from a laminar to a turbulent state, affecting both the aerodynamic performance and efficiency. The state of the boundary layer significantly influences surface friction and also affects the position of flow separation. The skin friction for a laminar boundary layer can be as low as 10% compared to a turbulent boundary layer [79], and so there is a great potential to reduce the overall drag of an aircraft if the laminar region can be extended over as large a region as possible over the wing; typically, so far, the flow over wings is mostly turbulent [6, 79, 149].

The efficiency of a gas turbine or jet engine can be significantly improved with increased turbine inlet temperature. Since the entry temperature is already higher than the allowable temperature of the components, great effort must be expended to ensure sufficient cooling of the turbomachinery blades. To optimise the design, the precise heat-transfer coefficients, which are dependent on the boundary layer state, need to be known in the different regions. Similarly, the thermal loads for a hypersonic vehicle can be very high, as is the case in the reentry of a space vehicle into the atmosphere [10, 106, 128, 177]. Understanding and accounting for the thermal load distribution in the design process can remarkably

improve efficiency. One specific example is the National Aero-Space Plane (NASP), where accounting for the laminar-turbulent transition location as opposed to the conservative approach of assuming a fully turbulent boundary layer increased the estimated payload by 60-70% [177] due to decreased friction and thermal load.

Therefore, understanding the processes that lead to laminar-turbulent transition and determining the location and extent of the transition region is important for many aerodynamic applications. Despite extensive research conducted over the last decades, there is a need for further research, especially in high Reynolds number flows relevant for aircraft aerodynamic surfaces, where both numerical and experimental studies are scarce.

## 1.2 Scope of this work

The main objective of this thesis is the quantitative and time-resolved investigation of the laminar-turbulent transition region for compressible subsonic flows at high local Reynolds numbers ( $1 \cdot 10^6 \leq Re_x \leq 6.5 \cdot 10^6$  with  $Re_x = \rho U_\infty x / \mu$ , where in this case  $x$  is the streamwise location at which the transition process occurs), which are relevant especially for commercial transport aircraft. Therefore, specifically the following aspects of laminar-turbulent boundary layer transition have been studied:

(1) Turbulent spots: these play a major role in the transition process and determine the length of the region where the boundary layer transitions from a fully laminar to a fully turbulent state. They grow in both streamwise and spanwise directions as they convect downstream. Important properties are the spreading angle and celerities of these spots. The celerity of a turbulent spot ( $c_{le}$  and  $c_{te}$  for the leading and trailing edge, respectively) refers to the propagation speed of the laminar-turbulent interface enclosing the spot relative to the boundary layer edge velocity  $U_e$ . It is not the same as the velocity of fluid particles or the convection speed of turbulent structures, as turbulent spots generate new turbulent structures around their interface. Therefore, the term celerity will be used throughout this thesis in line with several other researchers [20, 61, 62, 81]. Note that in literature, other terms are used, like velocity (e.g. [21, 181]), propagation rates (e.g. [23, 26, 75]) or convection velocities/speeds (e.g. [52, 80]), all referring to the same property of turbulent spots.

For the first time, this study aims to systematically investigate the independent influence of Reynolds number, Mach number, and pressure gradient experimentally for subsonic compressible conditions for the aforementioned properties of turbulent spots. Research concerning turbulent spots and their quantitative characteristics in these conditions is quite scarce. Literature reviews like those by Gostelow [61] and Wu [179] show a large scatter in experimental data, mainly due to differences in measurement techniques, wind tunnels, Reynolds numbers and interface identification techniques.

(2) Streamwise extent of the transition region: This is directly influenced by the properties and evolution of turbulent spots. The intermittency distribution characterises this region, the intermittency factor  $\gamma$  being the proportion of laminar and turbulent flow ( $\gamma = 0$  for fully laminar and  $\gamma = 1$  for fully turbulent flow). As turbulent spots grow and merge with increasing downstream coordinate, the proportion of the turbulent boundary layer will increase until eventually the whole boundary layer is fully turbulent. The skin friction increases continuously in the transitional region, which needs to be modelled accurately to

get a reliable prediction of the flow over the surface.

By determining the time-resolved heat flux at the wall, a distinction between laminar and turbulent boundary layers is made. Integrated over time, this enables one to directly determine the intermittency distribution which is compared with the average heat flux and temperature distribution that are often used to determine a transition location [21, 33].

(3) Turbulent wedges: these areas of turbulent flow result from isolated surface roughnesses that cause premature transition - i.e. without their presence, the flow would have remained laminar at that location. They are important for an operational environment because they can be induced by roughnesses caused by surface imperfections, debris or dead bugs on a wing and would lead to areas of larger wall shear stress and thus to an increase in drag. The turbulent area spreads laterally in the downstream direction, forming a triangular shape (hence the term “wedge”) with characteristic spreading angle  $\alpha$  (mostly  $\sim 5^\circ - 10^\circ$  [53, 58]). In most cases, these wedges are quasi-stationary in the sense that the core of the wedge is fully turbulent (bounded by an intermittent region [152]). This investigation quantifies the extent of the turbulent wedge for various flow conditions and also identifies and characterises intermittent turbulent wedges for which the core has an alternating laminar and turbulent boundary layer.

(4) Unstable two-dimensional waves present in 2D boundary layers: These so-called Tollmien-Schlichting waves (T-S waves) are amplified as they move downstream and eventually will lead to nonlinear phenomena that, in turn, lead to the formation of turbulent spots and the transition to turbulent flow. This led Walker & Gostelow [173] to calculate the minimum transition length for natural transition based on the assumption that all T-S waves lead to the formation of turbulent spots. The properties (frequency and wavelength) and amplification rates of T-S waves therefore have a direct influence on the length and onset of the intermittency region. The feasibility of measuring and quantifying T-S waves at flight-relevant flow conditions in a Ludwig-Tube (KRG) is investigated.

There has been extensive research on the topic of turbulent spots in subsonic and supersonic flows with extensive theoretical and experimental observations (e.g. [1, 21, 25, 49, 62, 114, 151, 152, 181]), their extent being due to their importance for understanding the laminar-turbulent transition process. Many of these studies, however, were conducted for incompressible flows and at low Reynolds numbers (most studies examine  $Re_x < 5 \cdot 10^5$ ) and for artificially generated spots as opposed to naturally occurring turbulent spots. Even to this day, studies in compressible high-Reynolds number flows are not widespread; this is most surely due to the experimental challenges involved and also to the high computational costs for numerical studies under these conditions [80, 114]. By encompassing high Reynolds numbers and a large subsonic range of Mach numbers ( $0.3 \leq M \leq 0.8$ ), varied independently from each other, this work aims to provide new insight into the formation and propagation of naturally occurring turbulent spots.

The aspects of laminar-turbulent transition mentioned above have been investigated in this thesis with the help of the temperature-sensitive paint (TSP) method. This measurement technique enables the non-intrusive quantitative measurement of surface temperature over a large spatial region, which can be used to determine the surface heat flux, which in turn

is directly related to the state of the boundary layer. In this work, the term “TSP” is used with respect to the general properties of the measurement technique and the classical use of stationary TSP, whereas “iTSP” will be used to refer to the specific time-resolved TSP, used in this investigation. iTSP is capable of resolving the small temperature changes at very high frequencies (20 kHz to 100 kHz) investigated here. This iTSP has been specially developed and characterised for the current application and applied for the first time in a compressible subsonic flow at high Reynolds numbers. New evaluation methods have been developed to identify heat flux traces of turbulent spots, a direct determination of intermittency distributions and the quantitative characterisation of the growth of turbulent spots and spread of turbulent wedges. These results are then compared with data acquired from simultaneous hot-film measurements, where applicable. So far, the temperature-sensitive paint measurement technique has often been used for steady-state measurements, including laminar-turbulent transition detection with temperature gradient and heat flux measurements [31, 33, 41, 43, 94, 122]. This work, however, focuses on unsteady flow phenomena and compares the results with established methods used for stationary transition measurements. This is the first time that the mechanisms of laminar-turbulent transition have been temporally and spatially resolved on a surface for compressible subsonic flows at high Reynolds numbers.

### 1.3 Outline

This thesis is divided into the following chapters:

- **Chapter 2** discusses previous work which focuses on laminar-turbulent transition, and in particular on the characterisation of turbulent spots, and the applicability of suggested methods for high Reynolds number flows.
- The experimental setup is presented in **Chapter 3**, which includes a description of the wind tunnel, the model, and its instrumentation. A focus is laid on characterising and applying the time-resolved temperature-sensitive paint measurement technique iTSP in the flow conditions and wind tunnel used in this work.
- In **Chapter 4**, the novel evaluation techniques needed for this work are presented. These include the quantitative determination of surface temperature and heat flux, the image processing and the quantitative determination of turbulent spot properties from iTSP data, and the evaluation of hot-film and wind tunnel data.
- The main results are presented and discussed in **Chapter 5**. It is divided into four sections: turbulent spots, transition length and intermittency distribution, turbulent wedges and Tollmien-Schlichting waves.
- **Chapter 6** concludes this work, summarises the findings and provides an outlook for future studies.



## Chapter 2

# Theory and Literature Review

### 2.1 Laminar-turbulent transition process

For a flow over a body, the flow velocity directly at the wall is zero according to the no-slip boundary condition. This results in a velocity gradient close to the wall as the streamwise velocity component increases from 0 at the wall to the outer flow velocity far from the wall. This region of reduced streamwise velocity due to the wall is called the velocity boundary layer. It can either be laminar, i.e. smooth with only little exchange of fluid particles in wall-normal direction or turbulent, characterised by a strong mixing motion and exchange of fluid particles throughout the boundary layer. For most aerodynamic applications, the boundary layer starts laminar at the upstream part of a body and then becomes turbulent further downstream. Many parameters can influence if and where the boundary layer transitions from a laminar to a turbulent state, the most important of which are the Reynolds number, the properties and disturbance level of the free stream, the surface texture and the pressure gradient along the streamwise direction. The physical state of the boundary layer is described by the intermittency factor  $\gamma$  - the fraction of time for which the boundary layer is turbulent at a certain position. An intermittency factor of  $\gamma = 0$  corresponds to fully laminar flow, and  $\gamma = 1$  corresponds to fully turbulent flow. Generally, areas in the transition region are partly laminar and partly turbulent in time, resulting in an intermittency distribution. This distribution will be discussed further in section 2.4. The process of laminar-turbulent boundary layer transition on a flat plate for a 2D flow as a representative flow model and the mechanisms that lead to it are outlined in the following. The stages of laminar-turbulent transition are visualised in figure 2.1.1. It is important to note that the different areas are not sharply delimited and may vary considerably in size depending on the flow conditions. Further details with a more complete description can be found in Schlichting [146] or White [176].

Immediately following the leading edge, the first area contains a stable laminar boundary layer. Small disturbances within the boundary layer are damped here.

Further downstream, after the boundary layer velocity profiles have further evolved, the boundary layer becomes unstable for small disturbances. The location at which disturbances start to become amplified is called the indifference point or point of primary instability and is expressed in terms of the indifference Reynolds number  $Re_{ind}$ . Downstream of

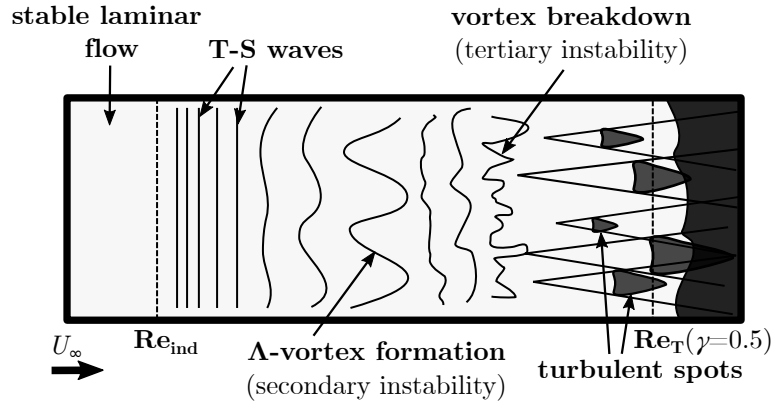


**Figure 2.1.1:** Qualitative sketch of the laminar-turbulent transition process over a flat plate for a 2D flow (based on White [176]).

this indifference point, harmonic oscillations in terms of flow quantities, called Tollmien-Schlichting waves (T-S waves), grow in a streamwise direction. They were first theoretically described by Tollmien in 1929 [167], and Schlichting in 1933 [145] for a Blasius boundary layer (for incompressible flow). Their description is based on 2D linear stability theory (LST): The flow quantities of velocity (in two dimensions streamwise  $x$  and wall-normal  $z$ ), density, pressure and temperature in the governing set of Navier-Stokes equations are divided into terms of steady mean flow and unsteady perturbations with the following assumptions:

- The steady mean flow poses a solution to the governing equations.
- The steady mean flow runs parallel to the wall.
- The unsteady perturbations are small with respect to the steady mean flow, allowing for the linearisation of the governing equations.

The function  $\Psi(x, z, t) = \varphi(z)e^{i(\alpha x - \beta t)}$  serves as the starting equation for the stream function. Here  $\alpha$  is the wavenumber, and  $\beta$  is the angular frequency. This ansatz yields the Orr-Sommerfeld equation, an ordinary differential equation of fourth order for the amplitude function  $\varphi(z)$ . A more detailed overview of the basics of LST for incompressible flow and extended for compressible flow is given, for instance, by Mack [98].

As the T-S waves grow, they alter the velocity profiles, making them unstable to three-dimensional disturbances. Klebanoff et al. [82] observed this secondary instability as the amplitude of T-S waves increased above a certain threshold. The two-dimensional structure disintegrates, and  $\Lambda$ -vortices arise. The arrangement of the  $\Lambda$ -vortices was experimentally investigated by Saric and Thomas [142] and can be divided into three types: C-type named after Craik [37], H-type named after Herbert [65], and K-type named after Klebanoff et al. [82], with different stream- and spanwise wavelengths.

The breakdown of the  $\Lambda$ -vortices marks the area of tertiary instability. The high amplitude of the disturbances leads to areas of high shear stress, which result in  $\Omega$ -shaped hairpin eddies at the peaks of the  $\Lambda$ -vortices.

Experiments by Elder [48] showed that once the intensity of the disturbances grew large enough, turbulent spots emerged, with the flow properties inside of these spots resembling

that of a fully turbulent boundary layer. These turbulent spots spread out in a wedge-shaped area and eventually merge to form a fully turbulent boundary layer. Coles & Barker [29] managed to obtain a turbulent boundary layer with several spots initiated at several spanwise locations.

Therefore, the laminar-turbulent transition process can not be attributed to one specific downstream location, but rather to a region reaching from the growth of the first disturbances at the indifference point to the formation of a fully turbulent boundary layer. A further definition of the transition region is for areas where  $0 < \gamma < 1$ , excluding the area where the boundary layer is laminar but unstable. The latter definition will be used in this thesis. The term “transition location” will be used for the streamwise location of 50% intermittency ( $\gamma = 0.5$ ).

The extent of the individual stages of the transition process varies depending on the flow conditions. However, the linear amplification phase of T-S waves is generally the largest part. Herbert [65] describes the development of secondary instability to develop within five T-S wavelengths and the onset of spikes and the breakdown to occur within one T-S wavelength, remarkably shorter than the slow growth of T-S waves. Obremski et al. [116] estimate the length of the linear amplification of TS-waves to cover about 75% to 85% of the transition region.

The path to transition outlined above is only valid for a low background turbulence level on a smooth surface. Therefore, the existence of T-S waves could only be experimentally shown by Schubauer & Skramstad [153] in 1947, several years after their theoretical postulation. For higher turbulence levels, present in many wind tunnel environments, the transition may exclusively consist of the formation and growth of turbulent spots. Since the stages of linear amplification and secondary instabilities don't occur, this process is generally described as “bypass” transition [109]. Depending on the freestream turbulence levels, there are other mechanisms that lead to laminar-turbulent transition involving transient growth, typically labelled “paths”. The mechanisms involved are discussed in references [109, 131].

## 2.2 Turbulent wedges

A particular case of bypass transition is caused by discrete roughness elements in a two-dimensional boundary layer (no mean flow in the spanwise direction). If large enough, this element causes a significant distortion of the laminar boundary layer, leading to bypass transition. The distortion initiates a turbulent wedge with a specific lateral spreading rate. The resulting spreading angle was surprisingly constant throughout many experimental and numerical investigations, only changing significantly for supersonic flows or strong pressure gradients, and changing weakly for different Reynolds numbers. Additionally, the wedge angles reported in literature -  $8^\circ$  to  $12^\circ$  [27, 34, 53, 56, 152, 185] - are very similar to those reported for the enveloping wedge-shaped area of turbulent spots [62, 152, 181]. Note that the spreading angle of turbulent wedges and spots are sometimes referred to as “half-angle” or “semi-angle”. In this work, the spreading angle refers to the angle between the centre line and the line along the spanwise extent of turbulent wedge or spot (see figures 2.2.1 and 2.3.2)

A sketch of a turbulent wedge can be seen in figure 2.2.1. It generally consists of a fully turbulent core ( $\gamma = 1$ ) and an intermittent outer region ( $0 < \gamma < 1$ ) with the definition

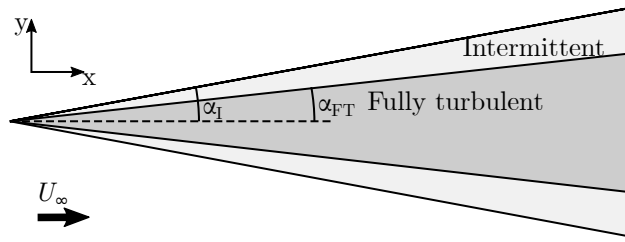


**Figure 2.2.1:** Sketch of a turbulent wedge with a fully turbulent core and an intermittent outer region in an otherwise laminar boundary layer.

of the intermittency factor  $\gamma$  as described above. Schubauer & Klebanoff [152] extensively studied turbulent wedges in an incompressible flow and found the wedge spreading angle to be  $\alpha_{FT} = 6.4^\circ$  for the fully turbulent core and  $\alpha_I = 10.6^\circ$  for the outer intermittent region. Gad-El-Hak et al. [56] used dye inserted at a roughness element in a water channel flow and observed the spreading angle of the dye to be much smaller than the spreading angle of the turbulent wedge that arises at the roughness element. They concluded that the spreading mechanism could not be attributed to turbulent mixing alone but is mainly driven by a destabilisation process in which the turbulence inside the wedge causes a destabilisation of the surrounding laminar flow.

Using thermochromic liquid crystals, Zhong et al. [185] reported a low spreading angle of only  $6.5^\circ$  for a turbulent wedge in a low-speed wind tunnel which they attribute to a considerable spanwise “overhang region” - the spreading angle being larger away from the wall than directly at the wall. They confirmed this hypothesis with additional hot-wire measurements. A similar conclusion was made by Krishnan & Sandham [88].

Clark et al. [27] in 1993 were the first to describe an intermittent turbulent wedge - a wedge-shaped area consisting of closely following but individual turbulent spots. The phenomenon was also found by Fiala et al. [51] in 2014. More details will be given in section 5.3.2.

## 2.3 Turbulent spots

This section covers the basic principles and properties of turbulent spots and compares previous studies. Distinctions have been made between “transitional-turbulent” spots and “turbulent-turbulent” spots. This distinction arises from the attempts to see turbulent-turbulent spots as the “basic module of the wall layer portion of fully turbulent zero-pressure gradient smooth flat-plate boundary layer” [179]. Coles & Barker [29], Zilberman et al. [187] and Savas & Coles [143] observed the pattern of artificially generated turbulent spots in the laminar boundary layer to also retain, to a certain degree, the basic pattern in the fully turbulent boundary layer. Throughout this thesis, however, turbulent spots will refer to transitional-turbulent spots, i.e. patches of turbulent flow within an otherwise laminar boundary layer.

### 2.3.1 General features of turbulent spots

Turbulent spots are isolated patches of turbulence that appear within an otherwise laminar boundary layer [49]. They can arise if the velocity fluctuation in the boundary layer exceeds a critical level of the order of 10% to 20% of the boundary layer velocity [48, 174]. Once initiated, these spots grow to become arrowhead-shaped structures as they

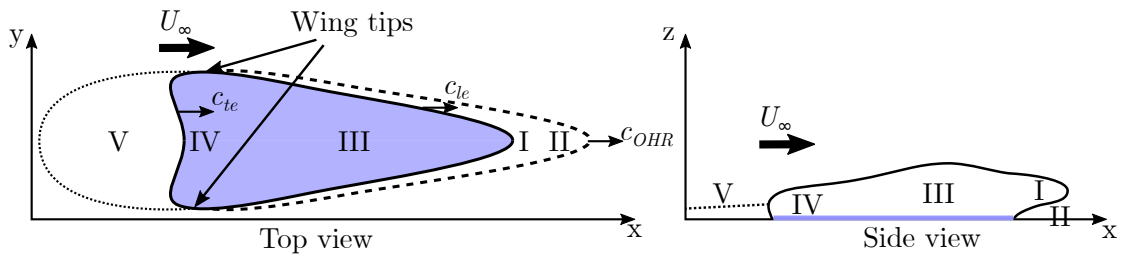


**Figure 2.3.1:** Top and side view of an isolated turbulent spot.

move downstream, with different leading and trailing edge celerities [181]. The general shape of a turbulent spot resembles a downstream pointing triangle and is shown in figure 2.3.1. It is bounded by a leading edge interface with a primarily constant celerity  $c_{le}$  and a trailing edge interface with rounded outer sides, referred to as wing tips [56, 62, 179]. Since the trailing edge interface propagates at a lower rate than the leading edge interface ( $c_{te} < c_{le}$ ), the spot grows in the streamwise direction. Based on findings by Gad-El-Hak [56], a spot can be divided into five distinct regions (labelled I - V in figure 2.3.1):

- An overhang region along the leading edge interface (marked by a dashed line in the left figure) for which the extent of the turbulent spot is smaller at the wall compared to locations away from the wall (**region I**). The point of the spot furthest downstream (downstream tip of region I) is approximately at the height of the surrounding laminar boundary layer thickness [56, 62, 158, 181]. Since the celerity of this foremost point (labelled celerity of the overhang region  $c_{OHR}$ ) is typically higher than the leading edge celerity  $c_{le}$  at the wall, the overhang region will grow with increased streamwise distance [181]. Sohn et al. [160] indirectly observed the effect of an overhang region, since the intermittency values they recorded for a laminar-turbulent transition varied depending on the distance to the wall. While the intermittency was lowest close to the wall, it was highest around the local displacement thickness.
- Below region I, the overhang region, **region II** is still laminar but with increased perturbations due to the presence of the overhang region. These perturbations are measured and predicted experimentally and numerically for various conditions [24, 56, 88]. It is still unclear what role the disturbances in region II play in the propagation of the turbulent spot.
- The core of the turbulent spot, **region III**, behaves similarly to that of a classical turbulent boundary layer on a flat plate with several features present in both (like individual, independent eddies, low- and high speed streaks and hairpin-like vortices [5, 48, 56, 124, 150, 151, 166, 179]). There are, however, some distinct differences: The distribution of the ensemble-averaged product of stream- and spanwise velocity fluctuations differs, as pointed out by Antonia et al. [3]. Schröder et al. state that “the turbulent spot does not exhibit a logarithmic region of the ensemble-averaged velocity profile” [151] and that the substructures inside a turbulent spot are denser but more orderly [150].
- **Region IV** is the trailing edge region of the spot and the one with the highest wall-shear stress. The trailing edge celerity is determined by the rate of turbulence generation in this region. The spanwise outer boundaries of this region (“wing tips”) are typically rounded. Some researchers state that the overhang region is also

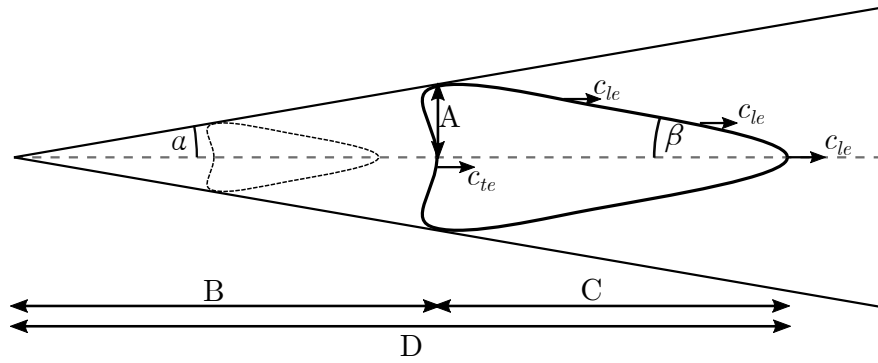


**Figure 2.3.2:** Sketch of a turbulent spot propagating downstream with spreading angle  $\alpha$  and opening angle  $\beta$ .

present in the wing tip region [17, 18, 23, 88], which may affect the interpretation of experimental results obtained with measurements at the wall (e.g. heat flux measurements with hot-films and thermographic measurement techniques) and in the boundary layer (e.g. hot-wire measurements).

- A calmed region trailing the actual turbulent spot (**region V**) was first described and observed by Schubauer & Klebanoff [152]. Whereas the leading edge caused a sudden increase in the velocity recorded by hot-wire measurements, an exponential-like decay to the laminar level was observed at the trailing edge of the spot. This region with a laminar boundary layer has a fuller (and therefore more stable) velocity profile than the surrounding laminar boundary layer. It plays an important role in the transition length as it directly influences the coalescence of turbulent spots [60]. Schubauer & Klebanoff [152] hypothesised that this region exists, since the celerity of the trailing edge ( $c_{te} \approx 0.5$ ) is higher than the propagation speed of trailing instabilities (typically stated at around  $0.3U_\infty$ ). In the calmed region, streaks resulting from hairpin-vortices inside the turbulent spots were observed by several researchers with flow visualization [56], thermochromic liquid crystal (TLC) thermography [139], and particle image velocimetry (PIV) [151].

Wyganski et al. [181] mapped all three velocity components inside a turbulent spot by hot-wire anemometry. They observed that the streamwise component of the velocity increased from the leading edge to the trailing edge of the spot, which must result in an increased wall shear stress along the length of the spot - the maximum wall shear stress located close to the trailing edge of the turbulent spot. This was later experimentally confirmed by several other authors, including Mautner and Van Atta [100] and Sabatino and Smith [139].

For an idealised isolated triangular turbulent spot propagating downstream with a singular point of origin, a relation exists between the spreading angle  $\alpha$ , opening angle  $\beta$  (between the centre line and outer leading edge interface - sometimes also referred to as “apex angle”) and the leading and trailing edge celerity, assuming these quantities remain constant (quantities sketched in figure 2.3.2).

Let A be the half-width, B the distance travelled by the trailing edge, C the length, and D

the distance travelled by the leading edge of the turbulent spot, as sketched in figure 2.3.2. Then one finds:

$$\begin{aligned}
 C &= D - B \\
 \tan(\beta) &= \frac{A}{C} \\
 \tan(\alpha) &= \frac{A}{B} = \frac{\tan(\beta)C}{B} \\
 &\text{with} \\
 \frac{C}{B} &= \frac{D}{B} - 1 = \frac{c_{le} \cdot \Delta t}{c_{te} \cdot \Delta t} - 1 = \frac{c_{le}}{c_{te}} - 1,
 \end{aligned}$$

which leads to

$$\tan(\alpha) = \tan(\beta) \cdot \left( \frac{c_{le}}{c_{te}} - 1 \right). \quad (2.3.1)$$

Schubauer & Klebanoff [152] reported values of  $c_{te} = 0.5$  and  $c_{le} = 0.88$  as well as spreading angle  $\alpha = 11.3^\circ$  and opening angle  $\beta = 15.3^\circ$  for a low speed ( $M = 0.033$ ) incompressible flow. These values have generally been accepted and confirmed in low-speed flows, and similar values were found in many following experimental investigations. Using equation 2.3.1 to calculate the leading edge celerity  $c_{le}$  based on the trailing edge celerity and the opening and spreading angle, one obtains  $c_{le} = 0.87$ , very close to the measured value. This result justifies the use of the simplification of triangular spots as used by several researchers [26, 114, 181, 186] and sketched in figure 2.3.2.

If the planar growth is characterised alone by a spanwise growth and a differing trailing and leading edge celerity, any small patch of turbulence will eventually grow into the shape of a downstream pointing triangle. This phenomenon was experimentally confirmed by Wygnanski et al. [181] who, using hot-wire anemometry, found that artificially created turbulent spots have the same (triangular) shape independent of the disturbance causing the turbulent spot and if viewed sufficiently far downstream of the origin.

The growth mechanism of turbulent spots is of great interest as it directly influences the transition length. Several researchers have proposed a similar spanwise growth mechanism as for a turbulent wedge [51, 58, 124, 141]. For subsonic conditions, this involves growth by destabilisation as proposed by Gad-El-Hak et al. [56]. The destabilisation is caused “mainly through the turbulent eddies inside a spot contaminating the low-speed streaks in the vicinity of the spot” [179] as shown numerically by DNS of Brinkerhoff & Yaras [15], Wu et al. [178], and Zhao et al. [184].

### 2.3.2 General remarks on the quantification of turbulent spots

A distinction must be made between artificially generated spots, as is the case for most investigations named above, and naturally occurring spots. Artificial turbulent spots have the advantage of repeatability - turbulent spot properties like leading and trailing edge celerity can be obtained by ensemble averaging many individual turbulent spots. It also makes it possible to investigate both isolated turbulent spots and the merging of spots

with well-defined parameters (time delay and spanwise distance) in a way which is not possible when investigating naturally occurring turbulent spots. There are, however, several disadvantages to studying artificial turbulent spots. One disadvantage becomes evident for typical hot-wire measurements at one downstream location: one must assume that the spot is convected downstream at a constant speed and that shape, size and propagation parameters are identical for all events [181]. Furthermore, artificially generated turbulent spots are triggered at the wall (e.g. through pressure fluctuations induced by a small hole or spark generators), as opposed to the boundary layer edge for naturally occurring turbulent spots (e.g. suggested by Jacobs & Durbin [72] or Wu et al. [180]). Wu et al. [180] even attributed a different observed shape of the turbulent spot (a triangle pointing upstream instead of downstream) in their direct numerical simulations to the origin at the boundary layer edge as opposed to the wall, as is mostly the case for artificially generated turbulent spots. Additionally, experiments are often performed in an otherwise near-stable environment where disturbance amplitudes are still low, i.e., far from the natural transition location. This inevitably affects the spreading mechanism and propagation of the turbulent spots (compare the growth by destabilisation as proposed by Gad-El-Hak [56] - see section 2.3.1); the extent of this remains to be seen.

While most studies cited in the following investigate artificially generated turbulent spots, this thesis investigates naturally occurring turbulent spots.

### 2.3.3 Properties of turbulent spots

Several studies are related to quantitative and qualitative propagation of turbulent spots, but only very few for the flow conditions present in this investigation. Along with the numerous studies in subsonic flow, this section summarises some of the results found in super- and hypersonic flow and numerical studies.

#### 2.3.3.1 Studies for super- and hypersonic flows

Several experiments and numerical calculations have investigated the development of turbulent spots in a super- and hypersonic boundary layer. The following gives an overview of some of the most notable studies.

As one of the earlier experimental observations of turbulent spots, James [73] used spark shadowgraph images to examine gun-launched projectile models at  $2.7 < M < 10$ . He noticed weak shock waves radiating from the spot trailing edges and used the angle that the burst shock wave makes with the stream direction to determine its celerity. The leading edge celerity can then be estimated by the expected spot origin and extent at the time of imaging. He was able to quantify leading and trailing edge celerities to values similar to those of newer investigations.

Mee [106], extending on previous experiments of Mee & Goyne [103], performed experiments on a flat plate in a free-piston shock tunnel to detect turbulent spots for a range of Reynolds numbers at Mach numbers around 6. He could extract leading and trailing edge celerities of  $0.9 \pm 0.1$  and  $0.5 \pm 0.1$  with an array of thin-film heat-transfer gauges. The (half-) spreading angle  $\alpha$  was further determined to be  $(3.5 \pm 0.5)^\circ$ .

Fiala et al. [52] also used an array of streamwise-aligned thin-film heat-transfer gauges to determine spot propagation celerities. Using the detected binary intermittency function, they determined leading and trailing edge celerity to be 0.81 and 0.4, respectively. With the heat flux signals along a further spanwise set of gauges, they could reconstruct the

heat-transfer footprint of spots that passed this array. As one of few previous studies, they determined the length/width ratio of turbulent spots to be  $2.5 \pm 0.25$ . One of the limitations of their measurements was that only a spanwise or streamwise array of heat-transfer gauges could deliver the small spacings required for the investigation, thus requiring the use of two different wind tunnel models, depending on the objective.

Zanchetta & Hillier [183] used high-speed heat transfer measurements to extract streamwise intermittency profiles for a  $5^\circ$  cone at Mach 9. Although not explicitly stated, the celerities can be estimated from the thin-film gauge time series to be 0.98 and 0.68 for the leading and trailing edges, respectively.

Raghunath et al. [127] investigated the characteristics of turbulent spots in a hypersonic transitional boundary layer with hot-films and Schlieren imaging. Experiments were conducted at  $M \approx 7$  at a local Reynolds number of the order of  $Re_x = 3 \cdot 10^6$ . They observed leading edge celerities of  $c_{le} = 0.9 \pm 0.05$  and trailing edge celerities of  $c_{te} = 0.63 \pm 0.05$ . Very similar values of  $c_{le} = 0.91 \pm 0.03$  and  $c_{te} = 0.63 \pm 0.04$  were observed by Jewell et al. [74] for a hypervelocity flow with fast-response thermocouples. Some individual turbulent spots, however, were measured to have a leading edge celerity about the same as the boundary layer edge velocity, indicating a certain degree of variation in celerity that cannot be explained by experimental accuracy alone.

### 2.3.3.2 Studies utilising thermal imaging

In a recent study, Pandey et al. [123] used TSP to visualise the thermal footprint of artificially generated turbulent spots (via electric discharge excitation) in a hypersonic boundary layer over a sharp cone. The spots were visualised in the boundary layer using the Schlieren technique, and the time-averaged footprint was recorded at 20 Hz.

Lemarechal et al. [91] used TSP to investigate turbulent spots in a low-speed laminar water channel. The high temporal and spatial resolution made it possible to resolve the dynamics of the turbulent spot as a whole and the flow structures within the turbulent spot; showing inrushes caused by sweeps, streaks and hairpin vortices. They recorded a leading edge celerity range of  $c_{le} = 0.72 - 0.90$  and a spreading angle of  $\alpha = (10.5 \pm 0.4)^\circ$ . Sabatino & Smith [139] also investigated the surface heat transfer with thermochromic liquid crystal (TLC) thermography for a flow in a water tunnel. While their results are consistent with other work, they admit that identifying the leading edge is somewhat subjective, and resulting leading edge celerities could lie in the range  $0.9 \leq c_{le} \leq 1.0$ .

A series of experiments were conducted with thermochromic liquid crystals in a water tunnel investigating turbulent spots artificially created with a pulsating water jet through a small hole in the wall [18, 19, 129, 163]. The leading and trailing edge celerities were found to be in the range  $0.74 \leq c_{le} \leq 0.84$  and  $0.5 \leq c_{te} \leq 0.66$ , respectively. Additionally, the longitudinal merging of turbulent spots was investigated by Srichan et al. [163] with thermochromic liquid crystals in a low-speed water tunnel. They observed an increase in local Nusselt numbers in the merging area of two consecutive turbulent spots.

In conclusion, while several publications covered the use of thermal imaging to characterise turbulent spots, all of them either examined low-speed flows or time-averaged properties like the spreading angle of turbulent spots. So far, there has not been any study resolving naturally occurring individual turbulent spots in a compressible flow with a thermal imaging technique or any other measurement technique with a high spatial resolution on the surface.

### 2.3.3.3 Modifiers of turbulent spot properties

Several modifiers have been identified to influence the turbulent spot properties. These were mainly the effect of pressure gradient, compressibility and Reynolds number but also wall to adiabatic wall temperature ratio, surface texture and freestream turbulence [102].

Fransson [55] saw an increase in leading edge celerity with higher freestream turbulence levels reaching up to  $c_{le} = 0.96$ . Strand & Goldstein [165] found that the spreading angle of turbulent spots could be decreased if the wall was made up of riblets, whereas Muhammad & Chong [110] did not observe an effect of riblets on the trailing end leading edge celerities of turbulent spots.

**Wall temperature ratio** In a numerical study, Joksch & Kleiser [76] found a lower leading edge celerity ( $c_{le} = 0.89$ ) for a cooled wall compared to an adiabatic wall ( $c_{le} = 0.96$ ) for a flow at  $M = 5$ . Redford et al. [130] saw a reduced lateral growth rate for cooled walls and concluded that different wall temperatures could help explain the scatter in experimental data, especially in supersonic conditions that often see a large range of wall to adiabatic wall temperature ratios. Experimentally, Gutmark and Blackwelder [62] investigated a heated but incompressible boundary layer (30 °C over room temperature resulting in  $T_w/T_{aw} \approx 1.1$ ). This temperature difference yielded only little effect on the celerities of turbulent spots. Mayle [102] concluded that the effect of heat transfer on the length of transition and therefore the spot production rate is negligible.

**Pressure gradient effects** Considering the effect of pressure gradients on the spatial growth of turbulent spots, one could expect an overall inhibition of turbulent spot growth for a favourable pressure gradient. For instance, Kline et al. [85] observed fewer “ejections” in a turbulent boundary layer with a favourable pressure gradient. The inhibition of newly formed vortices also occurs for turbulent spots, affecting the overall propagation. The effect is especially prominent in the trailing edge region, where an adverse pressure gradient promotes the steady generation of new turbulent structures, reducing the celerity of the trailing edge [56, 179]. Indeed, there have been several studies observing an effect of pressure gradient, with Mayle [102] concluding the influence of the pressure gradient to be greater than other factors.

Sankaran & Antonia [140] found an increase in both leading and trailing edge celerities in a flow with a favourable pressure gradient. With a Falkner-Skan pressure gradient parameter of  $m = 0.05$ , the leading edge and trailing edge celerity increased from  $c_{le} = 0.83$  to  $c_{le} = 0.86$  and  $c_{te} = 0.57$  to  $c_{te} = 0.66$ , respectively, compared to a flow with no pressure gradient. The same qualitative effect of increased trailing and leading edge celerities for a more favourable pressure gradient was observed in the experimental works of Gostelow et al. [60] (adverse pressure gradient) and Chaiworapuek et al. [20] (adverse pressure gradient), as well as in the numerical work of Johnson [77] (both favourable and adverse pressure gradients). However, Zhong et al. [186], stating the same increase in trailing edge celerity, observed a decreased leading edge celerity for a less adverse pressure gradient, contrary to the findings above. All of these works agree that the influence of the pressure gradient is stronger on the trailing edge celerity than on the leading edge celerity. Additionally, several researchers have stated an increase in spreading angle for adverse pressure gradients and vice versa [20, 38, 60, 61, 77, 81, 140, 170, 186].

**Compressibility effects** In some studies, the leading edge celerity (relative to the boundary layer edge velocity) is reported to not change with the local Mach number [25, 88] (i.e. different Mach numbers (sub- and supersonic) yield the same value for the leading edge celerity), but this is not necessarily conclusive, and may be caused by the large scatter in available numerical and experimental data. Van den Eynde and Steelant [168] conclude a general increase in leading edge celerities with increasing Mach number when considering available data for supersonic investigations. Their review of experimental and numerical data on convection speeds of turbulent spots investigated the effects of different wall temperature to adiabatic wall temperature ratios and local Mach numbers. Whereas the former showed no clear trend, trailing and leading edge celerities increased with higher local Mach numbers (investigated range:  $0 < M_e < 9$ ).

Krishnan and Sandham [88] performed DNS to investigate the dynamics of turbulent spots in compressible isothermal-wall boundary layers. They found that increasing the Mach number ( $M = 2, 4, 6$  investigated) significantly reduces the lateral spreading of turbulent spots. The leading edge celerity remained nearly constant at around 0.87, whereas the trailing edge celerity increased substantially from 0.53 at  $M = 2$  to 0.68 at  $M = 6$ . They observed a differing overall spot geometry close to the wall compared to further away with an upstream-pointing arrowhead for the former (closer to wall) case, compared to the traditional downstream-pointing arrowhead shape expected and seen for the latter case. They attributed this to the lateral overhang region, claiming the orientation of the arrowhead depends on the wall-normal distance.

Various experimental investigations observe a reduction in spreading angle with increasing Mach number [25, 52, 106]. Two distinct mechanisms are involved in the lateral growth of turbulent spots (and similarly for turbulent wedges) [130, 179]. One is simple convection of structures outward from the core along lateral jets of fluid. The other is the aforementioned growth by destabilisation mechanisms proposed by Gad-El-Hak [56], which is dominant for incompressible flows. Redford et al. [130] argue that the latter effect strongly decreases as the Mach number increases, and, at Mach 6, “contributes very little to the spot growth”.

**Reynolds number effects** Many researchers have attributed differences in experimental variations of turbulent spot characteristics to an effect of Reynolds number [171, 182]. Systematic experimental investigations, however, are scarce, especially for flows at higher Reynolds numbers ( $Re_x > 10^6$ ).

James [73] observed a reduced trailing edge celerity with increasing Reynolds numbers ( $3 \cdot 10^6 - 6 \cdot 10^6$ ), but due to limited data points available and uncertainty of the measurements, he was cautious with his interpretation. Ching & Lagraff [22] (thin-film heat flux gauges) measured turbulent spot celerities for unit Reynolds numbers at  $2.4 \cdot 10^6/\text{m}$  and  $4.2 \cdot 10^6/\text{m}$  with Mach number 0.05 and 0.1. They found an increase in leading edge celerity from 0.81 to 0.86 and a decrease in mean celerity from 0.68 to 0.63 for the small and large Reynolds numbers, respectively. Due to the small number of observed spots and large measurement uncertainties, they do not find these differences to be significant.

More solid evidence was found by Wagnanski et al. [182] by means of hot-wire anemometry, with the trailing edge significantly reduced at higher Reynolds numbers while the leading edge celerity remains the same within the uncertainty of the measurement. With the Reynolds number based on the boundary layer displacement thickness ( $Re_\delta$ ) at the turbulent spot initiation point increased from 500 to 1500, the trailing edge celerity reduces from  $c_{te} = 0.62$  to  $c_{te} = 0.5$ . However, the decrease is less significant at higher Reynolds numbers. Johnson [77], computing the three-dimensional linear perturbations for an incompressible flow, found both the leading and trailing edge celerities to decrease with increased Reynolds

number (based on the local momentum thickness Reynolds number  $Re_\Theta$ ). Regarding the leading edge, he argues that the proportion of the boundary layer occupied by the viscous sublayer decreases for higher Reynolds numbers. Hairpin vortices and associated structures move closer to the wall and hence propagate downstream slower. This effect, however, is limited, and celerities are almost unaffected for a momentum thickness Reynolds number above about 500. He observed the effect of Reynolds number on both leading and trailing edge celerity to be enhanced for a favourable pressure gradient.

Fransson [55] did not observe a significant influence of the Reynolds number on trailing and leading edge celerities. However, he only examined Reynolds numbers based on the displacement thickness,  $Re_\delta$ , up to 600. Supporting numerical studies by Levin & Henningson [92] for an asymptotic suction boundary layer, however, showed a small increase for the leading edge celerity (0.87 - 0.90) and a significant decrease for the trailing edge celerity (0.68 - 0.47) for Reynolds number  $Re_\delta$  investigated between 500 and 1200. Additionally, the spreading angle increased from about  $\alpha = 2.4^\circ$  at  $Re_\delta = 500$  to about  $\alpha = 5.1^\circ$  at  $Re_\delta = 1200$ .

From DNS of an incompressible boundary layer, Singer [158] found a lower spreading angle than typically observed in experiments and attributed this to the lower Reynolds number and more stable environment. This decrease in spreading angle was observed experimentally by Schubauer & Klebanoff [152] but not by Wygnanski et al. [182], who state the Reynolds number to have a minimal effect on the spreading angle.

## 2.4 Intermittency distribution

Based on a model of Emmons [49], it is possible to formulate a general intermittency ( $\gamma$ ) distribution with respect to the streamwise distance  $x$  for a quasi-2D flow (intermittency distribution is the same along the spanwise coordinate  $y$ ). The model assumes a “binary” boundary layer state, i.e. the boundary layer is either laminar or turbulent for a given position  $P$  at  $x, y$  at time  $t$  and that the boundary layer transition occurs through the coalescence of turbulent spots. Emmons [49] showed that the intermittency can then be expressed as:

$$\gamma(P) = 1 - \exp \left[ - \int_R g(P_0) dV_0 \right], \quad (2.4.1)$$

with a spot production function  $g(P_0)$  (the probability of spot production at a point  $P_0(x_0, y_0, t_0)$  per unit volume  $dV_0$ ) and  $R$  the dependence volume (spot sweep volume).  $R$  is assumed to be a cone with straight generators in the  $x, y, t$  volume, i.e. has a constant spreading angle in space and time.

Due to a lack of better knowledge, Emmons suggested  $g$  to be a constant independent of  $x$ , i.e. the probability of spot generation is uniform along the whole surface. This proposition was later improved by Dhawan & Narasimha [39]. They suggest  $g(x)$  to depend on the streamwise direction  $x$  with a maximum at some location  $x_t$ . Assuming a Gaussian distribution<sup>1</sup>, they found a best fit to experimental data with a standard deviation close to 0, i.e. close to a Dirac delta function  $\delta(x)$ . This is a model of concentrated breakdown where all turbulent spots arise within a narrow streamwise band. Several measurements have indicated that a Gaussian would fit the experimental data better [59, 173]. However, the limiting case of a Dirac delta function is deemed sufficient if the region of spot production

<sup>1</sup>This seemed sensible since Schubauer & Klebanoff [152] did not observe the origination of turbulent spots upstream of a certain point or very far downstream of that point

is small compared to the total transition length [102]. With  $g(x) = n\delta(x_0 - x_t)$  in equation 2.4.1 one obtains:

$$\gamma(x) = 1 - \exp\left[-(x - x_t)^2 \frac{n\sigma}{U_\infty}\right] \quad (2.4.2)$$

with a turbulent spot production rate per unit length  $n$  and Emmons' dimensionless spot propagation parameter  $\sigma$ .  $\frac{n\sigma}{U_\infty}$  is assumed to be a constant. Studies investigating the spot initiation rate  $n$  will typically assume  $\sigma$  to be constant in order to estimate  $n$  from intermittency distributions [104, 128]. For an idealised triangular shape of turbulent spots, the spot propagation parameter can be expressed as [61, 74, 111]:

$$\sigma = \left(\frac{1}{c_{te}} - \frac{1}{c_{le}}\right) \tan(\alpha). \quad (2.4.3)$$

Introducing a dimensionless streamwise coordinate

$$\xi = \frac{x - x_t}{x_{75} - x_{25}}, \quad (2.4.4)$$

where  $x_{75}$  and  $x_{25}$  are the streamwise locations with intermittency  $\gamma = 0.75$  and  $\gamma = 0.25$ , respectively, one obtains the Narasimha intermittency distribution<sup>2</sup> [39, 114, 115]

$$\gamma = 1 - e^{-\frac{(x-x_t)^2 n\sigma}{U_\infty}} = 1 - e^{-0.411\xi^2}. \quad (2.4.5)$$

Because of the reasonably good agreement with experimentally observed intermittency distributions (e.g. Mee & Goyne [103], Owen [119]), equation 2.4.5 is often referred to as ‘‘universal intermittency distribution’’ [88, 103, 114]. Solomon et al. [161] extended this distribution for the generalised case of a changing boundary layer edge velocity, as in a flow with strong pressure gradients, such as those relevant to turbomachinery flow cases.

Johnson & Fashifar [78] assume the probability of turbulent spot generation to increase linearly with  $x$ . Solving the resulting differential equation, they obtain

$$\gamma = 1 - e^{-0.0941\xi^3}. \quad (2.4.6)$$

Note the similarity to the Narasimha intermittency distribution of equation 2.4.5 but with  $\xi$  to the power of 3 instead of 2. This relation is phenomenologically similar to the empirical relation proposed by Abu-Ghannam & Shaw [1]  $\gamma = 1 - \exp(-5\eta^3)$ , with the dimensionless distance to the location of transition onset  $\eta = (x - x_s)/(x_e - x_s)$ , where  $x_s$  and  $x_e$  are the locations of start and end of the transition region respectively. Both have demonstrated excellent correlation with experimental data [54, 156].

---

<sup>2</sup>The original publication and many citations state a factor of  $a = 0.412$  in  $1 - e^{-a\xi^2}$ . A careful calculation, however, shows that with  $\tilde{x} = (x_{25} - x_t)/(x_{75} - x_{25})$  one obtains  $\ln(0.25) = -a \cdot (\tilde{x} + 1)^2$  and  $\ln(0.75) = -a \cdot \tilde{x}^2$  which solves as  $a = 0.411$  with 3-digit precision. Therefore, the value stated in equation 2.4.5 will be used throughout this thesis.



# Chapter 3

## Experimental Methods

### 3.1 Cryogenic Ludwieg-Tube Göttingen KRG

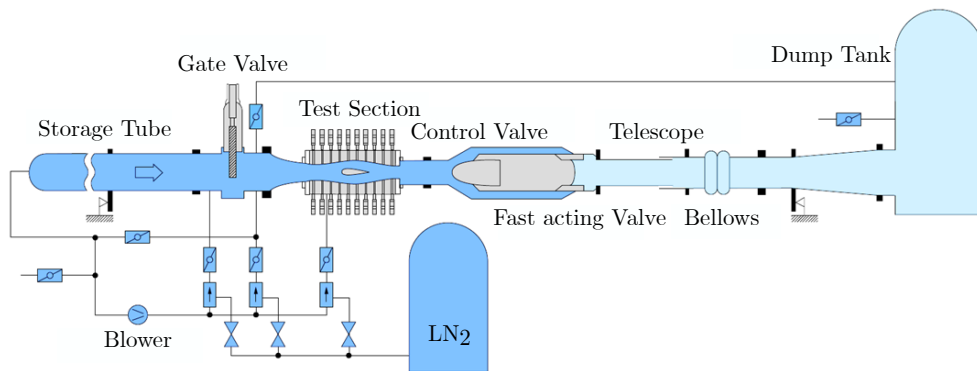


**Figure 3.1.1:** Sketch of the Cryogenic Ludwieg-Tube Göttingen (KRG) [87].

A specialised test facility with a low initial free stream turbulence level is necessary to systematically examine the effects of Mach number, Reynolds number and pressure gradient on the propagation and development of turbulent spots in a high Reynolds number subsonic flow. One suitable wind tunnel is a Ludwieg-Tube in a subsonic configuration, as used in this investigation. All tests were conducted in the Cryogenic Ludwieg-Tube Göttingen (KRG), using gaseous nitrogen as the test gas. A sketch of the facility is shown in figure 3.1.1. The key components are: the storage tube, test section, control valve, fast-acting valve and dump tank. Ludwieg-Tubes are often configured in a supersonic configuration, where the test section and control valve are the other way around [95, 96]. Areas marked dark blue can be pressurised to a charge pressure  $p_c$  and cooled to a charge temperature  $T_c$ . A fast-acting valve separates the pressurised area from an area with lower pressure, typically kept at atmospheric conditions. When opening the fast-acting valve, gas accelerates from high to low pressure regions, leading to the formation of an expansion fan travelling at the speed of sound downstream in the storage tube. The Mach number in the storage tube and the test section only depends on the ratio of cross-sectional areas of the control valve (lowest cross-sectional area in the case of KRG) and the storage tube and test section, respectively. The Reynolds number can be tuned by adjusting the charge temperature and pressure, which, in the case of KRG, are limited to above 105 K

and below 1.25 MPa. Therefore, Mach and Reynolds numbers can be adjusted and set independently within a specific range. In the present investigation, the charge temperature range was set between 273 K to 283 K and the pressure below 0.4 MPa due to limitations of the camera environment and considerations of the intensity and sensitivity of the iTSP. Each sequence of setting the desired charge temperature and pressure and the execution of the corresponding measurement is called a run. The measurement campaign consists of a series of individual runs labelled with an ascending data point number (DPN).

The test section is 0.4 m wide, 0.35 m high, and 2 m long. Airfoil models with chord length up to 0.2 m are installed onto turntable supports, allowing easy setting of various angles of attack. One key feature of KRG is the test section's adaptive upper and lower walls, which allow contours to be set for interference-free flow [2, 138].

The absence of moving parts, which are needed in other wind tunnel types for operating and regulating the flow, allows for good overall flow quality (mass flux density turbulence  $Tu_{pu} \approx 0.6\%$  [87]). The test time, in which quasi-stable conditions are present in the test section, is limited by the length of the storage tube and the time the expansion fan requires to pass down it and to return. The 130 m long storage tube allows for test times of several tenths of seconds, sufficient for the current investigations. Two specific advantages of this facility for investigating turbulent spots are discussed below. Further details of the KRG and investigations of laminar-turbulent transition in this wind tunnel can be found in [30, 40, 87].

#### **Suitability of quantifying turbulent spots with thermographic imaging in KRG**

A good general flow quality is required to examine naturally occurring turbulent spots in high Reynolds number flows. For a high turbulence level, the transition onset is too early and the transition length is too low [102], so that wind tunnels with atmospheric conditions and high turbulence levels are not suitable. Ludwig-tubes, on the other hand, in general, yield a low turbulence level and are a good candidate for transition measurements in the sub-sonic flow conditions that are investigated here. The parameter range is limited by the abilities of the wind tunnel and the properties of the wind tunnel model but can be set independently of each other.

A further advantage is the naturally occurring temperature step during a run due to the expansion, which allows to distinguish easily between laminar and turbulent regions by means of a thermographic imaging technique like TSP. Laminar and turbulent boundary layers have different heat-transfer coefficients for heat exchange between gas and surface, resulting in differing surface temperatures when a temperature difference between adiabatic wall and surface temperature ( $T_{aw}/T_w \neq 1$ ) is given. The adiabatic wall temperature refers to the temperature of the boundary layer close to the wall if the wall was thermally insulating (adiabatic). Due to heat transfer within the boundary layer, this temperature is lower than the freestream stagnation temperature and depends on the state of the boundary layer. Figure 3.1.2 shows the total pressure and freestream temperature development during a run at KRG. At about  $t = 2.6$  s, the fast-acting valve is opened, and the flow is considered quasi-stationary shortly after. In this case, the period of quasi-stationary flow conditions starts at about  $t = 3.0$  s. The wind tunnel data recorded at  $3.2 \text{ s} \leq t \leq 3.3 \text{ s}$  is used to determine the aerodynamic properties of the particular run. This interval is when the flow is considered most developed and stable [87].

Past measurements showed increased free stream turbulence during a run, causing turbulent events along the otherwise laminar boundary layer on the model [30, 42, 87]. These events are individual turbulent spots, as will be shown later. They are most likely caused by the side wall boundary layer of the storage tube growing during the run and thereby increasing

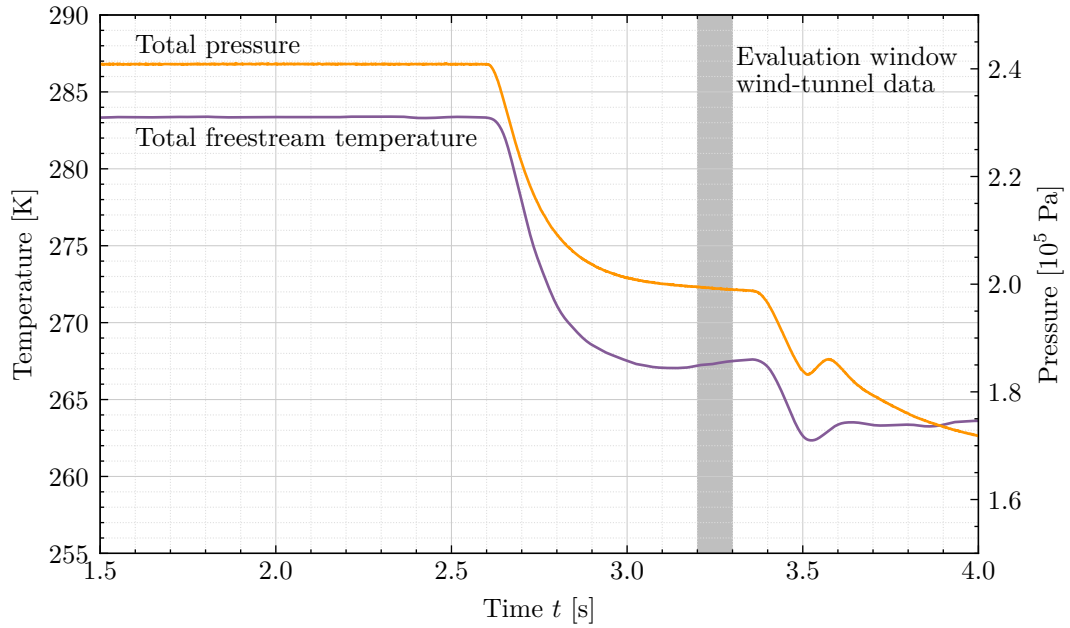


**Figure 3.1.2:** Total pressure and smoothed freestream temperature distribution for a typical run at KRG. The evaluation window is set to  $3.2\text{ s} \leq t_{eval} \leq 3.3\text{ s}$  with  $Re_c = 6 \cdot 10^6$  and  $M = 0.8$ .

the turbulence level in the test section. The spots, therefore, occur more towards the end of the run and closer to the side walls of the test section. This effect yields a unique possibility to visualise naturally occurring turbulent spots in a high Reynolds number flow with a thermographic method. It makes examining turbulent spots even far upstream of the transition location possible. For the run presented in figure 3.1.2 at the highest measured Mach number, the temperature step is approximately 15 K. The step is considerably lower for lower Mach numbers. The higher temperature difference for higher Mach numbers will yield a higher signal-to-noise ratio, making the turbulent spots easier to detect and quantify. Additionally, the turbulence level increases for higher Mach numbers [87], increasing the number of detectable turbulent spots during a run. The time window to detect turbulent spots was set to  $3.0\text{ s} \leq t \leq 3.3\text{ s}$ , during quasi-stable flow conditions, although most turbulent spots were detected between  $3.2\text{ s} \leq t \leq 3.3\text{ s}$ .

The iTSP used for this investigation (discussed in section 3.4) shows high levels of photodegradation (loss in intensity and sensitivity). However, the short run times in KRG and the dark, oxygen-free nitrogen environment limit this photodegradation to allow up to 150 runs before a recoating becomes necessary.

## 3.2 Principle of Temperature-Sensitive Paint (TSP)

The temperature-sensitive paint (TSP) measurement technique is a global and non-intrusive tool for surface temperature measurements in various applications [50, 84, 94]. It enables the visualisation and quantification of the temperature distribution on surfaces with high spatial and temporal resolution.

The fundamental principle behind TSP lies in the temperature-dependent fluorescence properties of specific molecules known as luminophores. With incident light of a particular wavelength, photons are absorbed to excite the luminophore from the ground electronic state to an excited electronic state [94]. They can return to the ground electronic state

through different radiating (fluorescence and phosphorescence) and non-radiating processes. In general, the non-radiating process is more likely at higher temperatures through a process known as thermal quenching. A relationship between the temperature of the TSP and the intensity of the remaining radiating processes can therefore be modelled by what is known as the Arrhenius-equation [94]:

$$\ln \frac{I(T)}{I(T_{ref})} = \frac{E_{nr}}{R} \left( \frac{1}{T} - \frac{1}{T_{ref}} \right) \quad (3.2.1)$$

with the activation energy for the non-radiating process  $E_{nr}$ , the universal gas constant  $R$  and a reference temperature  $T_{ref}$ .  $I(T)$  and  $I(T_{ref})$  refer to the luminescent intensities recorded for temperatures  $T$  and  $T_{ref}$ , respectively. For some applications, the Arrhenius equation 3.2.1 is not fully obeyed over a large temperature range and, therefore, an empirical relation

$$T = f(I(T)) \quad (3.2.2)$$

is used with a suitable function  $f$  that is invertible in the relevant temperature range [94]. The surface temperature can then be determined at every location by

$$T = f \left( \frac{I(T)}{I(T_{ref})} f^{-1}(T_{ref}) \right), \quad (3.2.3)$$

if the luminescent intensities  $I(T)$  and  $I(T_{ref})$  for a reference temperature  $T_{ref}$  are known. In KRG,  $I(T_{ref})$  is taken prior to the run with known charge temperature  $T_c = T_{ref}$ . A further non-radiating decay process is oxygen quenching, which is enhanced for higher partial pressures of oxygen. This process is exploited for pressure-sensitive paints (PSP) if the surrounding fluid contains oxygen. This process, unfortunately, is also present for many TSPs, yielding an additional pressure sensitivity which must be accounted for.

Before the excited molecule emits a photon while falling to its ground state, some energy is lost through internal (e.g. vibrational) relaxation processes. The emission wavelength is, therefore, longer (lower energy) than the excitation wavelength (higher energy), a difference known as the Stokes shift. With a choice of appropriate optical filters, this property can be used to separate the emission light from the excitation light. Since the emitted light intensity is much lower than the excitation light, this step is necessary to acquire quantitative temperature information.

For a TSP, the luminophores are mixed with a binder and a solvent or carrier that aids in applying and drying the paint onto the target surface. The properties of the TSP strongly depend on the binder and its interactions with the luminophore, which is why properties can only be attributed to the whole paint composition.

A TSP system typically consists of a coated surface of interest, an illumination source (typically a high-power LED or a laser) and an intensity measurement device, most often a camera, photomultiplier or photodiode. The optical access to the surface of interest is many times limited in a wind tunnel, requiring the excitation light source and camera to be installed at an oblique angle to the surface, requiring specialised image recording and post-processing. Lambert's cosine law states that the luminous intensity is directly proportional to the cosine of the angle between the light source and the wall-normal

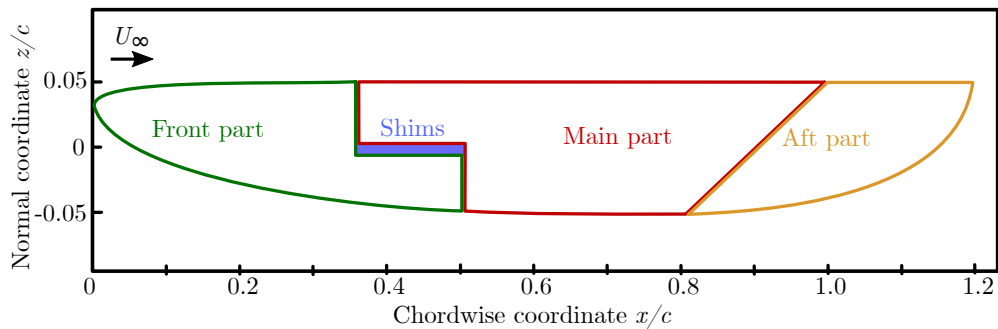


**Figure 3.3.1:** Cross-sectional view of the PaLASTra test model. Chord length  $c = 200$  mm.

direction. Therefore, installing the light source at an oblique angle will lower the excitation rate and must be compensated for by higher intensities of the excitation source. When using a camera to measure the emission intensity, equation 3.2.3 states that the surface temperature can be obtained when dividing the image with one recorded at a known surface temperature distribution.

### 3.3 Wind tunnel model

#### 3.3.1 Design and model cross-section

The wind tunnel model PaLASTra (an acronym for “flat plate for the analysis of the effect on laminar-turbulent transition of surface imperfections, wall temperature ratio and pressure gradient” [30]) used for this investigation is depicted in cross-section in figure 3.3.1. The cross-section design ensures a uniform pressure gradient over a large streamwise area on this upper side - especially in the investigated area - for a wide range of angles of attack and Mach numbers in the subsonic regime. Therefore, the influence of flow parameters could be investigated independently of the pressure gradient. Details on the model design can be found in [30]. The model has been used in various previous investigations examining the boundary layer transition for numerous modifiers, including: flow conditions [30, 136]; 2D-surface imperfections in the form of steps, gaps and combinations thereof [30, 35, 41, 43]; and the effect of suction [40, 41, 43]. The model width is  $b = 500$  mm (so it can be mounted in the side walls of the 400 mm wide test section), 20 mm maximum thickness and has a chord length of  $c = 200$  mm. It consists of three parts: A front part with a modified super-ellipse curved surface to reduce leading-edge receptivity to freestream disturbances, a main part that is flat on the upper side and an additional aft part, also flat. In the original design, the model consisted only of the front and main parts with an abrupt contour change on the lower side of the model at  $x/c = 80\%$ . It had been designed to force flow separation at this location, independent of the Mach number and angle of attack. Later studies presented in [137] showed a significant influence of pressure fluctuations inside the test section on the flow conditions on the upper side of the model, which are induced by a large separation region. Therefore, an additional aft part was added and used here to reduce the effect of the separation region [137]. For this investigation, a new main part was designed and manufactured. Its main purpose is to allow two independent measurement techniques at the same chordwise location but different spanwise regions: (1) iTSP capable of resolving fast temperature changes, denoted iTSP; and (2) hot-film anemometry. Two

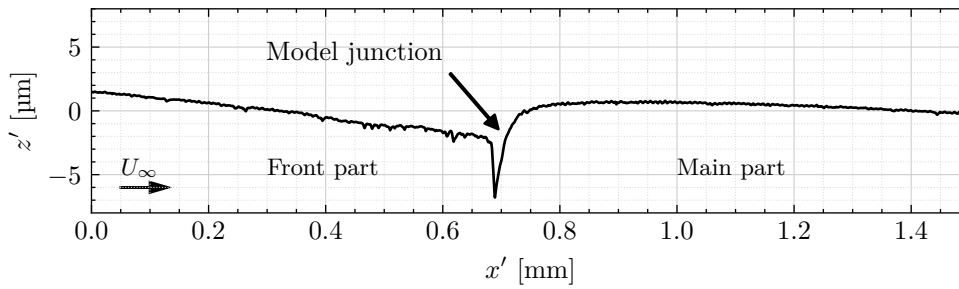


**Figure 3.3.2:** Profile of the model around the model junction after the test campaign.  $x'$  is the traverse coordinate of the profilometer in streamwise direction and  $z'$  the measured value in wall-normal direction.

pockets are incorporated in the main part of the model, one 120  $\mu\text{m}$  deep on the port side to accommodate iTSP, and one 110  $\mu\text{m}$  deep on the starboard side to accommodate the hot-films.

Shims of different thicknesses can be installed between the main and front parts to investigate the effect of steps and gaps. This investigation, however, focuses on a nominally flat configuration without 2D surface imperfection. The model was carefully assembled to ensure that no step or gap was present at the model junction. However, due to the extensive aerodynamic loads at KRG, a small surface imperfection could be detected after the measurements were performed at the spanwise location of the iTSP region of interest. Figure 3.3.2 shows the profile around the model junction after the test campaign. A small gap  $< 20 \mu\text{m}$  and forward-facing step  $< 3 \mu\text{m}$  could be measured. The dimension of this imperfection is small enough not to expect it to affect laminar-turbulent transition for the investigated test cases [35, 159].

#### 3.3.2 Conventional instrumentation

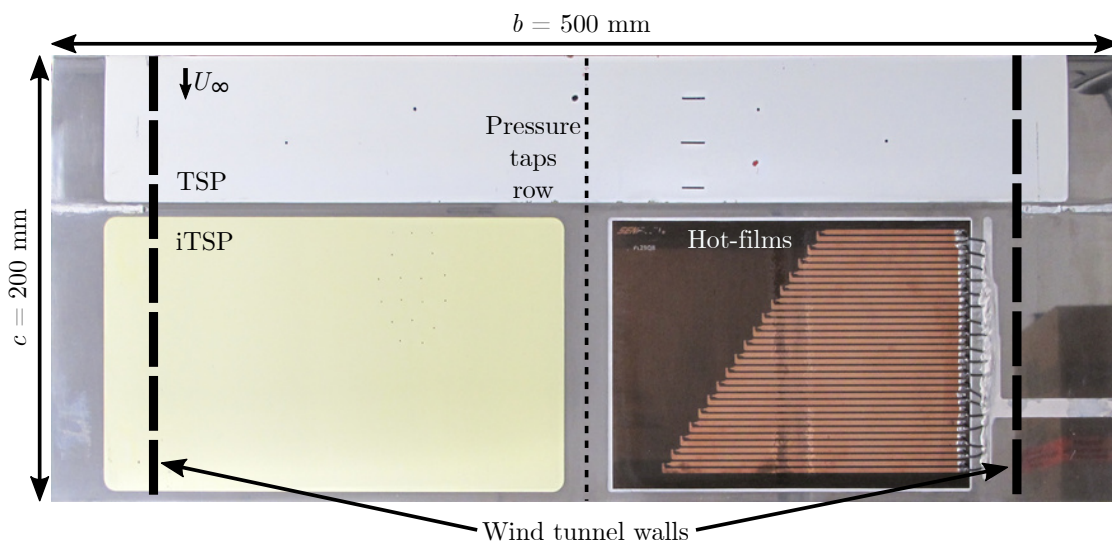


**Figure 3.3.3:** Top plan view of the wind tunnel model (flow from the top - aft part is not visible).

The top plan view of the wind tunnel model is presented in figure 3.3.3. On the left and right side of the model, the locations of the wind tunnel walls are indicated for when the wind tunnel model is installed in the test section.

#	$x$ [mm]	$y$ [mm]	$z$ [mm]
1 <sup>*,†</sup>	20.2	150.0	9.4
2 <sup>†</sup>	30.0	150.0	8.8
3 <sup>*</sup>	40.2	145.0	10.0
4	130.0	150.0	8.5
5 <sup>†</sup>	170.0	150.0	8.5

**Table 3.3.1:** Position of the thermocouples in the wind tunnel model. \* marks thermocouples that are located at the surface. † marks thermocouples that malfunctioned before or during the measurement campaign.

#	$x$ [mm]	$y$ [mm]	#	$x$ [mm]	$y$ [mm]
1	82.0	358.0	10 <sup>†</sup>	136.0	320.2
2	88.0	353.8	11	142.0	316.0
3	94.0	349.6	12	148.0	311.8
4	100.0	345.4	13	154.0	307.6
5 <sup>†</sup>	106.0	341.2	14	160.0	303.4
6	112.0	337.0	15	166.0	299.2
7	118.0	332.8	16	172.0	295.0
8	124.0	328.6	17	178.0	290.8
9	130.0	324.4	18	180.0	286.6

**Table 3.3.2:** Positions of the hot-film sensor on the wind tunnel model with  $z = 10$  mm for all sensors (on the upper surface). † marks hot-film sensors that did not function reliably during the measurement campaign.

The model is equipped with a total of 52 pressure taps on both the upper and lower surfaces of the model. They are aligned along the centre ( $y/b = 0.5$ ) of the model. A numerical study in the design process of the wind tunnel model revealed there was no significant difference in pressure distribution for a laminar or turbulent boundary layer. Since the pressure taps are not expected to influence succeeding ones, other than the pressure taps on the leading edge causing a turbulent wedge, a streamwise alignment allows for a larger spanwise area of undisturbed laminar flow compared to a staggered approach. Two of the pressure taps are installed with an offset at  $y/b = 0.48$  to increase the resolution of the pressure taps at the leading edge region. The positions of the pressure taps are identical to those listed in [30] also for the newly manufactured main part of the model. The pressure data are acquired at 100 Hz sampling rates with 16 bit resolution. Furthermore, five K-type thermocouples (0.08 mm wire diameter, accuracy  $\pm 0.3$  K) are installed: three in the front part of the model (of which two are installed inside the TSP layer at the surface) and two in the main part 1.5 mm below the surface. Table 3.3.1 lists the positions of the thermocouples in the model. During the current measurement campaign, three thermocouples had a malfunction (caused partly by damage obtained from previous measurement campaigns) - they are marked by † in table 3.3.1. The signals from the remaining two were recorded at 1000 Hz.

**Hot-films** The starboard side of the model is equipped with a custom Senflex<sup>®</sup> multiple hot-film sensor array (MHFS) designed by the author and manufactured by Tao of Systems Integration, Inc. 18 hot-films are staggered at an angle of  $35^\circ$  to avoid being influenced by the leads and heat input from preceding sensors. The positions of the individual sensors are given in table 3.3.2. The angle from one sensor to the outermost part of the lead of a preceding hot-film is  $17.5^\circ$  and, therefore, well outside the spreading angle of potential

disturbances caused by the preceding lead, estimated to spread at an angle of about  $10^\circ$  (see section 5.3 [53]). They are equally spaced 3% of chord length apart, ranging from  $x/c = 41\%$  to  $x/c = 92\%$  and covering the main region of uniform pressure gradient. The sensors themselves consist of a thin nickel layer that is 1.45 mm wide, 0.1 mm long (streamwise) and  $0.2\ \mu\text{m}$  thick; electrical connection is provided by copper leads ( $5\ \mu\text{m}$  thick). The leads were specifically manufactured to be thin due to the flow conditions at KRG and yet allow a sufficiently fast time response. They are therefore 2 mm wide and have a total lead resistance of  $0.4\ \Omega$  to  $0.7\ \Omega$ . The basis of the hot-film array is a  $51\ \mu\text{m}$  thick *Upilex*<sup>®</sup> *S* polyimide film that is glued in the pocket with double-sided adhesive tape (3M<sup>®</sup> VHB<sup>®</sup> Adhesive Transfer Tape F9460PC with a nominal thickness of  $58\ \mu\text{m}$  and measured thickness of  $60\ \mu\text{m}$ ). The remaining gaps between the film and model are filled with polyester fine filler (Presto<sup>®</sup> Polyester Feinspachtel) and sanded to ensure a flush mounting. Connection wires are soldered to the leads and embedded in a groove leading out of the test section. The soldering point had to be within the test section since the clamping jaws at the wind tunnel side wall would otherwise damage the leads. The soldering points are located close to the wind tunnel wall, so the influence on the surface of interest is considered negligible (see figure 3.3.3).

The wires are connected to custom-designed in-house constant-temperature anemometers (CTA) [87]. Each of the anemometers contains a Wheatstone bridge designed to keep the hot-film at a constant resistance and, with that, at a constant temperature. Variations in the heat transfer between flow and hot-films, caused by different boundary layer conditions (boundary layer transition and turbulent spots), change the power output required to keep the hot-films at a constant temperature, yielding a relation between the local heat transfer and the analogue output of the hot-film. The sensors were operated at an overheat ratio (OR) of  $\frac{R_S}{R_0} = 1.4$ , where  $R_S$  and  $R_0$  are the resistance at the operating level and ambient condition, respectively. Before every data point, the anemometers were experimentally checked and confirmed to have a frequency response of at least 50 kHz using a square-wave test. The OR influences the frequency response, with higher ratios enabling higher frequency responses. The analogue output of each anemometer was recorded with a separate digital data acquisition system (YOKOGAWA<sup>®</sup> SL 1000) with a sampling frequency of 1 MHz and resolution of 16 bit.

**Comparison and limitations of other measurement techniques** The conditions in the Cryogenic Ludwig-Tube at the DLR in Göttingen (KRG) prove challenging for the application of several further measurement techniques and indeed are often not feasible due to the large flow speeds, very thin boundary layers and short test times. Other thermographic measurement techniques, like thermochromic liquid crystals or infrared thermography, are not an option due to their limited temporal or spatial resolution. Pressure transducers like Kulites<sup>®</sup> or microphones require orifices that introduce flow disturbances. Similarly, hot-films introduce disturbances due to the high temperatures required for the temporal resolution. Therefore, hot-films must be arranged staggered, limiting the possibility of investigating individual turbulent spots. Even if they did not introduce disturbances and could be aligned streamwise, the spatial resolution and investigated area are minimal. To independently inspect the effect of Reynolds number, Mach number and pressure gradient, which each alter the transition location significantly, several models would be necessary, each focusing on different parts. Additionally, spanwise and streamwise propagation would need to be studied separately with different models [25, 75].

### 3.3.3 TSP instrumentation

Two areas of the model are coated with TSP: the front part including the leading edge, and the port side of the main part. The front part is coated with the same TSP used in previous investigations (in a pocket in order to reach the expected model contour), which has a Europium (Eu) complex as luminophore [117]. It could be sanded to very low roughness values (see section 3.4.2) and spans the entire leading edge up to 5% of the lower side of the model. The TSP applied on this area is not suitable for highly time-resolved measurements. It was utilised in previous measurements to detect turbulent wedges arising at the leading edge region. Due to the limited optical access at KRG, it was impossible to investigate this area with the current setup. Nevertheless, it remained coated with the original TSP to ensure the same model contour for comparison with previous measurements.

The pocket on the main part is coated with iTSP, which will be discussed in detail in section 3.4.2. It spans a chordwise region of 36.5% to 97.5% on the upper side of the model.

Around the area of the model junction, no TSP is applied to ensure a smooth surface in the area of the model junction. The aft part, whose sole purpose is to reduce the separation region as discussed above, was not coated.

## 3.4 iTSP setup in KRG

### 3.4.1 iTSP properties

The iTSP applied to the pocket in the main part of the model consists of three layers: (1) A thin primer layer (approx. 20  $\mu\text{m}$ ), to provide better adhesion to the metallic surface; (2) A thick white base layer (approx. 100  $\mu\text{m}$ ) for thermal insulation and to create a diffusive light-reflecting background; (3) The active layer (less than 1  $\mu\text{m}$  thickness) consisting of the luminophore dissolved in an organic binder material. Since the active layer is very thin, the roughness of the base layer plays a significant role in the final roughness. Therefore, the base layer is sanded and polished to the required thickness and roughness before applying the active layer. The active layer chosen for this investigation was developed for application in high-enthalpy wind tunnels and is capable of detecting very fast temperature changes.

Dichlorotris (1,10-phenanthroline) ruthenium (II) hydrate (98%) (Ru(phen) - CAS number: 207802-45-7) is used as luminophore, which has a very short luminescent lifetime of less than 1  $\mu\text{s}$  [107]. An ethanol-soluble polyamide-based polymer acts as a binder. Both are dissolved in ethanol and sprayed on the base layer of the iTSP section of the model with a SATAminijet Spraygun with a 1 mm diameter orifice. The luminophore concentration chosen was 0.16 mol/L based on the binder density. Similar iTSP formulations based on the same luminophore and polymer have already been used in other works [11, 99, 120, 125]. Figure 3.4.1 shows the normalised emission and excitation spectra of the iTSP at 283 K. The emission and excitation peaks are located at 600 nm and 459 nm respectively, so that the Stokes-shift is 141 nm. A spectrum of the LED output used to excite the iTSP and the filter properties used to separate excitation and emission light are described in section 3.4.3.

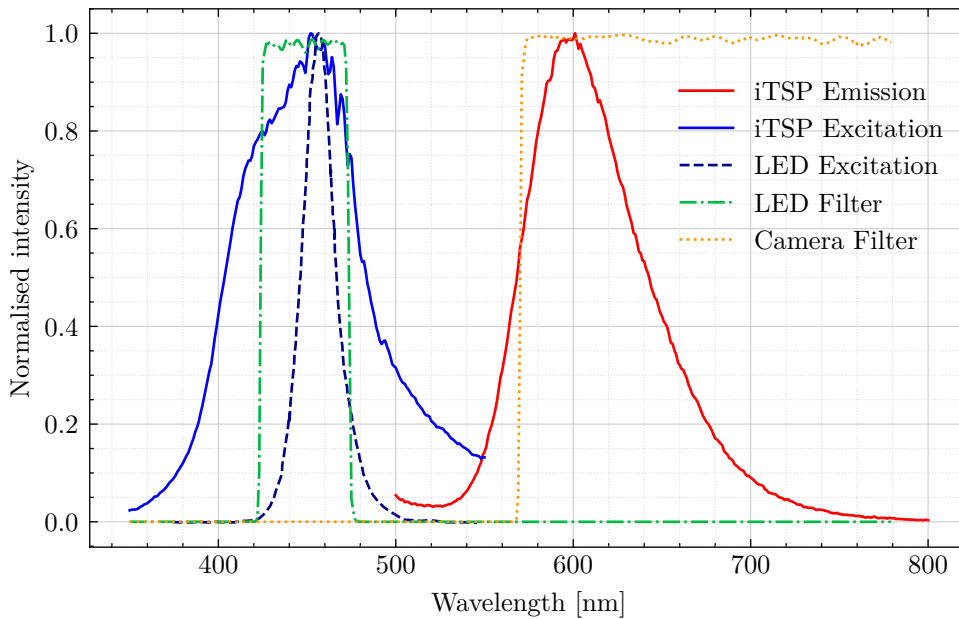


**Figure 3.4.1:** Emission and excitation spectra for Ru(phen) at  $T = 283$  K, LED spectrum and transmission spectra of the LED and camera filters.

**Calibration** The sensitivity of the iTSP is determined in a calibration chamber, where temperature and pressure can be set individually. Details on setup and properties of the chamber can be found in reference [46].

A small calibration sample (an aluminium plate) with dimension 15 mm by 15 mm is coated at the same time as the model to ensure that the coating has the same paint composition and thickness. For temperatures ranging from 273 K to 312 K, the luminescent intensity is captured with a CCD-camera and the signal averaged over an area of 40 by 40 pixels (about 10 mm by 10 mm). Excitation wavelength and filters must be the same as in the wind tunnel setup. The values normalised with the intensity recorded at  $T_{ref} = 283$  K are presented in figure 3.4.2(a). From this, the relative temperature sensitivity  $S(T)$  [%/K] at a temperature  $T$  is defined here by (linearised approximation)

$$S(T) = \frac{(I_+ - I_-) \cdot 100}{(I_+ + I_-)/2 \cdot (2\Delta T)}, \quad (3.4.1)$$

where  $I_- = I_{T-\Delta T}$  and  $I_+ = I_{T+\Delta T}$  are the intensity values at temperatures  $T - \Delta T$  and  $T + \Delta T$ , respectively. The determined sensitivities for the investigated iTSP are shown in figure 3.4.2(b). The error bars are determined with the standard deviation of the mean of the relative intensity and an assumed statistical temperature uncertainty of the calibration chamber of 0.1 K. Furthermore it takes into account an estimation for the dark current drift of the camera (2 counts) and scattered light from neighbouring samples. For the temperature range used in the experiments, the iTSP has a high initial sensitivity of around  $-5\%/K$ . The pressure sensitivity was determined to be only about  $-7\%/100kPa$ . Pressure sensitivity is caused by oxygen quenching, where the luminescent intensity depends on the partial pressure of oxygen [94] (see section 3.2). Since the experiments were conducted in a nitrogen environment without oxygen, the pressure sensitivity cannot influence the results. The intensity and sensitivity of a separate sample coated the same way as the calibration sample but without the luminophore (primer, base layer, and polyamide-based polymer)

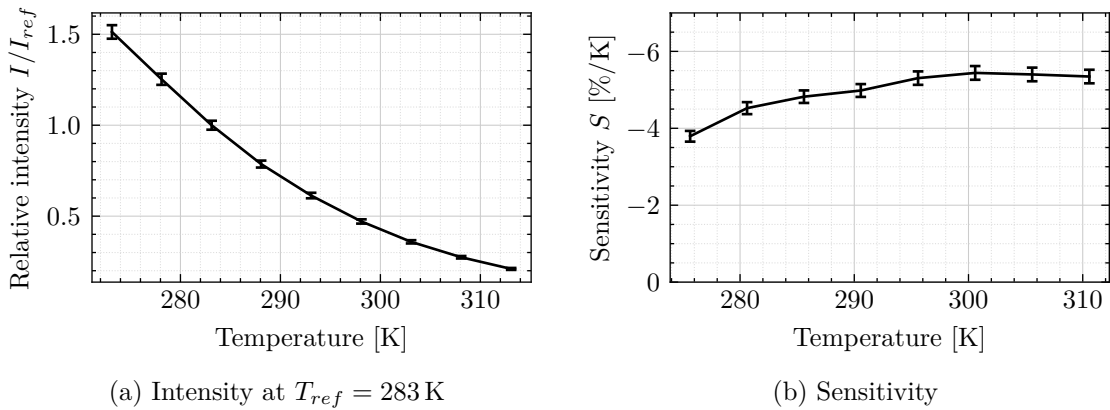


**Figure 3.4.2:** (a) Relative intensity (error bars are multiplied with a factor of ten for better visibility) and (b) Sensitivity of the iTSP in the relevant temperature range.

were also investigated. However, no luminescent intensity could be detected, confirming that all the luminescent intensity is caused by the luminophore alone.

**Photodegradation** The iTSP is sensitive to photodegradation - luminescent intensity and sensitivity decrease irreversibly with duration of illumination. A separate test was performed to estimate the photodegradation. Two samples coated with two different thicknesses of the active layer of iTSP were illuminated for up to 220 minutes and compared with samples coated identically but stored in a dark environment (reference samples). The thicknesses were measured to be  $0.4 \mu\text{m}$  and  $1.0 \mu\text{m}$  based on considerations discussed in section 3.4.2. The samples were illuminated with a Luminus CBT-90-B with a peak wavelength of  $456 \text{ nm}$  at a distance of  $10 \text{ cm}$ . Total LED power was set to  $1.32 \text{ W}$ . This intensity is estimated to be 1-2 orders of magnitude less than the illumination intensity during the wind tunnel tests. After fixed intervals of illumination exposure, the luminescent intensities and sensitivities were measured and compared to the reference samples. The respective intensity and sensitivity values at a temperature of  $283 \text{ K}$  are presented in figures 3.4.3 and 3.4.4. Like stated above, the error bars are determined with the standard deviation of the mean of the relative intensity and an assumed statistical temperature uncertainty of the calibration chamber of  $0.1 \text{ K}$  with an estimation for the dark current drift of the camera (2 counts) and scattered light from neighbouring samples taken into account. The luminescent intensity values drop significantly even for only short illumination times. The reference samples not exposed to the continuous illumination show no loss in luminescent intensity within the range of uncertainty of the measurement. After  $t = 240 \text{ min}$ , the luminescent intensity had already decreased to less than 20% of the starting value.

Similarly, the sensitivity also decreases after extended exposure to LED illumination. Even very short illumination exposures of 2 minutes negatively affect the sensitivity by around 5% to 10%. For very long illumination, the sensitivity only reduces slowly and remains at a level just below  $-2\%/K$ . For many applications, this sensitivity is sufficient to visualise temperature distributions. For the current investigation, where the signal-to-noise ratio is expected to be very low, greater sensitivity is needed to determine turbulent spot properties quantitatively. Therefore, it is necessary to account for the photodegradation and limit the adverse effects as much as possible; this is described in greater detail in section 4.1.

Generally, the thinner layer showed stronger degradation. The thin layer yields a lower sensitivity even with no controlled illumination exposure, possibly due to an initial decrease occurring during the painting and drying stage of the sample preparation. The

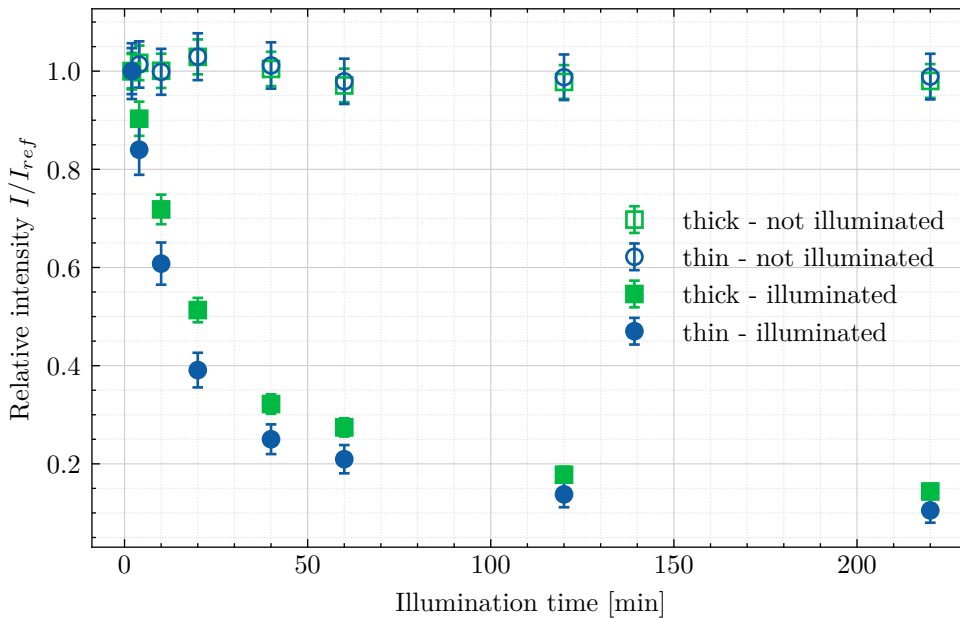


**Figure 3.4.3:** Intensity degradation with accumulated illumination time at  $T_{ref} = 283$  K.  $I_{ref}$  is the reference intensity recorded for the corresponding sample prior to the ageing test.

effect of paint thickness must also be considered for a quantitative temperature determination and plays a role in choosing a suitable paint thickness, as described in section 3.4.2.

The LED intensity chosen for this test ensured that the temperature remained constant (at room temperature) during exposure; i.e. there was no heating of the paint due to the illumination. Therefore, the possibility that the observed effect is merely due to thermal degradation is excluded. In a further measurement, the reference samples were stored in a dark location for 2 weeks. No significant decrease in luminescent intensity or sensitivity could be determined, confirming that the degradation is indeed caused only by light exposure.

### 3.4.2 Coating

The three layers comprising the whole iTSP - primer, base layer, and active iTSP layer - are sprayed consecutively using a spray gun with one day drying time between layers. The base layer was purposely coated thicker and then sanded down to ensure the right homogeneous thickness throughout the pocket and a sufficiently low roughness level. A total of 18 small markers (round dots) with a diameter less than 1 mm are applied with an edding 8400 felt tip marker on the base layer. These are later used for image alignment and mapping, as described in section 4.2.2. The number of markers is predicated by the fact that camera images were recorded at different resolutions and with differing fields of view; consideration of these various aspects led to the adopted number (and positioning) of the markers to facilitate accurate mapping.

**Roughness of TSP** The roughness of both the TSP layer on the front part and the iTSP layer on the main part of the model was measured with a contact profilometer (Mahr Perthometer S2 with MarSurf GD 25) with a vertical resolution of  $\pm 0.8$  nm. On

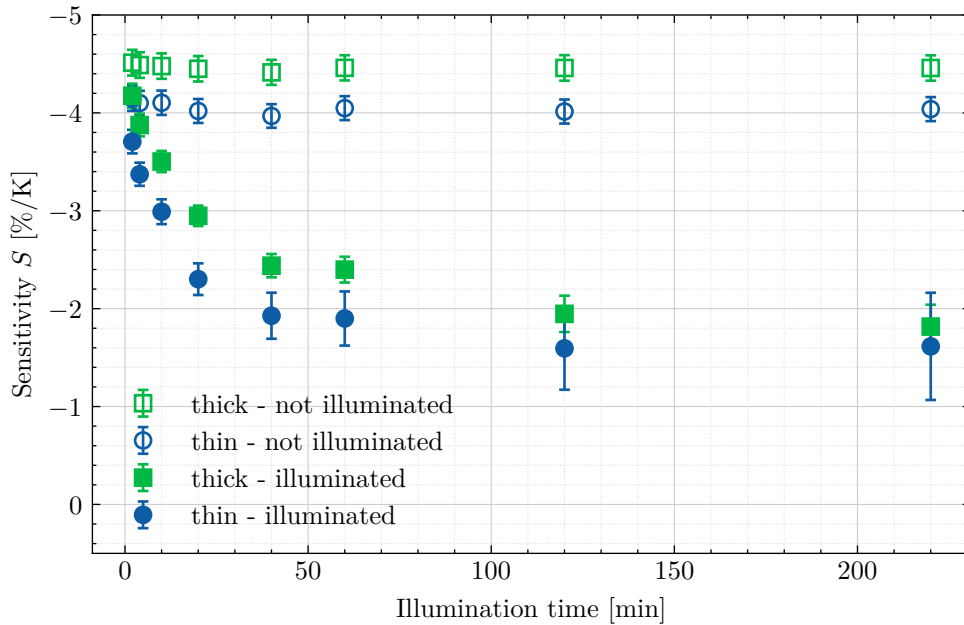


**Figure 3.4.4:** Sensitivity degradation with accumulated illumination time at  $T_{ref} = 283\text{K}$ .

the front part of the model, the TSP was polished to obtain a low surface roughness, which was critical to maintaining laminar flow in this region. The average ( $R_a$ ) and mean peak-to-trough ( $R_z$ ) roughnesses were determined here to be  $R_a = (0.033 \pm 0.002)\ \mu\text{m}$  and  $R_z = (0.28 \pm 0.03)\ \mu\text{m}$ . On the iTSP layer, where no polishing of the active layer was possible except for minor work, the average roughness is higher with  $R_a = (0.15 \pm 0.03)\ \mu\text{m}$  and  $R_z = (1.7 \pm 0.4)\ \mu\text{m}$ . Still these values are well below critical values stated in literature for three-dimensional roughness elements and are therefore not expected to influence the laminar-turbulent transition location [30, 159].

**Thickness of the iTSP** The base layer thickness for this investigation was selected to a value of about  $100\ \mu\text{m}$  as confirmed with a coating thickness gauge. It is based on the following considerations: If the base layer is too thick, the insulating properties dominate. After turbulent spots pass, the active layer takes too long to heat up again, thus making it difficult to detect the trailing edge. The general temperature of the active layer cools down too far, and the temperature difference between the flow and the model is too small and does not stay constant for the considered time scale of turbulent spots. However, a strong temperature gradient would occur within the base layer if the base layer is too thin. Therefore, the onset of turbulence with higher surface heat transfer is partly compensated, and it is difficult to detect the leading interface of turbulent spots. Furthermore, the base layer must have a minimum thickness to cover the primer layer optically to ensure a homogeneously light scattering surface. Since the pocket depth determines the base layer thickness, it is not adjustable once the model has been manufactured.

The thickness  $h$  of the active iTSP layer plays a crucial role in its time response (proportional to  $h^2$  [155]). If the thickness is too great, the paint reacts slowly to temperature changes in the boundary layer. Being too thin, however, limits the paint's total intensity (and sensitivity - see figure 3.4.4). This effect limits the achievable signal-to-noise ratio; therefore, the temporal resolution decreases, as a higher exposure time is necessary to reach an

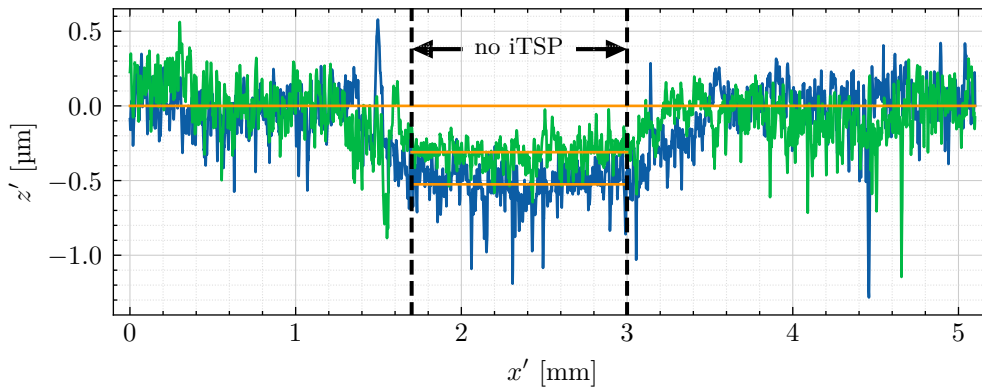


**Figure 3.4.5:** Two thickness measurements of the active iTSP layer using a profilometer.  $x'$  is the traverse coordinate of the profilometer in streamwise direction and  $z'$  the measured value in wall-normal direction. In the centre, the active layer has been removed - region between the dashed lines. The long orange line indicates the average baseline with the active layer.

acceptable signal-to-noise ratio.

Determining the thickness of a thin active layer is not easy due to the paint properties. The active layer has a certain degree of inhomogeneity, is easily wipeable and is not much thicker than the roughness of the active iTSP layer itself. Therefore, it is not feasible to accurately determine paint thickness with a conventional coating thickness gauge.

One possible way to determine coating thickness is with the help of the profilometer mentioned above. The active layer was removed along a narrow strip with a toothpick drenched in ethanol. It relied on the fact that the active layer is easily removable with ethanol, the base layer remaining unaffected. Several wipes were taken using a fresh toothpick for each one, and minimal force was applied to prevent damage to the underlying base layer. As a final step, excitation with a blue LED confirmed that no luminophore remained in the investigated strip, indicating that all of the active layer had been removed. The result of two independent measurements at different locations is shown in figure 3.4.5, revealing a measured thickness between  $0.3\ \mu\text{m}$  to  $0.6\ \mu\text{m}$ .

Another way to estimate the thickness of the active layer is by geometric considerations of the sprayed amount of paint. Assuming that most of the dried active layer consists of the binder, that all solvent has evaporated, and that the luminophore does not alter the density of the paint, the density and quantity of the sprayed paint would be the same as the undissolved binder. Measuring the amount of paint before and after spraying showed that  $60\ \text{mg}$  of binder had been applied. It is estimated that roughly half the amount of used paint is lost by transferring paint to and from the spray gun and through spray mist. Furthermore, the total area coated, including the masked regions around the surface of interest, is approximately twice the size of the surface of interest alone. Since the density of the binder is  $1.14\ \text{g}/\text{cm}^3$ , these various approximations yield an estimated thickness of about  $0.8\ \mu\text{m}$ , which is in acceptable agreement with the previous measured values.

### 3.4.3 LEDs and filters

The emission filter chosen for the camera is a Chroma<sup>®</sup> ET570lp long pass interference filter to capture a large part of the relatively broad emission peak of the iTSP (compare figure 3.4.1). Note that at  $570\ \text{nm}$  the emission intensity is still more than 50% of the peak height at  $600\ \text{nm}$ . Figure 3.4.6 shows the sensitivity of the iTSP at an excitation

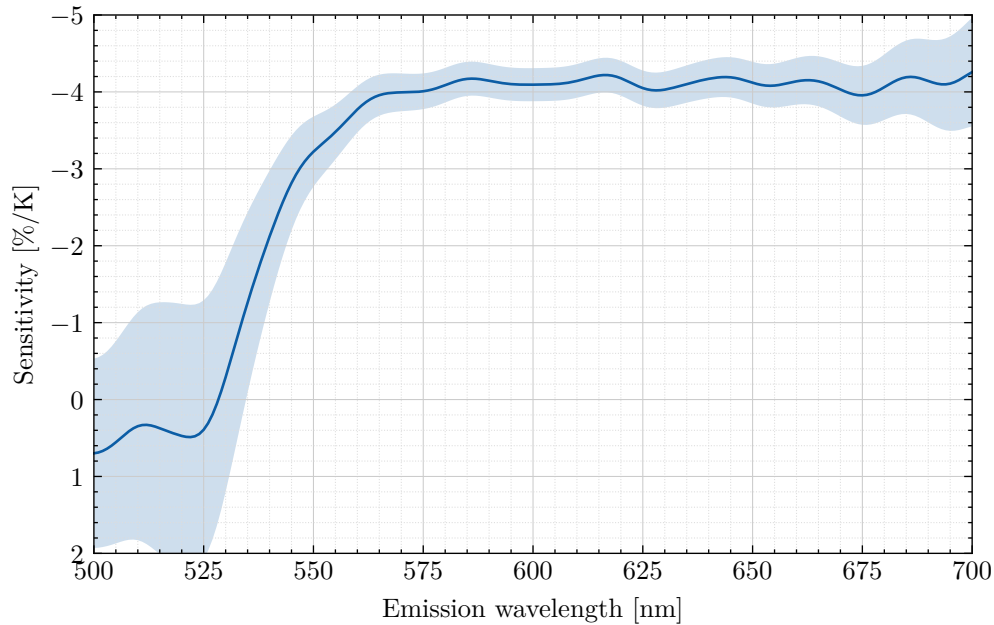


**Figure 3.4.6:** Sensitivity of Ru(phen) excited at 459 nm at 283 K as function of emission wavelength.

wavelength of 459 nm, the peak of the excitation wavelength. A significant drop-off in sensitivity for low wavelength can be seen starting at around 570 nm. A filter transmitting light lower than 570 nm would result in a higher recorded intensity but at the cost of reduced sensitivity. This limitation is further relevant since dichroic filters, as used in this case, are angle-sensitive. When the filter is at an angle to the incident light, the peak (for band pass) or edge (for long pass) wavelengths of the filter are shifted to a lower wavelengths; this also applies to the long pass filter used here. In an extreme case, this would alter the sensitivity depending on the viewing angle. Therefore it is desirable to only record the light on the sensitivity plateau as shown in figure 3.4.6. That the sensitivities also become positive at wavelengths below 525 nm can be explained as an artefact due to a shift of the spectral emission curve with temperature and the very low recorded emission intensities.

No infrared light was captured with the camera despite the long pass filter potentially allowing infrared light to pass. This was confirmed without LED illumination, whereat the camera detected no light. This test also assures that no disturbing ambient light was present during the tests.

Altogether, seven high-power LEDs are installed in KRG outside the test section (compare figures 3.4.7 and 3.4.8). Two LEDs (LEDENGIN LZ4-00DB00) each are installed in both flanges on each wind tunnel side. Three are equipped with Chroma<sup>®</sup> ET470/40x filters, whereas the fourth one, which is closest to the surface of interest, is equipped with a Chroma<sup>®</sup> ET450/50x filter. The latter filter is expected to have a slightly higher transmittance for the used LED. Furthermore, an array of 3 LED's (OSRAM LE B P3W 01) is installed on the opposite wind tunnel side to the camera, utilising the flange window. One of these LEDs is fitted with a Chroma<sup>®</sup> ET470/40x filter. Due to the distance from the surface of interest (approximately 30 cm), the other two are equipped with 50 mm lenses to focus the light on the surface of interest. Chroma<sup>®</sup> ET450/50x filters were used for these LEDs. These LEDs provide most of the excitation light. The lenses cause a

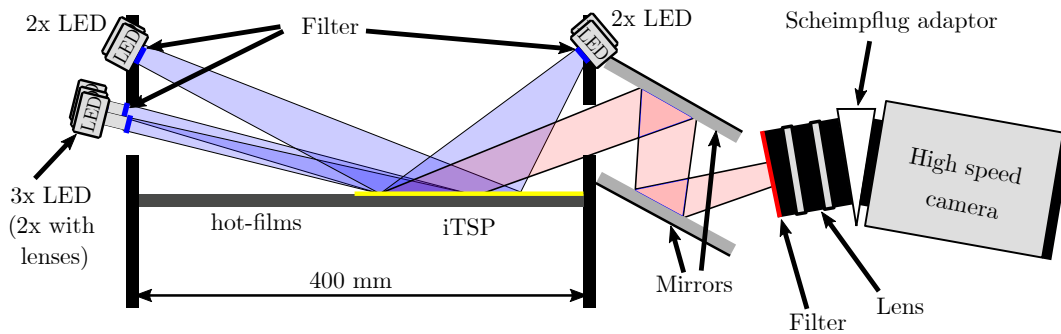


**Figure 3.4.7:** Setup sketch of the wind tunnel model in KRG as cross section of the test section. View is in streamwise direction.

non-uniform illumination pattern on the surface of interest. Without these lenses, however, there would not be enough light intensity reaching the model surface, so that the high camera frame rates could not be used. Due to the space restrictions in KRG, only two of the three LEDs and none of those installed in the flanges could be fitted with lenses.

### 3.4.4 Camera

A Photron<sup>®</sup> Fastcam Mini AX200 high-speed camera is used to capture the iTSP intensity images. It features a 1-megapixel (1024 x 1024) CMOS image sensor with a global shutter and 12-bit dynamic range. Due to its compact build and suitability for applications in high-G environments (which can occur in KRG due to the vibrations during operation), it is well suited for this investigation. A Scheimpflug adaptor is used to increase the depth-of-field focus. Note that even the Scheimpflug adaptor set at its maximum angle could not fully compensate for the shallow angle-of-view and concomitant de-focusing in some regions (compare figure 4.1.1). An 85 mm f/1.4 Nikon lens is combined with a macro extender to allow focusing to the short distances. The lens must be set at full aperture to ensure the camera detects sufficient luminescent light. The resulting loss in depth-of-field focus was tolerated as the images needed to be strongly filtered anyhow, as discussed later in chapter 4. Two mirrors are used in a periscope setup to enable a view of the region of interest, especially in this spatially constricted environment. A similar setup had been used and described by Risius et al. [134, 136, 137] and adapted for the current investigation. This setup and lens enabled a very high streamwise resolution of 17 px/mm.

### 3.4.5 Wind tunnel implementation

Figure 3.4.8 shows the installed wind tunnel model from the front (view in streamwise direction) with the blue excitation light (a) and the red light emitted from the iTSP surface (b). The measurement equipment can only be installed and adjusted after the model has been installed in the wind tunnel. To maximise the captured luminescent light and ensure the correct field-of-view, a careful alignment of LEDs and camera is necessary, which is very time-consuming considering the small field-of-view and degrees of freedom of the setup (number of LEDs, lenses, illumination angle and mirrors for periscope setup). To minimise the effect of photodegradation during this process, the setup was prealigned as much as possible with an old iTSP coating. Still, the final alignment had to be done with the final coating. Furthermore, the model was recoated once during the test campaign.

Two camera frame rates were chosen for most of this investigation: 20 kHz with a resolution

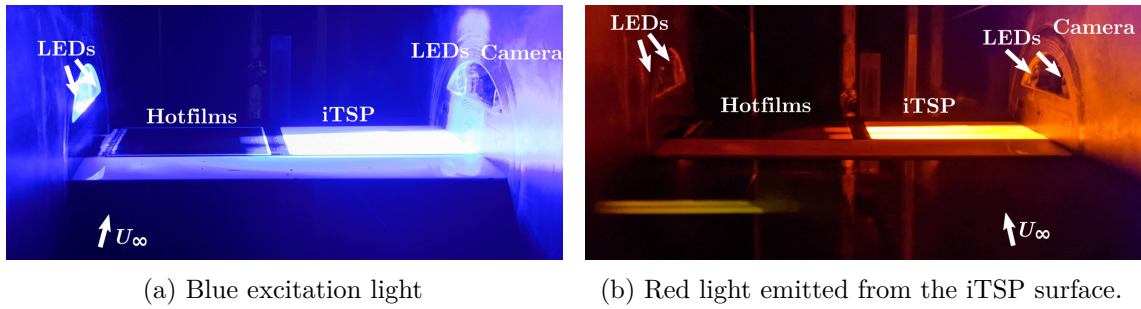


**Figure 3.4.8:** Installed wind tunnel model viewed from the front (view in streamwise direction).

of 1024 x 256 pixels and 40 kHz with a resolution of 1024 x 128 pixels. Both have distinct advantages: The lower frame rate allowed the LEDs to be operated at lower power for more homogeneity and less illumination intensity loss. Further, it enables a larger field of view at the same resolution and exhibits a higher signal-to-noise ratio due to the longer exposure. The higher frame rate allows more consecutive images of one turbulent spot over the field of view, which is especially useful for the high Mach number cases. The exposure time was set to a maximum of 48.3  $\mu\text{s}$  and 23.3  $\mu\text{s}$  with a duty cycle of 96.6 % and 93.1 % for the 20 kHz and 40 kHz cases respectively. This exposure time means the captured luminescent intensity is a time average invoking a motion blur when capturing the footprints of turbulent spots. This motion blur must be considered and is discussed in section 4.2.3. The faster frame rate, therefore, inherently yields less motion blur. Due to these distinct advantages, both frame rates were used for all conditions. Most conditions were repeated with the 20 kHz frame rate to increase the total amount of detectable turbulent spots (three total runs per test condition). This also allows a repeatability study. For some selected flow conditions, images were additionally acquired at 100 kHz with a limited resolution of 1024 x 32 pixels.

### 3.4.6 Limitations

In the current setup, the field of view is limited. Depending on the transition location, only a small area of the visible region has a laminar boundary layer, or if the transition onset is far downstream, the boundary layer tends to be so stable that only very few turbulent spots are detectable. The small field-of-view is necessary to achieve the required resolution and is limited by the optical access to KRG. Furthermore, a larger area could not be sufficiently strongly illuminated to enable use of the required high frame rates.

The number of markers (18) was needed for accurate image registration for all recorded frame rates. Recoating the model required one to two days because it involved its unmounting and the reinstallation of the camera and LED system.



## Chapter 4

# Evaluation Techniques

This chapter describes and discusses the data reduction and evaluation techniques used in this work. An interpretation of the results relies on novel image processing methods since the quantitative characterisation of turbulent spots with thermal imaging has not been investigated yet for high-speed flows. Image filtering proves crucial in determining turbulent spot characteristics since the thermal footprint (signal strength) for the examined conditions is very small and lies well within the noise floor. Where not stated otherwise, the procedures were performed with custom Python code developed by the author based mainly on the open-source packages *NumPy* [63], *SciPy* [172] and *scikit-image* [169].

### 4.1 Calibration

As described in section 3.2, the luminescent intensity for a typical TSP will decrease with rising temperature. This is used to identify the temperature distribution on a model with the help of equation 3.2.3 and a suitable calibration function  $f$ . Typically, a calibration is performed in an external calibration system with a separate TSP sample coated simultaneously with the wind tunnel model (see section 3.4.1).

Since the iTSP applied in this investigation is photodegradable, i.e. luminescent intensity and sensitivity decrease with cumulative exposure to light (compare section 3.4.1), such a calibration alone is not suitable here. Preliminary measurements showed a significant difference in sensitivity between the calibration sample and the iTSP of the model after the KRG test, which consisted of model alignment and 140 runs (-4.6%/K vs. -2.0%/K, both at 283 K).

Unfortunately, the illumination conditions pertaining in KRG during the test campaign cannot be reproduced outside of the test section (for a possible simultaneous degradation of the calibration sample). Furthermore, the illumination distribution inside the test section is not homogeneous (see section 3.4.3 for details), yielding different degradation rates for different parts of the model. Figure 4.1.1 shows a raw intensity image for the field of view, illustrating the intensity differences.

A procedure was developed to nevertheless still be able to obtain quantitative results, despite these difficulties. It includes

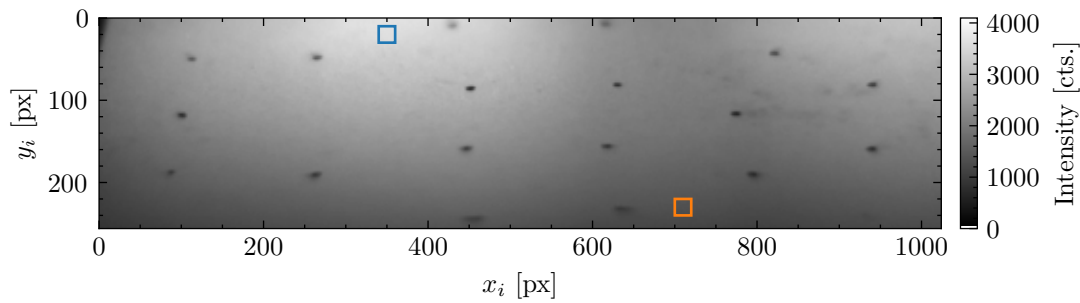


**Figure 4.1.1:** Raw intensity image without flow (reference conditions). Blue and orange rectangles indicate the regions examined in figure 4.1.2. For a run, flow direction would be from left to right.

- the reduction of light exposure to keep the ageing of the iTSP to a minimum,
- an in-situ calibration of the iTSP on the model before and after the test,
- and an external calibration of a small sample in a dedicated calibration chamber to correct the results of the in-situ calibration.

The last step is necessary since a quantitative calibration inside the test section alone was not possible, due to the changing ambient temperatures and resulting effects on the LED intensity. The procedure is explained in detail in the following.

**Reduction of light exposure** Great care was taken to dry the model in a dark place directly after coating. During model installation, the ambient light was dimmed. The alignment of the camera and LEDs was prepared in advance with a coating from a previous measurement campaign. This was only possible to a certain extent, as the final positioning of the camera and LEDs was only possible after the model had been installed into the test section. The duration of this final alignment was kept as short as possible at the lowest LED intensity. After installation, the model was continuously kept in a nitrogen environment. The whole process of coating, drying and model installation was completed within the same day.

Even though being driven with constant electrical current, high power LEDs typically exhibit a loss of efficiency after turning on due to warming up, resulting in a loss of intensity. A long time after switching on the LED (typically  $t > 10$  s), a quasi-steady state is reached where the intensity only varies by a small amount over time. This is generally preferred for a quantitative measurement but is not suitable here since the amount of time the LED is on in advance of the actual wind-on phase must be kept as short as possible to reduce photodegradation. This meant that the LED was not in a quasi-steady thermal state. Therefore the intensity loss during a run must be compensated for. Figure 4.1.2 shows the decay for a bright and dark area as indicated in figure 4.1.1. This was recorded with the same settings as during a run but without flow. In the cases with 40 kHz acquisition rate, the intensity loss was much higher and close to 10 % (instead of about 1 % to 2 % for the cases with an acquisition rate of 20 kHz) because the LEDs had to be operated at maximum allowable power and therefore the stabilisation time would have been even longer. Since the intensity loss differs depending on the location of the model, a correction curve was determined for each position separately. Since the LED intensity distribution is gradual and without strong gradients, the images are heavily spatially filtered. In many cases, an exponential decay accurately describes the decay for a single LED. Since the intensity

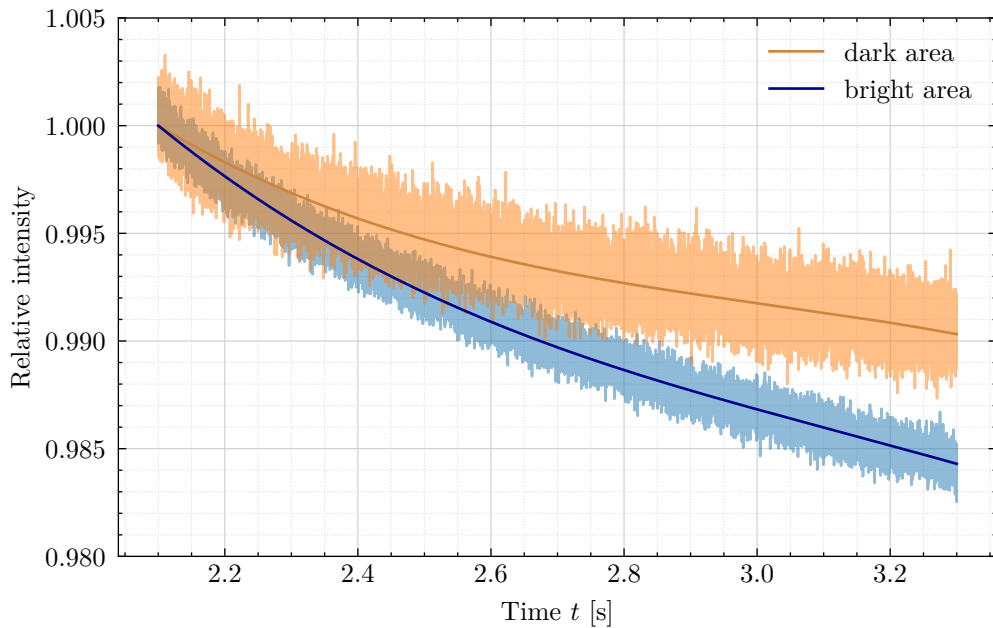


**Figure 4.1.2:** Time dependence of luminescence light for bright and dark areas as marked in figure 4.1.1. The same settings as during a run were used but without the wind-on phase. LEDs were turned on at  $t = 2.0$  s.

distribution on the surface is a superposition of 7 LEDs with differing thermal properties depending on position and type, a polynomial approach appeared more appropriate. The temporal intensity curve was therefore fitted with a third-order polynomial and used to correct for the intensity loss during a run.

**In-situ calibration** The test section at KRG can be detached from the storage tube with a wedge gate valve (see figure 3.1.1) and set to specific temperatures with the help of liquid nitrogen and convection heat introduced by fans. This is exploited to perform an in-situ calibration with the same optical setup and model as during the measurement campaign. The temperature is slowly increased from 268 K to 288 K over several hours, which covers the temperature range of the current investigation. This slow procedure allows the surface and thermocouples in the model to be considered isothermal - as required for the calibration. The luminescent intensities recorded with the camera are associated with the mean temperature of the thermocouples which are also used as temperature reference in the test runs. The process is performed once at the beginning and again at the end of the measurement campaign to capture the loss in sensitivity of the iTSP coating. The same timing sequence and LED settings were used for both calibrations.

Since the whole test section warms up during the procedure, the ambient temperature surrounding the LEDs is also warmed, resulting in a decreased excitation light intensity and distorting the calibration - this results in an overestimation of the sensitivity by about 1%/K. For this reason, an external calibration is also needed.

**External calibration** For the external calibration, a square aluminium sample was attached to the wind tunnel model just outside the area of interest and coated together alongside the model. It remained on the model until immediately before closing the test section - thus having the same light exposure during coating, drying, installation and

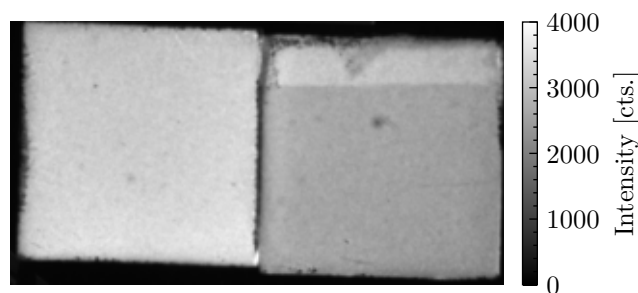


**Figure 4.1.3:** Two calibration samples coated along the wind tunnel model. Left: stored in a dark environment. Right: attached to the model during model installation.

alignment of the camera and LEDs. The calibration is performed in the calibration chamber discussed in section 3.4.1. The luminescent intensity was evaluated in a 200 x 175 pixel region. Figure 4.1.3 shows two calibration samples that were coated alongside the model. One (left) was stored in a dark environment during model installation and the other (right) was attached to the wind tunnel model. Note the bright strip on the top of the right sample: This is where the sample had been attached to the model with light-blocking adhesive tape, thus leading to less photodegradation. The difference in intensity was around 20% from one sample to the other at 283 K.

**Correction of in-situ calibration** Since the external and in-situ calibration are expected to yield the same sensitivities, the former can be used to correct the in-situ calibration by calculating an LED ambient temperature-intensity relation for the wind tunnel calibration that yields the same sensitivity. The illumination of the model so far was mostly homogeneous (ambient light and low power LED), so the sensitivity along the whole area of interest is assumed to be roughly constant. This is a simplification relying on the assumption that the iTSP thickness is constant. Different coating thicknesses would result in different sensitivity losses as discussed in section 3.4.1. With this correction method, the relative intensity (reference temperature 283 K) at the start and the end of the campaign was adjusted. The result can be seen in figure 4.1.4. The overall loss in sensitivity was between 10% and 20%, dependent upon illumination and iTSP inhomogeneities.

**Final calibration** The iTSP sensitivity is not homogeneous over the surface due to different illumination conditions and iTSP inhomogeneities. Therefore the calibration parameters (see section 3.4.1) have to be calculated independently for each location. The quantitative temperature information is determined analogously following the procedure described in section 3.4.1. Since the overall loss in sensitivity was shown to be relatively small, a linear interpolation of the temperatures calculated with both (corrected) in-situ calibrations was chosen, weighted by the relative position of the data point within the test campaign.

The intensity loss during the test campaign was 4-5% for the less illuminated areas and 8-10% for the more illuminated areas. These comparatively low values are due to the measures of reduction of light exposure as described above. If these measures are not implemented, an intensity loss of over 40% would be expected as seen in previous measurements.

This procedure improved the overall quality of attained temperature information but itself is susceptible to errors: Since the calibration in the wind tunnel was done at the same time as the sample plate was being calibrated in the calibration chamber, an identical optical

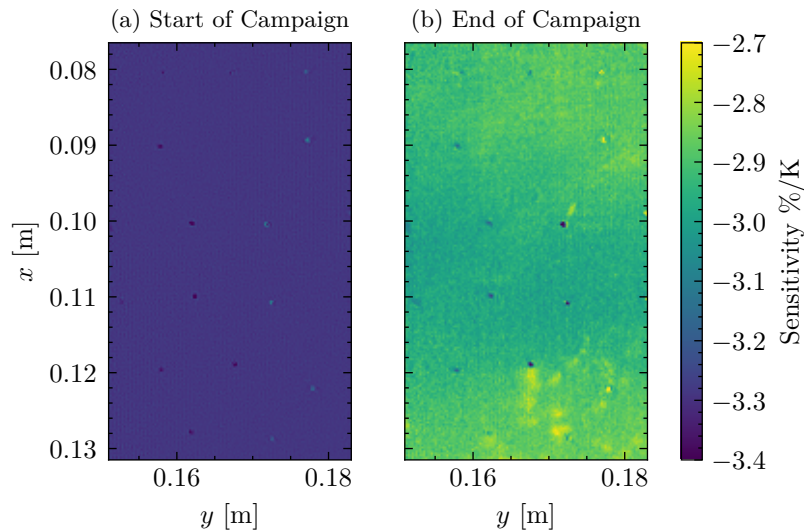


**Figure 4.1.4:** Sensitivities on the area of interest at 283 K at the start and end of the test campaign.

setup could not be used. It was therefore carefully taken into account to choose similar LEDs and filters and a scientific-grade CCD camera with a similar spectral response curve to perform the separate calibration. Thus the expected error would be small, since the sensitivity of the iTSP varies very little for the excitation and emission wavelength utilised in this measurement (see section 3.4.1 for details).

The light emitted by the LEDs is expected to be the same at the start and the end of the test campaign, neglecting possible degradation of the LED due to the high thermal stresses during the measurements.

## 4.2 Image processing

### 4.2.1 Marker detection and image alignment

Accurate image alignment is necessary for all cases for which a mapping to model coordinates is required (see section 4.2.2), when longer time series are to be investigated, and where temperature information is desired. For the latter case, images acquired with the flow are divided by reference images with known temperature distributions. Due to the small field of view of the camera (caused by the large magnification), the images are highly susceptible to even very small camera and model movement. To improve the results obtained with the iTSP measurement technique, markers applied below the active layer (see section 3.4.2) are used to align the individual images and compensate for any movement. It is necessary to precisely detect the marker position with sub-pixel accuracy. As can be seen in Figure 4.2.1(b), the shape, size and boundary of the markers are mostly not ideal for standard marker detection algorithms like centre-of-mass detection or cross-correlation with standard marker templates. This is due to the difficulty in creating sufficiently small yet distinct markers and the acute viewing angle of the camera. Instead, for every marker, a small area of 19 x 19 pixels was cropped around each marker and used as a template for cross-correlation for an image series for each marker. In this way, the individual sharpness and shape of the marker could be accounted for. To reach sub-pixel accuracy, a spline

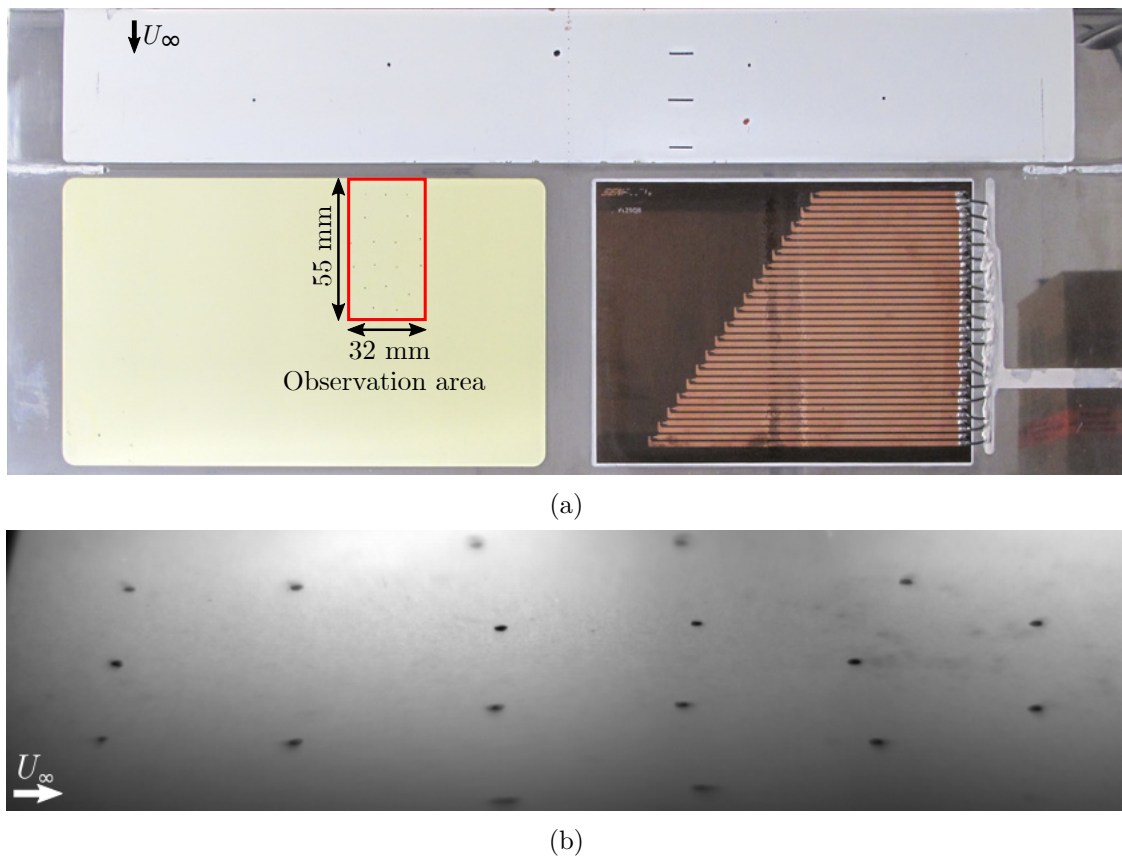
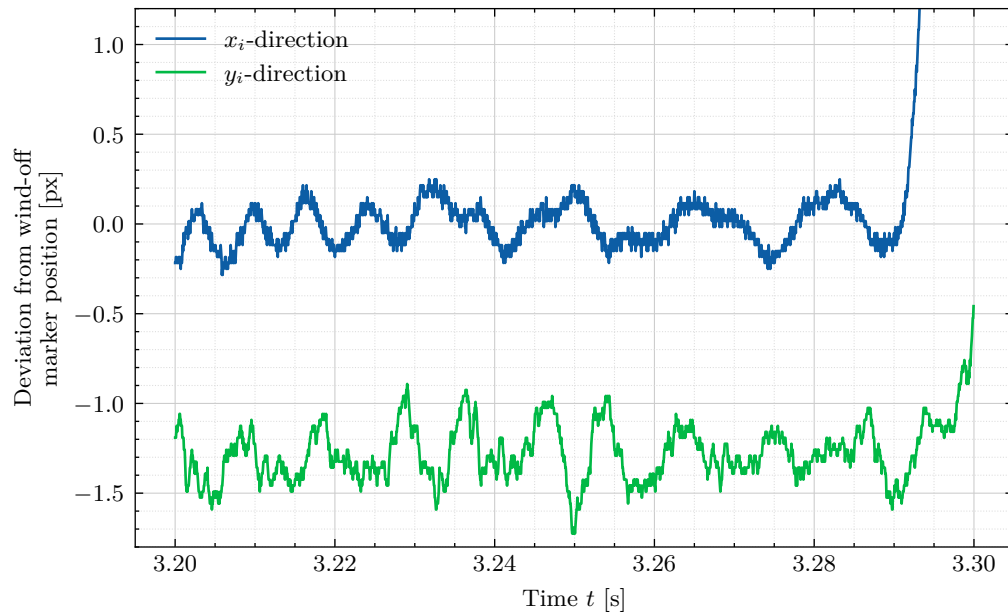


**Figure 4.2.1:** (a) Top view of the model: the red rectangle within the iTSP coated area indicates the observation area for the case with a 20 kHz acquisition rate. (b) Wind-off raw image as seen from the camera mounted behind the wind tunnel side wall. It corresponds roughly to the area marked with the red rectangle in (a).

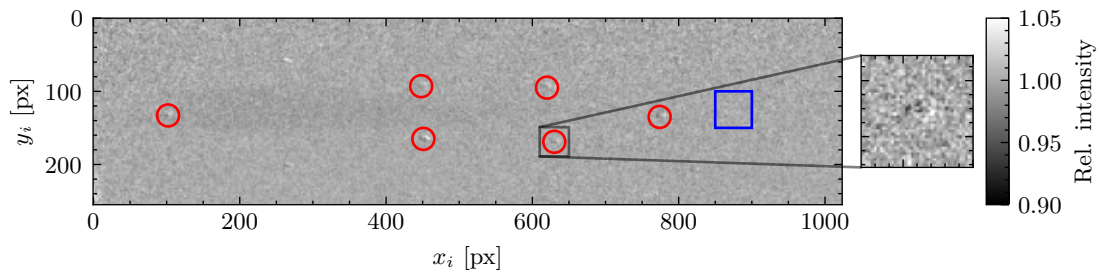
of order 3 is fitted to the resulting cross-correlation matrix and evaluated around the maximum with a resolution of 1/30th of a pixel. The resulting marker positions are used to align the wind-on images by quadratic warping in a way that the wind-on (run) marker positions correspond to those of the wind-off (reference) positions (calculated by averaging the determined wind-off marker positions). Most of the alignment is achievable with an affine transformation (rotation, translation and zooming) but due to the complex interaction of model deformation under aerodynamic load, camera and optical setup movement and optical effects caused by the overall pressure and sudden pressure drop during a run, a quadratic alignment yielded better visual results. The operation uses bicubic subpixel interpolation. The alignment process is performed with the in-house software package *ToPas* [83].

Figure 4.2.2 shows an example of the detected marker position for marker number 7 in the x and y direction in the image plane during the measurement interval of the aerodynamic parameters in the wind tunnel run. In this example and for this time window, the mean variation of the marker movement was in the range of 0.5-1 pixel and probably mainly caused by oscillations of the camera, since the model itself is very rigid.

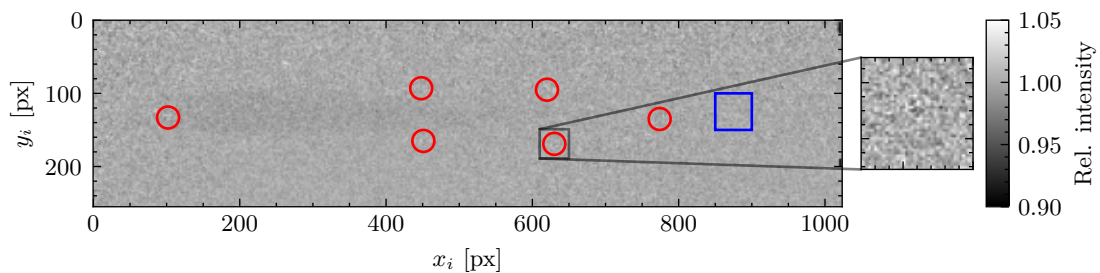
It is necessary to align images even when only neighbouring images are to be investigated. This is the case for detecting turbulent spots with the gradient method, as discussed in



**Figure 4.2.2:** Marker movement in x- and y-direction in pixels from the wind-off detected marker position.



(a) Temporal gradient with images not aligned



(b) Temporal gradient with images aligned

**Figure 4.2.3:** Comparison of visualising a turbulent spot with and without alignment. According to the marker detection algorithm explained in section 4.2.1 the average marker displacement was found to be less than 0.1 px. RMS value in the blue rectangle decreased from 0.021 to 0.017 with alignment. Red circles indicate the location of some markers and their effect on image division.

section 4.5. The respective image displacement is expected to be small for successive images in most cases. It was still found that even small displacements affect the resulting image quality, as can be seen in figure 4.2.3. A sample result with a turbulent spot is displayed with and without image alignment. For the case without alignment, the noise level is higher and the effect of non-aligned markers (indicated by red circles) can be seen - this leads to the typical dark-light image patches. Due to the coating limitations of the selected iTSP, the surface and resulting brightness were found to be fairly inhomogeneous. Even though not as pronounced as with the markers, this inhomogeneity would result in increased noise when dividing two images if they are not aligned properly. In figure 4.2.3 the RMS value of the calculated gradient in the blue rectangle, which contains a completely laminar boundary layer, could be decreased from 0.021 to 0.017 with alignment. Therefore, even for cases with only little displacement between respective images, the algorithm explained above was utilised.

### 4.2.2 Mapping to model coordinates

A mapping from image coordinates to a 3D orthogonal model grid is required to view and evaluate the iTSP results. Once again, the mapping process is performed with *ToPas* by using the detected marker positions in the aligned images and mapping them to the coordinates of the orthogonal model grid. The mapping process takes account of 11 independent parameters: translation (3), rotation (3), perspective (3), scaling (1) and lens correction (1). Table 4.2.1 lists the grid dimensions. The value for every grid point is calculated by linearly interpolating adjacent pixels. The grid layout is finer than the camera resolution to ensure no information is lost in the mapping process. Due to the high magnification, the marker positions on the model surface must be known accurately.

Acquisition frequency	grid points	grid spacing	dimension
20 kHz	1375 x 800	0.04 mm	55 x 32 mm <sup>2</sup>
40 kHz	1375 x 400	0.04 mm	55 x 16 mm <sup>2</sup>

**Table 4.2.1:** Grid parameters.

**Marker localisation** To accurately determine the marker positions, images were taken from a distance from above the model with a commercial Canon EOS 450D camera at high resolution (4272 x 2848 px<sup>2</sup>). The large distance ensured minimal lens distortion in the area of interest. With known, well-defined locations on the model flat surface (e.g. junction between the main and front part of the model) and with the help of a custom python code, the marker positions could be identified. For this, the markers were localised with a centre-of-mass algorithm similar to that applied to the measurement images in the mapping process. Repeating this process several times independently increased accuracy and yielded an error of less than 0.07 mm for each marker.

### 4.2.3 Image filtering

The mapped images are filtered with a temporal and spatial filter to increase the signal-to-noise ratio before further evaluation. Filtering in the grid rather than the image domain was considered favourable since the filter sizes are based on physical considerations. This will further become evident in section 4.5 as the detection algorithms for turbulent spots rely

on filtering in the model coordinate system. A 2D Gaussian filter was chosen as a spatial filter with variable sigma in the spanwise and streamwise directions. It was chosen since the noise in the iTSP image is considered mainly Gaussian and since it preserves the location of strong gradients. The kernel size was set to  $\sigma_x = 60$  grid points in the streamwise direction and  $\sigma_y = 15$  grid points in the spanwise direction which are appropriate values for the study of turbulent spots. In fact the motion blur expected considering the exposure time for the acquisition frequency of  $f_{acq} = 20$  kHz, lowest examined Mach number ( $M = 0.35$  - slowest spot celerity) and estimated trailing edge celerity of a turbulent spot of  $U_{te}/U_\infty = 0.4$  is 60 grid points, ensuring no observed features are smoothed away with this kernel size. The value for  $\sigma_y$  was selected balancing a sufficient amount of smoothing while still retaining the overall spot shape: the leading edge interface being the main limiting factor in this case. Choosing an even larger kernel size would have compromised the accurate location of turbulent spot interfaces.

Furthermore, a temporal filter was necessary as the signal filtered with the spatial filter alone was not smooth enough and yielded several non-physical local minima in the intensity signal within a turbulent spot. As a temporal filter, a Savitzky-Golay filter [144] was chosen and applied for every grid position separately. A similar filter was used by Mee et al. [105] for the heat-transfer signals identifying intermittency distributions and Miozzi et al. [108]. Since the acquisition frequency is in the range of that of observed features, the parameters for any temporal filter must be chosen with great care. One of the properties of a Savitzky-Golay filter is that it preserves peak width and heights better than comparable filters, making it especially useful in this case where intensity peaks induced by turbulent spots are often only a few time instances wide. With the parameters implemented here, a second-order polynomial was fitted to a 5-time instance sliding window and evaluated at the centre point. The parameters were determined considering the average peak width.

## 4.3 Numerical methods

### 4.3.1 Boundary layer parameters

Boundary layer computations are performed with the boundary layer solver COCO for compressible flows [147]. It computes velocity and temperature profiles for steady, laminar boundary layers along (swept) wings. The calculations are performed based on the measured pressure distribution along the model. COCO is capable of calculating with isothermal wall conditions, if the surface temperature distribution is known, as used for example in [30, 41, 43, 137]. Since in the present investigation only a part of the temperature distribution is known due to the limited viewing angle, an adiabatic wall case is used for the calculations. Previous test campaigns show a negligible difference for the calculated boundary layer quantities considered in this investigation for the adiabatic or isothermal wall calculations. If not stated otherwise, boundary layer quantities are averaged over the region of interest. The dimensionless pressure gradient parameter used in this investigation is  $\lambda_\theta$ , as also used in several other publications investigating the effect of pressure gradient on turbulent spots [38, 62, 77, 181]. It is defined as

$$\lambda_\theta = \frac{\theta^2}{\nu} \frac{dU_e}{dx}, \quad (4.3.1)$$

where the momentum thickness  $\theta$ , the kinematic viscosity  $\nu$  and the boundary layer edge velocity gradient  $dU_e/dx$  are determined with COCO and averaged over the region of interest. Note this parameter also considers the state of the boundary layer in form of the momentum thickness Reynolds number  $Re_\theta = U_e\theta/\nu$  as compared to the acceleration parameter  $K$  with  $K = \nu/U_e^2 dU_e/dx$ , since  $\lambda_\theta = K \cdot Re_\theta^2$ .

### 4.3.2 Linear stability analysis

The boundary layer profiles computed by COCO are used to perform local linear stability analysis with LILO [148]. For the used 2D-model, Tollmien-Schlichting waves are mainly responsible for boundary layer transition (see section 2.1), and they are assumed to be quasi-2D for the Mach numbers considered in this investigation [32]. Non-parallel flow effects are not expected to be significant for the test model and conditions considered here [30, 64]. LILO calculates the amplification rates of Tollmien-Schlichting waves with differing frequencies. Amplification rates are expressed as N-factors where  $e^N = A/A_0$ , with amplitude  $A$  and initial amplitude  $A_0$  of the Tollmien-Schlichting waves.

## 4.4 Heat flux determination

The time-dependent heat flux distribution on the surface gives a direct indication of the boundary layer state, with a turbulent boundary layer yielding a higher heat flux compared to a laminar-boundary layer, assuming the temperature difference between  $T_{aw}$  and  $T_w$  to be similar in both cases. Based on the assumptions listed below, the heat flux can be calculated with the time-resolved, surface temperature distribution measured by the iTSP and the thermal properties of the iTSP layers and wind tunnel model.

For a 1D heat transfer, which is a common approximation in short-duration wind tunnels [90, 121, 122, 135, 154, 155], the time-dependent temperature distribution along an axis  $z$  is determined by [9]

$$\rho(z, T)c(z, T)\frac{\partial T}{\partial t} = \frac{\partial}{\partial z} \left( k(z, T)\frac{\partial T}{\partial z} \right), \quad (4.4.1)$$

a parabolic partial differential equation with temperature  $T$ , thermal conductivity  $k$ , density  $\rho$  and specific heat capacity  $c$ . At any given position, the heat transfer is given by (Fourier's law) [9]

$$\dot{q}(t) = -k\frac{\partial T(t)}{\partial z}. \quad (4.4.2)$$

These equations can be used to calculate the heat flux on the surface of the wind tunnel model coating  $\dot{q}_w(t) = -k\frac{\partial T(t)}{\partial z}|_{z=z_w}$  with  $z_w = z_0$  the surface location. Before every run, the temperature is assumed to be constant throughout the model, which is a reasonable assumption for a blow-down tunnel with significant equalisation time between runs, and its absolute value is determined by thermocouples in the model and the test section. The time-dependent temperature distribution is acquired by iTSP as discussed in section 4.1. In general, the thermal properties of a material varies with temperature. Since the total temperature change is small in this investigation (change of surface temperature measured to be  $< 6$  K for all cases), the thermal properties of the iTSP layers and model are approximated to be constant with respect to temperature, i.e.  $\rho(z, T) = \rho(z)$ ,  $c(z, T) = c(z)$ , and

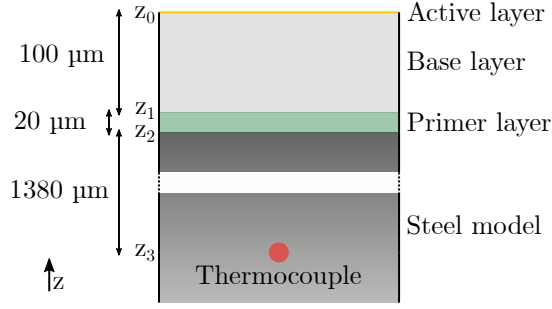


**Figure 4.4.1:** Layer model of the iTSP with approximate thicknesses. A thermocouple is located 1500  $\mu\text{m}$  below the surface.

$k(z, T) = k(z)$ . Furthermore, the change of these properties in respect to  $z$  is assumed to be constant within one material layer and only vary at the layer intersections (piecewise constant).

Equation 4.4.1 is solved numerically with the method of lines based on the finite-difference method with a forward differential in time

$$\frac{\partial T}{\partial t} = \frac{T_i^{n+1} - T_i^n}{\Delta t} \quad (4.4.3)$$

and central differential in space

$$\frac{\partial T}{\partial z} = \frac{T_{i+1/2}^n - T_{i-1/2}^n}{\Delta z}, \quad (4.4.4)$$

with location node  $i$  and time instance  $n$ . With

$$\kappa = \alpha_{max} \frac{\Delta t}{\Delta z^2}, \quad (4.4.5)$$

where  $\alpha_{max}$  corresponds to the maximum thermal diffusivity ( $\alpha = k/(\rho c)$ ) of the layers, the temperature at a given location node  $i$  and time instance  $n + 1$  is only dependent on its node and neighbouring nodes at time instance  $n$ :

$$\rho_i c_i \frac{T_i^{n+1} - T_i^n}{\Delta t} = \frac{1}{\Delta z^2} \left[ k_{i+1/2} T_{i+1}^n - (k_{i+1/2} + k_{i-1/2}) T_i^n + k_{i-1/2} T_{i-1}^n \right] \quad (4.4.6)$$

$$\Rightarrow T_i^{n+1} = \kappa \left[ \alpha_{i+1/2} T_{i+1}^n - (\alpha_{i+1/2} + \alpha_{i-1/2}) T_i^n + \alpha_{i-1/2} T_{i-1}^n \right] + T_i^n \quad (4.4.7)$$

where

$$\alpha_{i+1/2} := \frac{k_{i+1} + k_i}{2\rho_i c_i \alpha_{max}} \quad (4.4.8)$$

$$\alpha_{i-1/2} := \frac{k_i + k_{i-1}}{2\rho_i c_i \alpha_{max}}. \quad (4.4.9)$$

Since the thermal properties are not defined at the interface of the different layers but they are considered constant within a layer,  $\alpha_{i+1/2}$  and  $\alpha_{i-1/2}$  are set to be the values corresponding to the value of the material at node  $i + 1$  and  $i - 1$ , respectively. Note, that is a simplification, since it ignores the thermal contact resistance and assumes perfect heat transfer between two layers. This simplification is reasonable, since the layers are

#### 4.4 Heat flux determination

Material	Thermal diffusivity $\alpha$ [m <sup>2</sup> /s]
Maraging steel (1.6359) (Manufacturer information)	$5.67 \cdot 10^{-6}$
Primer layer [162]	$5.8 \cdot 10^{-6}$
Base layer [122]	$1 \cdot 10^{-7}$

**Table 4.4.1:** Thermal diffusivity for the materials relevant to calculate the heat flux.

spray painted reducing the thermal contact resistance compared to two solids. The same simplification is also applied for the measurements of thermal parameters of the individual layers described later in this section [162].

The calculation is numerically stable for

$$\Delta t \leq \frac{\Delta z^2}{2\alpha_{max}} \quad (4.4.10)$$

according to the von Neumann stability analysis. A cubic interpolation of temperature data is performed in time to enable a sufficiently small spatial resolution. For a spatial resolution of 1  $\mu\text{m}$ , the temporal interpolation length is set to  $\Delta t = \frac{\Delta z^2}{2\alpha_{max}} \approx 8.7 \times 10^{-8}$  s, fulfilling equation 4.4.10.

The result of the preceding numerical calculation is then used to determine the heat flux according to equation 4.4.2 with the time-resolved temperature values of two neighbouring grid points in z-direction at the surface ( $T_1^t$  and  $T_0^t$ ) and the thermal conductivity of the base layer ( $k = k_b$ ):

$$\dot{q}_w(t) = -k_b \frac{T_1^t - T_0^t}{\Delta z} \quad (4.4.11)$$

$$= \frac{-\sqrt{\rho_b c_b k_b}}{\sqrt{2}} \sqrt{\frac{\alpha_b}{\alpha_{max}}} \left( \frac{T_1^t - T_0^t}{\sqrt{\Delta t}} \right). \quad (4.4.12)$$

Due to the uncertainties related to the thermal properties of the layers, no precise absolute values in terms of heat flux can be given, and so the heat flux values will be normalised by  $\sqrt{\rho_b c_b k_b}$ , the thermal effusivity of the base layer, throughout this thesis with the index  $b$  referring to the base layer (since the active layer is neglected in this case). Based on values provided in Ozawa et al. [122], an estimate for the scaling parameter is given by  $\sqrt{\rho_b c_b k_b} = (612 \pm 68) \text{K}^{-1} \text{s}^{-5/2} \text{kg}$  but varies for other publications.

The simplification of using a one-dimensional approximation is justified as the temperature gradient in the streamwise direction on the surface is much lower than the temperature gradient toward the inside of the model. For a typical case, this is more than two orders of magnitude (0.4 K/mm compared to 50 K/mm) in the area of 50 % intermittency region and even more outside this region. Therefore, expanding the calculations to a full 3D model is not expected to alter the results significantly. However, this assumption may not be valid for a much thinner base layer than considered here.

The thermal properties of thin layers are not easy to determine. They can vary depending on the thickness of the layer and depend on the layer interfaces, as these can have a significant influence on the thermal diffusivity. Table 4.4.1 lists the thermal diffusivities  $\alpha$  used to determine the heat flux. The most important value is that of the base layer, as this contains the largest temperature gradient over its thickness. Several differing values are reported in literature, determined directly and through in-situ calibration [50, 122, 135].

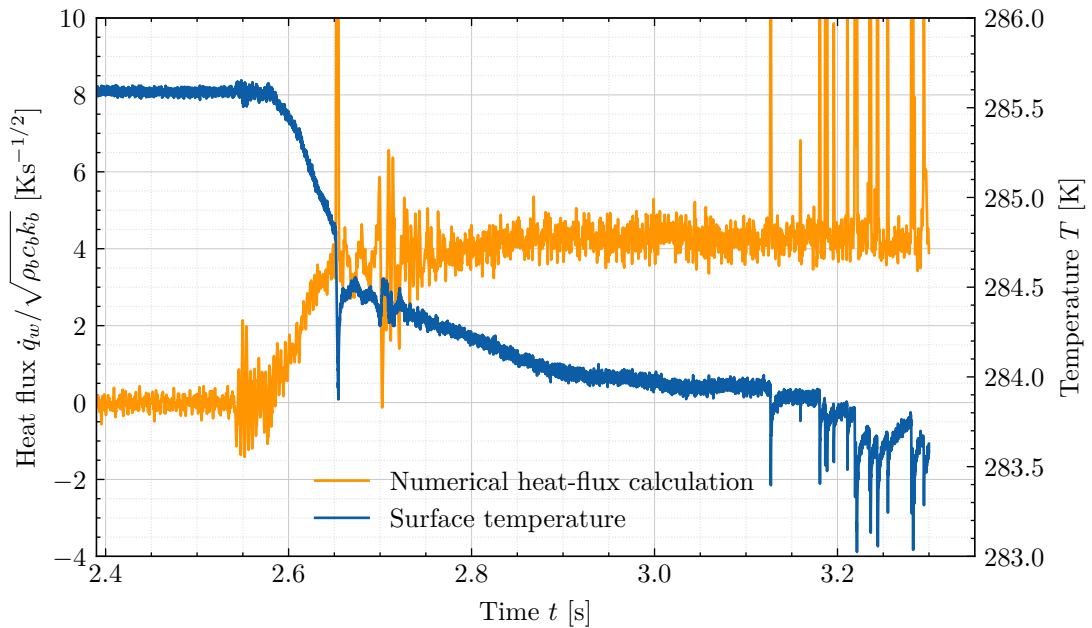


**Figure 4.4.2:** Calculated heat flux with equation 4.4.7 as well as the temporal temperature distribution at  $x = 0.1$  m,  $y = 0.167$  m for  $Re_c = 6 \cdot 10^6$ ,  $M = 0.8$ , and  $\lambda_\theta = 19.0 \cdot 10^{-3}$ .

The images were binned to a grid with  $137 \times 80$  grid points and further filtered with a Gaussian filter with kernel size  $3 \times 1$  (corresponds to  $1.2 \times 0.4$  mm<sup>2</sup>) in a streamwise direction to achieve a sufficient signal-to-noise ratio before the heat flux calculation. The calculated heat flux and temperature distribution for a predominantly laminar boundary layer are presented in figure 4.4.2. The heat flux values are filtered with a running Gaussian filter in time (kernel size 5). Towards the end of the run (at  $t = 3.1$  s to  $3.3$  s), the spikes in temperature and heat flux are caused by turbulent spots, the last one of which close to  $t = 3.3$  s corresponds to the turbulent spot discussed in detail in section 4.5. The surface temperature at around 3.0 s and consequently the wall temperature ratio  $T_w/T_{aw}$  are close to constant, inferring an expected constant heat flux. The heat flux is constant for most of the run for the numerical heat flux calculation, demonstrating the validity for the choice of the thermal parameters. Further remarks on the heat flux determination and a comparison with the semi-infinite approximation typical for short-duration wind tunnels [122, 135, 155] is given in appendix A.1.

## 4.5 Turbulent spot celerities

The following section discusses the techniques to determine turbulent spot celerities for the leading  $c_{le}$  and trailing edge  $c_{te}$ . The celerities are the propagation velocities of the turbulent spots normalised with the boundary layer edge velocity  $U_e$ , as determined by the boundary layer calculations discussed in section 4.3. The use of computational methods is necessary as the boundary layer edge velocity cannot be measured directly.  $U_e$  is averaged over the region of interest since the variation is very small for the investigated flow conditions. A similar approach using numerically calculated boundary layer data was also taken by Fiala et al. [52]. For zero-pressure gradient cases, some researchers normalise the celerities with

the freestream velocity, but  $U_e$  is used here as normalisation parameter because of the accelerated boundary layer.

#### 4.5.1 Techniques discussed in the literature

Many studies have previously quantified turbulent spots with a variety of measurement techniques. The processing ideas of some of these studies are presented here:

Zhong et al. and Chaiworapuek & Kittichaikarn [19, 186] identify the footprint of turbulent spots at a threshold level of 10% of the maximum (turbulent) heat flux. This is similar to the method used by Fiala et al. [52], who set the threshold to 1.6 times the local laminar CFD prediction. This value was purposely chosen rather high to prevent noise triggering false alarms.

Clark et al. [25, 26], Chong & Zhong [24] and Ching & LaGraff [22] use the intermittency signal of thin-film heat transfer gauges to determine turbulent spot celerities. A detector and criterion function similar to those used in classical intermittency investigations with hot-film and hot-wire anemometry distinguishes the boundary layer state binary in either laminar or turbulent. The changes from laminar to turbulent and vice versa are identified as leading and trailing interfaces, respectively. These traces are then cross-correlated between two streamwise aligned gauges and the peak is identified as corresponding celerity. For artificially generated spots, hot-wire anemometry is often used with varying laminar-turbulent identification techniques to obtain ensemble-averaged results with many individual spots [61, 181].

Gutmark & Blackwelder [62] use a rake equipped with thermocouples and a threshold on the temperature derivative to distinguish laminar and turbulent signals.

Pandey et al. [123] identified the spanwise extent of turbulent spots as the maxima of the second derivative of intensity profiles across the footprint.

Hogendorn [68] uses the heat flux level for turbulent spot identification. The intercept of the extrapolated rising and falling slope with the laminar and turbulent level determine the time of leading and trailing edges, respectively.

These methods have been investigated for practicability in this work but are not suitable due to one or more of the following reasons:

- The temporal resolution of the recorded iTSP signal is not high enough.
- The heat flux can not be determined consistently and accurately enough across the different freestream conditions, due to the low signal-to-noise ratio.
- The limited signal-to-noise ratio of the iTSP data would require manual identification of trailing and leading edges, and no automated data reduction would be possible.

Therefore, new identification and quantification tools need to be developed. These are discussed in the following sections.

#### 4.5.2 Trailing edge celerity

The trailing edge of a turbulent spot can in this case be defined as where the iTSP intensity  $I$  is at a local minimum in time ( $\partial I/\partial t = 0$  and  $\partial^2 I/\partial t^2 > 0$ ) [129]. The validity of this is

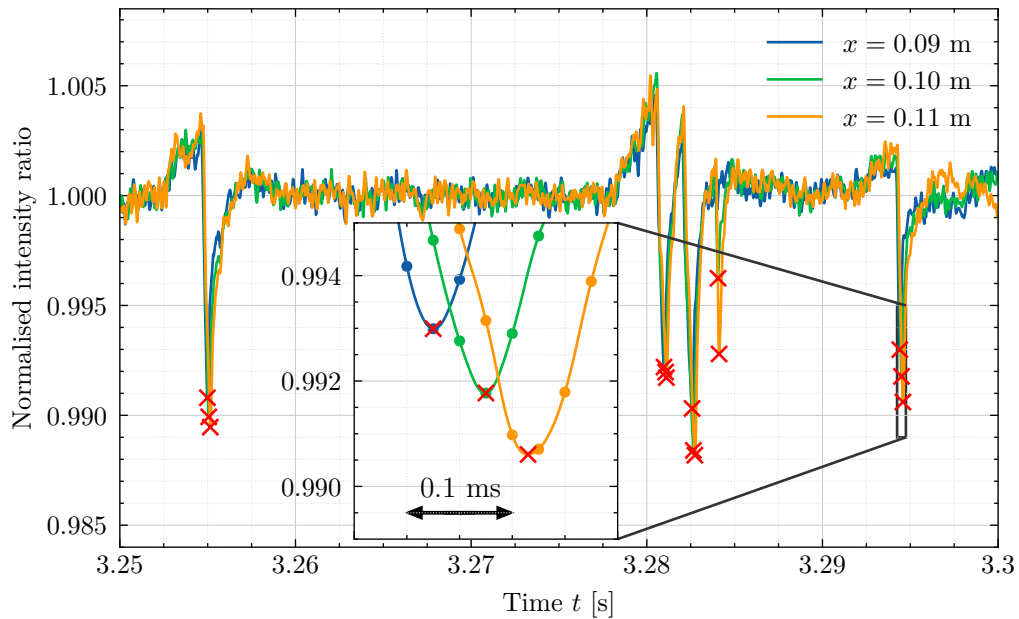


**Figure 4.5.1:** Normalised intensity traces for three streamwise positions at  $y/b = 0.334$  and peak positions (red crosses), determined as explained in section 4.5.2. Flow conditions are  $Re_c = 6 \cdot 10^6$ ,  $M = 0.8$ , and  $\lambda_\theta = 19.0 \cdot 10^{-3}$ . The peak positions in the highlighted area correspond to celerities  $c_{te} = 0.42$ ,  $c_{te} = 0.47$  and  $c_{te} = 0.52$  between the blue and green, blue and orange, and green and orange curve respectively. Note: the peaks (normalised intensity above 1) before and after local minima are caused by the normalisation with a running mean and have no physical meaning.

further discussed in section 4.5.5, where the surface heat flux is considered. Based on this consideration the trailing edge celerities are determined as follows:

**Trailing edge detection** The filtered images (filtered as described in section 4.2.3) are subsequently binned 10 x 10 grid points to reduce the complexity of the following procedure and further increase the signal-to-noise ratio. In doing this it is not expected that information would be lost, as would be the case for the unfiltered images, as the images had already been heavily filtered in the previous step. The time series for every grid point is then normalised by a running mean (100 data points equivalent to 5 ms which is much longer than the average intensity peak width). This helps to set an appropriate threshold, as the minimum in intensity is not so much influenced by preceding turbulent spots. This step does not affect the location of the local minima in a range required for the attempted accuracy. The signals are further interpolated with a quadratic spline to improve the temporal resolution by a factor of 10. Figure 4.5.1 shows the interpolated signals for three streamwise locations and the underlying data points for the last 0.05 s of the run. Five traces of turbulent spots can be observed. The turbulent spot at  $t = 3.2835$  s originates on the investigated surface area and is only visible in the traces for  $x = 0.10$  m and  $x = 0.11$  m. Local minima are located if the normalised intensity goes below 0.998 with a minimum prominence of 0.002. The latter helps prevent the false detection of spots and allows a threshold closer to the noise floor. The peaks are indicated by red crosses in figure 4.5.1. A footprint of a turbulent spot is detected at  $t = 3.2835$  s for  $x = 0.10$  m even though the streamwise spot extension is very small at this spanwise location since no intensity drop is detected at  $x = 0.09$  m. Note also that the threshold value set requires a surface temperature change of only 0.06 K (with an iTSP sensitivity of  $-3.3\%/K$ ).

**Trailing edge celerity determination** For every grid point pair in the streamwise direction with a fixed distance between them, the detected peaks are compared and pairs of peaks that fulfil certain criteria are identified as corresponding trailing edges with an associated celerity based on the streamwise distance and time delay. These criteria are necessary to define since turbulent spots can form and/or merge on the investigated surface. A perfect matching of trailing edge events for different streamwise locations is therefore not possible. As the first step, all detected peaks that are not within a certain time interval are exempted from further calculation. The upper value of this interval is set to the assumed lowest possible trailing edge celerity of a turbulent spot ( $c_{te} = 0.3$  - compare section 2.3.3). This way false correlations of two closely followed trailing edges can be minimised. As long as this time interval is set high enough, it does not influence the final result. The lower value of the interval is the assumed highest possible trailing edge celerity ( $c_{te} = 0.6$  - compare section 2.3.3). Furthermore, only grid point pairs with a streamwise distance of more than 200 grid points ( $\Delta x/c = 0.04$  corresponding to 8 mm) are considered, excluding very short time lags. The 200 grid point threshold corresponds to the assumed highest possible trailing edge celerity  $c_{te} = 0.6$  for the  $M = 0.8$  case with a minimum time lag of two succeeding images (0.05 ms for the 20 kHz cases). Therefore all considered correlations have a time lag larger than one frame interval.

Ideally, the celerity should be obtained individually for each spot. This, however, is not possible in an automated way because of the frequent generation and merging of spots within the field of view. Instead, the trailing edge events are divided into temporal sections with the maximum interval being that which a turbulent spot, with assumed lowest possible trailing edge celerity, would take to pass the entire field of view. For isolated turbulent spots, this will accurately separate them, for non-isolated turbulent spots, this criteria ensures there are at least as many spots as temporal sections so as not to mistakenly divide a turbulent spot into two sections. For closely following, merging or parallel running turbulent spots, this procedure will connect the resulting trailing edge celerity to the celerity of one turbulent spot. Temporal sections with too few events are excluded since they represent either very small developing turbulent spots, turbulent spots with only a small portion in the field of view or turbulent spots that were split during the last step. For each temporal section, the time lags for all streamwise distances are averaged and associated with a trailing edge celerity. The average of the single celerities yields a resulting trailing edge celerity for the corresponding data point with standard deviation of the mean as reported uncertainty. Note, the error will be slightly overestimated, since the number of temporal sections will always be smaller or equal to the number of turbulent spots examined for the trailing edge celerity determination, as explained above. Figure 4.5.2 depicts the number of trailing edge events for the field of view for the run also shown in figure 4.5.1. For reasons explained in section 3.1, there are more turbulent spots to the left which is closer to the wind tunnel wall. Since more turbulent spots originate in the field of view, there are generally more trailing edge events in the downstream area of the field of view. The maximum number of trailing edge events in one spatial location is 35, the total number of temporal sections for this case was 37. The trailing edge celerity for this case was determined to  $c_{te} = 0.498 \pm 0.006$ . Note there is a significant variation in trailing edge celerities for individual events: the standard deviation of the individual celerities is higher at  $\sigma_{c_{te}} = 0.036$ .

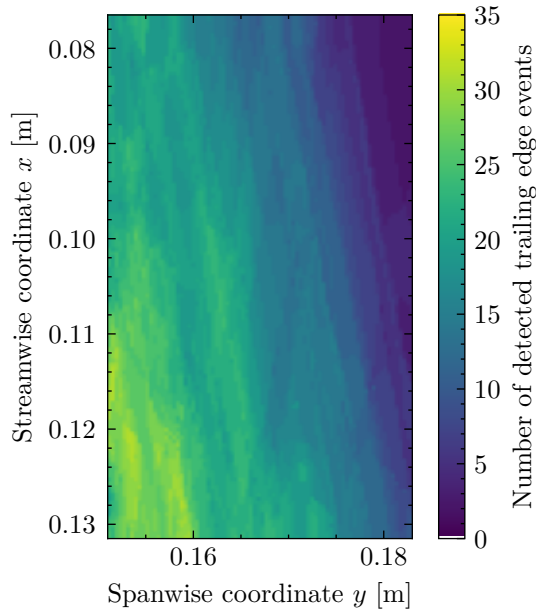


**Figure 4.5.2:** Number of detected trailing edge events over the surface of interest. Flow conditions are the same as for figure 4.5.1.

**Parameter dependency** One key feature of an automated celerity determination is to reduce the number of selectable parameters and limit their dependency on the result. This section deals with parameters still required for the trailing edge detection method. Although parameters were kept to a minimum, five remain: threshold level, normalisation span, minimum and maximum allowable celerity and interpolation level (see above). Table 4.5.1 shows some variation of parameters with their influence on detected trailing edge celerities. The values chosen for the current investigation are indicated in bold.

Threshold		Normalisation		Interpolation	
0.995:	(0.493 ± 0.007)	20:	(0.505 ± 0.007)	1:	(0.476 ± 0.005)
0.997:	(0.494 ± 0.007)	50:	(0.503 ± 0.006)	5:	(0.497 ± 0.006)
<b>0.998:</b>	(0.498 ± 0.006)	<b>100:</b>	(0.498 ± 0.006)	<b>10:</b>	(0.498 ± 0.006)
0.999:	(0.494 ± 0.006)	200:	(0.496 ± 0.006)	50:	(0.498 ± 0.006)
		min. celerity		max. celerity	
	0.25:	(0.485 ± 0.008)	0.5:	(0.483 ± 0.005)	
	<b>0.30:</b>	(0.498 ± 0.006)	<b>0.6:</b>	(0.498 ± 0.006)	
	0.35:	(0.506 ± 0.005)	0.7:	(0.501 ± 0.007)	

**Table 4.5.1:** Parameter dependency for the trailing edge detection method for the flow conditions as present in figure 4.5.1. Values are in per cent of freestream velocity. **Bold** parameters were chosen for this investigation.

The influence of threshold value is very low and mainly affects the ratio of found trailing edges to false positives. A value of 0.998 proved reliable in all investigated flow conditions. The influence of normalisation span and interpolation on trailing edge celerity is negligible as long as a sufficiently high interpolation factor was chosen. With no interpolation (interpolation factor 1) the temporal step size is not sufficient as explained above in this

section and is especially visible in this high Mach number case. An interpolation factor of 10 was sufficient in this case with reasonable computational effort.

The influence of minimum and maximum allowable celerity is slightly more pronounced as this determines what are considered false positive correlations. Generally, keeping the bounds symmetrically around the expected trailing edge celerity does not change the result significantly - this is because if a trailing edge is detected early compared to its real time of arrival, it will yield a celerity higher or lower than the real celerity depending on whether it is compared to an upstream or downstream reference position. Since all trailing edge celerities were found to be in the range of 0.4-0.5 of the freestream velocity, a range of 0.3-0.6 is reasonable for all investigated flow conditions.

**Repeatability** Since several wind tunnel runs had been conducted for most conditions with different camera acquisition frequencies, the reproducibility and robustness of the method can be tested. Table 4.5.2 lists the determined trailing edge celerities for some conditions and the two camera acquisition frequencies. The results show a good reproducibility well within the stated standard deviation for a wide range of conditions, demonstrating the suitability of the proposed method. For most cases, the runs with a camera acquisition frequency of 40 kHz yield a slightly different trailing edge celerity - lower for high Mach number cases and higher for low Mach number cases.

DPN	$Re_c$ [ $10^6$ ]	$M$	AoA	camera frequency [kHz]	$c_{te}$
174	6	0.5	-1.8	20	$(0.455 \pm 0.010)$
175	6	0.5	-1.8	20	$(0.458 \pm 0.008)$
176	6	0.5	-1.8	40	$(0.474 \pm 0.009)$
183	6	0.7	-1.8	40	$(0.465 \pm 0.007)$
184	6	0.7	-1.8	20	$(0.478 \pm 0.008)$
185	6	0.7	-1.8	20	$(0.480 \pm 0.008)$
291	6	0.8	-3.0	40	$(0.484 \pm 0.005)$
292	6	0.8	-3.0	20	$(0.498 \pm 0.006)$

**Table 4.5.2:** Examples of repeatability of trailing edge celerity determination for different run numbers (DPN) at the same conditions with varying camera acquisition frequencies.

### 4.5.3 Leading edge celerity

Identifying the location and time traces of the leading edge interface poses more difficulties as it can not be associated with a local extremum of the intensity. One possible definition is a local minimum of the second derivative of the intensity corresponding to the highest change in heat flux. The data, however, is not suitable to accurately determine extrema in the second derivative due to the relatively low signal-to-noise ratio. Instead, a new method is suggested to determine leading-edge interfaces for the current study. Figure 4.5.3 illustrates the individual steps for two time traces at two streamwise positions  $x/c = 0.45$  and  $x/c = 0.55$ .

In the first step, the signal is filtered in space and time and normalised as described in section 4.2.3. Analogous to the previous chapter, the filtered signal is binned spatially and interpolated in time to increase the temporal resolution. A central difference gradient (in %/frame) indicates times of high-temperature decays associated with turbulent spots. Setting all positive gradients to zero and only investigating the negative gradients (Criterion

function in figure 4.5.3) helps the identification procedure described below.

A turbulent spot is identified when the minimum temporal gradient reaches a threshold of -0.1 or below with a minimum peak width of 20 interpolated points (1 in the indicator function or 0 otherwise). In a physical interpretation, this corresponds to a 0.6 K/ms surface temperature decay over at least 0.1 ms for a 20 kHz case. This criterion only includes turbulent spots at least 5 mm in length for a low Mach number case. The minimum peak width requirement allows setting a fairly high minimum threshold while still excluding random peaks caused by noise, as can be seen for some cases before  $t = 3.28$  s in figure 4.5.3. This way, it is possible to set one global threshold parameter (-0.1) for all investigated flow conditions, including the low Mach number cases.

The leading edge interface can be defined as when the temporal gradient reaches a specific value leading up to the minimum. An adaptive threshold of 50% of the peak height was chosen and makes use of properties of the motion blur and filters applied: An idealised turbulent spot with binary heat flux levels corresponding to a laminar and turbulent boundary layer will invoke the highest temperature gradient at the leading edge interface. For a short time scale, before the temperature distribution in the model alters too much, the gradient can be described as a step function. Both the motion blur and the spatial Gaussian filter, as described in section 4.2.3, will spread this temperature gradient step but retain the position at 50% of the height of the step. Therefore, despite the strong filtering, a reasonable estimate of the leading edge interface can be obtained, and the Gaussian filter proves a suitable filter choice. For this reason, it is possible to keep the same definition of 50% of the gradient peak height as a threshold value throughout the different flow conditions instead of setting a fixed threshold level. The results obtained for an alternating threshold level for  $Re_c = 6 \cdot 10^6$ ,  $M = 0.8$ , and  $\lambda_\theta = 19.0 \cdot 10^{-3}$  are listed in table 4.5.3. Note: Using the maximum gradient as an indicator for leading-edge celerities is not suitable, as this location is very susceptible to noise. Even though the temperature decay is expected to taper off as the turbulent spot progresses due to the internal temperature distribution of the temperature-sensitive paint, noise can cause the maximum to be detected later than the initial peak in the intensity ratio gradient.

Gradient Parameter	$c_{le}$
1.0	(0.987 ± 0.015)
0.9	(0.994 ± 0.017)
0.8	(1.007 ± 0.019)
0.7	(1.000 ± 0.019)
0.6	(0.991 ± 0.019)
<b>0.5</b>	<b>(0.973 ± 0.021)</b>
0.4	(0.955 ± 0.021)
0.3	(0.935 ± 0.021)
0.2	(0.916 ± 0.196)
0.1	(0.888 ± 0.186)

**Table 4.5.3:** Parameter variation for the leading edge investigation. The gradient parameter is the proportion of the maximum gradient identified at the leading edge. Flow conditions are  $Re_c = 6 \cdot 10^6$ ,  $M = 0.8$ , and  $\lambda_\theta = 19.0 \cdot 10^{-3}$ . Bold indicates the chosen gradient parameter for the leading edge celerity.

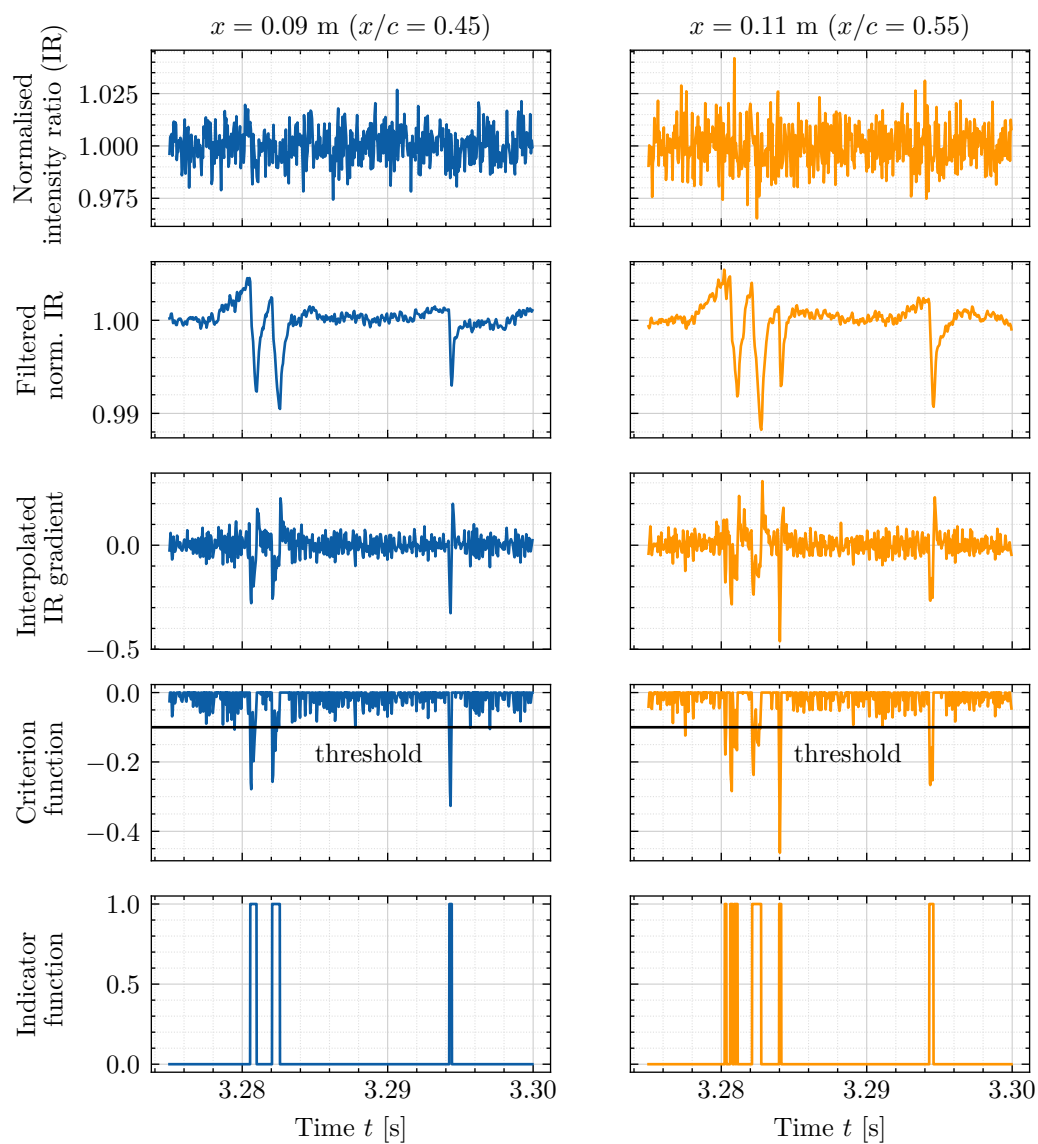


**Figure 4.5.3:** Leading edge detection algorithm for two time traces at  $x/c = 0.45$  and  $x/c = 0.55$  for  $Re_c = 6 \cdot 10^6$ ,  $M = 0.8$ , and  $\lambda_\theta = 19.0 \cdot 10^{-3}$ .

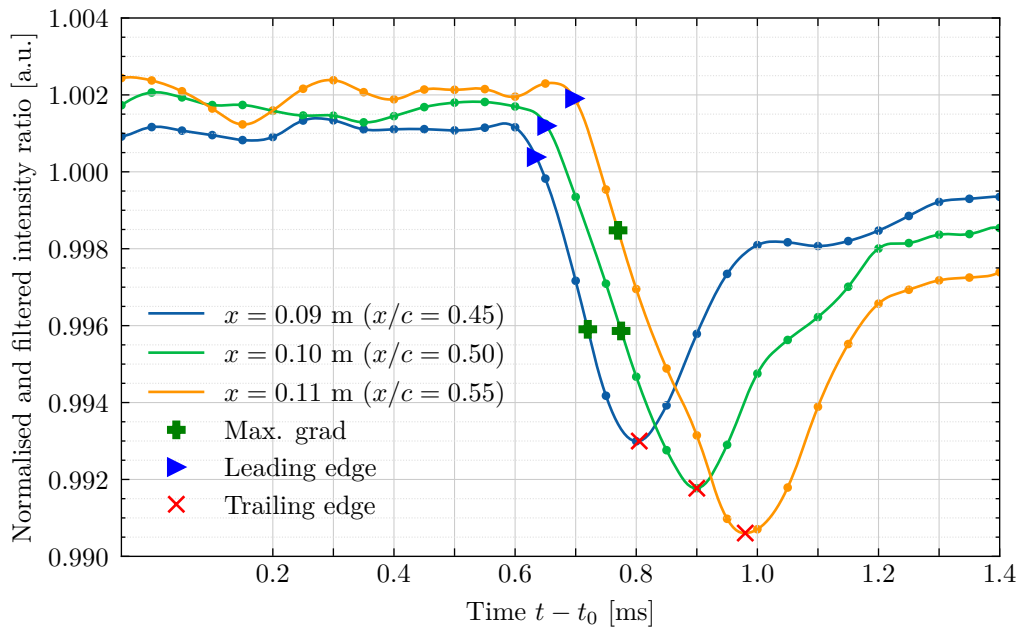


**Figure 4.5.4:** Normalised and filtered intensity traces for three streamwise positions at  $y = 0.167$  m with  $t_0 = 3.2936$  s. Flow conditions are  $Re_c = 6 \cdot 10^6$ ,  $M = 0.8$ , and  $\lambda_\theta = 19.0 \cdot 10^{-3}$ . The intensity gradient images for this spot are depicted in figure 4.5.5.

Figure 4.5.4 shows the intensity signals for three streamwise positions and the detected maximum gradient and trailing and leading edge interfaces described above. The lines represent the interpolated signal of the underlying data points acquired per frame (coloured dots). The leading edge interfaces are detected after the initial intensity decrease caused by the effect of motion blur and filtering. The detected leading edge interface is relatively far away from the maximum gradient but is essentially at the start of the intensity curvature associated with the turbulent spot.

To retrieve the overall celerity for the leading edge of the turbulent spot, the same method as described in section 4.5.2 for the trailing edge celerity is applied for all spanwisely aligned pairs of grid points, but this time with a minimum streamwise spacing of 400 grid points ( $\Delta x = 16$  mm). The assumed celerity range for the leading edge was set to  $0.5 \leq c_{le} \leq 1.3$ . Note that the uncertainties stated are for the mean celerity of all turbulent spots. There may be a physical variation in spot celerities other than measurement uncertainty [181]. Gutmark and Blackwelder [62] for instance, saw a standard deviation in celerities of about 3%, which could not be explained by experimental uncertainty alone and they attributed to a random celerity distribution.

To exclude closely following turbulent spots from this calculation, as their celerities are expected to change significantly compared to the celerities of isolated turbulent spots, a delay time was defined: All leading edges that follow within 0.5 ms (10 images for the 20 kHz case) of a preceding trailing edge are ignored. The effect of this measure is discussed in section 5.1.6.4.

#### 4.5.4 Manual detection of leading edge celerity

The automated leading edge detection method and those found in the literature for naturally occurring spots have inherent simplifying assumptions. For one, they assume the leading

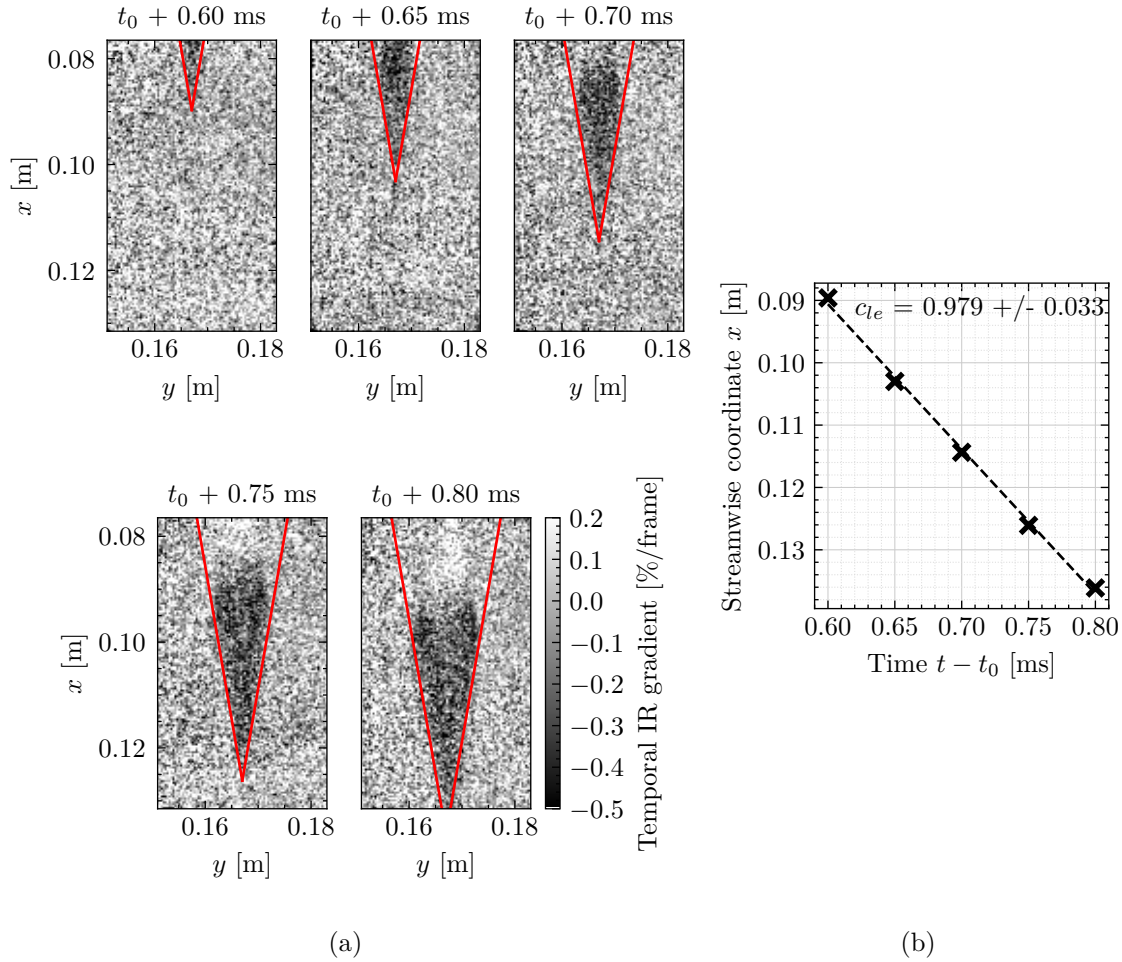


**Figure 4.5.5:** (a) Temporal intensity ratio (IR) gradient images with aligned opening angle wedge. In this case, the opening angle was  $9.8^\circ$ . Time intervals between consecutive images are 0.05 ms (20 kHz acquisition frame rate) with  $t_0 = 3.2936$  s. Intensity signals for one position are presented in figure 4.5.4. (b) location of the tip of the wedge. Flow conditions are  $Re_c = 6 \cdot 10^6$ ,  $M = 0.8$ , and  $\lambda_\theta = 19.0 \cdot 10^{-3}$ .

edge celerity to be constant throughout the leading edge interface, not just at the tip. For another, merging of turbulent spots is expected not to influence the celerity. Lastly, they cannot easily distinguish closely following turbulent spots. A further manual evaluation method was applied here to address these issues. The procedure is shown in figure 4.5.5(a). A wedge with an opening angle is manually aligned with the leading edge region of a turbulent spot. The opening angle is variably chosen from spot to spot but fixed for one turbulent spot, as it is not expected to change during the lifetime of a spot. An attempt to automate this process proved non-reliable, especially for the low Mach number cases with their low signal-to-noise ratios. This way, also the opening angles of individual spots are determined. The streamwise wedge tip position is plotted in figure 4.5.5(b) with respect to the corresponding image time. The celerity for this particular turbulent spot measured manually is  $c_{le} = (0.979 \pm 0.033)$ . One further advantage of this method is that the variation in celerity from spot to spot can be determined since the celerity for individual spots is known directly and must not be estimated with time intervals. The manually determined leading edge celerities are used in section 5.1.2 to compare the results with those obtained with the automated method.

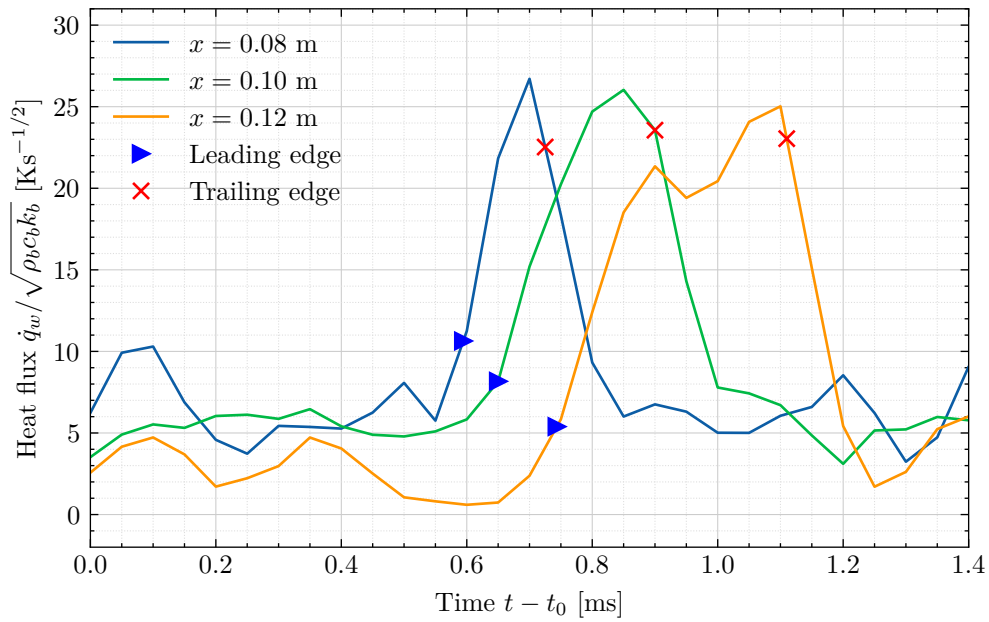


**Figure 4.5.6:** Detected leading and trailing edges relative to the heat flux signal for three streamwise positions at  $Re_c = 6 \cdot 10^6$ ,  $M = 0.8$ , and  $\lambda_\theta = 19.0 \cdot 10^{-3}$  with  $t_0 = 3.2936$  s.

#### 4.5.5 Comparison of leading and trailing edge interfaces with heat flux levels

Figure 4.5.6 shows the normalised heat flux time signal for three different streamwise locations for the turbulent spot presented in figures 4.5.4 and 4.5.5. The detected passover times of the leading and trailing edges are marked with blue triangles and red crosses, respectively. Note that these were determined from the intensity signals, as described above, and not from the heat flux traces. For the leading edge, the determined positions are very similar to the 10% “deviation of local laminar heat flux level to the maximum difference within the spot” as described by Zhong et al. (TLC) [186] and Chaiworapuek et al. (TLC) [19] and 5% for Jewell et al. (heat transfer gauges) [74]. The trailing edge was defined by Zhong et al. as the sudden “rapid decrease from the turbulent level” and by Hogendorn et al. [68, 69] as the location where the falling heat flux flank meets the average turbulent level. Both of these trailing edge definitions are similar to the locations defined in this work and the same as used by Rakpakdee et al. with thermal liquid crystals [129].

## 4.6 Spreading and opening angles of turbulent spots

The spreading angle  $\alpha$  of turbulent spots was determined with an ensemble average. This procedure is similar to determining the spreading angle of a turbulent wedge. Spreading angles of individual spots with a thermographic imaging technique have so far only been determined in low-speed water channels [19, 91, 186], whereby the spreading angle is calculated by the position of successive wing tips of the respective spots.

For this study, the following method was implemented:

- The temporal intensity ratio gradient is computed.
- The images are filtered with a 3x3 median filter and a 5x5 Gaussian filter to reduce noise.
- For an image series containing an isolated turbulent spot, the minimum temporal gradient is determined at each position (resulting in one image - see figure 4.6.1).
- Otsu's method [118] is applied to determine an appropriate threshold value  $c_{th}$  to separate locations with a low and high minimum temporal intensity ratio. The method uses a nonparametric approach to identify a robust threshold for bimodal inputs. It is a common technique in the field of image processing. Hereby, the desired threshold is achieved when the intra-class variance is minimised for all possible threshold values. This work makes use of the implementation of the python module *scikit-image*[169].

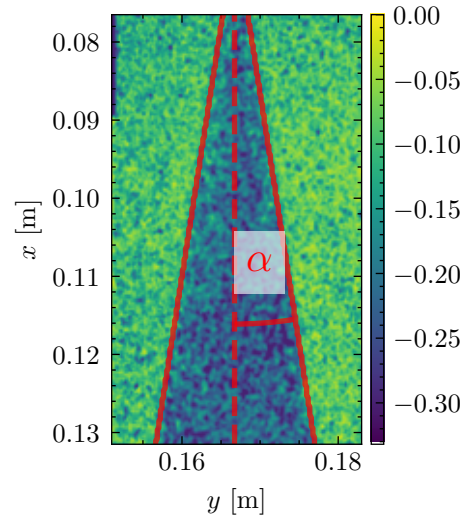


**Figure 4.6.1:** Minimum temporal intensity ratio (IR) gradient in %/frame for the determination of spreading angle for the turbulent spot presented in figures 4.5.4 and 4.5.5. Spreading angle here is  $\alpha_s = 10.4^\circ$ .

- Extreme values are capped at zero (for non-negative gradients throughout the series) and at two times the threshold value ( $2c_{th}$ ).
- The threshold value  $c_{th}$  (negative) is subtracted from the image, resulting in positive values (previously above the threshold - for areas assumed not to be affected by the turbulent spot) and negative values (previously below the threshold - for areas assumed to be affected by the turbulent spot).
- An open-ended triangle is fitted to the resulting image from the previous steps with a virtual point of origin and (half-)spreading angle  $\alpha$  as parameters. The underlying function minimises the product of the triangle (an image of the same dimension as the underlying image, where the inside of the triangle are ones and the outside zeros) and the image resulting from the previous steps.

An example can be seen in figure 4.6.1 for the turbulent spot presented in figures 4.5.4 and 4.5.5. It is only possible to determine the spreading angle  $\alpha$  of isolated turbulent spots.

The opening angles  $\beta$  were determined as described in section 4.5.4 with a manual identification method.

## 4.7 High-frequency iTSP evaluation

For the iTSP test cases with measurements at 100 kHz, not enough markers were visible within the field-of-view for accurate image alignment and mapping. For the method described in section 4.2.2 with 11 independent parameters, at least six accurately detected markers are required. Due to the limitations of the camera field-of-view, applying six markers in the field of view was not feasible. For a frame rate of 100 kHz and covering 1024 pixels in a streamwise direction, the spanwise resolution could be at a maximum of 32 pixels for the camera model used here. Covering as much distance in a streamwise direction as possible was considered favourable to get maximum information on the streamwise development of instabilities, albeit at the cost of spanwise resolution. Due to the shallow viewing angle, the vibrations of the camera and the model movement, it was still necessary to align and map the images to achieve the best signal-to-noise ratio. To achieve an accurate estimate, the two visible markers were aligned by affine transformation to the same two markers visible in a different run with a larger field of view (and consequently lower frame rate). Two markers allowed for translation in the x and y direction (2 parameters  $t_x$  and  $t_y$ ) as well as rotation and scaling (1 parameter each - angle  $\theta$  and scaling factor  $s$ ). Every pixel  $x, y$  is then associated with a new position  $x', y'$  via following relation:

$$\begin{pmatrix} x' \\ y' \\ 1 \end{pmatrix} = \begin{pmatrix} s \cos(\theta) & -s \sin(\theta) & \cos(\theta)t_x \\ s \sin(\theta) & s \cos(\theta) & \cos(\theta)t_y \\ 0 & 0 & 1 \end{pmatrix} \begin{pmatrix} x \\ y \\ 1 \end{pmatrix} \quad (4.7.1)$$

Since the general position of the camera did not change from run to run, this affine transformation is expected to account for most of the movement in the images. Sub-pixel alignment is achieved by linear interpolation of neighbouring pixels to use the precision of the marker detection algorithm described in section 4.2.1. After alignment, the mapping transformation determined for the larger field-of-view is applied.

## 4.8 Hot-film anemometry

Hot-films are typically used to extract information on the local wall shear stress  $\tau_w$ . This is based on the Reynolds analogy, which relates momentum exchange and heat transfer to each other. The power required to keep the hot-films at a constant temperature  $P_{el}(t) = \frac{U(t)^2}{R}$  is equivalent to the energy transferred to the environment. It is a composite of conductive heat transfer to the model, heat radiation and convective heat transfer to the flow. Bellhouse and Schultz [7] showed it was possible to determine quantitative values of wall-shear stress with a suitable calibration for each hot-film. A calibration is particularly challenging in a compressible flow [87] and was not attempted here. Instead, the principle of quasi wall shear stress, as introduced by Hodson et al. [66] is used. It is based on the assumption that conductive heat transfer to the model and heat radiation are approximately constant with and without flow. The quasi wall shear stress  $\tau_q$  can be expressed as

$$\tau_q := \left( \frac{P_{el}(t) - P_{el,0}}{P_{el,0}} \right)^3, \quad (4.8.1)$$

where  $P_{el,0}$  is the electrical power required to keep the hot-film temperature constant without flow. Since the hot-films are operated in constant temperature mode, the resistance  $R$  is kept constant and equation 4.8.1 can be written as:

$$\tau_q := \left( \frac{U(t)^2 - U_0^2}{U_0^2} \right)^3. \quad (4.8.2)$$

For quantitative measurements of the wall shear stress it would be necessary to correct the measured raw voltage signals for a change in ambient temperature [70]. For this investigation, however, the uncorrected quasi wall shear stress is sufficient for analysing the hot-film data and determining intermittency factors (section 5.2) and the frequencies of the most amplified T-S waves (section 5.4.1) but only gives limited validity for quantitative comparisons. Further details on the correction procedure and reasoning on why it is not necessary in this investigation can be found in appendix A.3.

# Chapter 5

## Results and Discussion

### 5.1 Turbulent spots

#### 5.1.1 General features of turbulent spots

##### 5.1.1.1 Thermal footprint

Figure 5.1.1 shows the surface temperature distribution for the passage of an isolated naturally occurring turbulent spot, which appears as a dark shadow passing over the investigated surface area. In these images, other thermal features can also be seen: black and white dots, and the nearly horizontal dark and bright stripes.

The dots arise from the markers used for image alignment and mapping. The markers are applied under the active layer and above the screen layer (see section 3.4.2). They appear darker in the raw images because they cover the screen layer below which prevents the reflection of the excitation and emission light. When dividing two correctly aligned images to retrieve qualitative temperature information, this should, in theory, cancel out since the luminescent intensity ratio depends solely on the temperatures and not on the total luminescent intensity. The markers are still visible, however, primarily due to image blurring, incomplete alignment and differing temperatures. A further discussion on the various reasons for the appearance of the markers is outlined in Appendix A.5.

Despite the efforts for a precise calibration described in section 4.1, the apparent temperature distribution is not completely homogeneous, which is especially pronounced in the dark and light stripe patterns (top and bottom: “apparent” low temperatures, and in the middle: “apparent” high temperature), as well as a somewhat weaker stripe near the top of the images. They are caused by inhomogeneous paint ageing and uneven distribution of excitation light, which could not be fully accounted for here (see section 4.1 for details). The spatial temperature distribution in each image does not directly yield the shape and characteristics of a turbulent spot, as the surface temperature depends on the history of the heat flux at each location. The enveloping wedge of the spot can still be distinguished several frames after the turbulent spot itself has passed, as it takes time for heat convecting from the model core to the surface to restore a temperature equilibrium associated with a laminar boundary layer. However, the general features of a turbulent spot are visible: Images (c) to (g) yield the triangular-shaped downstream-pointing leading edge, the surface area of

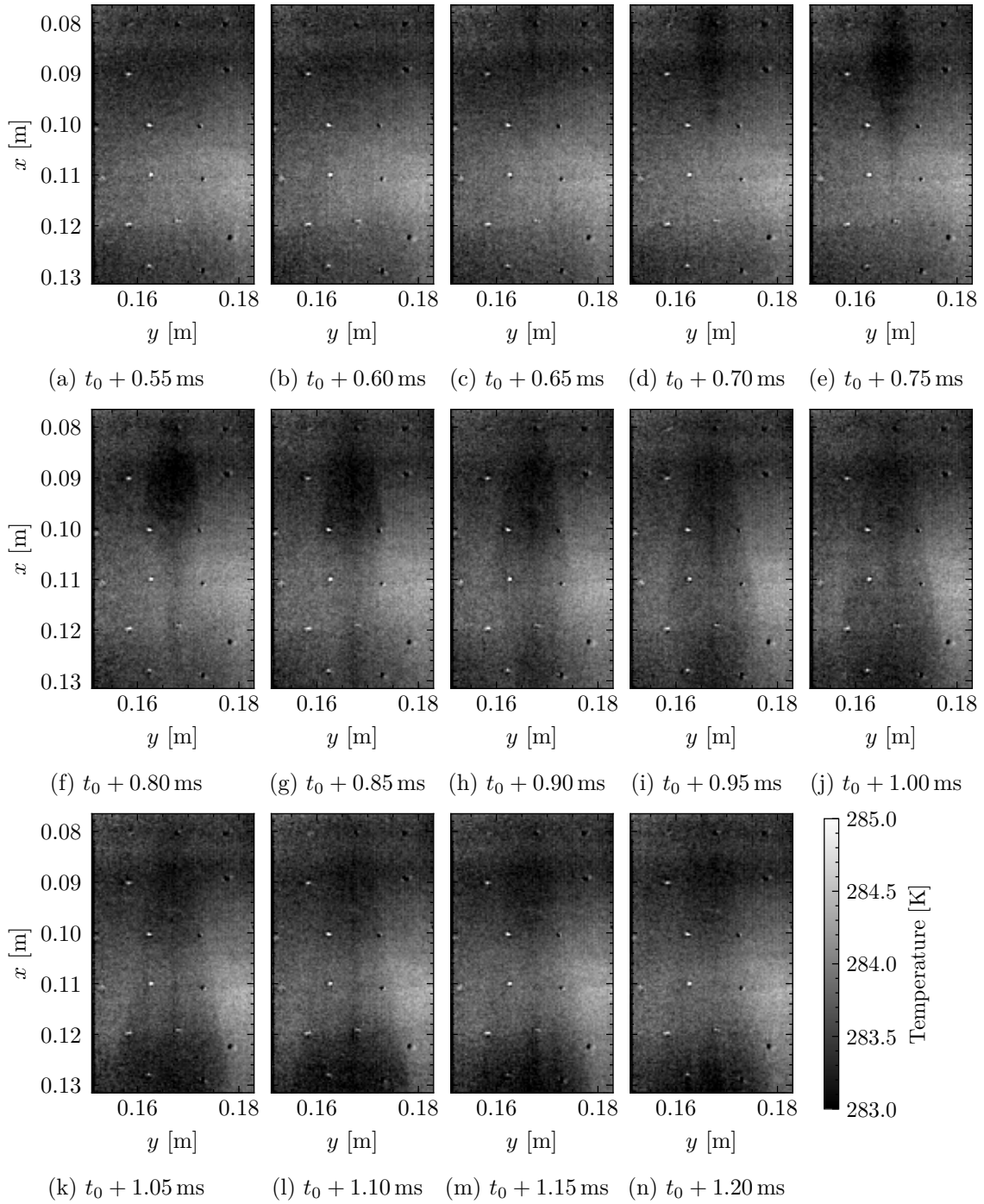


**Figure 5.1.1:** Surface temperature distribution for an isolated turbulent spot with  $Re_c = 6 \cdot 10^6$ ,  $M = 0.8$ , and  $\lambda_\theta = 19.0 \cdot 10^{-3}$  at  $t_0 = 3.2936$  s.

the spot grows in the streamwise and spanwise direction, and it covers a wedge-shaped area.

For a qualitative visualisation, examining the temporal temperature gradient is more suitable, as can be seen in figure 5.1.2. Here, dark areas (negative temperature gradient) correspond to areas with a high heat flux (turbulent boundary layer), and light areas (positive or zero temperature gradient) correspond to areas with a low heat transfer, i.e.

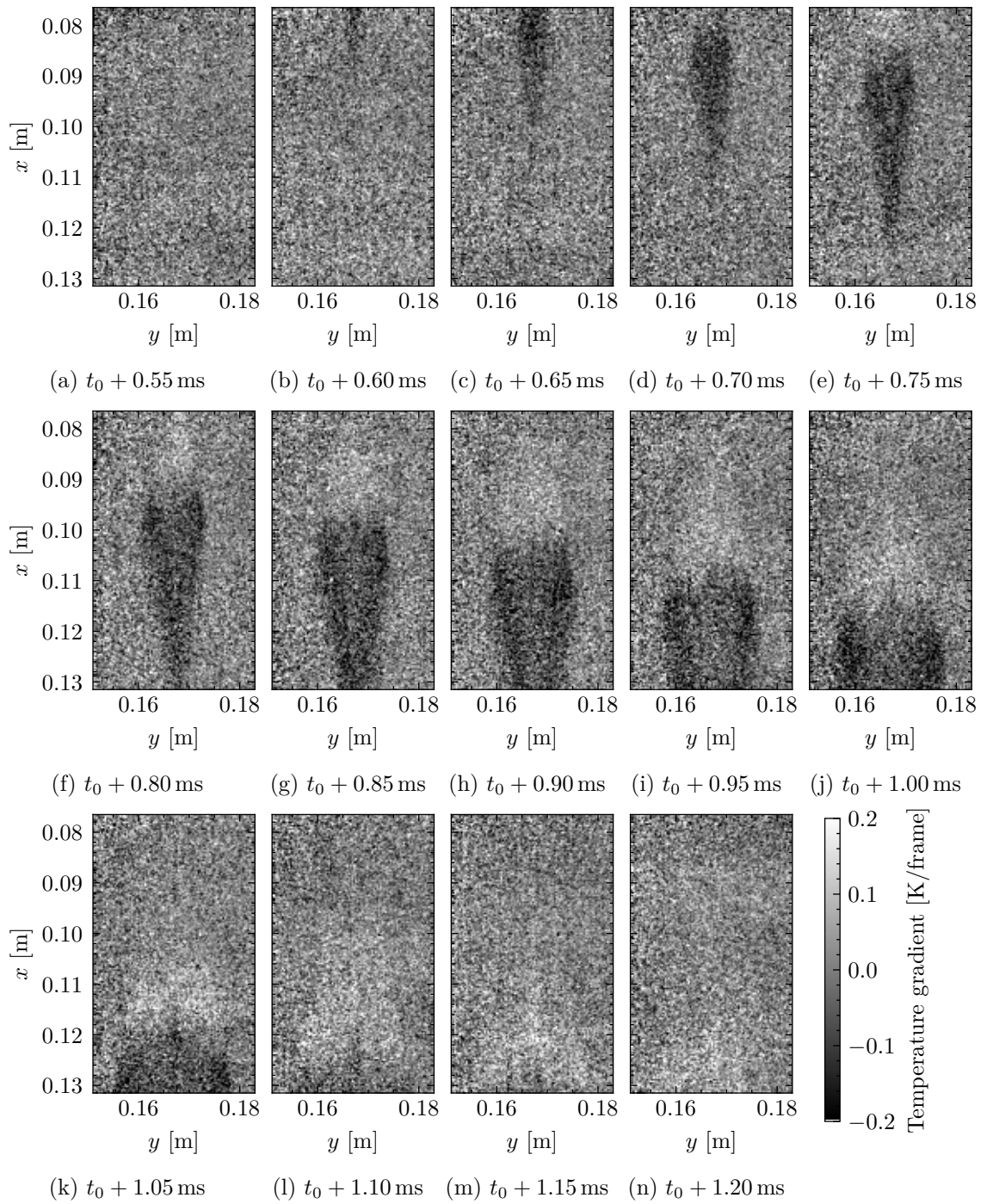


**Figure 5.1.2:** Temporal temperature gradient for an isolated turbulent spot with  $Re_c = 6 \cdot 10^6$ ,  $M = 0.8$ , and  $\lambda_\theta = 19.0 \cdot 10^{-3}$  at  $t_0 = 3.2936$  s. 0.1 K/frame corresponds to 2000 K/s. The surface temperature distribution for this spot is presented in figure 5.1.1.

a laminar boundary layer. This representation clearly shows the streamwise pointing triangular shape of the turbulent spot. The light area trailing the turbulent spot is where the conductive heat flux inside the model and paint exceeds the convective heat transfer to the boundary layer, thus heating the active iTSP layer.

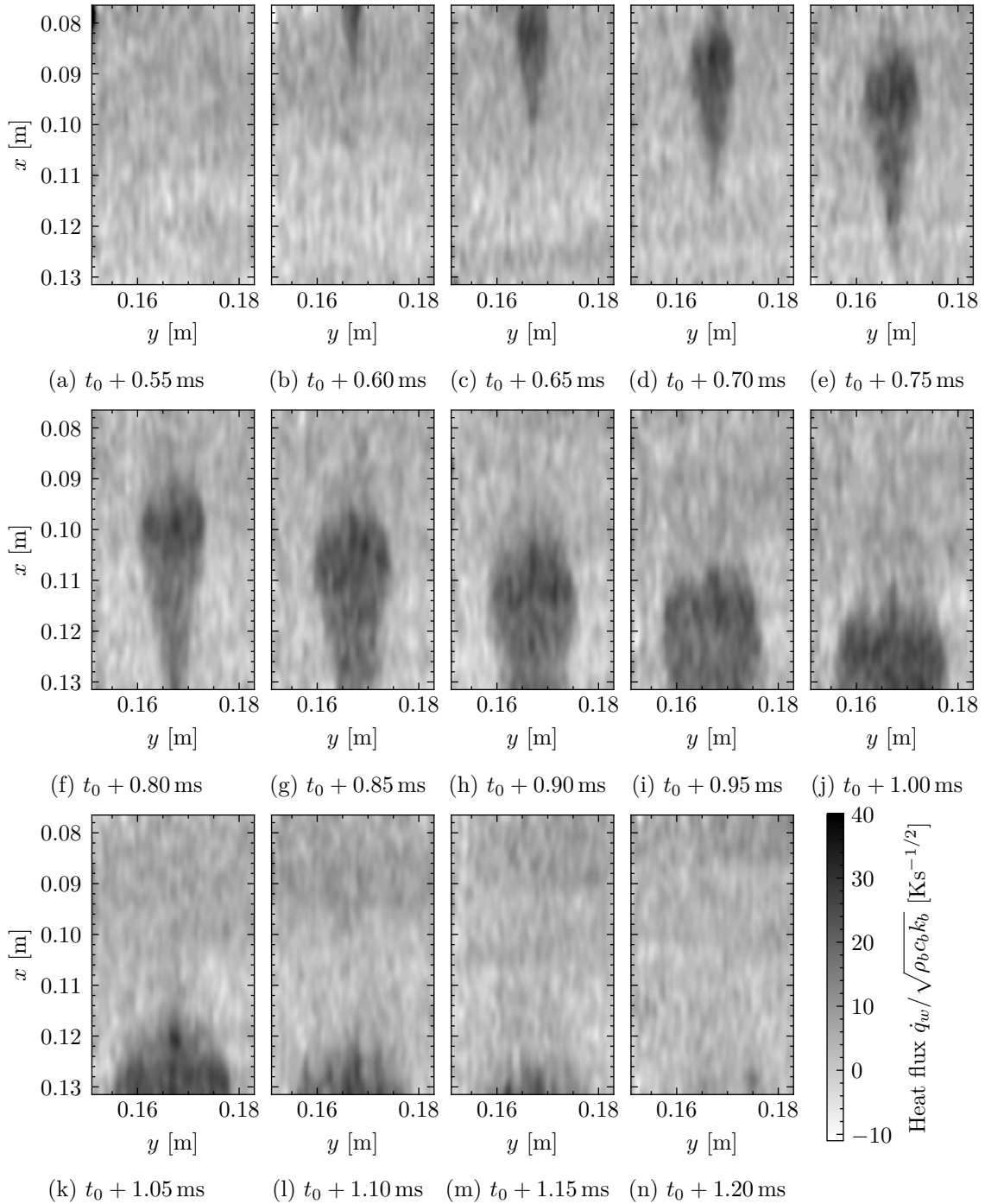


**Figure 5.1.3:** Surface heat flux distribution for an isolated turbulent spot with  $Re_c = 6 \cdot 10^6$ ,  $M = 0.8$ , and  $\lambda_\theta = 19.0 \cdot 10^{-3}$  at  $t_0 = 3.2936$  s. Figure 5.1.1 and 5.1.2, respectively, show the surface temperature distribution and the corresponding temporal temperature gradient.

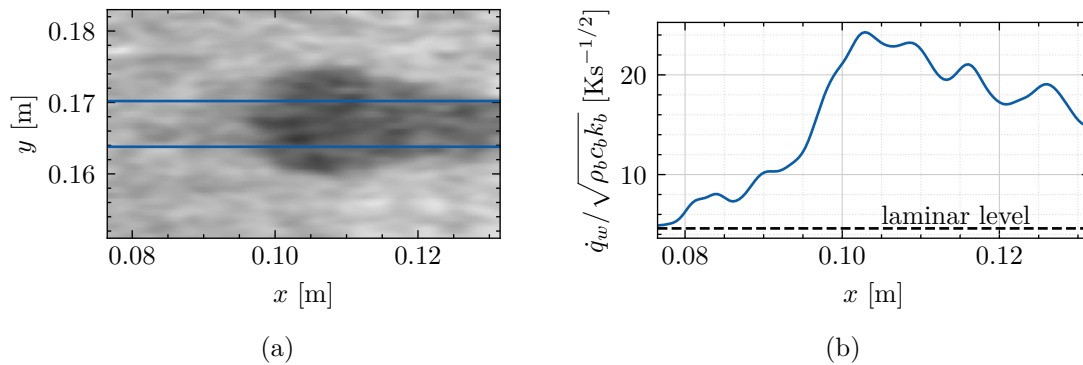


**Figure 5.1.4:** Streamwise heat flux distribution for a turbulent spot presented in figure 5.1.3(h) with  $Re_c = 6 \cdot 10^6$ ,  $M = 0.8$ , and  $\lambda_\theta = 19.0 \cdot 10^{-3}$  at  $t = 3.29425$  s. Colourmap as in figure 5.1.3. The streamwise distribution in (b) is averaged between the two blue lines indicated in (a). Flow is from the left.

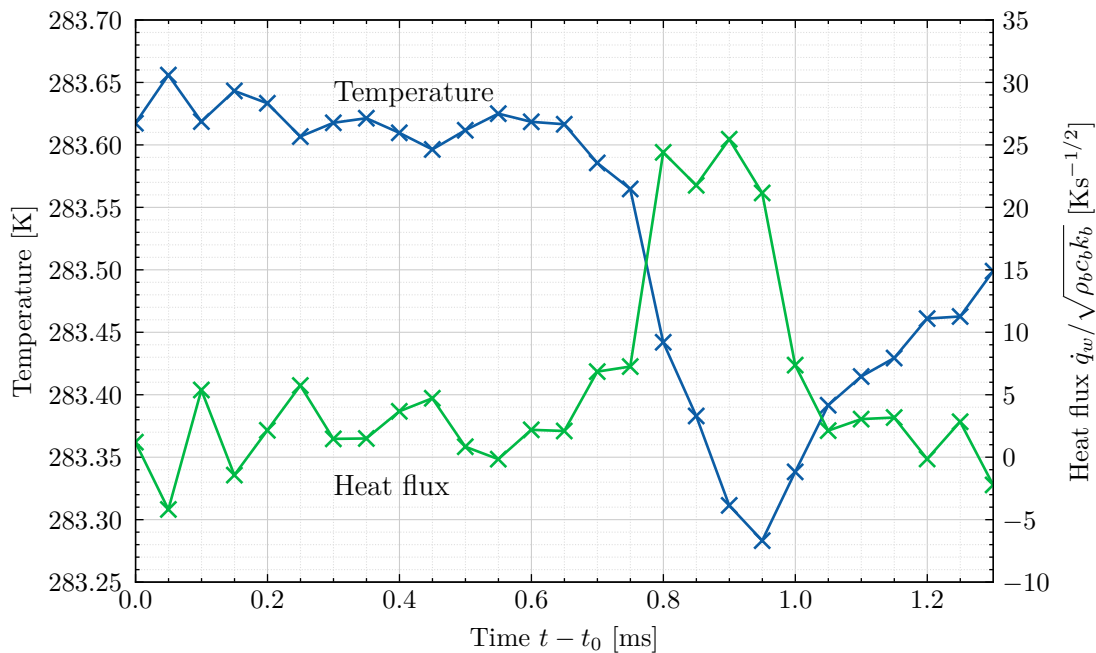
### 5.1.1.2 Heat flux measurements

Figure 5.1.3 shows the calculated, normalised surface heat flux for the turbulent spot presented in figures 5.1.1 and 5.1.2, as described in section 4.4. The heat flux is normalised by the base layer thermal property  $\sqrt{\rho_b c_b k_b}$ . Based on the estimation of section 4.4, the surface heat flux is in the range of  $10 \text{ kW/m}^2$  to  $15 \text{ kW/m}^2$  under the turbulent spot and about  $3 \text{ kW/m}^2$  for a laminar boundary layer. In this case, the heat flux is representative of the convective heat-transfer coefficient since the temperature difference between wall temperature and adiabatic wall temperature is essentially close to constant throughout the passage of the spot. The heat flux is, therefore, a direct representation of the state of the boundary layer. As expected, the shape is the same as represented by the temporal temperature gradient. The resolution is lower due to the binning prior to the heat flux calculations, as discussed in section 4.4. The general downstream-pointing triangular shape is visible. The leading edge tip is seen to be pointed, at least within the limitations of the image resolution, as can also be seen in figure 5.1.2. The wing tips of the turbulent spot are rounded, in contradistinction to the idealised triangular shape. This effect has also been observed in numerical calculations for supersonic flows [88, 130, 181]. The trailing edge interface is mostly flat, but with some bulges.

There is only a faint appearance of a calmed region on the heat flux level that can be seen trailing the turbulent spot in figure 5.1.3. A better visualisation is given in figure 5.1.4: There is an area of increased heat flux compared to the values observed in the purely laminar boundary layer between  $0.08 \text{ m} \leq x \leq 0.10 \text{ m}$ . The calmed region is expected to span about the same duration as the turbulent spot itself [101] and, therefore, should cover a significant streamwise portion in images 5.1.3(f) to 5.1.3(j). Van Hest et al. [170] stated the length to be between one- and two-times the length of the spot itself, depending on the pressure gradient. In this case the observable calmed region is shorter than one spot length which could be partly due to the uncertainties of the heat flux determination.

The heat flux intensifies throughout the spot, and reaches its maximum towards its trailing edge. This finding agrees well with the findings of Hogendoorn et al. [67], who examined the heat flux of turbulent spots for flow at  $M = 0.33$ . It is also in line with the expected wall shear stress increase towards the trailing edge, as discussed in Chapter 2.

Figure 5.1.5 shows the surface temperature and heat flux temporal development for the turbulent spot presented above at one location ( $x = 0.1 \text{ m}$  and  $y = 0.168 \text{ m}$ ). An uncertainty range for the presented values can be estimated by evaluating the standard deviation



**Figure 5.1.5:** Heat flux (green) and temperature (blue) temporal development for the turbulent spot previously presented with  $Re_c = 6 \cdot 10^6$ ,  $M = 0.8$ , and  $\lambda_\theta = 19.0 \cdot 10^{-3}$  at  $x = 0.1$  m and  $y = 0.168$  m and  $t_0 = 3.2936$  s.

of the values for a time range with no turbulent spots and short enough for the heat flux and surface temperature to be approximately constant ( $\Delta t < 0.01$  s - compare figure 4.4.2). Evaluating the time range  $3.1 \text{ s} \leq t \leq 3.11 \text{ s}$  yields a standard deviation of  $\sigma_{\dot{q}_w / \sqrt{\rho_b c_b k_b}} = 2.6 \text{ K s}^{-1/2}$  and  $\sigma_T = 0.016 \text{ K}$ .

Once again, it is apparent that the trailing edge of the spot correlates well with the minimum of the temperature distribution. Furthermore, the four consecutive images representing the inside of the turbulent spot ( $3.2944 \text{ s} \leq t \leq 3.29455 \text{ s}$ ) have a roughly constant heat flux, the maximum being towards the end of the spot. Due to the high noise floor in the heat flux signal, the calmed region is not clearly distinguishable here.

### 5.1.1.3 Spot geometry

In addition to the turbulent spot examined above, figure 5.1.6 shows the shape of three further isolated turbulent spots at different flow conditions. They are representative of most of the isolated turbulent spots detected throughout the entire investigation. The images are temporal gradients of the luminescent emission intensity ratio (which correspond to temperature gradients), where the red lines indicate the outlines of the spots, determined as described in section 4.5. All three spots display the characteristic overall downstream-pointed triangular shape. The leading edge apex in figures 5.1.6(a) and 5.1.6(b) appear more rounded compared to figure 5.1.6(c). In the case of figure 5.1.6(a), a more pointed central part of the spot can be seen. As discussed in the previous section, all spots feature the rounded wing tip region.

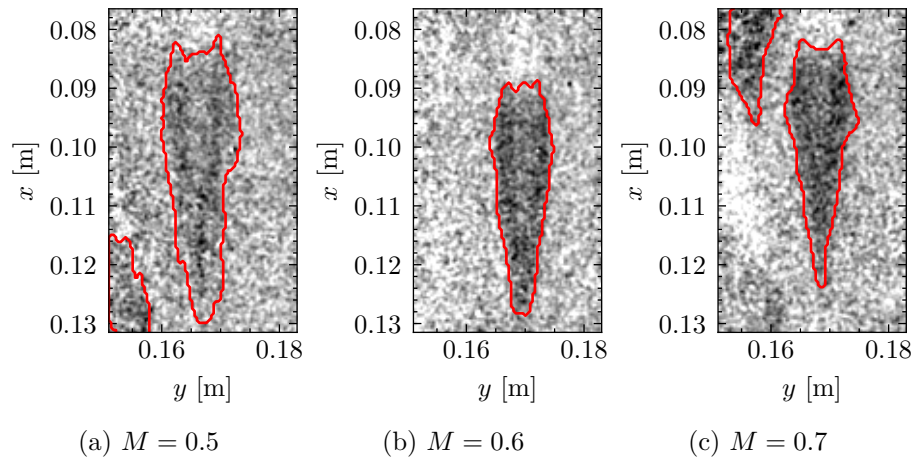


**Figure 5.1.6:** Temporal intensity ratio (IR) gradient for three different isolated turbulent spots from three different runs. Colourmap as in figure 4.5.5. Red lines mark the detected turbulent spot interfaces. Flow conditions are: (a)  $Re_c = 6 \cdot 10^6$ ,  $M = 0.5$ , and  $\lambda_\theta = 9.1 \cdot 10^{-3}$  at  $t = 3.2482$  s; (b)  $Re_c = 6 \cdot 10^6$ ,  $M = 0.6$ , and  $\lambda_\theta = 12.3 \cdot 10^{-3}$  at  $t = 3.2814$  s; and (c)  $Re_c = 6 \cdot 10^6$ ,  $M = 0.7$ , and  $\lambda_\theta = 11.0 \cdot 10^{-3}$  at  $t = 3.21825$  s.

### 5.1.2 Turbulent spot celerities

This section describes and discusses the turbulent spot celerities at the different run conditions: pressure gradient, Mach number, and Reynolds number which have been independently varied during the measurement series. For all cases, three celerities are given: trailing edge celerity, as described in section 4.5.2; leading edge celerity, as described in section 4.5.3; and leading edge celerity obtained via the manual leading edge detection, as described in section 4.5.4. Although most results show a good agreement between the two leading edge celerity detection methods, both have distinct advantages. To be able to reliably distinguish trends, an accurate celerity determination is required. Therefore, both methods are presented and compared with one another to increase confidence. Note that although both methods are applied to the same experimental data, they are entirely independent of each other, further serving to demonstrate the overall accuracy of the leading edge celerity detection.

#### 5.1.2.1 Pressure gradient effects

Figure 5.1.7 shows the effect of pressure gradient on the leading and trailing edge celerity of turbulent spots for  $Re_c = 6 \cdot 10^6$  and  $M = 0.8$ . The angles-of-attack associated with the presented pressure gradients vary from  $-1.8^\circ$  to  $-3.0^\circ$ . The resulting pressure distributions on the upper side of the model, measured with the installed pressure taps, are plotted in figure 5.1.8. The leading and trailing edge celerities increase with increasing (more favourable) pressure gradient parameters  $\lambda_\theta$ . For the lowest  $\lambda_\theta$ , the area with a predominantly laminar boundary layer only covers less than half of the field-of-view, compared to the other cases with higher pressure gradient parameters where the predominantly laminar boundary layer covers more or all of the field-of-view. The limited number of available consecutive images of single turbulent spots leads to high uncertainties, especially so for the leading edge celerity. For all investigated cases, the celerities of the spots scale with the boundary layer edge celerity to within the uncertainty of the measurement.

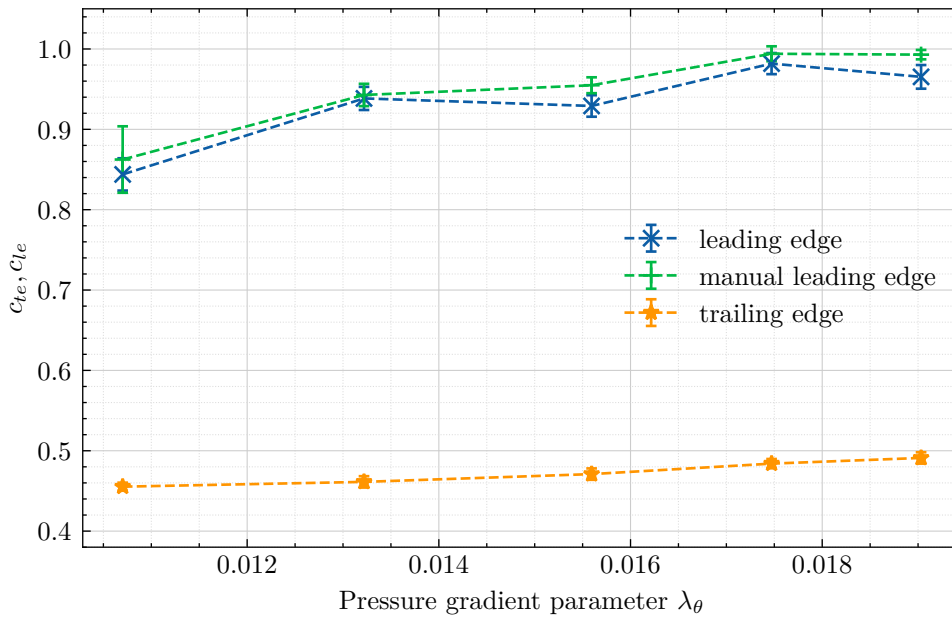


**Figure 5.1.7:** Leading and trailing edge celerities for different pressure gradient parameters for  $Re_c = 6 \cdot 10^6$  and  $M = 0.8$ .

Both methods of evaluating the leading edge celerity agree well within their respective confidence intervals. The values range from  $c_{le} = 0.844 \pm 0.020$  for the least favourable pressure gradient to  $c_{le} = 0.982 \pm 0.014$  for the second most favourable pressure gradient (blue line). Although a significant overlap is present for most neighbouring data points, an overall trend can be identified. A similar trend holds true for the trailing edge celerity: Although the change is relatively small from  $c_{te} \approx 0.45$  for the least favourable pressure gradient to  $c_{te} \approx 0.49$  for the most favourable pressure gradient, and although the uncertainty range is not much smaller than the value range, a trend is still clearly visible.

Additional results regarding the influence of pressure gradient on turbulent spot celerities are presented in Appendix B.1: Figure B.1.1 for  $Re_c = 3.5 \cdot 10^6$  and  $M = 0.35$ , figure B.1.2 for  $Re_c = 6 \cdot 10^6$  and  $M = 0.4$ , figure B.1.3 for  $Re_c = 6 \cdot 10^6$  and  $M = 0.6$ , and figure B.1.4 for  $Re_c = 6 \cdot 10^6$  and  $M = 0.7$ . In general, these results further support the findings described above, especially for the trailing edge celerity, which can be determined more reliably, despite the larger confidence intervals due to the lower Mach numbers.

### 5.1.2.2 Compressibility effects

The effect of the different Mach numbers up to 0.8 at different Reynolds numbers and streamwise pressure gradients was examined. Figure 5.1.9 shows the influence of Mach number on trailing and leading edge celerity for  $Re_c = 6 \cdot 10^6$  and  $\lambda_\theta = (8.0 - 11.9) \cdot 10^{-3}$ . Additional results are presented in Appendix B.1 for  $Re_c = 7.5 \cdot 10^6$  and  $\lambda_\theta = (11.1 - 14.5) \cdot 10^{-3}$  in figure B.1.5 and  $Re_c = 4.5 \cdot 10^6$  and  $\lambda_\theta = (0.5 - 1.0) \cdot 10^{-3}$  in figure B.1.6. Once again, low Mach numbers lead to production of fewer turbulent spots, but with lower signal-to-noise ratios, hence generally increasing the uncertainty. For the highest Mach numbers in each case, the transition location is situated in the field of view, limiting the number of subsequent images for individual spots.

No effect on the leading edge celerity can be seen up to  $M = 0.6$  for all cases. For higher Mach numbers, the leading edge celerity decreases significantly. For the case presented

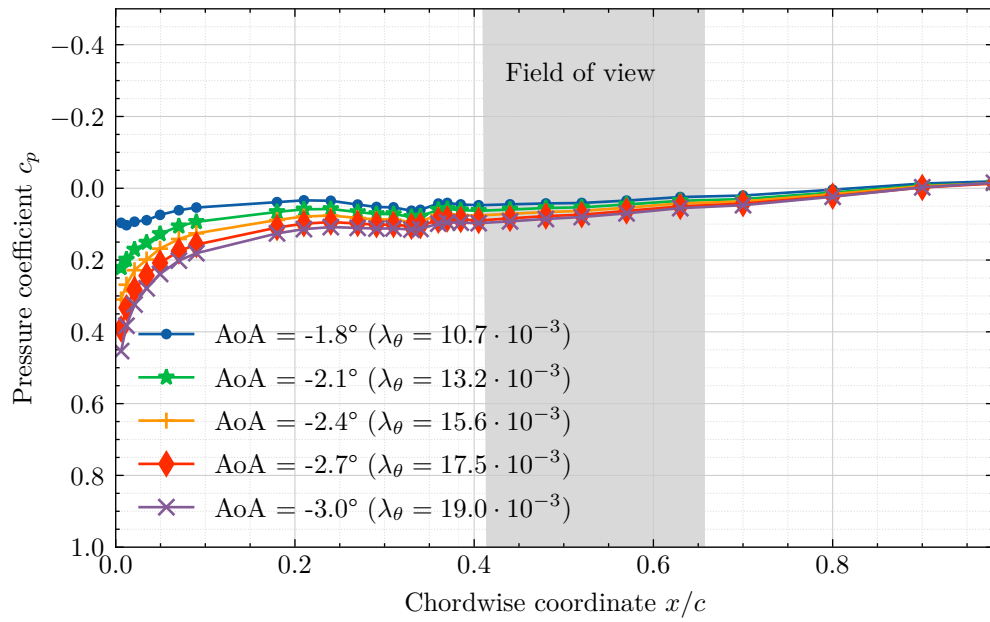


**Figure 5.1.8:** Pressure distribution for different angles-of-attack AoA that are presented in figure 5.1.7.

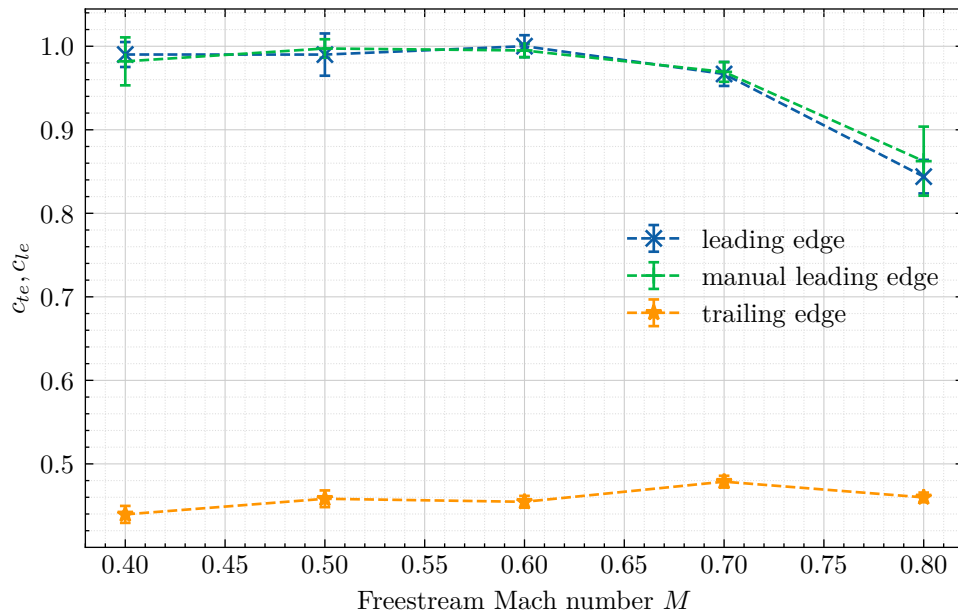


**Figure 5.1.9:** Leading and trailing edge celerities for different Mach numbers for  $Re_c = 6 \cdot 10^6$  and  $\lambda_\theta = (7.9 - 11.9) \cdot 10^{-3}$ .

in figure 5.1.9, the decrease is from  $c_{le} \approx 1.0$  for  $M \leq 0.6$  to  $c_{le} < 0.9$  for  $M = 0.8$ . The manual detection method yields higher leading edge celerities for the high Mach number cases than the automatic method, although both still lie within the stated uncertainties. The trailing edge shows a slow increase of celerity with Mach number except for the case of  $M = 0.8$ , but here the change is small compared to the uncertainty range.

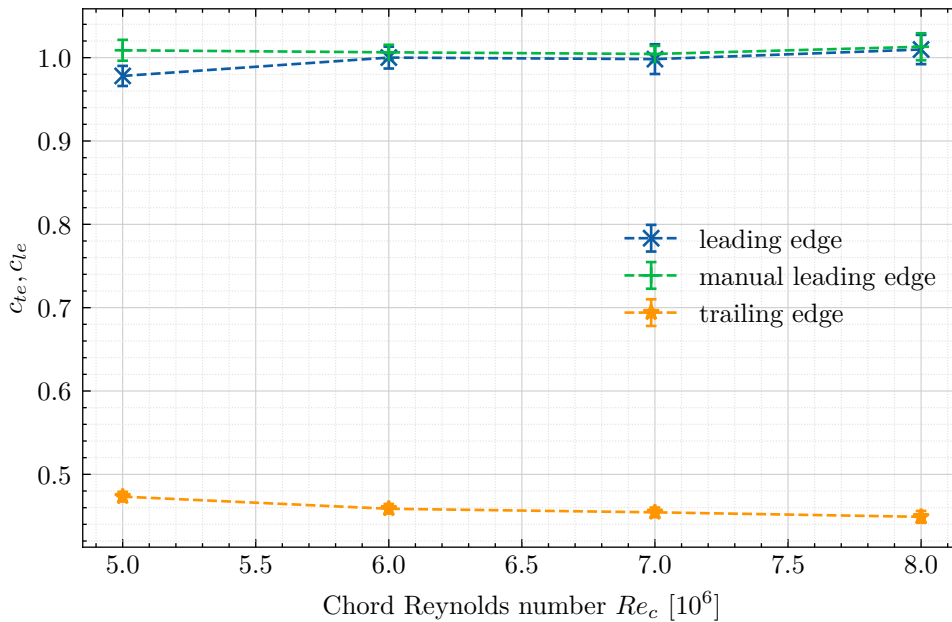


**Figure 5.1.10:** Leading and trailing edge celerities for different chord Reynolds numbers for  $M = 0.6$  and  $\lambda_\theta = (9.6 - 10.0) \cdot 10^{-3}$ .

### 5.1.2.3 Reynolds number effects

Two independent series of measurements were conducted with chord Reynolds numbers ranging from  $6 \cdot 10^6$  to  $10 \cdot 10^6$  and  $5 \cdot 10^6$  to  $8 \cdot 10^6$  to examine the effect of Reynolds number on the celerities of turbulent spots. The first with  $M = 0.6$  and  $\lambda_\theta = (9.6 - 10.0) \cdot 10^{-3}$  is presented in figure 5.1.10 and the second with  $M = 0.8$  and  $\lambda_\theta = (18.9 - 19.5) \cdot 10^{-3}$  is presented in figure 5.1.11. The trailing edge celerity decreases with increasing chord Reynolds number in both cases. For the case presented in figure 5.1.11, the leading edge celerity decreases from  $c_{le} \approx 0.98$  for the lowest chord Reynolds numbers to  $c_{le} \approx 0.9$  at chord Reynolds number  $Re_c = 10 \cdot 10^6$ , using the manual evaluation method. For this series, there is a discrepancy in the celerities obtained with the two leading edge methods. Still, a small reduction in leading edge celerity with Reynolds number can be seen for the automatic method in figure 5.1.11. This effect was not observed for the case presented in figure 5.1.10, where the leading edge celerity remains roughly constant at  $c_{le} \approx 1$  for all investigated chord Reynolds numbers  $Re_c = 5 \cdot 10^6 - 8 \cdot 10^6$ .

Note that the transition location for the high chord Reynolds numbers in both cases is within the camera's field of view, limiting the number of subsequent images for individual spots.

In the following, the decrease in trailing edge celerity is further investigated. Figure 5.1.12 shows the relative streamwise coordinate of the trailing edge for two separate turbulent spots with chord Reynolds number  $Re_c = 6 \cdot 10^6$  and  $Re_c = 10 \cdot 10^6$  at  $M = 0.8$  and  $\lambda_\theta = 19 \cdot 10^{-3}$ . The streamwise position is plotted relative to the respective initial trailing edge location. The location of the trailing edge was determined as described in section 4.5.2. The trailing edge celerity for the higher chord Reynolds number case is significantly lower, which is representative of most of the detected spots.

Figures 5.1.13 and 5.1.14 show the trailing edge celerity for the same data points presented

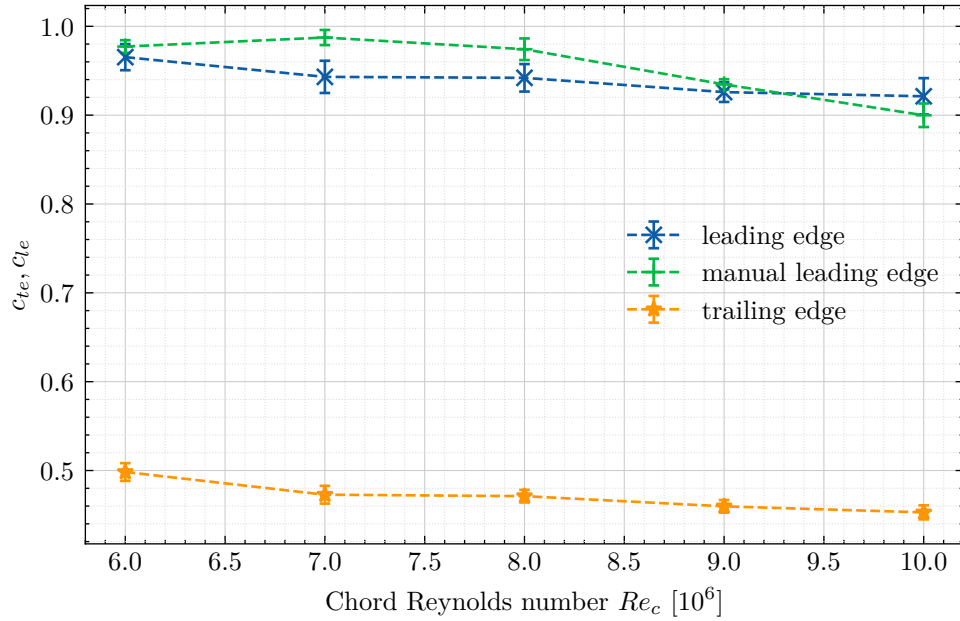


**Figure 5.1.11:** Leading and trailing edge celerities for different chord Reynolds numbers for  $M = 0.8$  and  $\lambda_\theta = (18.9 - 19.5) \cdot 10^{-3}$ .

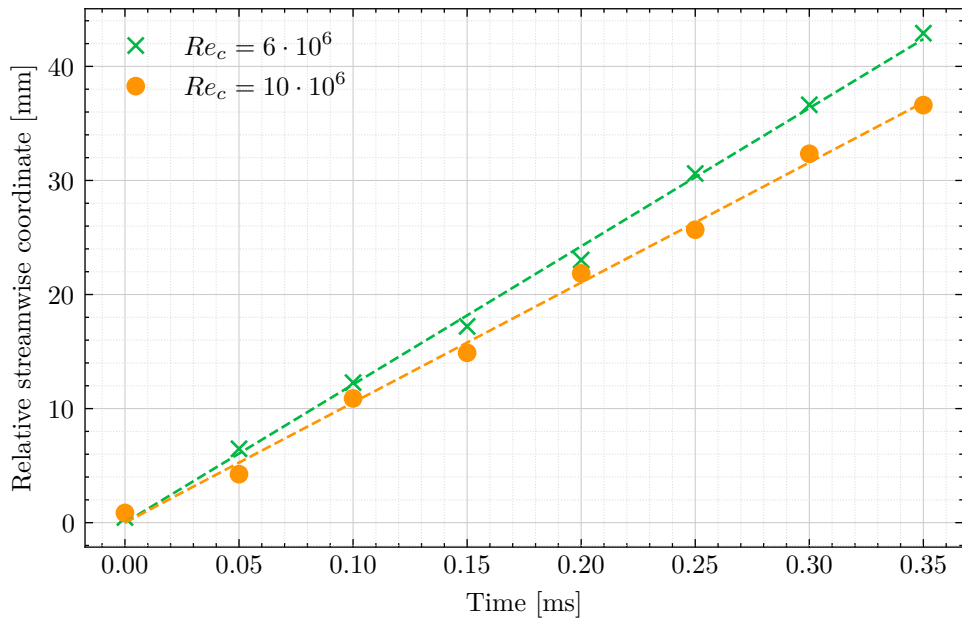


**Figure 5.1.12:** Trailing edge celerity for two isolated turbulent spots for two chord Reynolds numbers  $Re_c = 6 \cdot 10^6$  and  $Re_c = 10 \cdot 10^6$  at  $\lambda_\theta = 19.0 \cdot 10^{-3}$  and  $\lambda_\theta = 19.5 \cdot 10^{-3}$ , respectively, and at Mach number  $M = 0.8$ . Streamwise coordinates and time delta are stated relative to both turbulent spot first detected trailing edge locations.

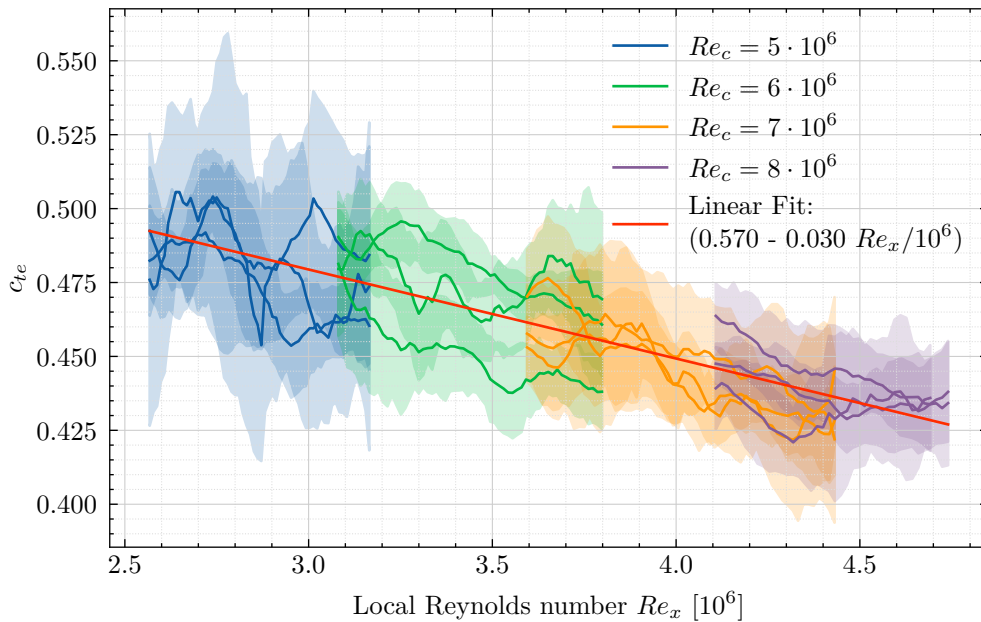


**Figure 5.1.13:** Trailing edge celerity with respect to local Reynolds number  $Re_x$  for a fixed distance two-point correlation and four chord Reynolds numbers  $Re_c = 5 - 8 \cdot 10^6$ . Flow conditions are  $M = 0.6$  and  $\lambda_\theta = (9.6 - 10.0) \cdot 10^{-3}$  and camera acquisition frequency 20 kHz (2x) and 40 kHz (1x) per chord Reynolds number.

in figures 5.1.10 and 5.1.11, respectively. They are evaluated using the automatic method described in section 4.5.2 but with a fixed distance of 450 grid points (18 mm) between the correlation points. They are averaged in the spanwise direction and associated with the local Reynolds number mid-way between the two points. In this way, the streamwise variation of the trailing edge celerity can be investigated. The solid lines are individual runs with different colours corresponding to different chord Reynolds numbers. The shaded areas are the streamwise standard deviation of the obtained celerities. The standard deviation is quite high since a fixed distance between the two correlation points has been chosen, and each streamwise position has been investigated separately. Still, the repeatability (different lines with the same colour) is excellent, with a difference in celerity smaller than 0.02 for most cases.

For both presented cases, the local Reynolds number  $Re_x$  has an influence on the trailing edge celerity. Extrapolating the linear fit to very low local Reynolds numbers ( $< 10^5$ ) would yield a projected trailing edge celerity of  $c_{te} = 0.570$  and  $c_{te} = 0.565$  for the flow at  $M = 0.6$  and  $M = 0.8$ , respectively. The agreement of these values is remarkable, although the dependency on the local Reynolds number (slope) is different for the two series. Even though the similarity may, to some extent, be coincidental and only cover the conditions for the present investigation, the repeatability and the fact that several hundred turbulent spots are considered here support the findings.

#### 5.1.2.4 Discussion on turbulent spot celerities

**General remarks** Compared to other research discussed in section 2.3.3, this investigation, in general, yielded higher leading edge celerities and lower trailing edge celerities. For a significant number of investigated cases, the leading edge celerity was close to or slightly above 1.0, compared to a generally proposed value of  $c_{le} \approx 0.9$ . However, recent studies

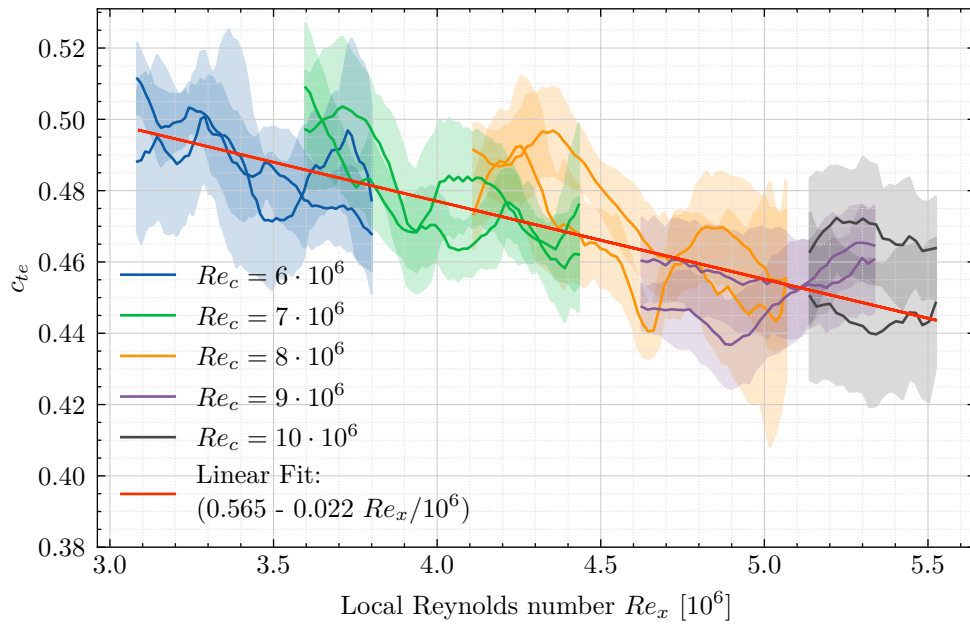


**Figure 5.1.14:** Trailing edge celerity with respect to local Reynolds number  $Re_x$  for a fixed distance two-point correlation and four chord Reynolds numbers  $Re_c = 6 - 10 \cdot 10^6$ . Flow conditions are  $M = 0.8$  and  $\lambda_\theta = (18.9 - 19.5) \cdot 10^{-3}$  and camera acquisition frequency 20 kHz (1x) and 40 kHz (1x) per chord Reynolds number.

suggest leading edge celerities close to one for some supersonic flow conditions, such as the experimental work of Jewell et al. [74] or DNS by Egorov et al. [47]. For all following considerations, it is important to note that many experimental studies on the celerities of turbulent spots are conducted within the boundary layer (e.g. with hot-wire anemometry) and for artificially generated turbulent spots. This study examines non-intrusively naturally occurring turbulent spots directly on the surface. Furthermore, the typical local Reynolds numbers in previous investigations are much lower (of the order of  $10^5$ ) than in this study, and only a few experimental studies investigated a compressible flow.

Note that the turbulent spots examined here are isolated (closely following spots are ignored as outlined in section 4.5.3). Only considering isolated turbulent spots has limited significance for the laminar-turbulent transition process, as in that case, by definition, the growth will be influenced by the streamwise and spanwise merging of spots, which will be discussed later in this section. Nevertheless, it is of interest to examine and characterise isolated turbulent spots, as the influence of flow parameters on their characteristics is readily discernible, and they can be compared with each other. As discussed below, there are several points to consider concerning the high leading edge celerities.

**Considerations on the overhang region** While the turbulent spot celerity is widely expected to be below one at the surface, many researchers report a celerity of the leading edge overhang region at around or close to one [17, 62, 152], considerably higher than the respective celerities closer to the wall. If we assume a leading edge celerity of 0.9 for the foot and 1 for the overhang region, the growth of the overhang region is about 6 mm in the field of view alone (longer for turbulent spot origins upstream of the field of view). Considering boundary layer thicknesses (laminar displacement thickness) to be about  $\delta_1 = 50 \mu\text{m}$  to  $100 \mu\text{m}$  for the test cases examined here, this would imply the length of the overhang region to be about of  $100\delta_1$ . This length is much greater than

the maximum overhang extents of  $25\delta_1$  and  $30\delta_1$  measured by Gutmark and Blackwelder [62], and Antonia et al. [3], respectively. The scaling with  $\delta_1$  is reasonable since the most downstream point of the turbulent spot is generally located at a height of around  $\delta_1$ . It seems unlikely that this aspect ratio of the overhang region would not affect either of the celerities at the foot or the tip of the overhang region because the turbulence in the overhang region spreads towards and reaches the wall prior to the foot of the spot, as would be the case without an extensive overhang region. If the celerity of the overhang is expected to be constant and mainly driven by convection, this could cause the effective foot celerity to be higher in these cases. Some researchers, most notably Wygnanski et al. [181, 182], did not detect a significant difference in leading edge celerity dependent on the wall distance. For all wall normal distances, they observed a constant celerity of 0.89. A direct consequence of a constant celerity along the wall-normal leading edge interface is that the 3D shape of the turbulent spot cannot be considered self-similar, as the streamwise and spanwise extents grow, but the leading edge shape remains the same.

Even if the leading edge celerity close to the wall is not affected by the extent of the overhang region, it is unlikely that a large overhang region does not influence the heat flux on the surface below the overhang region. The heat flux is not simply driven by the state of the boundary layer immediately above the wall but rather by the temperature distribution and boundary layer state throughout the boundary layer. In the case of the overhang region, the temperature gradient within the boundary layer will be higher than a fully laminar boundary layer, causing a higher heat flux on the surface. For a small overhang region, the effect may be considered small compared to the change in heat flux on the wall of the turbulent spot itself, but this is not necessarily true for a large overhang region. A large overhang region could cause the leading edge interface at the wall to be detected further downstream, depending on the extent of the overhang region.

Gutmark and Blackwelder [62] argue that the growth of the spot is dependent on “the scale and intensity of eddies within the overhang and the stability characteristics of the laminar boundary layer”. They mention a study by Lindberg et al. [93] of turbulent spots generated on a water table. Since no freestream was present, the turbulent spot propagated considerably slower, the leading edge region relaminarised, and the general shape was different to the classical triangular shape typical in boundary layer flows. Both works attribute this behaviour to a lack of entrainment of high-energy freestream fluid into the overhang region, emphasising the overhang region’s importance on the growth behaviour of turbulent spots. Gad-el-Hak et al. [56] show that perturbations due to the presence of the spot are “felt” in the areas below and downstream of the overhang region, which was further proposed by Glezer et al. [57]. In contrast to many previous studies for artificially generated spots in an otherwise stable laminar boundary layer, the turbulent spots in this study arise naturally and grow in a more unstable laminar boundary layer. Therefore, the area below the overhang region might be affected more here than in other, more stable flow conditions, which could explain the high leading edge celerities observed for some flow conditions. Additionally, the growth-by-destabilisation hypothesis popularised by Gad-el-Hak et al. [56] would allow leading edge celerities to be larger than one since the downstream growth is not solely dependent on the convection of turbulent structures downstream. The trailing edge celerity, being generally lower than the values reported in the literature, can largely be attributed to the Reynolds number effect discussed in more detail below.

**Pressure gradient effect** Numerous researchers have previously investigated the effect of pressure gradient on turbulent spot celerities. An increase of trailing edge celerity

with  $\lambda_\theta$  was reported by Clark et al. [25]. However, they did not see an influence on the leading edge celerity. Since the celerity of the trailing edge is low due to an adverse pressure gradient at the trailing edge promoting the generation of turbulent structures [56, 140], an increase in trailing edge celerity with a favourable pressure gradient is reasonable and due to the stabilising effect of the pressure gradient. Johnson [77], in a numerical study, predicted the increase of both trailing and leading edge celerity for considerably high Reynolds numbers  $Re_\theta = 1000$  with a favourable pressure gradient, although not as pronounced as was found in this study. This effect was also shown experimentally in an incompressible flow by Sankaran & Antonia [140]. Chaiworapuek et al. [20], studying an adverse pressure gradient in a water tunnel, found a decrease of leading edge celerity with an adverse pressure gradient, in agreement with the findings here with a favourable pressure gradient. That contradicts findings by Chong and Zhong [23], who report a decrease in leading edge celerity with a favourable pressure gradient for an incompressible flow. Wygnanski et al. [182] found that the (dimensional) propagation speed of the leading and trailing edge interfaces did not change along the streamwise direction even though the local boundary layer edge velocity did increase due to a favourable pressure gradient, resulting in a decrease of the celerities along the streamwise direction. This led Narasimha [113] to describe a “memory” of turbulent spots of the flow conditions at their inception location.

**Compressibility effect** The pressure gradient is not constant for all examined Mach numbers. For the series presented in figure 5.1.9, the pressure gradient parameter increases from  $\lambda_\theta = 7.9 \cdot 10^{-3}$  for the low Mach number to  $\lambda_\theta = 11.9 \cdot 10^{-3}$  for the high Mach number. If the effect of the pressure gradient discussed in the previous section holds true for these conditions, this would increase the effect of the Mach number, yielding an even higher difference in leading edge celerity between low and high Mach numbers.

When also considering supersonic Mach numbers, a general decrease in the spreading angle of both turbulent wedges and spots has been observed [25, 52, 106]. This decrease is explained by Redford et al. [130] in that the lateral growth by destabilisation as proposed by Gad-el-Hak [56] becomes subdued at high Mach numbers, and the less efficient spanwise transport of turbulence from the interior of the spot dominates the lateral growth. Considering the effect of destabilisation on the growth of the overhang region discussed above, a decreased effect for high Mach numbers could explain the decrease in leading edge celerity observed here. A further aspect is that a compressible boundary layer is more stable due to a fuller velocity profile [146], possibly diminishing the growth of the overhang region and its spread.

Mayle et al. [102] estimated that transition length would increase by 8% to 30% for  $M = 1$  compared to an incompressible boundary layer, which would be caused either by a decrease in spreading angle or in spot propagation parameter  $\sigma$ . Clark et al. [25, 26] attributed this to the diminished spanwise growth since the streamwise growth was almost unaffected in the range  $0.24 \leq M \leq 1.86$ . Their subsonic measurements were only conducted for the two Mach numbers  $M = 0.24$  and  $M = 0.55$ , not covering the range in which the significant variation of the leading edge celerity was found in this study. Furthermore, they saw a decrease in leading edge celerity from  $0.86 \pm 0.01$  at  $M = 0.24$  to  $0.81 \pm 0.01$  at  $M = 0.55$ , which they attribute to experimental and statistical error. As will be discussed in section 5.1.3, no significant influence on the spreading angle could be observed in this study. The results here instead propose an effect of the celerities that could explain the findings by Mayle et al.

The only other experiment conducted in compressible subsonic flow is by Hogendoorn [68], who measured leading edge celerities of  $c_{le} = 0.98 \pm 0.10$  for a  $M = 0.33$  flow at zero pressure gradient. Those values are very similar to the ones measured in this study.

**Reynolds number effect** Due to experimental limitations, the effect of Reynolds number has yet to be thoroughly studied, especially for high Reynolds numbers. Although there seems to be agreement on the decrease of trailing edge celerity with increasing Reynolds number [22, 73, 77, 182], there is no consistent evidence for the leading edge celerity. Ching & Lagraff [22] see an increase with increasing Reynolds number, Johnson [77] predicts a decrease, and Wygnanski et al. [182] observed no influence. However, all agree on a certain degree of uncertainty and the necessity for further experimental investigations. Furthermore, there is ambiguity in the choice of Reynolds number: based on displacement or momentum thickness or on streamwise location of either turbulent spot initiation or measurement station. One advantage of the current investigation is that the Reynolds number is varied independently of the Mach number. The results in figures 5.1.13 and 5.1.14 suggest a dependency on the local Reynolds number directly since a decrease of trailing edge celerity can be seen with increasing streamwise distance. The small increase in momentum thickness over the field-of-view cannot explain the differences. A possible explanation for this behaviour is that for higher Reynolds numbers at the same streamwise position and the same Mach number and pressure gradient, the general state of the boundary layer will be less stable. Any possible destabilising of the trailing edge will likely be enhanced with a more unstable boundary layer. While this is a reasonable explanation for the effect on the trailing edge celerity, it does not explain the effect on the leading edge celerity. Johnson [77] suggests a role of the viscous sublayer. The proportion of the boundary layer occupied by the viscous sublayer is larger for higher Reynolds numbers. Therefore, the turbulent structures are closer to the wall in a lower mean velocity flow than the boundary layer edge velocity. He, however, proposes the effect to be mainly for Reynolds numbers based on the momentum thickness  $Re_\theta$  below 500, which is considerably lower than the  $Re_\theta$  in this study at around 1000.

The evaluation region for the two highest chord Reynolds numbers was smaller than that of the others due to the transition location being within the field-of-view. Since the pressure gradient parameter  $\lambda_\theta$  increases in streamwise direction for the accelerated boundary layers,  $\lambda_\theta$ , which is averaged over the evaluation region, will be smaller for these cases of high chord Reynolds numbers. Based on the observations presented above for the pressure gradient effect, this will lower the average of both the trailing and leading edge celerities, albeit not in any significant way: its effect is not expected to be strong enough to explain the observations.

Some researchers observed a decrease in spreading angle as the Reynolds number was decreased [152, 182]. Based on equation 2.3.1, this could be caused by a change in leading and/or trailing edge celerity. If the spanwise growth of a spot remains the same, larger spreading angles would be caused by a decrease in trailing edge celerity, as observed in this work.

### 5.1.3 Spreading and opening angles

The spreading angles determined for different Mach numbers at a chord Reynolds number of  $Re_c = 6 \cdot 10^6$  are listed in table 5.1.1. Due to the compressible flow, the pressure gradient parameter  $\lambda_\theta$  is not constant between the Mach numbers even though the angle-of-attack was set to  $-1.8^\circ$  for all cases presented here. The angles are stated as (half) spreading

Mach number $M_\infty$	Pressure gradient parameter $\lambda_\theta$ [ $10^{-3}$ ]	Spreading angle $\alpha$ [ $^\circ$ ]
0.4	8.6	$10.7 \pm 0.6$
0.5	9.2	$10.7 \pm 1.1$
0.6	9.8	$10.3 \pm 0.5$
0.7	10.9	$10.2 \pm 0.4$
0.8	11.8	$9.6 \pm 0.6$

**Table 5.1.1:** Turbulent spot spreading angles  $\alpha$  for different Mach numbers at chord Reynolds number  $Re_c = 6 \cdot 10^6$ .

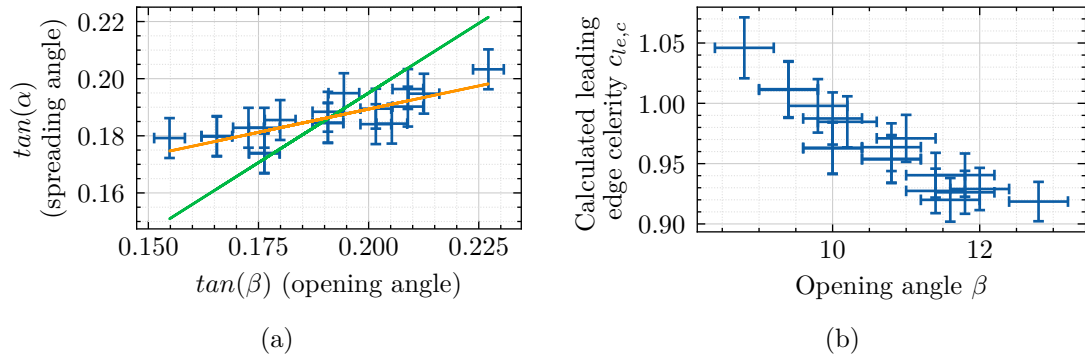


**Figure 5.1.15:** (a) Tangent of spreading angle  $\tan(\alpha)$  in dependence of opening angle  $\tan(\beta)$  (green and orange line: see text) and (b) calculated leading edge celerity according to equation 2.3.1 for  $Re_c = 6 \cdot 10^6$ ,  $M = 0.8$ , and  $\lambda_\theta = 19.0 \cdot 10^{-3}$ .

angles with standard deviation. A spreading angle  $\alpha$  decrease is observed for increasing Mach numbers.

The values agree well with the accepted value at incompressible Mach numbers of about  $10^\circ$  [62, 133, 152, 182] for all investigated Mach numbers. Gutmark & Blackwelder [62] report the spreading angle to be a random variable with a standard deviation of  $1^\circ$  to  $2^\circ$ . The present measurements also observed a variation, although less pronounced. The decrease with respect to Mach number is in line with previous measurements in compressible boundary layers [26, 44], although the effect is not as pronounced here. Clark et al. [26] report a decrease in spreading half angle from  $(9.3 \pm 1.9)^\circ$  for  $M_\infty = 0.26$  to  $(7.6 \pm 1.2)^\circ$  for  $M_\infty = 0.55$ , which is lower and shows a higher Mach number dependency compared to this study.

Chong and Zhong [23] report a spanwise overhang of a turbulent spot, causing their spreading angles to be smaller when measured at the wall than in the boundary layer. Their reported values of  $8.6^\circ$  for a zero-pressure gradient flow and  $4.4^\circ$  for a favourable pressure gradient flow are considerably lower compared to the values found here.

The opening angle  $\beta$  showed a significant variation and was generally measured to be between  $7^\circ$  to  $12^\circ$ , which can not be attributed to measurement uncertainties alone. Due to this scatter, it was not possible to identify any dependencies of  $\beta$  on the flow parameters. The values are in agreement with measurements in incompressible flow by Gutmark & Blackwelder [62], who report  $\beta \approx 10^\circ - 11^\circ$ , and flow visualisations by Gad-el-Hak et al. [56] and Cantwell et al. [17] but significantly smaller than the value reported by Schubauer & Klebanoff [152] of  $\beta = 15.3^\circ$  and Wygnanski et al. [181] of  $\beta = 15.2^\circ$ . For the first time, the current study presents the opening angle  $\beta$  for subsonic compressible flow conditions.

Figure 5.1.15(a) shows the tangent of the spreading angle  $\alpha$  and its dependence on the tangent of the opening angle  $\beta$  for an example flow condition of  $Re_c = 6 \cdot 10^6$ ,  $M = 0.8$ , and  $\lambda_\theta = 19.0 \cdot 10^{-3}$ . A linear relationship is evident, with larger opening angles corresponding to larger spreading angles (orange line). However, the relationship is not as strong as expected for a constant trailing and leading edge celerity based on the theory of triangular-shaped turbulent spots and the relation given by equation 2.3.1. This expected relationship is indicated by the green line for a constant ratio of leading to trailing edge celerity ( $\tan(\alpha) = c \cdot \tan(\beta)$  with constant  $c$ ). Therefore, both spreading and opening angles depend on the respective celerities.

Based on equation 2.3.1, a leading edge celerity  $c_{le,c}$  can be calculated from the detected angles and trailing edge celerity alone, if the simplification of triangular spots is justified. As outlined in previous sections, the trailing edge celerity could be determined more accurately and reliably in this investigation. Furthermore, the trailing edge exhibited either none or only very low variation for a fixed flow condition within the uncertainty of this investigation. A constant trailing edge celerity was applied with  $c_{te} = 0.48$  based on results for these conditions from section 5.1.2. Using a known trailing edge celerity provides a new, independent method of estimating the leading edge celerity. The results are presented as a function of the opening angle  $\beta$  in figure 5.1.15(b). Higher leading edge celerities correspond to lower opening angles, as is expected if the trailing edge celerity is constant. The range covers  $0.92 \leq c_{le,c} \leq 1.05$ , with several values close to or above 1.

Table 5.1.2 lists the calculated mean leading edge celerity (labelled “angles (calculated)”) with its standard deviation and compares its value obtained with other methods - automatic and manual being the standard methods presented above and explained in sections 4.5.3 and 4.5.4, respectively. “Selected spots” refers to the turbulent spots where opening and spreading angles could be determined, i.e. spots that are isolated in the field of view. The agreement of the average leading edge celerity with those determined with the other methods is remarkable. It must be noted that this is only true for the average value, as the variation is large for individual spots. It also shows that the selected spots (i.e. isolated) are a good representation of all spots detected for these conditions (including partly merged spots, closely neighbouring spots and spots on the side of the field-of-view). The leading edge celerities determined with the automatic and manual methods are slightly higher but still lie within the indicated error ranges.

One disadvantage of the leading edge detection method described in section 4.5.3 is that the celerity is assumed to be constant along the leading edge interface. While most researchers agree on this [62, 152], Wygnanski et al. [181] report a slightly concave shape of the leading edge interface, resulting from a decrease of leading edge celerity towards the outer sides of the spot. To investigate this observation, a further method using only the tip of the turbulent spot is used to determine the leading edge celerity, the leading edge being determined as laid out in section 4.5.3. The 50 spanwise grid positions with the leading interface furthest downstream are averaged to account for small spot tip irregularities caused by noise. A linear regression of determined tip locations for consecutive frames yields the leading edge celerity for individual spots (labelled “tip”). The results for this evaluation method (selected spots and all determinable spots) are also listed in table 5.1.2. They are in good agreement to the other methods presented. Note that the methods presented in table 5.1.2 are four different ways of determining the leading edge celerity, of which three are totally independent. This emphasises the accuracy and reliability of the presented evaluation techniques.

Method	Range of spots	Leading edge celerity $c_{le}$
Angles (calculated)	selected	$0.964 \pm 0.008$
Tip	selected	$0.967 \pm 0.027$
Tip	all	$0.965 \pm 0.018$
Automatic	all	$0.974 \pm 0.021$
Manual	all	$0.977 \pm 0.007$

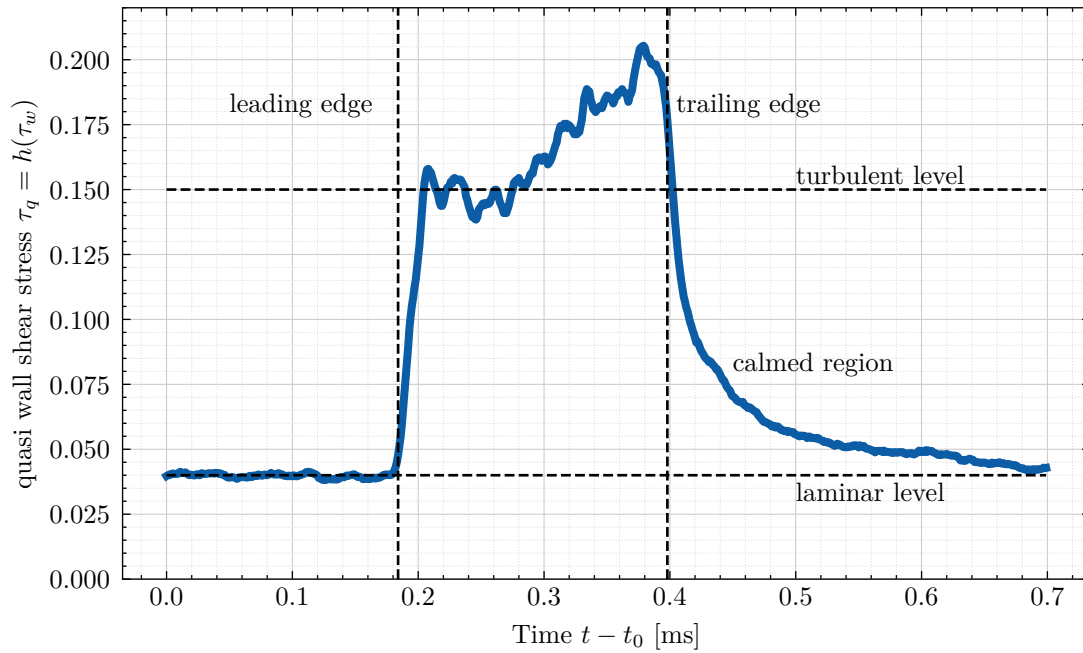
**Table 5.1.2:** Leading edge celerities calculated based on the angles of selected turbulent spots (19 in total) and compared using other methods presented in the previous sections. Flow conditions are  $Re_c = 6 \cdot 10^6$ ,  $M = 0.8$ , and  $\lambda_\theta = 19.0 \cdot 10^{-3}$ .

## 5.1.4 Comparison with hot-film data

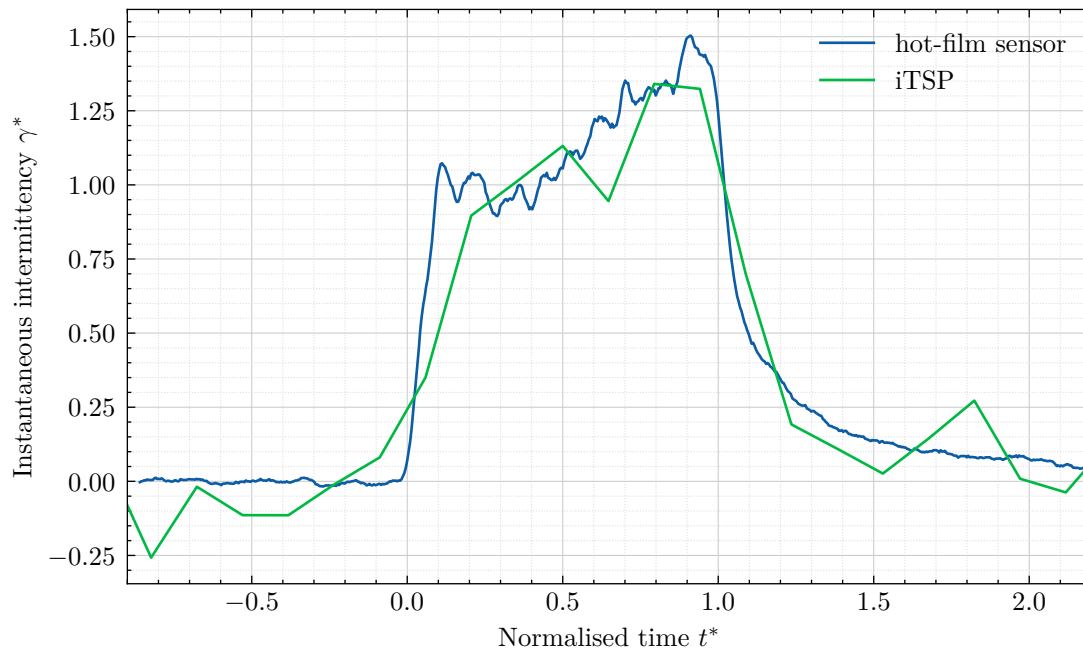
### 5.1.4.1 Turbulent spot traces

Figure 5.1.16 shows the quasi wall shear stress  $\tau_q$  for a typical example of a turbulent spot recorded with hot-film sensor 3 (see section 3.3.2) for flow conditions  $Re_c = 6 \cdot 10^6$ ,  $M = 0.8$ , and  $\lambda_\theta = 19.0 \cdot 10^{-3}$ . As the leading edge arrives,  $\tau_q$  increases sharply from its laminar level until it reaches its turbulent level, which indicates the turbulent spot has eventually covered the whole extent of the hot-film sensor. The gradient of  $\tau_q$  occurs since it takes some time for the turbulent spot to cover the whole spanwise extent of the sensor, and it depends only on the opening angle and leading edge celerity of the passing turbulent spot. In theory, it can be used to estimate the leading edge celerity if the opening angle and extent of the hot-film sensor are known, and if it can be excluded that the centre line of the turbulent spot is within the spanwise extent of the hot-film sensor. However, the difficulties in determining the gradient and turbulence level make this a non-robust method, and no reliable estimations could be obtained. In this case, the turbulent spot covers the sensor for about  $t = 0.22$  ms, during which time  $\tau_q$  steadily increases. While, to some extent, this is expected (compare sections 2.3.1 and 5.1.1.2), the magnitude is surprising, as  $\tau_q$  increases around 30% during the passage of the spot. This increase is considerably more than observed, for example, by Hogendoorn et al. [67] in a flow at  $M = 0.33$  at 15% to 20% and may therefore be partly explained with the uncertainty concerning the determination of the quasi wall shear stress pointed out in section 4.8. One further aspect is the increased heat flux of leads and carrier material in the vicinity of the sensor, which will increase its total heat transfer with a temporal delay, promoted by the comparably high over-heat ratio to achieve the desired temporal resolution.

Figure 5.1.17 shows the comparison of the quasi wall shear stress of the turbulent spot presented in figure 5.1.16 (spot passage time 0.22 ms) and the heat flux of a separate turbulent spot recorded with iTSP (spot passage time 0.34 ms) for the same flow conditions. The time is normalised with the time interval from leading to trailing edge passage of the spot,  $t_{le}$  and  $t_{te}$  respectively, with  $t^* = (t - t_{le}) / (t_{le} - t_{te})$ . The instantaneous intermittency  $\gamma^*$  is the respective signal with the laminar level set to 0 and the turbulent level set to 1. The calmed regions following the respective turbulent spots are clearly visible. It extends longer than the spot duration itself for the spot recorded with the hot-film and contributes considerably to the total quasi wall shear stress caused by the turbulent spot.



**Figure 5.1.16:** Sample turbulent spot recorded with hot-film sensor 3 at  $t_0=3.2812$  s. Flow conditions are  $Re_c = 6 \cdot 10^6$ ,  $M = 0.8$ , and  $\lambda_\theta = 19.0 \cdot 10^{-3}$ .



**Figure 5.1.17:** Comparison of two independent turbulent spot traces recorded with hot-film sensor 3 (quasi wall shear stress - see figure 5.1.16) and iTSP at  $x = 0.12$  m,  $y = 0.168$  m (heat flux - see figure 5.1.3). Flow conditions are  $Re_c = 6 \cdot 10^6$ ,  $M = 0.8$ , and  $\lambda_\theta = 19.0 \cdot 10^{-3}$ .

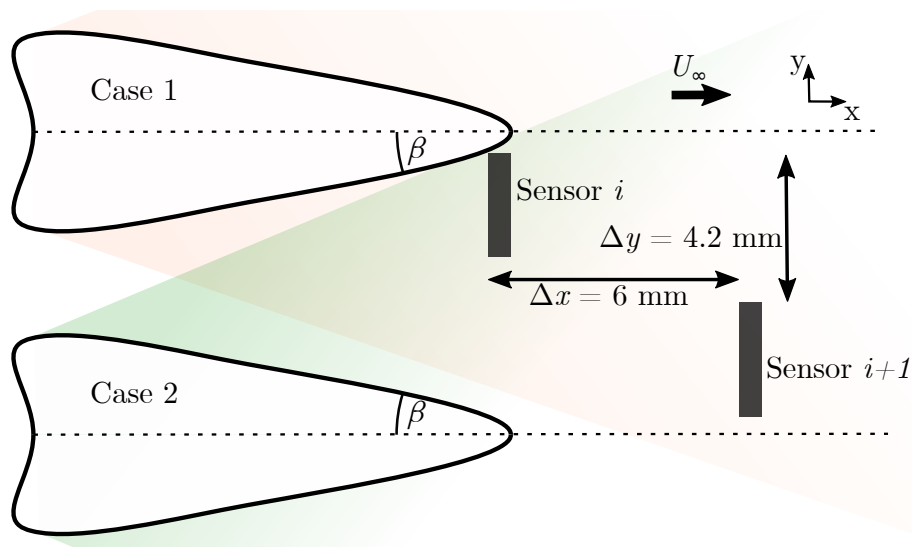


**Figure 5.1.18:** Two geometric cases of turbulent spots passing two consecutive hot-film sensors. Sketch is not to scale and hot-film sensor leads are not shown for clarity. Red and green areas illustrate the spot sweep area for the turbulent spots in case 1 and case 2, respectively.

#### 5.1.4.2 Turbulent spot celerities and opening angles

Since all hot-films are arranged in a staggered order, a direct measurement of the turbulent spot celerities is not possible. If, however, the opening angle  $\beta$  of turbulent spots is known and isolated turbulent spots are large enough to cover at least two consecutive hot-film sensors  $i$  and  $i + 1$ , an approximation is possible. Figure 5.1.18 shows two possible cases for determining the leading edge celerity. Case 1 for the turbulent spot centre line above sensor  $i + 1$  and case 2 for the turbulent spot centre line below sensor  $i + 1$ , as seen in sketch. For both cases the turbulent spot is assumed to fully cover both sensors at some point (but not necessarily the same time). Based on observations from the iTSP measurements, such spots are seldom, but they do nevertheless occur for some flow conditions. The celerity can then be determined with simple geometric considerations assuming a constant leading edge celerity along the leading edge interface and over time :

$$\text{Case 1:} \quad c_{le} = \frac{\frac{\Delta y}{\tan(\beta)} + \Delta x}{\Delta t_1} \quad (5.1.1)$$

$$\text{Case 2:} \quad c_{le} = \frac{\frac{\Delta y}{\tan(\beta)} - \Delta x}{\Delta t_2} \quad (5.1.2)$$

where  $\Delta t_1$  and  $\Delta t_2$  are the time delays of the detected turbulent spot leading interface for consecutive hot-film sensors  $i$  and  $i + 1$  for cases 1 and 2, respectively. Combining equations 5.1.1 and 5.1.2, it is also possible to determine the leading edge celerity without knowledge of the opening angle  $\beta$  and vice versa if both time delays,  $\Delta t_1$  and  $\Delta t_2$ , are known:

$$c_{le} = \frac{2\Delta x}{(\Delta t_1 - \Delta t_2)} \quad (5.1.3)$$

and

$$\tan(\beta) = \frac{\Delta y(\Delta t_1 - \Delta t_2)}{\Delta x(\Delta t_1 + \Delta t_2)}. \quad (5.1.4)$$

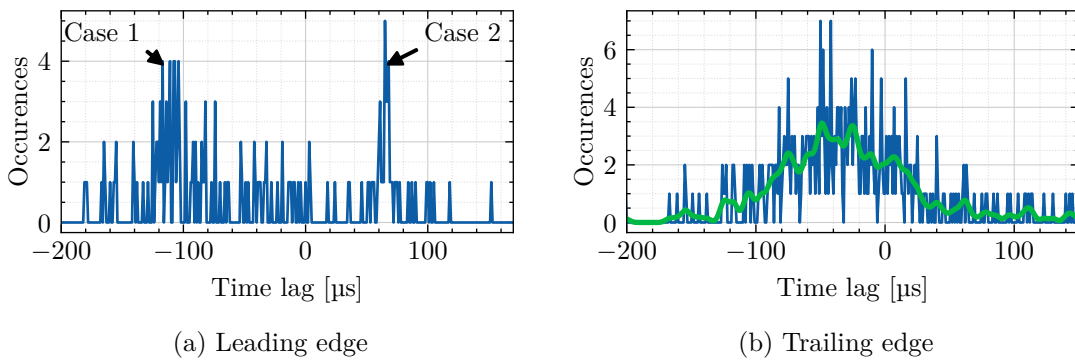


**Figure 5.1.19:** Cross-correlation function for the leading and trailing edge interfaces for the first ten neighbouring hot-film sensor pairs. Flow conditions are  $Re_c = 6 \cdot 10^6$ ,  $M = 0.8$ , and  $\lambda_\theta = 19.0 \cdot 10^{-3}$ .

The laminar-turbulent interfaces must be identified to determine the time delays. A similar procedure to the one described in Clark et al. [26] was used, which was also utilised in several other studies. A detector function is defined as  $D_i = m\tau_{q,i}^{\prime 2}$  with  $m$  the relative magnitude of the signal  $m = (\tau_{q,i} - \tau_{q,min}) / (\tau_{q,max} - \tau_{q,min})$  and  $\tau_q'$  the gradient of  $\tau_q$ , with  $\tau_{q,i}$  the quasi wall shear stress at time instance  $i$  as described in section 4.8. This detector function is smoothed with an exponential function with time constant  $7 \mu\text{s}$  and thresholded with a selected value of  $1 \cdot 10^{-8}$  to receive a binary time series - 0 for a laminar and 1 for a turbulent boundary layer. The threshold value was carefully chosen and did not significantly influence the results presented below. The advantage of using a detector function compared to the quasi wall shear stress alone is that it also accounts for fluctuations associated with a turbulent boundary layer. The leading and trailing edges (where the resulting signal switches from 0 to 1 and vice versa) are cross-correlated for two neighbouring hot-film sensors.

The time lags that correspond to the maximum of the cross-correlation function of both the trailing and leading edge interfaces are presented in Figure 5.1.19 for a sample case with flow conditions  $Re_c = 6 \cdot 10^6$ ,  $M = 0.8$ , and  $\lambda_\theta = 19.0 \cdot 10^{-3}$ . They are all occurrences of the first ten hot-film sensor pairs added up, excluding hot-film sensor 5 due to a malfunction of this sensor (see section 3.3.2). Only neighbouring hot-film sensors could be used here since it was found that no sufficient correlation could be obtained for sensors two or more apart. For the trailing edge, the correlation is filtered with a running Gaussian with  $\sigma = 3 \mu\text{s}$  (green line). The correlation lag is the same for all pairs of hot-film sensors, assuming a straight trailing edge interface. There is a large spread, which can be attributed to merging and closely following turbulent spots and the staggered ordering of the hot-film sensors. The maximum lag is located at  $-48 \mu\text{s}$ , resulting in an estimated trailing edge celerity of  $c_{te} = 0.53 \pm 0.10$  in good agreement with the trailing edge celerity determined with iTSP of  $c_{te} = 0.498 \pm 0.010$  for these flow conditions. The uncertainty results from an estimated time lag uncertainty of  $9 \mu\text{s}$ .

The correlation of the leading edge interfaces yields two peaks, which correspond to Cases 1 and 2. Instead of using a maximum of a smoothed curve as utilised for the trailing edge, the outside values of the corresponding peaks were manually identified. This procedure is necessary because of a bias towards shorter time lag which is caused if the centre line of a turbulent spot is over one of the sensors compared to being spanwise displaced from it. Using an opening angle determined to be  $\beta = (10.73 \pm 1.05)^\circ$  (compare section 5.1.3), one obtains  $c_{le} = 0.97 \pm 0.08$ ,  $c_{le} = 0.99 \pm 0.14$  according to equations 5.1.1 and 5.1.2,

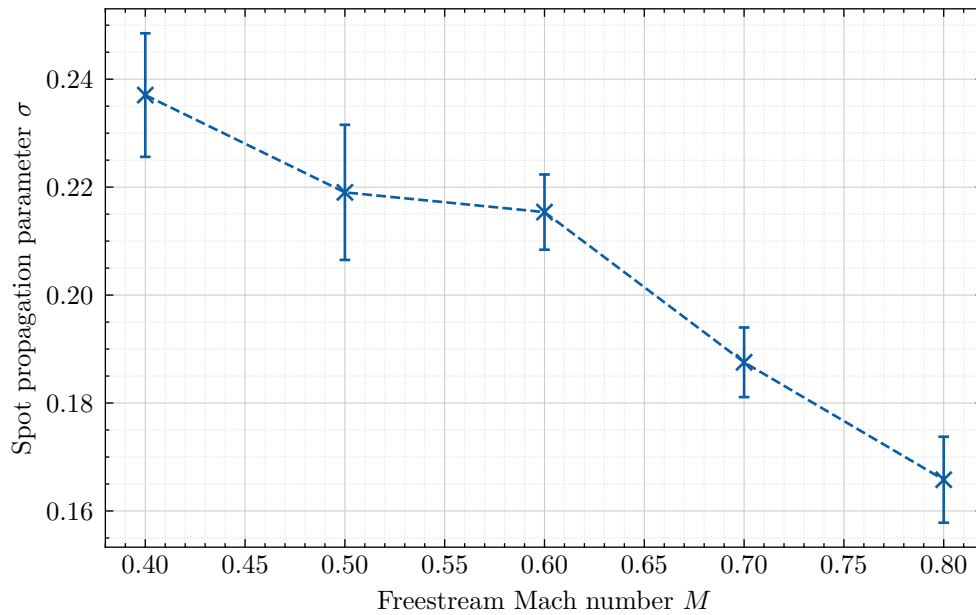


**Figure 5.1.20:** Spot propagation parameter  $\sigma$  for different Mach numbers at  $Re_c = 6 \cdot 10^6$ . The corresponding pressure gradient parameters are listed in table 5.1.1.

respectively and  $c_{le} = 0.95 \pm 0.08$  with opening angle  $\beta = 11.0 \pm 0.9$  according to equations 5.1.3 and 5.1.4. This result also is in excellent agreement with the leading edge celerity as determined with the iTSP, namely  $c_{le} = 0.965 \pm 0.015$ .

Due to the difficulties in determining the correlation peaks for both cases, the comparatively large uncertainty, and since the method only works in cases where many isolated turbulent spots are present, it is not deemed suitable to determine the effects of parameter variations, as presented beforehand.

### 5.1.5 Spot propagation parameter

Based on equation 2.4.3, the spot propagation parameter can be calculated with the leading and trailing edge celerity  $c_{le}$  and  $c_{te}$  and the spreading angle  $\alpha$ . The dependency of the spot propagation parameter on the Mach number is presented in figure 5.1.20. For increasing Mach numbers,  $\sigma$  reduces to  $\sigma = 0.166 \pm 0.008$  for  $M = 0.8$ , a reduction of about 1.4 compared to the  $M = 0.4$  case. The error bars are higher for the low Mach numbers due to difficulties in determining the celerities. These values are considerably higher than the value obtained by Clark [28] for  $M = 0.55$  at  $\sigma = 0.10 \pm 0.01$ . They are also higher than typical values reported for zero-pressure gradient flow by Schubauer & Klebanoff [152] ( $\sigma = 0.173$ ), Wygnanski et al. [182] ( $\sigma = 0.102$ ), and Sankaran & Antonia [140] ( $\sigma = 0.084$ ). The difference is mainly due to the differing leading edge celerities, but is also affected by differing opening angles  $\alpha$ . Johnson [77] explains the differences with the effect of the Reynolds number, as he states that a significant increase of  $\sigma$  with increasing Reynolds number is due to the effects on the properties of the turbulent spots. The values for low Mach numbers, however, agree well with the models of Steelant & Dick [164] and Karsch et al. [80], who state spot propagation parameters for incompressible flow of  $\sigma = 0.27$  and  $\sigma = 0.25$ , respectively.

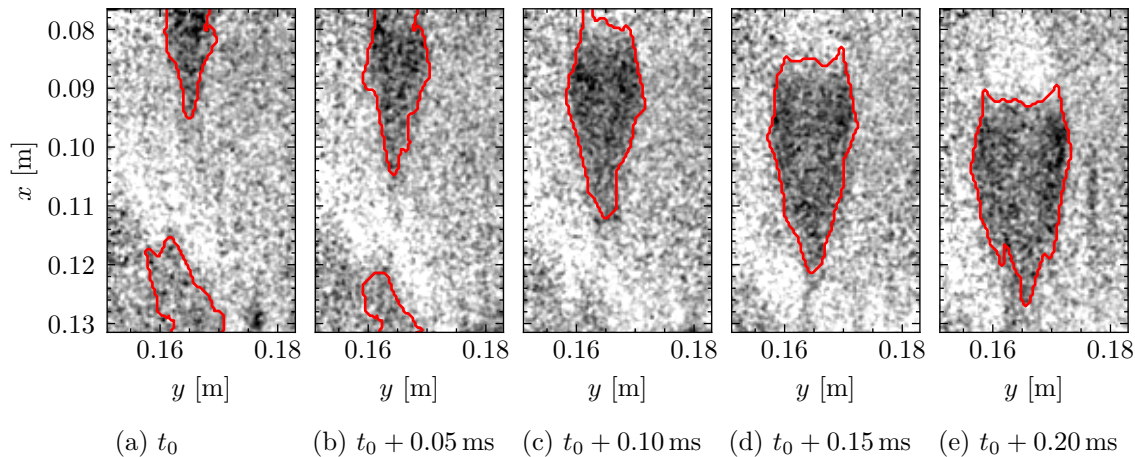


**Figure 5.1.21:** Temporal intensity ratio gradient (colourmap as in figure 4.5.5) for a turbulent spot with blunt leading edge region for  $Re_c = 6 \cdot 10^6$ ,  $M = 0.7$ , and  $\lambda_\theta = 11.0 \cdot 10^{-3}$  at  $t_0 = 3.2188$  s.

## 5.1.6 Merging turbulent spots

### 5.1.6.1 Longitudinal merging

In general, turbulent spots that follow shortly after preceding turbulent spots have a different appearance and yield lower leading edge celerities [61, 62, 76, 88]. An example can be seen in figure 5.1.21. The depicted turbulent spot closely follows the one further downstream that can be seen in images 5.1.21(a) and 5.1.21(b). It follows 0.55 ms behind the spot depicted in 5.1.6(c), which is an isolated turbulent spot. In a direct comparison, the spot in figure 5.1.21 appears much wider. The aspect ratio of length to width of the spot is significantly reduced to 2.4 compared to 3.7 for the spot presented in figure 5.1.6(c). Furthermore, the leading edge region is more rounded and blunt, an effect that could also be seen in other cases. However, the trailing edge region seems unaffected, which becomes further evident when comparing the spot celerities. The leading edge celerity is reduced to  $c_{le} = (0.798 \pm 0.039)$ , compared to the average celerity measured for this condition of  $c_{le} = (0.990 \pm 0.027)$ . The trailing edge celerity, however, is within the expected range measured at  $c_{te} = (0.487 \pm 0.012)$ , compared to the average case of  $c_{te} = (0.480 \pm 0.008)$ . This result is further discussed below where the influence on celerities is considered.

A special case of longitudinal merging is presented in figure 5.1.22. The bulge in the trailing edge is thought to be caused by a secondary turbulent spot that forms and merges immediately with the preceding established spot. The spots are then indistinguishable and appear as one large spot with an irregular trailing edge shape. The apparent trailing edge celerity for this specific location at  $y = 0.17$  m is only  $c_{te} = (0.378 \pm 0.015)$ . This result further demonstrates the advantages of a spatial measurement technique to identify natural turbulent spots.

### 5.1.6.2 Lateral merging

Figure 5.1.23 shows a large, developed turbulent spot (most probably consisting of several already merged spots, based on its irregular shape) and a young turbulent spot originating next to it in the field of view. They start to merge in image 5.1.23(c), but the separate leading-edge regions can still be seen 10 ms later in figure 5.1.23(e). Both leading edge

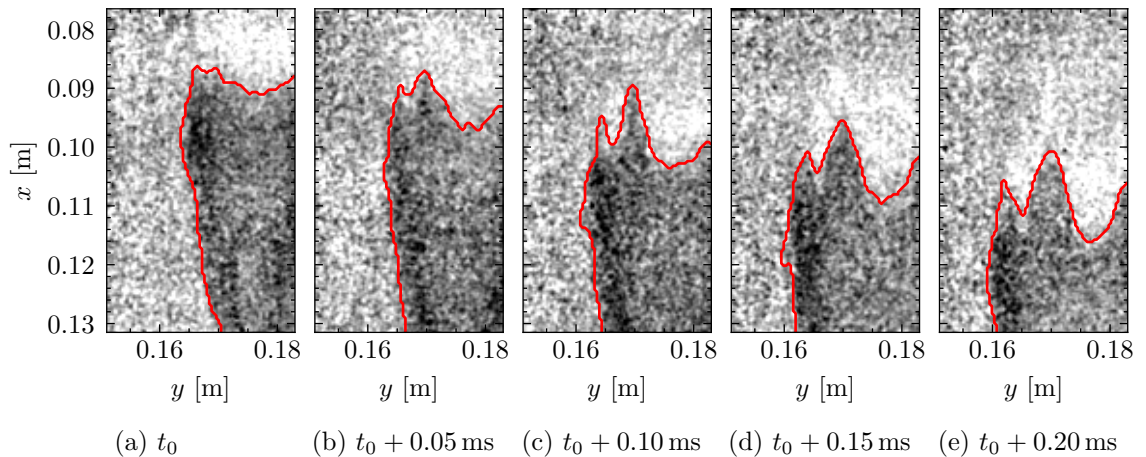


**Figure 5.1.22:** Temporal intensity ratio gradient (colourmap as in figure 4.5.5) for a turbulent spot for  $Re_c = 6 \cdot 10^6$ ,  $M = 0.8$ , and  $\lambda_\theta = 19.0 \cdot 10^{-3}$  at  $t_0 = 3.1865$  s.

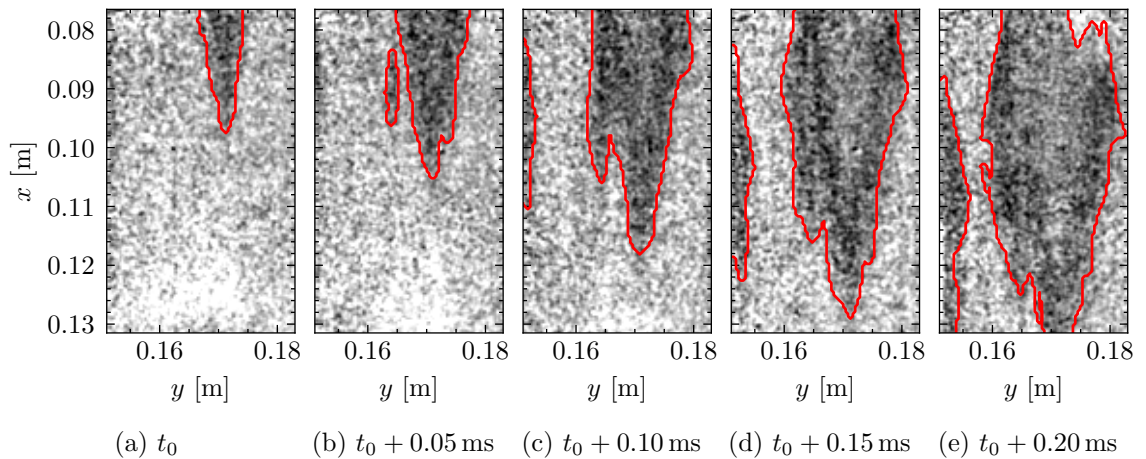


**Figure 5.1.23:** Temporal intensity ratio gradient (colourmap as in figure 4.5.5) for two lateral merging spots for  $Re_c = 6 \cdot 10^6$ ,  $M = 0.8$ , and  $\lambda_\theta = 19.0 \cdot 10^{-3}$  at  $t_0 = 3.2361$  s.

celerities were found to be almost identical:  $c_{le} = (0.883 \pm 0.041)$  for the large spot on the right, and  $c_{le} = (0.880 \pm 0.037)$  for the young spot on the left. Additionally, a further spot can be partially seen on the far left side of the field of view. No celerity could be determined here due to the limited region visible. All spots seem to grow independently of each other in both the streamwise and spanwise directions until they merge or interact with the calmed region of a preceding spot.

Figure 5.1.24 shows the measured (normalised) heat flux distribution for several spots, where all the phenomena of merging turbulent spots, as mentioned above, are present in the same short image sequence. A turbulent spot trails and merges with a preceding spot on the right side. It is not possible to detect the exact location of the leading edge, but once again, it is more blunt and rounded compared to the preceding spot. This finding is in line with hot-wire measurements from Gutmark & Blackwelder [62] that describe smaller temperature ranges and more moderate gradients between the laminar and turbulent regions than in the preceding spot. In figures 5.1.24(g) to 5.1.24(i), a further turbulent spot arises in the trailing edge region, causing the bulge in the top right region of the spot. To the left, two additional spots develop. It is not possible to accurately determine

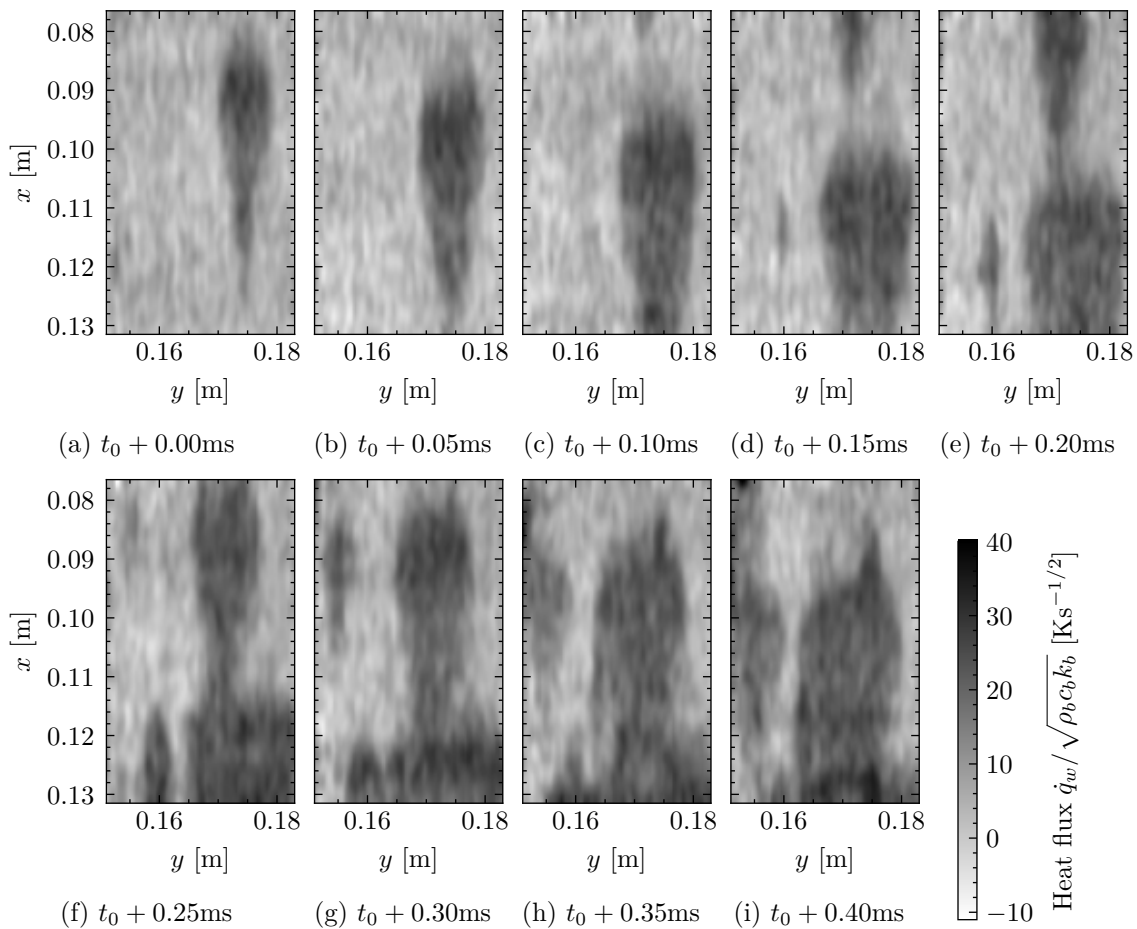


**Figure 5.1.24:** Normalised heat flux signal for merging spots for  $Re_c = 6 \cdot 10^6$ ,  $M = 0.8$ , and  $\lambda_\theta = 19.0 \cdot 10^{-3}$  at  $t_0 = 3.2348$  s.

spreading angles and propagation celerities, but they do not seem to be affected by the other turbulent spots and develop independently.

### 5.1.6.3 Merging with turbulent wedges

For some flow conditions, turbulent wedges were visible in the field-of-view. They are further discussed in section 5.3. In general, the turbulent spots were observed not to be affected by the turbulent wedges. The parts of the turbulent spot not merged with the turbulent wedge seem to be convecting downstream like isolated turbulent spots. One example is presented in figure 5.1.25. In this case, the temporal intensity ratio gradient is chosen for visualisation to distinguish the turbulent spot from the turbulent wedge. The turbulent wedge is the same as presented in figure 5.3.4, and the determined line of 50% intermittency is shown in green for orientation. The wedge is not visible in these temperature gradient images since the surface temperature is lower compared to a laminar boundary layer but close to constant. Note that only a part of the turbulent spot is visible, and the other part has already merged with the turbulent wedge. It is, therefore, not possible to determine the total extent of the spot, but looking at the left side of the wedge suggests the spot spans further than the wedge. The tip of the turbulent spot cannot be identified as it has probably merged with the wedge. For the visible part of the spot not affected by the wedge, the shape is similar to that of isolated turbulent spots with a

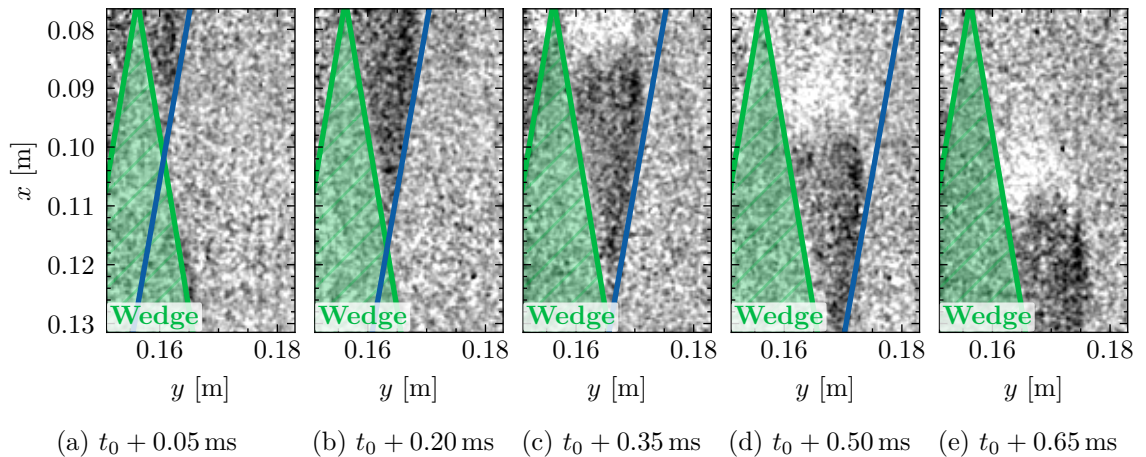


**Figure 5.1.25:** Temporal intensity ratio gradient (colourmap as in figure 4.5.5) of a turbulent spot merging with a turbulent wedge (50% intermittency indicated by the green wedge) at  $t_0 = 3.16675$  s. The leading edge interface is marked with a blue line at an opening angle of  $10^\circ$ . Flow conditions are  $Re_c = 7.5 \cdot 10^6$ ,  $M = 0.6$ , and  $\lambda_\theta = 11.8 \cdot 10^{-3}$ .

straight line leading edge interface, rounded wing tip and a flat trailing edge. The spanwise extent of the trailing edge remains constant, indicating that the spreading angles of the turbulent spots and wedge are similar. This finding will be further discussed in section 5.3. A leading edge celerity can only be calculated using one side of the spot, rather than from the tip region. A straight line with an opening angle of  $10^\circ$  was manually placed along the leading edge interface, excluding the wing tip region. The streamwise distances of these lines at different times are plotted in figure 5.1.26, the bold markers indicating the cases presented in figure 5.1.25. A least-square fit yields a leading edge celerity of  $c_{le} = 1.02 \pm 0.02$ . Similarly, the trailing edge celerity is calculated with the trailing edge positions, as determined in section 4.5.2 as  $c_{te} = 0.481 \pm 0.006$ . Both agree with the celerities observed for isolated spots for these flow conditions, supporting the concept of independent growth.

#### 5.1.6.4 Influence on celerities

As mentioned in the previous sections, the longitudinal merging of turbulent spots influences the leading edge celerity. When determining the leading edge celerity, all turbulent spots following within a certain distance of the trailing edge of a preceding turbulent spot are excluded. In this case a threshold of ten consecutive images (0.5 ms) for the 20 kHz case was chosen. Lowering this threshold to a lower value leads to a reduction in leading edge celerity, as can be seen in table 5.1.3. The critical value seems to be around 0.3 ms, which is about the average passage time for most of the turbulent spots. A significant reduction of leading edge celerity can be seen if no threshold is applied. The exact values depend, of course, on the fraction of closely following spots, their extent (as the extent of the calmed region is related to the spot size itself), and hence only serves as an orientation. If only spots that follow within 0.5 ms of the trailing edge of a preceding spot are considered, the celerity reduces to  $c_{le} = (0.859 \pm 0.031)$ , a significant change compared to undisturbed turbulent spots. This finding could explain the discrepancy of celerities compared to the values of Clark et al. [25, 26], which are considerably lower than in the current study. They study naturally occurring spots in a compressible flow but do not account for the distance between consecutive spots. A precise characterisation of celerities based on the distance of

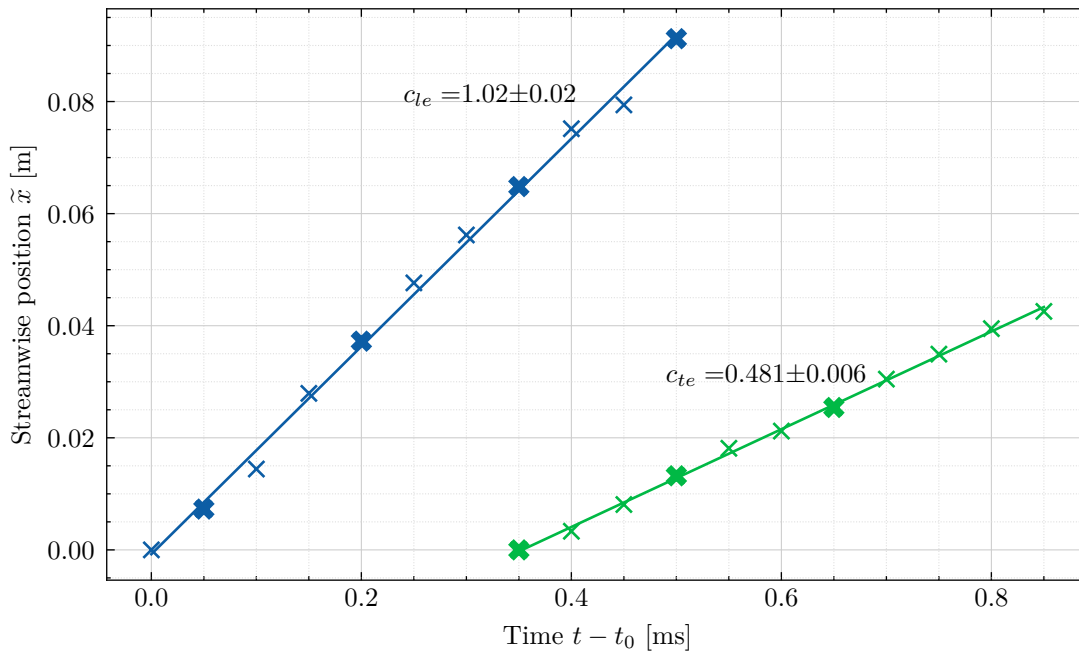


**Figure 5.1.26:** Leading and trailing edge celerities for the turbulent spot presented in figure 5.1.25 at  $t_0 = 3.16675$  s and  $\tilde{x}$  the streamwise position in respect to the first located position for the leading and trailing edge. The points corresponding to the shown images are marked in bold. Flow conditions are  $Re_c = 7.5 \cdot 10^6$ ,  $M = 0.6$ , and  $\lambda_\theta = 11.8 \cdot 10^{-3}$ .

Threshold value [ms]	Leading edge celerity $c_{te}$
0.5	$(0.974 \pm 0.021)$
0.3	$(0.973 \pm 0.019)$
0.15	$(0.967 \pm 0.019)$
0	$(0.954 \pm 0.020)$

**Table 5.1.3:** Effect on leading edge celerities dependent on the exclusion threshold for turbulent spots trailing preceding spots for  $Re_c = 6 \cdot 10^6$ ,  $M = 0.8$ , and  $\lambda_\theta = 19.0 \cdot 10^{-3}$ .

preceding spots is not possible due to the limited amount of turbulent spots detected. No effect on trailing edge celerity was observed.

Gostelow et al. [61] explained the reduction in leading edge celerity in terms of the calmed region following a turbulent spot having a fuller velocity profile than the ambient laminar boundary layer. Therefore, the growth of turbulent spots is inhibited inside the calmed region of preceding turbulent spots, lowering their leading edge celerity.

The findings of this investigation are coherent with observations by Gutmark & Blackwelder [62] for an incompressible flow. They observe a reduction of leading edge celerity of up to 15% for the leading edge close to the wall and up to 20% for the overhang region for artificially generated turbulent spots closely following each other. This difference gradually decreases as the time interval between the spot initiations increases. No influence on the leading edge celerity could be measured when the spots were separated by roughly the passage time of the initial spot. Krishnan & Sandham [88] also observed a suppression of growth of a trailing turbulent spot in direct numerical simulations for a Mach 2 flow, further supported by findings from Jocksch & Kleiser [76].

## 5.2 Laminar turbulent transition

With the high temporal resolution of the surface temperature measurements by means of iTSP, it is possible to determine the intermittency factor  $\gamma$  of the boundary layer for every location. The intermittency factor  $\gamma$  is defined as the fraction of time the boundary layer is turbulent and varies from 0 to 1, corresponding to a fully laminar or turbulent boundary layer, respectively. Figure 5.2.1 shows the average surface temperature distribution for  $Re_c = 7.5 \cdot 10^6$ ,  $M = 0.8$ , and  $\lambda_\theta = 12.9 \cdot 10^{-3}$  - a case where the flow transitions from fully laminar to fully turbulent in the field of view.

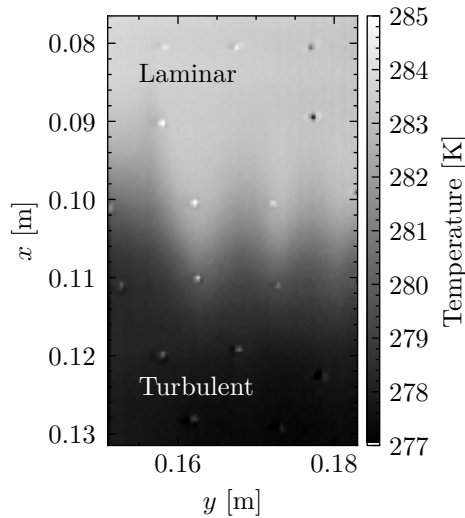


**Figure 5.2.1:** Temperature distribution averaged for  $3.0\text{ s} < t < 3.1\text{ s}$ . Flow conditions are  $Re_c = 7.5 \cdot 10^6$ ,  $M = 0.8$ , and  $\lambda_\theta = 12.9 \cdot 10^{-3}$ .

The histograms of the calculated heat flux at the surface, as described in section 4.4 for three streamwise locations  $x = 0.08\text{ m}$ ,  $x = 0.108\text{ m}$ , and  $x = 0.13\text{ m}$  at  $y = 0.169\text{ m}$ , are shown in figure 5.2.2, for the cases where the boundary layer is expected to be fully laminar, transitional and fully turbulent, respectively. A nearly binary separation is apparent, with lower heat flux levels associated with a laminar and higher heat flux levels associated with a turbulent flow. The heat flux depends on the heat transfer coefficient and the temperature difference between the wall and adiabatic wall temperature. For the present test cases, the adiabatic wall temperature is smaller than the wall temperature for both the laminar and turbulent boundary layers, resulting in a net energy transfer from surface to flow. Based on the heat flux calculations for a whole streamwise section, Otsu's method leads to a threshold value of  $\dot{q}_w / \sqrt{\rho_b c_b k_b} = 13.6\text{ Ks}^{-1/2}$  (compare section 4.6 for details of Otsu's method). Based on this threshold value, the boundary layer state is determined binary as either laminar or turbulent. The time span for evaluation is set to  $3.0\text{ s} < t < 3.1\text{ s}$ , an interval in which flow condition is already stable but before the majority of turbulent spots appear in the far upstream laminar section.

The intermittency factors calculated are presented in figure 5.2.3, alongside the results based on the Narasimha [39, 114, 115] and Johnson [78] intermittency models, the surface temperature, a normalised  $\sigma_T$  distribution and the intermittency factors determined by

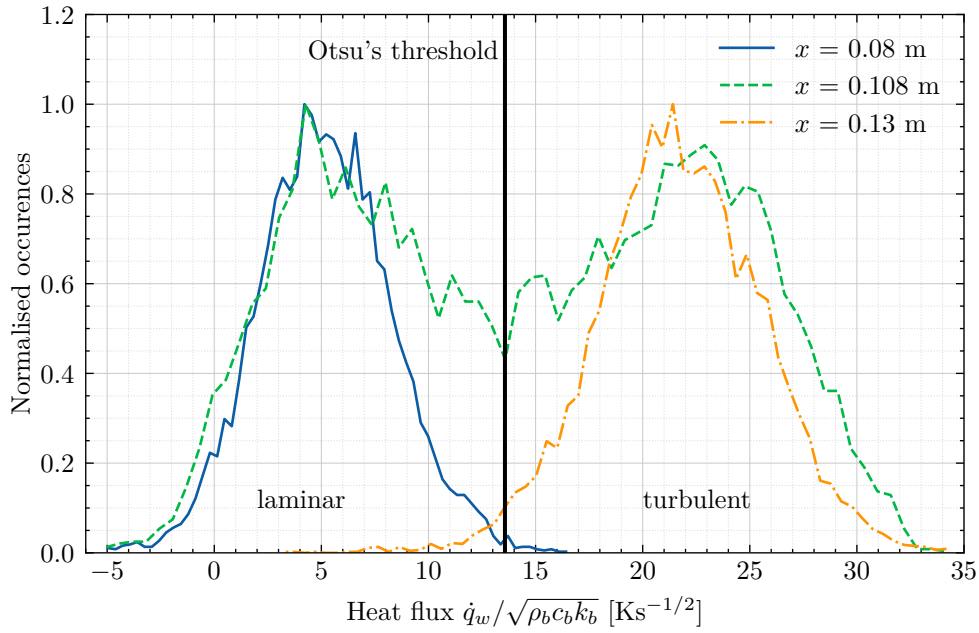


**Figure 5.2.2:** Heat flux distribution for 3 streamwise positions at  $y = 0.169$  m for  $3.0 \text{ s} < t < 3.1 \text{ s}$ . Flow conditions are  $Re_c = 7.5 \cdot 10^6$ ,  $M = 0.8$ , and  $\lambda_\theta = 12.9 \cdot 10^{-3}$ .

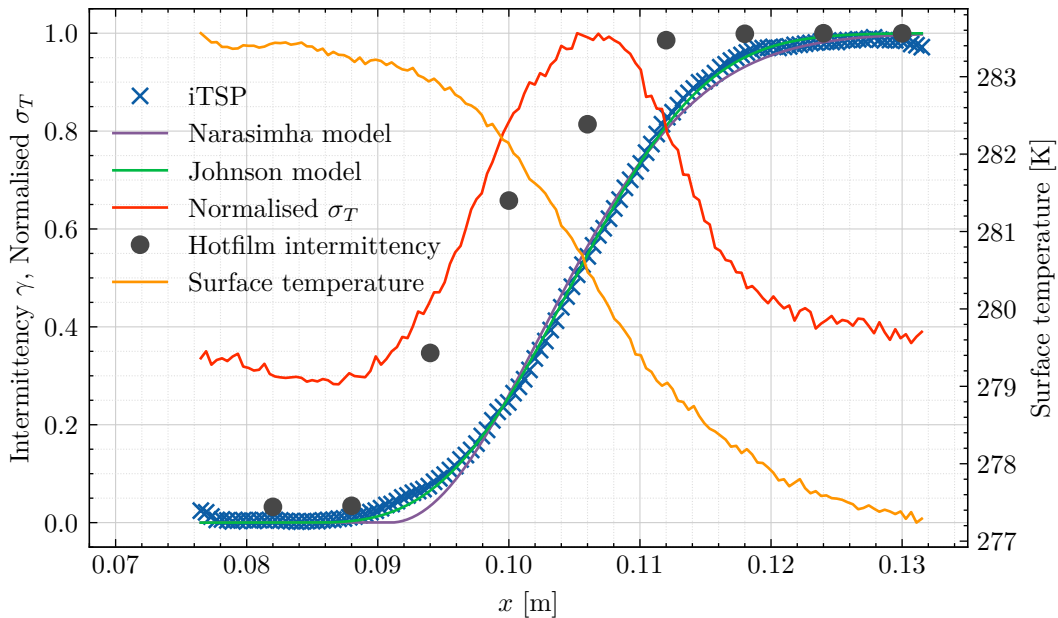


**Figure 5.2.3:** Comparison of intermittency distribution with surface temperature and  $\sigma_T$  for  $3.0 \text{ s} < t < 3.1 \text{ s}$  at  $y = 0.169$  m. Flow conditions are  $Re_c = 7.5 \cdot 10^6$ ,  $M = 0.8$ , and  $\lambda_\theta = 12.9 \cdot 10^{-3}$ .

the hot-films. It must be emphasised that the iTSP intermittency distribution results from a *direct* determination of time-resolved laminar and turbulent periods and does not rely on time-averaged quantities, as is often utilised in these flow conditions for thermal imaging. Figure 5.2.2 showed an overlap of heat flux quantities associated with laminar and turbulent flow, caused by the signal random noise and the limited temporal resolution. For areas around  $\gamma = 0.5$ , the effect of false detections is expected to cancel out. Only close to the areas of fully laminar and turbulent flow will the distribution be slightly “squashed”, as false detections cause the distribution to never fully reach 0 (for a laminar flow) or 1 (for a turbulent flow). This effect is small for the considered case with a high Mach number due to the high signal-to-noise ratio.

The artefacts close to the leading and trailing edge of the iTSP area ( $x < 0.078$  m and  $x > 0.130$  m) are caused by a decreased signal-to-noise ratio towards the edges. A discussion on the accuracy and reliability of the aforementioned intermittency distribution is given in appendix A.4.

The Johnson and Narasimha models in Figure 5.2.3 are fitted with a least-square algorithm to estimate the transition onset and length. The Narasimha model underestimates the distribution for values close to 0 and 1 but shows a reasonable agreement in the intermediate part. On the other hand, the Johnson model shows a good agreement throughout the distribution and seems a better model for this investigated test case. As opposed to the model of concentrated breakdown as the basis for the Narasimha model that leads to an abrupt start but comparably smooth ending of the intermittency levels, the Johnson model, which includes a streamwise distribution of turbulent spot initiation points, starts more smoothly. This assumption is more appropriate for the environment of KRG (and wind tunnels in general) where the disturbance levels are not uniform in time. Their amplification will, therefore, lead to laminar-turbulent breakdown in different streamwise locations.

The intermittency values determined with the hot-films show a similar distribution but with a transition further upstream. Note the intermittency value of hot-film sensor five is questionable due to the difficulties mentioned in section 3.3.2. This discrepancy of an upstream shifted intermittency distribution could be caused by surface imperfections related to the hot-film foil and its installation in the wind tunnel model. As shown in figure 5.2.4(a), the transition location is not uniform in the spanwise direction. Since the hot-films are staggered in a spanwise direction, each sensor is associated with a different transition location, making the interpretation of transition length and shape questionable.

### 5.2.1 Standard deviation of iTSP temperature distributions

A further way to quantify laminar-turbulent transition is to investigate the standard deviation of the temperature distribution  $\sigma_T$  (compare Miozzi et al. [108] and Ashill et al. [4]). This method has the benefit of not needing to compute the heat flux, but rather instead utilising the directly measured quantity of surface temperature. For every streamwise location, the standard deviation of the mean of the surface temperature time series is calculated. Figure 5.2.3 shows the  $\sigma_T$  distribution normalised with the maximum detected  $\sigma_T$  value. The  $\sigma_T$  value is higher for the transitional region compared to areas associated with fully laminar and fully turbulent flow, which is due to the fast drops in surface temperature due to turbulent spots and subsequent recovery during passages of laminar flow. The intermittency factor is expected to be close to 0.5 at the maximum of the  $\sigma_T$  value, which relies on the assumption that the turbulent spots are equally distributed.

The  $\sigma_T$  value is higher in the fully turbulent area than in the fully laminar area. One must be cautious with the interpretation as these areas are associated with different surface temperatures and temperature gradients inside the model. Still, it suggests that the turbulent structures that cause a large variation in convective heat flux are still detectable here.

### 5.2.2 Surface temperature distribution

Due to the increased heat flux associated with a turbulent flow and the ratio between model surface temperature and adiabatic wall temperature  $T_w/T_{aw}$  being larger than one, the surface temperature decreases from a laminar to a turbulent boundary layer. This relationship is often used to reliably define a transition location [33] to be at the location of the highest streamwise temperature gradient. To determine this location, the procedure described in Costantini et al. [33] serves as a basis and is applied to every spanwise position. The temperature signal is filtered with a uniform filter and a subsequent Gaussian filter, both with kernel size of 5%. The maximum gradient that lies within 20% to 80% of the minimum and maximum recorded temperature is identified as the transition location.

The aforementioned quantities (maximum temperature gradient, intermittency distribution, and temperature standard deviation) and the averaged normalised heat flux are presented in figure 5.2.4 for the investigated surface area. Furthermore, the transition locations obtained using the three methods are shown and directly compared in figure 5.2.5. All three methods show remarkable agreement, with the variation between the locations detected by these methods being much smaller than the spanwise variations of the transition itself. The transition front is not a straight line but appears frayed, this being a consequence of a natural transition front for which instabilities are amplified [32, 34, 137]. Spanwise variations in the model contour, of the surface roughness in the leading edge region and in the freestream properties lead to different amplifications of boundary layer disturbances. These cause transition onset and extent to vary in the spanwise direction. The total variation, in this case, is about 4% of the chord length and is caused by the upstream transition in the region  $y = 0.15$  m to 0.16 m. It is probably caused by a surface defect in the leading edge region or close to the iTSP surface. When applying the active layer, the regions that are not meant to be coated are masked with masking tape. When it is removed, occasionally, the transition of areas without to areas with an active layer is not perfectly smooth. Although the total thickness of the active layer is below 1  $\mu\text{m}$ , this could be much larger at the edges if the paint runs up the masking tape. The edges were carefully treated to remove large irregularities. Because the active layer of the iTSP cannot be sanded conventionally, some smaller irregularities might still persist, causing a transition further upstream for the high Reynolds number cases. This aforementioned defect, however, could not be identified. Note, the area in which transition onset is furthest upstream (as can be seen in all quantities displayed in figure 5.2.4) is the same as the location of a turbulent wedge for different flow conditions, as discussed in section 5.3.

For the spanwise region  $y = 0.16$  m to 0.18 m the variation in transition location is much smaller, being around 1%. For both the  $\sigma_T$  value and the maximum temperature gradient, the measured locations are influenced by interference from the presence of the marker at  $y = 0.163$  m; this has a great influence on the measured surface temperature and cannot be fully compensated for (compare section 4.1).

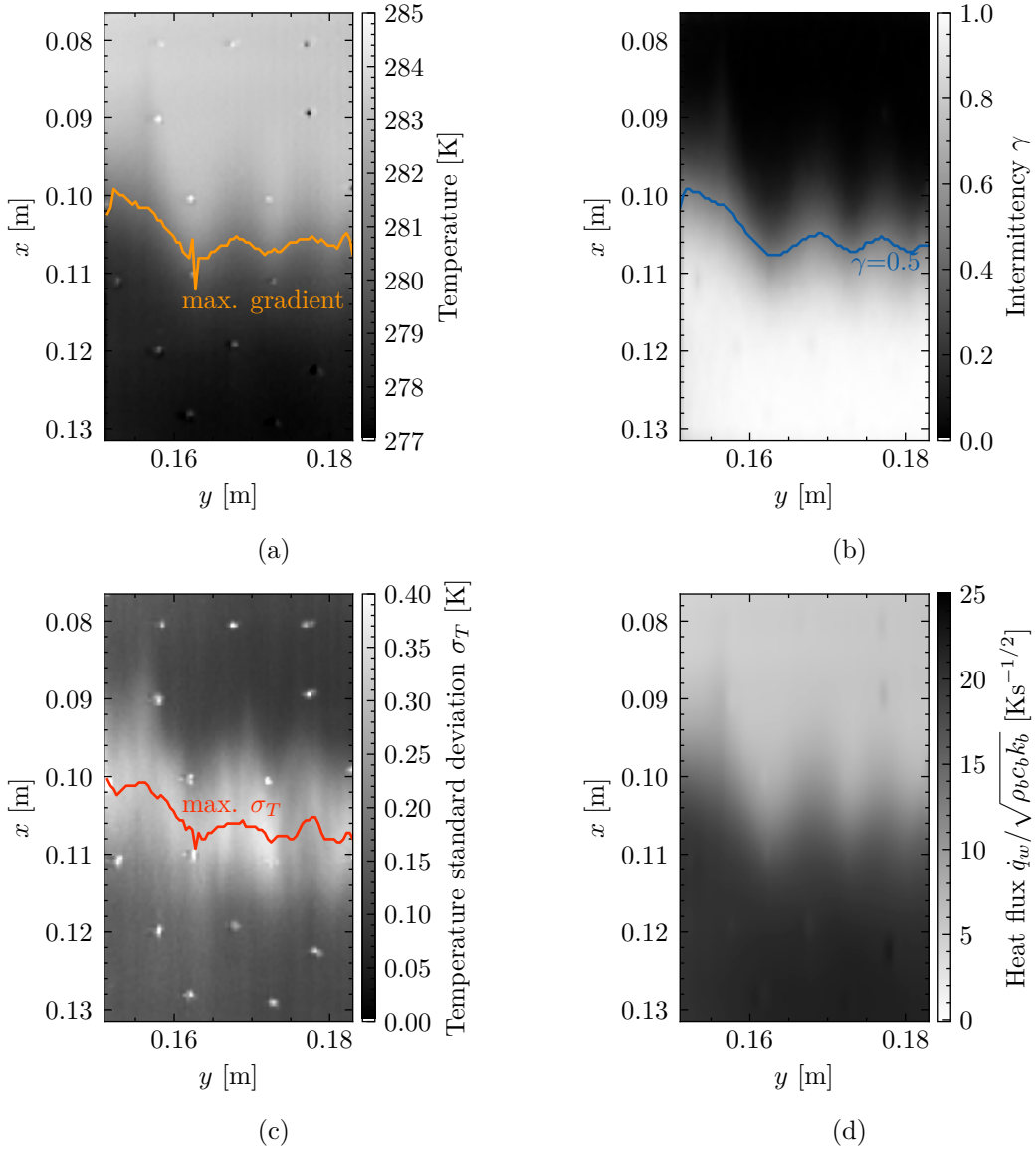


**Figure 5.2.4:** (a) Comparison of surface temperature distribution, (b) intermittency distribution, (c) standard deviation of temperature  $\sigma_T$ , and (d) average normalised heat flux  $\dot{q}_w / \sqrt{\rho_b c_b k_b}$ , along with the corresponding detected transition locations for (a)-(c). A direct comparison of transition locations can be seen in figure 5.2.5. Time span is  $3.0\text{ s} < t < 3.1\text{ s}$  with flow conditions  $Re_c = 7.5 \cdot 10^6$ ,  $M = 0.8$ , and  $\lambda_\theta = 12.9 \cdot 10^{-3}$ .

The streamwise evolution of the boundary layer condition can further be evaluated with a non-dimensional average surface temperature and average heat flux distribution. The non-dimensional temperature distribution is defined here as

$$T^* = \frac{T - T_{lam}}{T_{tur} - T_{lam}} \quad (5.2.1)$$

and  $\overline{T^*}$  is  $T^*$  averaged over the respective time span.  $T_{lam}$  and  $T_{tur}$  are calculated as an average over the respective time span of the first and last ten grid points ( $0.0765\text{ m} < x_{lam} < 0.0805\text{ m}$  and  $0.1275\text{ m} < x_{tur} < 0.1315\text{ m}$ ) respectively, where the boundary layer is expected

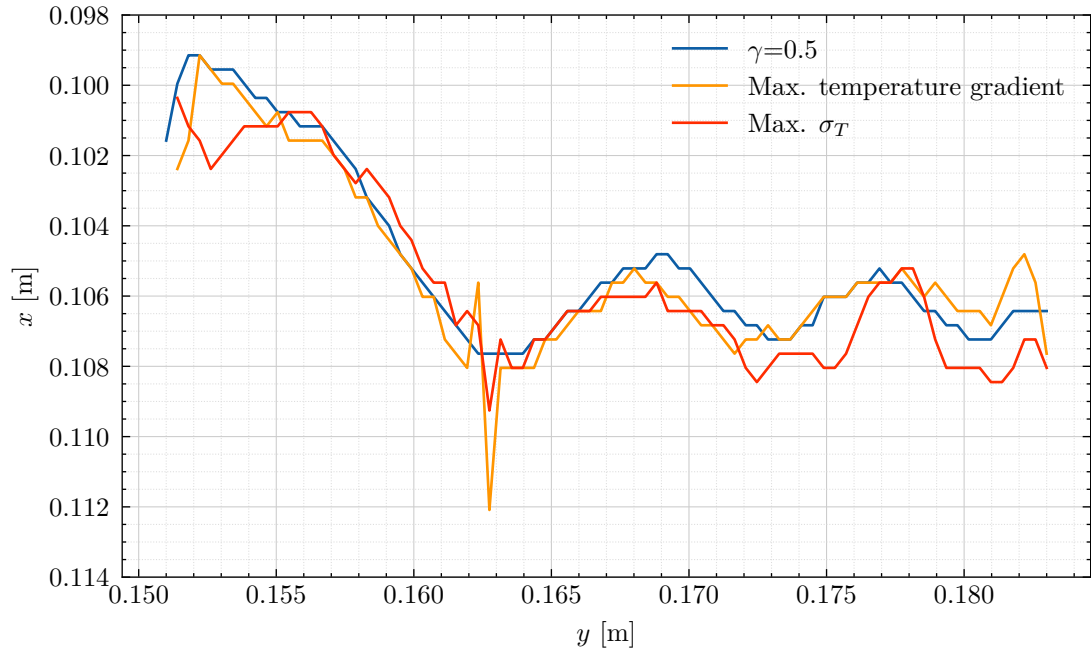


**Figure 5.2.5:** Detected transition locations for the direct intermittency determination, maximum temperature gradient and maximum  $\sigma_T$  for  $3.0\text{ s} < t < 3.1\text{ s}$  with flow conditions  $Re_c = 7.5 \cdot 10^6$ ,  $M = 0.8$ , and  $\lambda_\theta = 12.9 \cdot 10^{-3}$ .

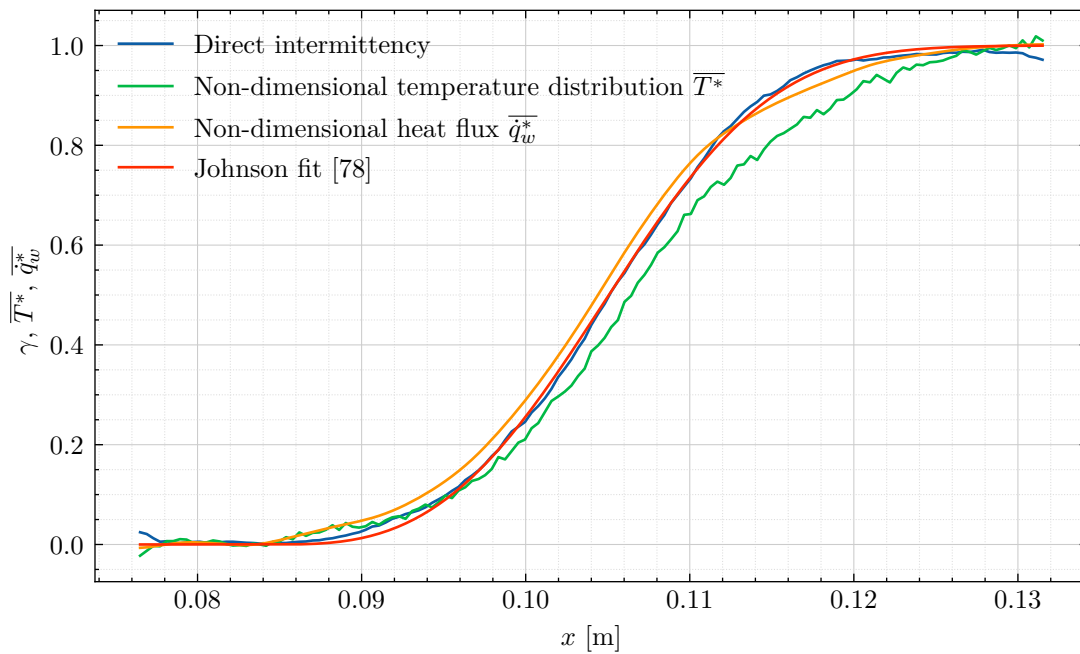


**Figure 5.2.6:** Intermittency distribution and non-dimensional temperature and heat flux distribution for  $3.0\text{ s} \leq t \leq 3.1\text{ s}$  at  $y = 0.169\text{ m}$  with flow conditions  $Re_c = 7.5 \cdot 10^6$ ,  $M = 0.8$ , and  $\lambda_\theta = 12.9 \cdot 10^{-3}$ .

to be fully laminar or fully turbulent. Accordingly, a non-dimensional heat flux can be defined analogously as

$$\dot{q}_w^* = \frac{\dot{q}_w - \dot{q}_{w,lam}}{\dot{q}_{w,tur} - \dot{q}_{w,lam}} \quad (5.2.2)$$

with the average laminar and turbulent heat flux  $\dot{q}_{w,lam}$  and  $\dot{q}_{w,tur}$  and the average value  $\overline{\dot{q}_w^*}$  calculated analogously to above. According to Dhawan & Narasimha [39] and Chen & Thyson [21], the non-dimensional time-averaged heat flux is equivalent to the intermittency distribution. Contrary to their proposal, the laminar and turbulent heat flux level is taken to be constant here rather than as function of the streamwise coordinate. Evaluating flow conditions that result in a fully turbulent or laminar boundary layer for the field-of-view yielded only a small streamwise change in surface heat flux, within the uncertainty range of the present measurement technique. The non-dimensional temperature and non-dimensional heat flux distributions are presented in figure 5.2.6 along with the direct intermittency and the corresponding fitted Johnson distribution. The averaged surface temperature is well below the intermittency curve for the latter stages of transition; this is considered to be due to the specific working principle of KRG. When the flow is established in the early stages of the run, the transition location moves upstream until it reaches a quasi-steady state for the remainder of the run. Therefore, the regions far downstream will generally be cooler compared to turbulent regions closer to the transition region, since there was a longer time span with a high heat flux to cool the iTSP and the underlying layers. Using the streamwise temperature distribution to detect laminar-turbulent transition, and in particular, the onset and end location of the transition region, depends on the temperature history, and may therefore be unreliable. In contrast, the detected transition location (corresponding to 50% intermittency determined and via the maximum gradient method) is reliable in this case and shows a good agreement with the other techniques.

In general, the transition zone is expected to also contain very short spells of laminar and turbulent flow, shorter than can be resolved with iTSP in this investigation. This is valid even in an idealised binary-state boundary layer, and even more so in a natural boundary layer where inrush, high- and low-speed streaks and developing vortices blur the line between laminar and turbulent flow. Therefore, intermittency values determined with a temporally resolved measurement technique will always be fraught with uncertainty to some degree. However, the comparably high temporal resolution of 20 kHz in this case is expected to result in sufficiently accurate results (compare section A.4).

### 5.3 Turbulent wedges

This section describes the findings of turbulent wedges on the investigated surface of interest. Two fully developed turbulent wedges are presented in section 5.3.1 and an intermittent wedge in section 5.3.2. They arise from a surface imperfection just upstream of the iTSP coating. Unfortunately, this imperfection could not be identified after the test campaign. It must have had a small size, presumably only around 10 microns, as the wedges were only present at some of the investigated test cases<sup>1</sup>. Figure 5.3.1 shows the surface temperature distribution for the investigated wedges. Whereas the difference in contrast between the first two images (a) and (b) is due to the different Mach numbers (i.e. to the stronger heat flux caused by the higher  $T_w/T_{aw}$  ratio associated with the higher Mach number), the much lighter wedge in (c) is due to the intermittent nature of the wedge, in spite of its high Mach number of  $M = 0.8$ ; this will be shown and discussed in section 5.3.2.

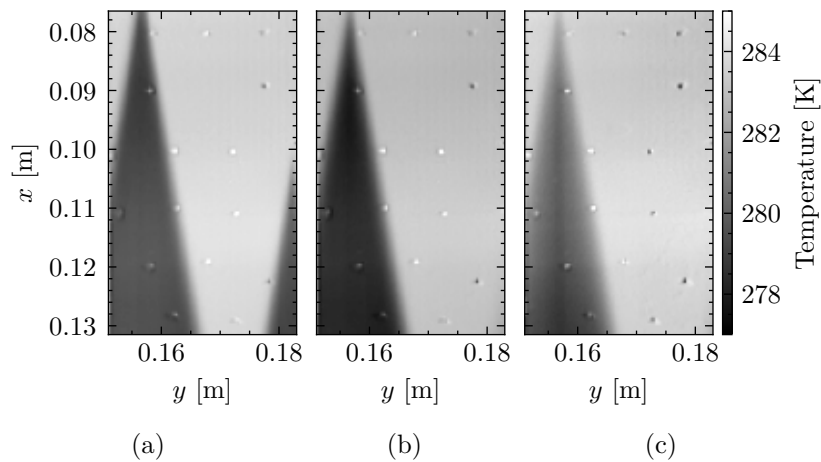


**Figure 5.3.1:** Surface temperature distribution of turbulent wedges in an otherwise laminar boundary layer with flow conditions  $Re_c = 7.5 \cdot 10^6$ ,  $M = 0.5$ , and  $\lambda_\theta = 10.4 \cdot 10^{-3}$  for (a),  $Re_c = 7.5 \cdot 10^6$ ,  $M = 0.6$ , and  $\lambda_\theta = 11.8 \cdot 10^{-3}$  for (b), and  $Re_c = 8 \cdot 10^6$ ,  $M = 0.8$ , and  $\lambda_\theta = 19.4 \cdot 10^{-3}$  for (c).

#### 5.3.1 Fully turbulent core wedges

The turbulent wedges can be quantified in the same manner as described in section 5.2 by evaluating the intermittency distribution over the surface. Figure 5.3.2 shows the distribution for the case with a flow at  $M = 0.5$ . In figure 5.3.2(b) the locations of  $\gamma = 0.1$ ,  $\gamma = 0.5$ , and  $\gamma = 0.9$  are shown. Note that the  $y$ - and  $x$ -axes are not to the same scale in order to emphasise the intermittent region. The distinct areas of a fully turbulent core and an intermittent outer part are visible. The location closest to the respective intermittency factor is identified for every spanwise location. The spreading angles are then calculated using a least-square fit algorithm. The results are presented in table 5.3.1. Due to limitations of the measurement technique, it is not possible to determine the exact location of onset and full turbulence,  $\gamma = 0$  and  $\gamma = 1$ , respectively. Instead, the values  $\gamma = 0.1$  and  $\gamma = 0.9$  are used as approximations. The difference in spreading angle for these two intermittency values is about  $1.5^\circ$ . In figure 5.3.3, the spanwise cross sections of

<sup>1</sup>Smith & Clutter [159] state an isolated roughness element to be in the “safe region”, i.e. not causing a turbulent wedge, for  $Re_{k,k} < 25$ , where  $Re_{k,k}$  is the roughness Reynolds number based on the height  $k$  and conditions at  $k$  with an otherwise undisturbed laminar boundary layer.  $Re_{k,k} = 25$  corresponds to a roughness height  $k$  of about 9  $\mu\text{m}$  for the cases presented in figure 5.3.1.

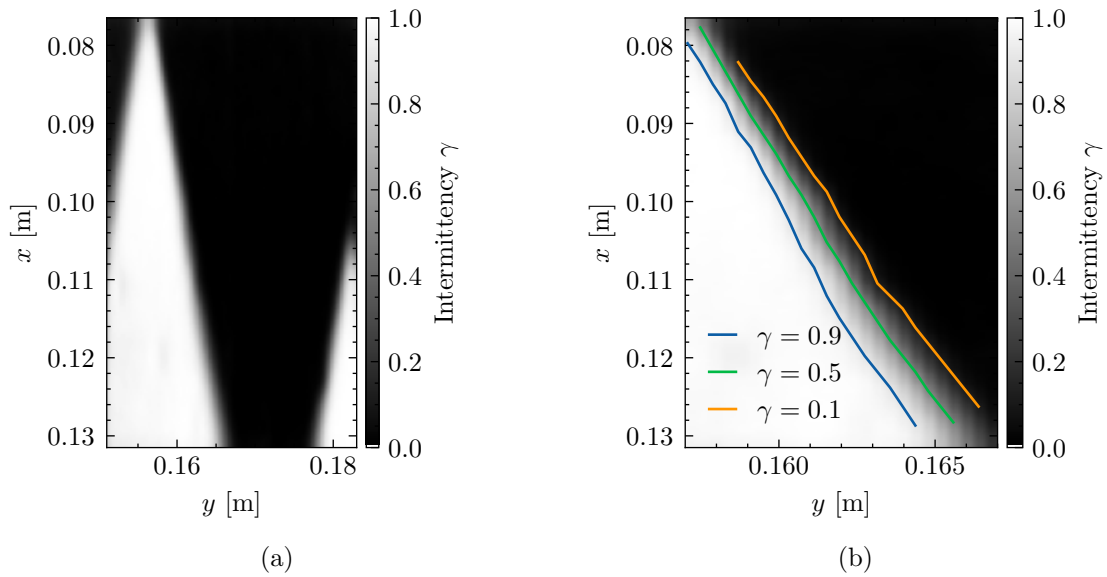


**Figure 5.3.2:** Intermittency distribution of a turbulent wedge (a) and lines of fixed intermittency (b) for  $Re_c = 7.5 \cdot 10^6$ ,  $M = 0.5$ , and  $\lambda_\theta = 10.4 \cdot 10^{-3}$ .

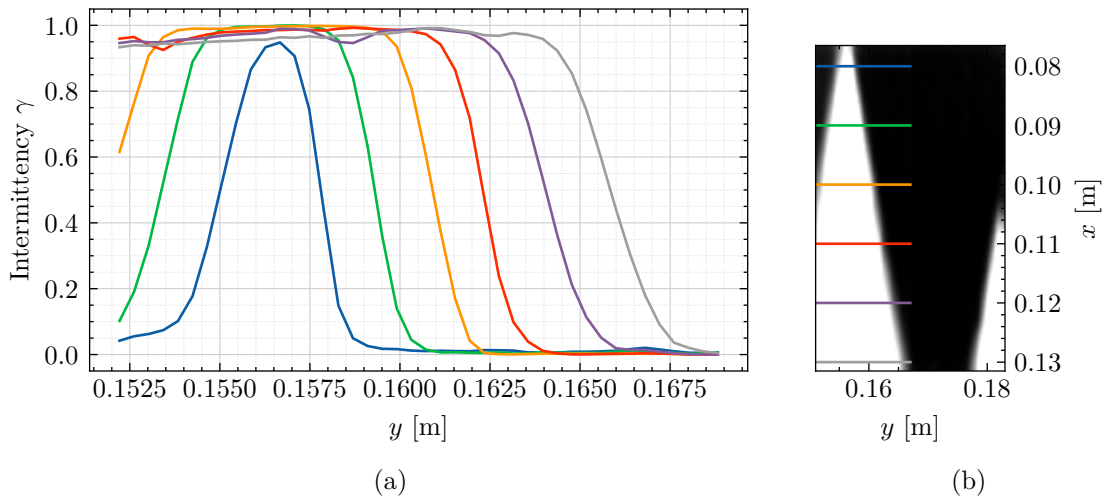


**Figure 5.3.3:** (a) Plot of spanwise intermittency distributions along the turbulent wedge at the different streamwise locations shown in (b), for run conditions  $Re_c = 7.5 \cdot 10^6$ ,  $M = 0.5$ , and  $\lambda_\theta = 10.4 \cdot 10^{-3}$ .

the intermittency levels of the turbulent wedge can be seen for six different streamwise locations. Note that apart from the section at  $x = 0.11$  m (red line), which is an artefact probably caused by a marker, the intermittent region (between  $\gamma = 0.1$  and  $\gamma = 0.9$ ) grows in spanwise direction for increasing  $x$ . This relation further exemplifies the dependence of the different spreading angles on the intermittency factor.

Figures 5.3.4 and 5.3.5 show analogously the intermittency distributions and spanwise sections for the  $M = 0.6$  case. The fully turbulent core of the wedge is significantly delayed as it only starts at  $x = 0.09$  m. In contrast, for the  $M = 0.5$  case, the turbulent core was already fully developed at  $x = 0.08$  m, despite very likely originating from the same surface imperfection. Furthermore, the intermittent region is more elongated in the streamwise direction. The wedge spreading angles for this case  $M = 0.6$  are also listed in table 5.3.1.

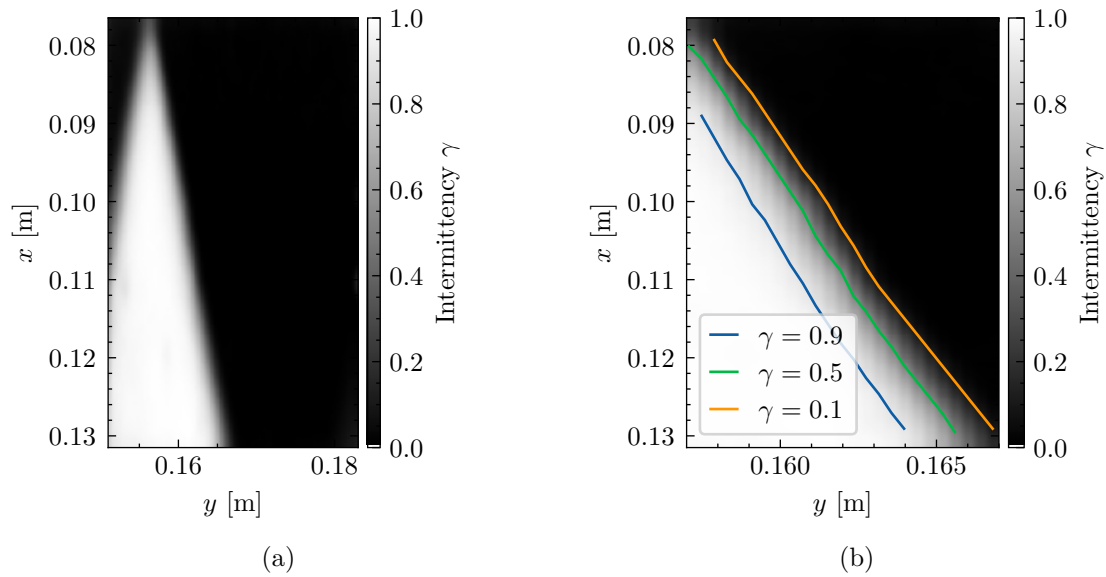


**Figure 5.3.4:** Intermittency distribution of a turbulent wedge (a) and lines of fixed intermittency (b) for  $Re_c = 7.5 \cdot 10^6$ ,  $M = 0.6$ , and  $\lambda_\theta = 11.8 \cdot 10^{-3}$ .

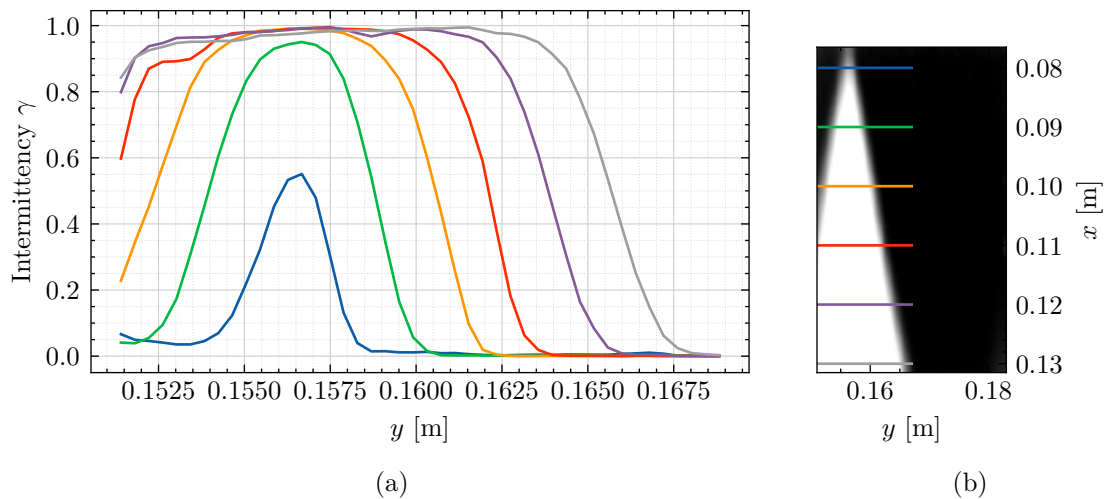


**Figure 5.3.5:** (a) Plot of spanwise intermittency distributions along the turbulent wedge at the different streamwise locations shown in (b), for run conditions  $Re_c = 7.5 \cdot 10^6$ ,  $M = 0.6$ , and  $\lambda_\theta = 11.8 \cdot 10^{-3}$ .

For all intermittency factors, the angles are larger than those for the  $M = 0.5$  case. The difference in spreading angle between the fully turbulent core and intermittent region is about  $1^\circ$ , significantly smaller than in the case for a flow at  $M = 0.5$ .

**Discussion of the results for fully turbulent core wedges** The turbulent wedge develops further downstream for the  $M = 0.6$  case compared to the  $M = 0.5$  case. Previous investigations on the same model have already shown that, at a lower Mach number, but with the same other run conditions, there are greater numbers of turbulent wedges [30]. This observation was attributed to the thinner boundary layer. The size of an imperfection leading to the wedge, taken in relation to the boundary layer thickness, is greater for cases with a lower Mach number and, therefore, more susceptible to bypass transition; this could also be the cause for the effect seen here.

Intermittency factor $\gamma$	$M = 0.5$	$M = 0.6$
0.1	$(9.68 \pm 0.12)^\circ$	$(10.02 \pm 0.09)^\circ$
0.25	$(9.45 \pm 0.11)^\circ$	$(9.75 \pm 0.09)^\circ$
0.5	$(8.89 \pm 0.09)^\circ$	$(9.49 \pm 0.07)^\circ$
0.75	$(8.60 \pm 0.15)^\circ$	$(9.32 \pm 0.08)^\circ$
0.9	$(8.10 \pm 0.11)^\circ$	$(8.96 \pm 0.10)^\circ$

**Table 5.3.1:** Spreading angles  $\alpha$  for the two fully turbulent core wedges at  $M = 0.5$  and  $M = 0.6$  for different intermittency factors.

The spreading angles  $\alpha$  for the turbulent spots were  $(10.03 \pm 0.49)^\circ$  for the flow at  $M = 0.5$  and  $(10.24 \pm 0.40)^\circ$  for the flow at  $M = 0.6$ . These values are the same, within the given accuracy, as the spreading angle for the turbulent wedges at  $\gamma = 0.1$ . This correlation demonstrates the similarity of spanwise growth of turbulence for both turbulent spots and wedges. The intermittent part of the wedge could consist of turbulent spots that are initiated further upstream of the turbulent core. The wing tips of the spot propagate downstream on either side of the turbulent core. This explanation is supported by DNS calculations by Goldstein et al. [58], who state that the spreading mechanism is confined to the outer section of the spot and not dependent on the structure inside the spot. Therefore, the extent of the intermittent region depends on the flow conditions and the initial phase of the turbulent wedge. This could explain the smaller intermittent region in this case compared to values reported in the literature: For the turbulent core and the intermittent region, Schubauer & Klebanoff [152] report  $10.6^\circ$  and  $6.4^\circ$ , respectively, for an incompressible flow and Fiala et al. [51] report  $6.9^\circ$  and  $4.6^\circ$ , respectively, for a flow at  $M = 3$ .

In both cases presented here, the spreading angle increases with Mach number. This result contradicts other research findings and has already been discussed in section 5.1.3.

The intermittent region in these presented cases is only a few grid points long in streamwise direction and just large enough to be identified with the current method. Even a perfectly sharp and steady interface between a laminar boundary layer and a fully turbulent wedge would falsely yield a small intermittent region due to the limited resolution, signal-to-noise ratio and filtering applied to the images. This region is estimated to be around 1 mm in this study based on the grid size and filters applied and is considerably smaller than the intermittent region detected in these cases at  $\Delta x$  of around 5 mm to 10 mm. Furthermore, this would infer constant spreading angles independent of the intermittency factor  $\gamma$ , contrary to what was found in this investigation. Therefore, the intermittent region of the turbulent wedge detected in this study is expected to be of physical significance.

### 5.3.2 Intermittent turbulent wedges

Contrary to the preceding section on turbulent wedges with a fully turbulent core, this section deals with intermittent turbulent wedges that do not have a turbulent core in the field-of-view. Due to its intermittent nature, the average temperature signature will not be as pronounced as for the fully turbulent wedges. This phenomenon was first described by Clark et al. [27] in a low-speed flow and was termed “transitional wedge”. Clark et al. suspected this wedge to be composed of a train of turbulent spots. However, an exact description and proof that the intermittency distribution was indeed caused by independently growing turbulent spots was not possible due to the limited amount of hot-wire traces available and to the time-averaging nature of their thermochromic liquid

crystals. Fiala et al. [51] later also described intermittent wedges behind a roughness of height  $k = 0.15\delta$  ( $\delta$  being the boundary layer thickness), which lies in between a roughness height where laminar flow is preserved ( $k = 0.10\delta$ ) and one which caused a turbulent wedge with fully turbulent core ( $k = 0.20\delta$ ). Although they could resolve heat flux signals in a spanwise direction via heat transfer gauges, they also lacked an instantaneous heat flux distribution to characterise the turbulent spots.

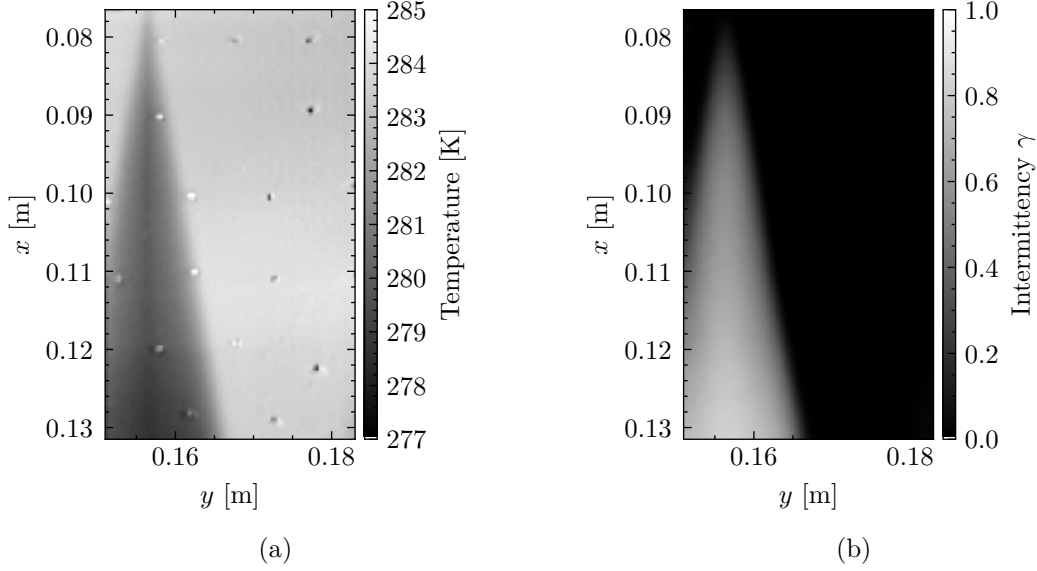


**Figure 5.3.6:** Average surface temperature distribution (a) and intermittency distribution (b) for the intermittent wedge for  $Re_c = 8 \cdot 10^6$ ,  $M = 0.8$ , and  $\lambda_\theta = 19.4 \cdot 10^{-3}$ .

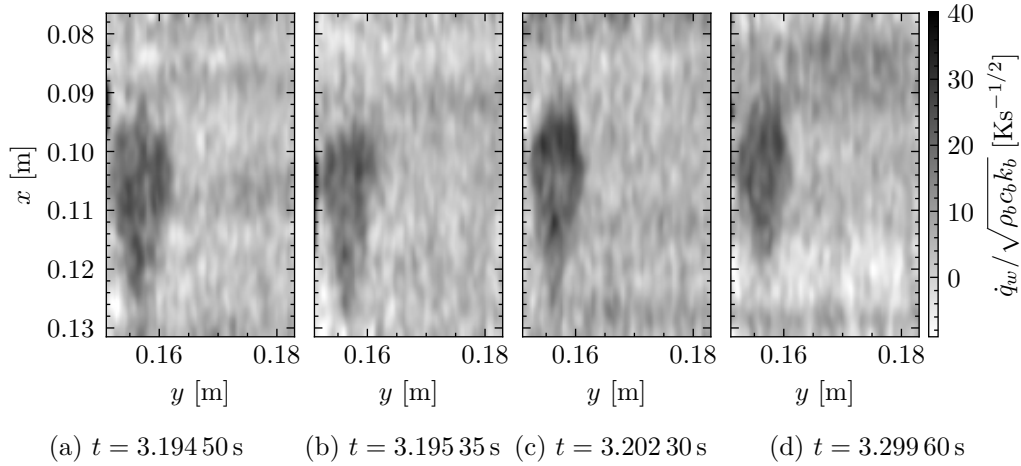


**Figure 5.3.7:** Heat flux distribution for 4 examples of individual turbulent spots comprising the intermittent turbulent wedge for  $Re_c = 8 \cdot 10^6$ ,  $M = 0.8$ , and  $\lambda_\theta = 19.4 \cdot 10^{-3}$ .

Figure 5.3.6 shows the surface temperature and intermittency distribution for the wedge at  $Re_c = 8 \cdot 10^6$ ,  $M = 0.8$ , and  $\lambda_\theta = 19.4 \cdot 10^{-3}$ . It is presumably caused by the same surface imperfection that causes the fully turbulent wedges discussed in section 5.3.1. The intermittency never reaches 1 in the field-of-view and the surface temperature difference from the inside to the outside of the wedge is not as pronounced as in the previous fully-developed cases. This finding is caused by the presence of a train of independent turbulent spots, as will be shown in the following.

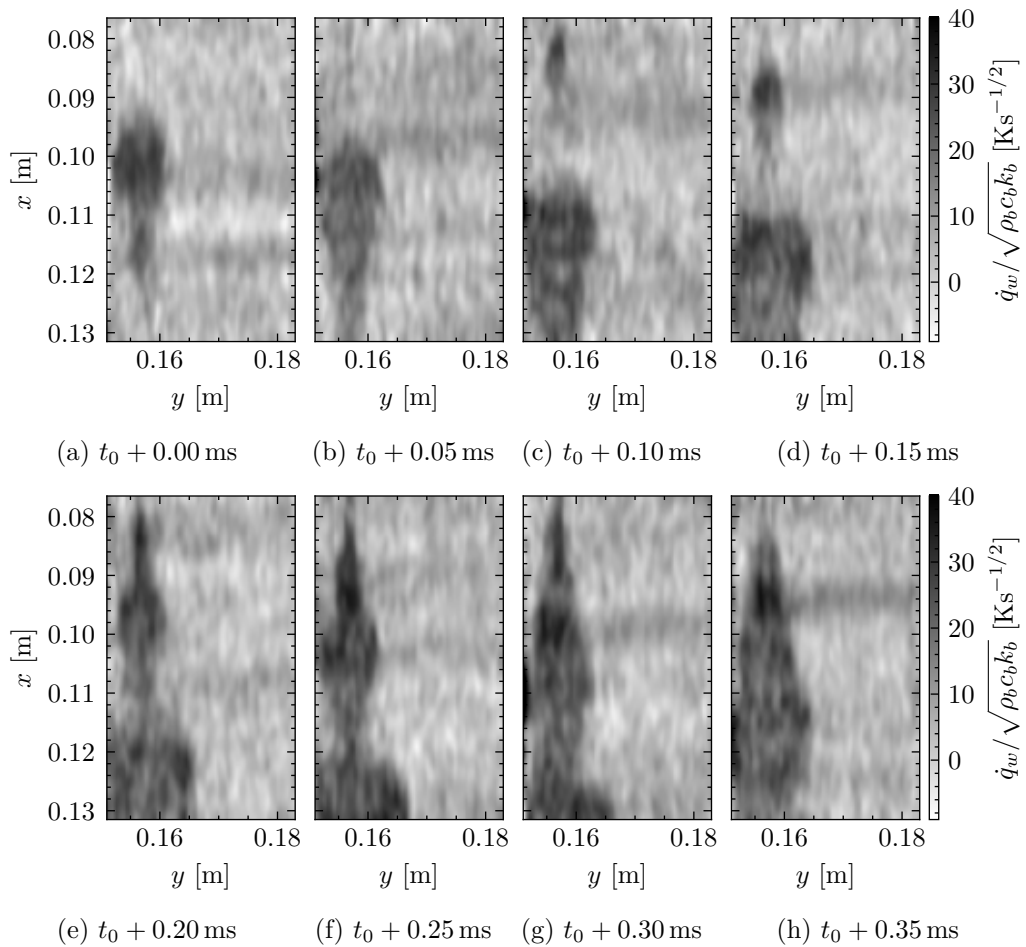


**Figure 5.3.8:** Heat flux distribution for merging turbulent spots for  $Re_c = 8 \cdot 10^6$ ,  $M = 0.8$ , and  $\lambda_\theta = 19.4 \cdot 10^{-3}$  at  $t_0 = 3.15025$  s.

Four examples of isolated turbulent spots can be seen in figure 5.3.7. In general, many spots yield the same classical shape of a streamwise pointing triangle. There are, however, some differences to the isolated spots discussed in section 5.1. The leading edge is rounded for many spots, in line with the findings for streamwise merging turbulent spots. The time interval between spots is mostly well below 1 ms; therefore, spots develop in the calmed region of preceding turbulent spots. Additionally, the trailing edge is often not flat, as would be the case for triangular-shaped spots. Instead, the trailing edge region is more trapezoid-like, as can be seen in figure 5.3.7(c), and even more so in figure 5.3.7(d), resulting in more of a diamond shape.

An extreme case of this is demonstrated in figure 5.3.8. The spot that is seen at  $t_0 = 3.15025$  s (a) travels downstream, and upstream a new turbulent spot forms that merges with the original one at around  $t_0 + 0.20$  ms (e). Subsequently, further spots forming upstream quickly merge with the preceding turbulent spots. It gives the appearance of one large spot with a triangular head pointing in the upstream direction in this single snapshot. Only in the image series does it become clear that these are a series of spots that have merged into one larger one. The point at which consecutive turbulent spots merge varies depending on the time interval between them and where they originate. Both of these quantities did not seem to follow specific patterns and appeared to be randomly distributed.

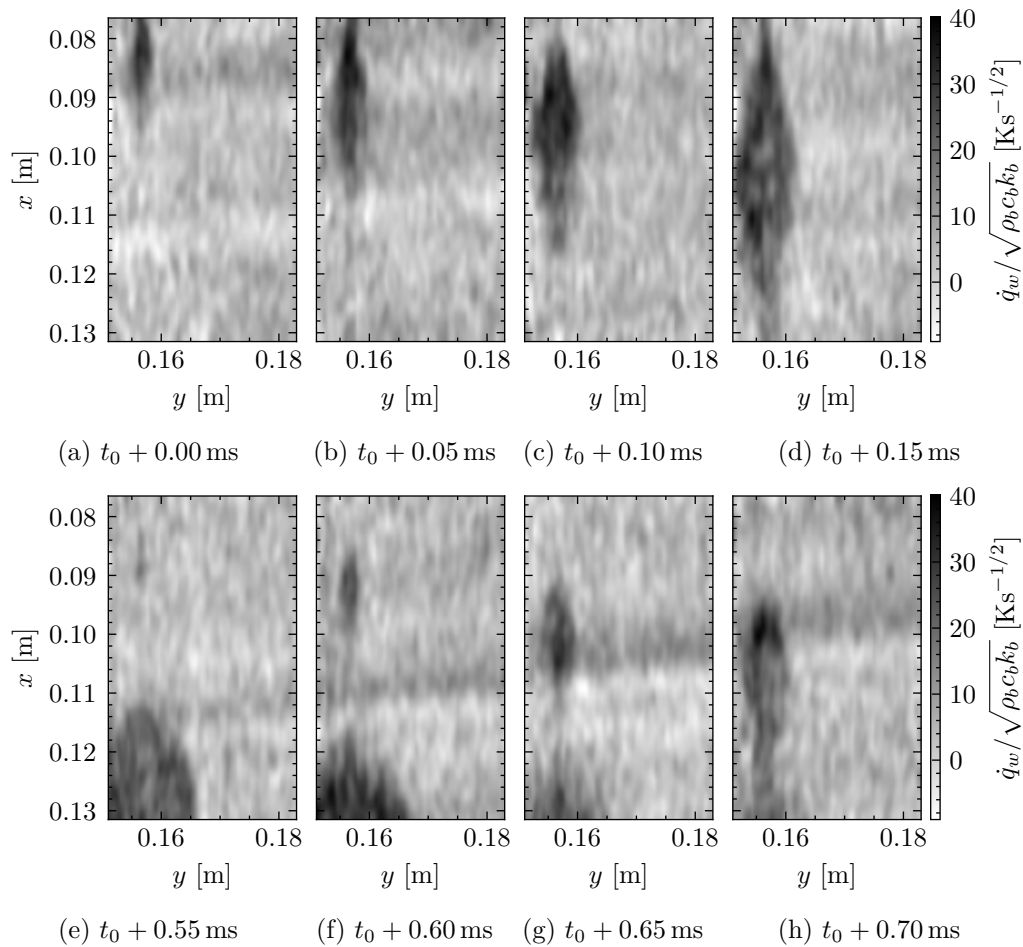


**Figure 5.3.9:** Heat flux distribution for turbulent spots with different streamwise origins for  $Re_c = 8 \cdot 10^6$ ,  $M = 0.8$ , and  $\lambda_\theta = 19.4 \cdot 10^{-3}$  at  $t_0 = 3.1559$  s.

The dark-light stripe that can be seen dominantly in figures 5.3.8 (e)-(h) travelling against the freestream direction is probably caused by an aero-optical effect: upstream moving pressure waves alter the perceived iTSP intensity resulting in dark and light stripes in the calculated heat flux distributions. Further remarks are given in appendix B.2.

Two examples of different spot origins are presented in figure 5.3.9. The first spot, that arises before  $t_0 = 3.1559$  s, originates outside the field-of-view ( $x_{origin} < 0.08$  m). This turbulent spot is a further example of where the following spots merge and form an upstream-pointing triangular leading edge. Another following spot that arises at around  $t_0 + 0.55$  ms (e), originates significantly further downstream between  $0.08 \text{ m} < x_{origin} < 0.09$  m. A precise determination of the origin location is not possible due to the limited temporal and spatial resolution. However, a comparison of images (a) and (g), in which both turbulent spots have a similar size, indicates the point of origin must be around 0.02 m apart from each other. This value is based on the assumption that both turbulent spots grow in a similar manner in the beginning stages. No spot was detected that originated downstream of  $x = 0.10$  m.

Figure 5.3.10 illustrates one example in which the leading edge of the turbulent spot is rounded. This observation is similar to that of section 5.1.6.1 of closely following turbulent

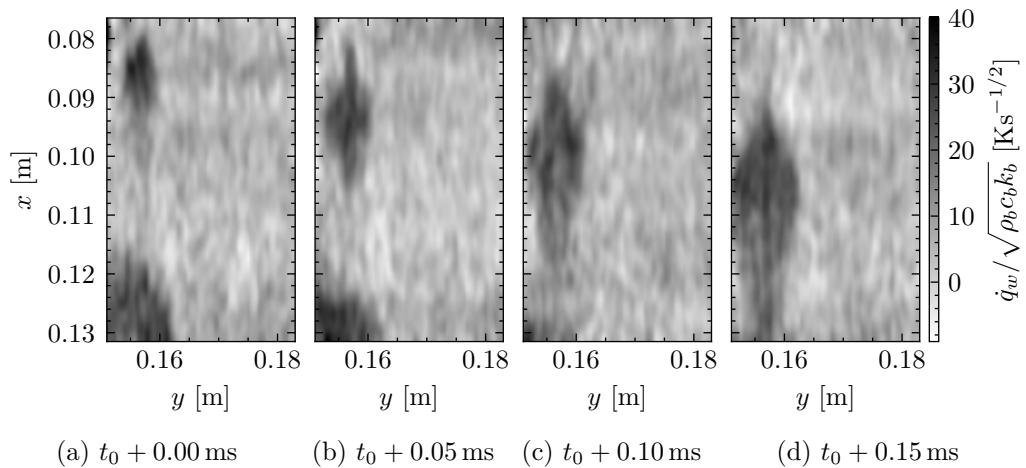


**Figure 5.3.10:** Heat flux distribution for a turbulent spot with rounded leading edge following a preceding spot for  $Re_c = 8 \cdot 10^6$ ,  $M = 0.8$ , and  $\lambda_\theta = 19.4 \cdot 10^{-3}$  at  $t_0 = 3.2044$  s.

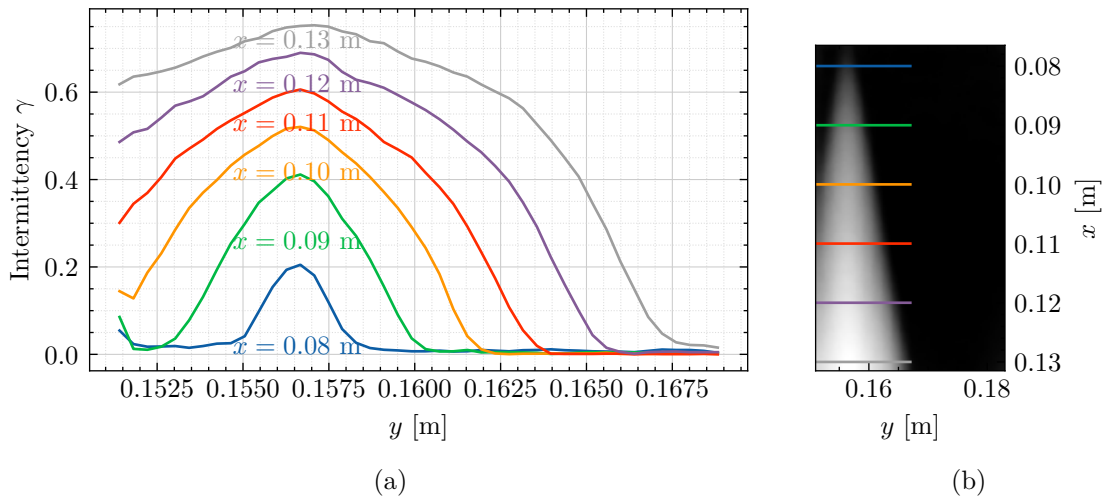


**Figure 5.3.11:** Spanwise intermittency distributions along the intermittent turbulent wedge (a) as indicated in (b) for  $Re_c = 8 \cdot 10^6$ ,  $M = 0.8$ , and  $\lambda_\theta = 19.4 \cdot 10^{-3}$ .

spots affected by the preceding spot calmed region. Due to the high turbulent spot density, this can be seen for a large number of spots in this intermittent wedge. Additionally, the image of the heat flux at the leading edge has poorer contrast (signal-to-noise ratio) compared to the core of the spot, making it challenging to locate the leading edge interface.

In the same manner as for the fully turbulent core wedge cases, figure 5.3.11 shows the intermittency cross sections for the intermittent turbulent wedge of figure 5.3.6. Two different spanwise intermittency gradients are visible for the streamwise positions of  $x = 0.11$  m,  $x = 0.12$  m, and  $x = 0.13$  m. A triangular cross-section is expected for all positions for ideal triangular turbulent spots that do not merge and emanate from the same origin. This is not the case here. The rounded intermittency peak at  $y = 0.157$  m is caused by the streamwise distribution of spot origins. The two distinct gradients downstream of  $x = 0.11$  m are probably caused by the longitudinal merging of spots, the centres of which will merge prior to the outer sections of the spots.

The intermittent nature of this wedge is probably due to an isolated roughness with close to a critical height, similar to one described by Fiala et al. [51]. It is probably caused by variations in the free stream conditions that will, in some cases, cause bypass transition close to the roughness element. This explanation was also proposed by Fiala et al. [51]. Minor changes to the roughness height with respect to boundary layer thickness are expected to change the intermittency of the wedge region, resulting in either completely laminar or turbulent regions.

## 5.4 Tollmien-Schlichting waves

As discussed in section 2, transition is mainly caused by amplified T-S waves in the flow conditions considered in this work. They can be quantified and observed with the hot-films installed on the model. Additionally, an attempt was made to resolve T-S waves with the iTSP measurement technique.

### 5.4.1 Hot-film analysis

Figure 5.4.1 shows the voltage signal recorded with hot-film sensor 4 ( $x/c = 0.50$ ) with the visible T-S waves and the turbulent spot being shown in comparison. Behind the turbulent spot, in the calmed region, the amplitude of any T-S waves is clearly diminished, and is only visible in the raw signal at about 0.7 ms behind the trailing edge, which represents about the time span of the turbulent spot itself. The hot-film signals can be used to evaluate the frequencies of the most amplified T-S waves.

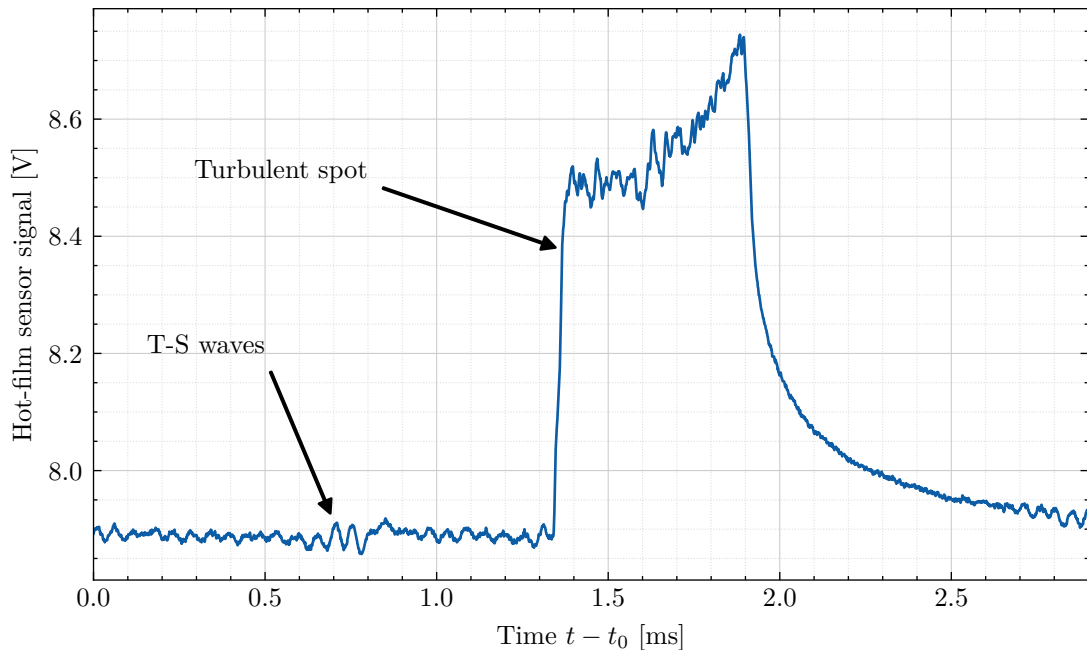


**Figure 5.4.1:** Measured signal for hot-film sensor 4 ( $x/c = 0.50$ ) with  $t_0 = 3.232$  s.

Figure 5.4.2 shows the power spectral density (PSD) for the first four hot-film sensors. A digital bandpass filter ( $1 \text{ kHz} \leq f \leq 50 \text{ kHz}$ ) was applied to the raw signal and evaluated for  $2.8 \text{ s} \leq t \leq 3.2 \text{ s}$ . The power spectral density was then obtained using Welch's method [175] with segment size of  $2^{14}$  ( $\approx 0.016 \text{ s}$ ) and an overlap of 50%.

Additionally, the power spectrum is obtained numerically using LILO (see section 4.3.2). The amplitude amplification rates are calculated according to linear stability theory at the locations corresponding to the hot-film positions. For the graphical representations, the calculated amplification rates are squared and normalised with the peak in power spectral density of the hot-film sensors close to the highest amplified frequency. The resulting curve is also presented in figure 5.4.2. No statement can be made concerning the amplification rate from sensor to sensor as they have not been calibrated. The same also applies to the quantitative comparison between sensor PSD results and numerical

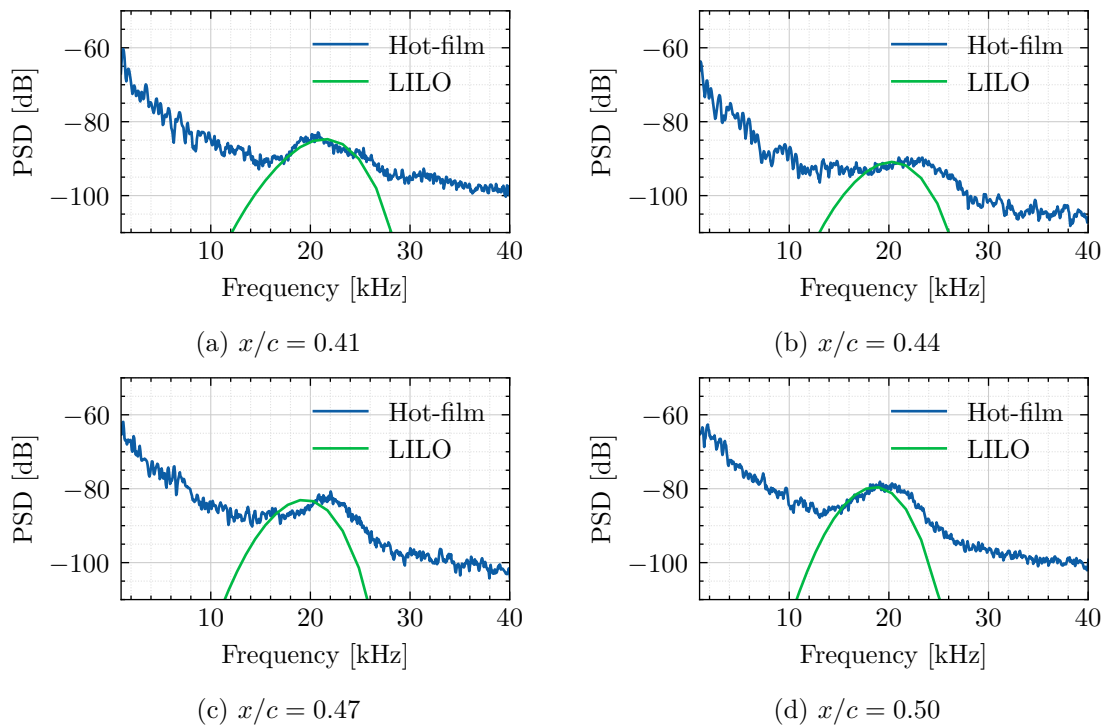


**Figure 5.4.2:** Power spectral density (PSD) of hot-film sensor intensity signal for  $2.8\text{ s} \leq t \leq 3.2\text{ s}$  for the first four hot-films and comparison with numerical calculation with LILO. Flow conditions are  $Re_c = 6 \cdot 10^6$ ,  $M = 0.5$ , and  $\lambda_\theta = 3.5 \cdot 10^{-3}$ .

calculations. Furthermore, the results provided by LILO are amplification rates rather than absolute amplitudes.

As mentioned in section 3.3.2, the hot-films sensors are staggered in a spanwise direction. Therefore, the PSD of hot-film sensors cannot be directly compared; this is due to spanwise variations in model imperfections and/or wind tunnel disturbances influencing the amplification rates measured for the corresponding hot-film sensor.

In general, the agreement between the calculated frequency of the most amplified T-S wave (LILO) and that of the experimental data is very good. For hot-film sensors 2, 3, and 4 the experimental result shows a slightly higher most amplified T-S wave frequency ( $\approx 21.0\text{ kHz}$  (exp.) compared to  $19.5\text{ kHz}$  (num.) for hot-film sensor 3).

Previous measurements by Dimond et al. [42], showed good agreement between experimental and numerical results obtained with LILO for the frequency of the most highly amplified T-S wave for flows between  $M = 0.3$  to  $M = 0.75$  for the same experimental setup used here. It was possible to reliably detect T-S waves at frequencies between  $10\text{ kHz}$  to above  $30\text{ kHz}$ .

### 5.4.2 iTSP analysis

The visibility of T-S waves in the raw signal of the hot-film sensors (compare figure 5.4.1) begs the question of whether T-S waves are detectable with iTSP. T-S waves cause variations in wall shear stress that in turn cause small fluctuations in surface heat transfer which, in theory at least, should be recordable as surface temperature and luminescent

intensity signals of the iTSP, if the signal-to-noise ratio is sufficiently high. A time constant resolvable by iTSP can be estimated by [155]

$$t^* = \frac{h^2}{0.5\alpha} \quad (5.4.1)$$

with  $h$  the paint thickness and  $\alpha$  the thermal diffusivity<sup>2</sup>. For an assumed paint thickness of  $1\ \mu\text{m}$  (measured to be less than that for this investigation - see section 3.4.2) and  $\alpha = 1 \times 10^{-7}\ \text{m}^2/\text{s}$  this equates to a resolvable frequency of about 50 kHz, higher than the frequencies of the most amplified T-S waves expected for the flow conditions examined in this study according to the LILO calculations. The luminescent lifetime of the luminophore is below  $1\ \mu\text{s}$ . In theory, the iTSP should therefore be able to resolve T-S waves for a sufficiently high signal-to-noise ratio.

Based on the comparison of turbulent spot and T-S waves in figure 5.4.1 and the low signal-to-noise ratio observed for turbulent spots with iTSP (compare section 5.1), the raw intensity signal of the iTSP is not expected to be able to resolve these T-S waves directly for individual locations. Therefore, an evaluation method was implemented to estimate a  $k - f$  wavenumber-frequency-diagram of the whole investigated surface covered by a laminar boundary layer. The  $k - f$  (i.e. angular wavenumber and linear frequency) representation was chosen to enable a consistent comparison of frequencies with the hot-film results of the previous section. In a simple approach, the  $k - f$ -diagram can be estimated by a 2D-Fast-Fourier-Transformation (FFT) of an intensity signal in time and space. The image series recorded at an acquisition frequency of 100 kHz, is aligned and mapped to model coordinates according to the procedure described in section 4.7 and normalised with the mean of image series. Because T-S waves are assumed to be quasi-2D for the spanwise extent investigated here (about 3.2 mm) as mentioned in section 4.3.2, the mapped and normalised image series are averaged in a spanwise direction, resulting in a 2D array in time and space (streamwise direction). The time interval spans 2.8 s to 3.2 s in order to exclude the influence of a large part of turbulent spots present after 3.2 s, and the streamwise extent was chosen depending on the transition location, but in any case upstream of  $x$  with  $\gamma = 0.5$ . The spectral density is obtained by averaging the modulus squared of the two-dimensional Fourier transform of overlapping time intervals of 200 time steps of the temperature signal each (50% overlap) to which a Hamming window is applied in both dimensions. The results are then presented in a decibel scale.

An example of the resulting  $k - f$  wavenumber-frequency-diagram can be seen in figure 5.4.3(a) for flow conditions  $Re_c = 6 \cdot 10^6$ ,  $M = 0.5$ , and  $\lambda_\theta = 3.5 \cdot 10^{-3}$ . These are the same flow conditions as shown for the hot-film results in figures 5.4.1 and 5.4.2. The high values adjacent to the frequency and wavenumber axes are mainly caused by (camera) noise. A distinct area with increased power spectrum compared to its surroundings is visible between  $f \approx 15\ \text{kHz}$  and  $f \approx 30\ \text{kHz}$  with corresponding wavenumbers between  $k \approx 500\ \text{rad/m}$  and  $k \approx 900\ \text{rad/m}$ . Additionally, towards lower frequencies and wavenumbers an area of increased power spectrum is observed.

Parallel to the iTSP wavenumber-frequency diagram, the amplification rates calculated with LILO are associated with the corresponding frequency and wavenumber and integrated over all streamwise positions corresponding to the streamwise iTSP evaluation window, therefore taking into account all excited T-S waves in this area. The amplification rates

<sup>2</sup>Considering a semi-infinite approach (valid when the active layer has a similar thermal diffusivity  $\alpha$  as the underlying base layer as in this case), the time constant states when the temperature change at the bottom of the active layer with thickness  $h$  is roughly half that of the surface temperature change caused by step function for the heat flux.

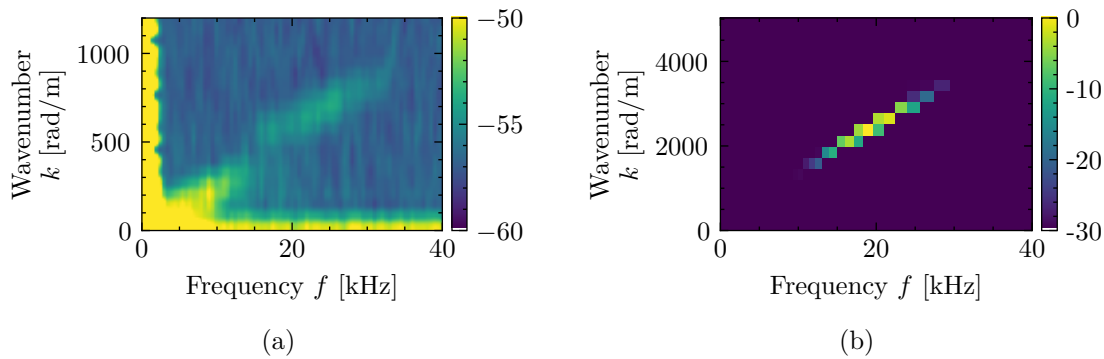


**Figure 5.4.3:** (a) Power spectrum  $k - f$ -diagram obtained from iTSP results. (b) Amplitude spectrum obtained from LILO-calculations. Intensity values are in dB scale (different quantities for iTSP and LILO). Flow conditions are  $Re_c = 6 \cdot 10^6$ ,  $M = 0.5$ , and  $\lambda_\theta = 3.5 \cdot 10^{-3}$ .

are normalised with the maximum amplification rate and the values are presented in dB scale and shown in figure 5.4.3(b). Due to the different normalisations, the dB values of numerical and experimental results can not be compared to each other.

There is a qualitative agreement of the shape of extent and a quantitative agreement in frequencies for the distinct area with increased power spectrum and amplified T-S waves as calculated with LILO. On the other hand, there is a difference in wavenumber by a factor of about four. The phase velocity  $v_p$  of a 2D wave is obtained with

$$v_p = \frac{2\pi f}{k}. \quad (5.4.2)$$

In the case of iTSP, the observed disturbances therefore propagate with a phase velocity of  $v_p \approx 200$  m/s, whereas the T-S waves as calculated by LILO propagate with  $v_p \approx 50$  m/s, which consequently would correspond to celerities relative to the boundary layer edge velocity ( $U_e = 156$  m/s) of 1.3 and 0.3, respectively. The propagation velocity of the apparent disturbances seen in the iTSP wavenumber-frequency diagram is therefore larger than the boundary layer edge velocity, which speaks, as a cause, against physical disturbances in the boundary layer associated with a change of wall temperature distribution.

The distinct area of increased power spectrum density is reproducible and was observed for many different flow conditions. Figures 5.4.4 and 5.4.5 show the iTSP  $k - f$ -diagram for flows at two different Mach numbers  $M = 0.4$  and  $M = 0.8$ , which result in different frequencies of the maximum amplified T-S waves. In both cases, the frequencies of the area of increased power spectrum density match the frequencies of the maximum amplified T-S waves as determined with LILO. Figure 5.4.6(a) shows the results for a mostly turbulent boundary layer. In this case no distinct area of increased power spectrum density is visible, but rather a continuous band that reaches to above 20 kHz. Figure 5.4.6(b) shows the results that would be expected for the frequencies of maximum amplified T-S waves for these flow conditions based on a laminar boundary layer.

While the frequencies and the shape of the area of increased power spectrum density match those of the expected maximum amplified T-S waves, the wavenumbers and resulting propagation velocities do not.

Based on the observed power spectrum, the amplitude of the disturbances causing the distinct area of increased power spectrum density is expected to be in the order of 1 mK to 10 mK, which is reasonable considering the relation of turbulent spot to T-S wave amplitude

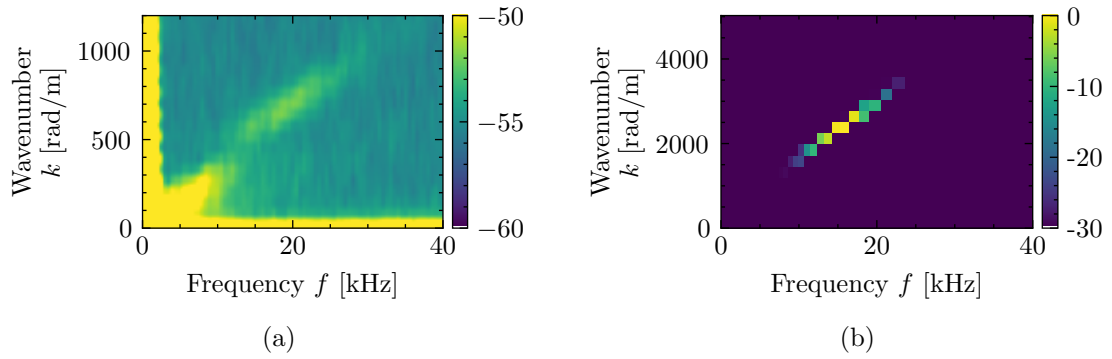


**Figure 5.4.4:** (a) Power spectrum  $k - f$ -diagram obtained from iTSP results. (b) Amplitude spectrum obtained from LILO-calculations. Intensity values are in dB scale (different quantities for iTSP and LILO). Flow conditions are  $Re_c = 5.2 \cdot 10^6$ ,  $M = 0.4$ , and  $\lambda_\theta = 1.9 \cdot 10^{-3}$ .

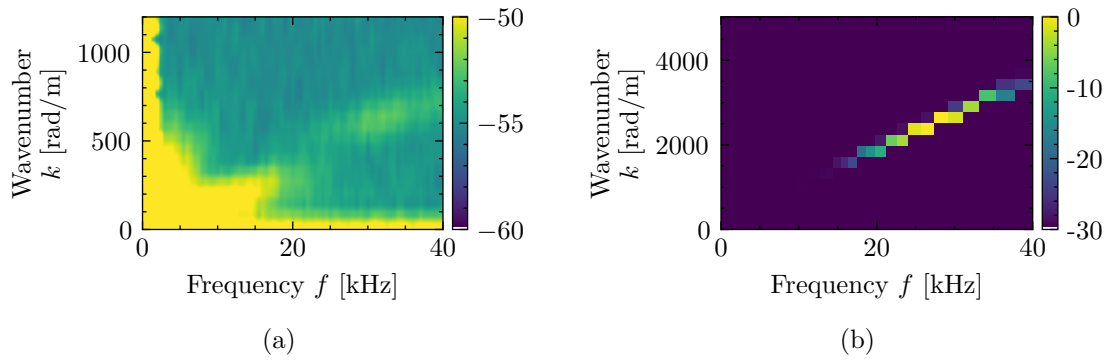


**Figure 5.4.5:** (a) Power spectrum  $k - f$ -diagram obtained from iTSP results. (b) Amplitude spectrum obtained from LILO-calculations. Intensity values are in dB scale (different quantities for iTSP and LILO). Flow conditions are  $Re_c = 8 \cdot 10^6$ ,  $M = 0.8$ , and  $\lambda_\theta = 1.6 \cdot 10^{-3}$ .

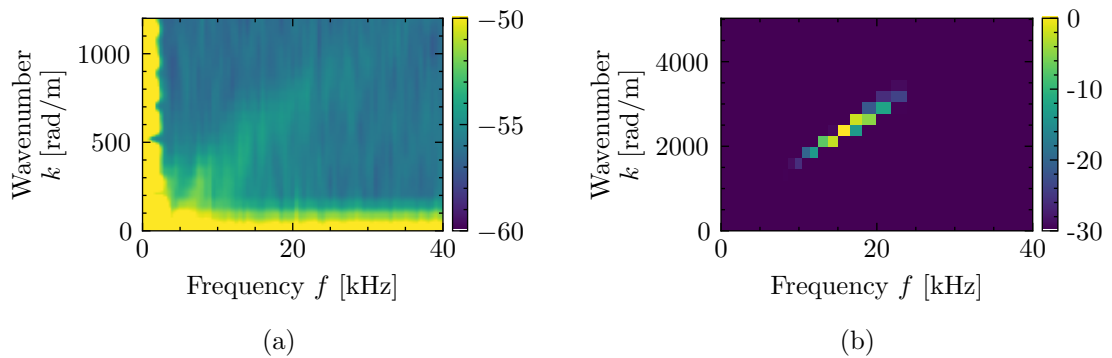


**Figure 5.4.6:** (a) Power spectrum  $k - f$ -diagram obtained from iTSP results. (b) Amplitude spectrum obtained from LILO-calculations. Intensity values are in dB scale (different quantities for iTSP and LILO). Flow conditions are  $Re_c = 5.2 \cdot 10^6$ ,  $M = 0.4$ , and  $\lambda_\theta = -1.1 \cdot 10^{-3}$ .

for the hot-film sensors (compare figure 5.4.1) and the surface temperature change caused by turbulent spots in the range of tenths of Kelvin. No precise calibration of the surface temperature was attempted here.

While there is some evidence that the phenomena observed with the iTSP are related or even somehow caused by T-S waves, it is worth considering what other possibilities could cause the observation. Further results showed that the distinct area of increased power spectrum density did not depend on camera acquisition frequency and was not visible without flow, excluding the possibility of random camera noise as the cause of the observed effect. One error source often present in experimental imaging techniques is pressure fluctuations in the line of sight from camera to model causing diffraction of luminescent light, which leads to false temperature detections. Pressure fluctuations, like shock waves or acoustic waves if strong enough, travelling at given velocities with corresponding frequencies could lead to an ill-informed interpretation of the results. However, in this case, at low Mach numbers, no shock waves are present, and the propagation velocities observed do not correspond to  $M = 1$ , the propagation velocity for pressure fluctuations, neither up- nor downstream. As stated in section 2.1, T-S waves lead to vortices of different formations, of which C-type and H-type  $\Lambda$  vortices have  $2\lambda_{TS}$  wavelength, which still cannot explain the observed factor 4 stated above. Oblique T-S waves, in which the propagation of direction is not parallel to the streamwise direction and typically present for higher Mach numbers, could explain the observed higher apparent wavelength in streamwise direction if high angles of obliques are considered, but are unlikely to be the cause here because of the flow conditions considered in the present work ( $M \leq 0.8$ ) and the spanwise averaging of the evaluation procedure which spans a wider region than the typical wavelengths of T-S waves for the current flow conditions. Therefore, so far no satisfactory explanation for the observed phenomenon could be found.

# Chapter 6

## Conclusions

### 6.1 Overview and summary

Time-resolved measurements were conducted in this experimental work, performed at high Reynolds numbers for a subsonic, compressible flow using fast-responding temperature-sensitive paint. This iTSP technique was specifically characterised and adapted in this work for the purpose of carrying out these measurements. The investigations focused on the visualisation and measurement of different phenomena occurring in (originally quasi-two-dimensional) transitional flows: turbulent spots, intermittency, turbulent wedges, and Tollmien-Schlichting waves. To enable this, a Ru(phen)-based temperature-sensitive paint was examined for its use in the current investigation. A major problem encountered with this paint was its significant ageing: the reduction of its luminescent intensity and sensitivity with accumulated illumination, which was found to depend on the paint thickness and composition. With the help of a calibration taking into account this ageing of the paint at every location (due to paint inhomogeneities and different illumination depending on the position on the model) and the decay of the excitation light during the test, a time-resolved quantitative measurement of surface temperature recorded at frame-rates of 20 kHz to 100 kHz was possible. By considering the surface temperature development and the thermal properties of the paint and model, it was possible to estimate the heat flux at the surface, which mainly depends on the boundary layer state for a given ratio of wall to adiabatic wall temperature. The experiments were performed in the Cryogenic Ludwig-Tube Göttingen (KRG) with a model designed to achieve a uniform pressure gradient along the investigated area. The parameter ranges covered chord Reynolds numbers  $3.5 \cdot 10^6 \leq Re_c \leq 10 \cdot 10^6$ , freestream Mach numbers  $0.35 \leq M \leq 0.8$ , and pressure gradient parameters  $-3.9 \cdot 10^{-3} \leq \lambda_\theta \leq 19.5 \cdot 10^{-3}$ , which could all be varied independently of each other. With this, it was possible to observe and measure turbulent spots, the intermittency distribution, turbulent wedges, and Tollmien-Schlichting-waves.

The main characteristics of turbulent spots, i.e. general shape of the laminar-turbulent interface, leading and trailing edge celerity ( $c_{le}$  and  $c_{te}$ ), spreading and opening angles ( $\alpha$  and  $\beta$ ), and spot propagation parameter  $\sigma$ , could be identified for various flow conditions at the wall. For this, new methods were developed to identify the laminar-turbulent interfaces of the spots and to utilise these to determine the leading and trailing edge

celerities. This study is the first to have experimentally investigated turbulent spots using an image based thermographic measurement technique at such high values of local Reynolds numbers. For isolated turbulent spots, the general shape at the wall was found to be a downstream-pointing triangle with a rounded wing tip region, similar to that found by other researchers for a low-speed flow. In general, the leading edge celerity was slightly higher than most values reported in literature, but this is explained by the general flow conditions and naturally occurring turbulent spots observed here. The calmed region trailing the spot was faintly visible in the iTSP results and could clearly be observed in the hot-film traces.

With increasing pressure gradient parameter  $\lambda_\theta$  (more favourable pressure gradient), both leading and trailing edge celerities increased significantly. The leading edge celerity was not found to be influenced by increasing Mach number up to about  $M = 0.6$ , but strongly decreased for a flow at  $M = 0.7$  and  $M = 0.8$ . In contrast, the trailing edge celerity showed little variation with Mach number, at least within the bounds of the measurement uncertainties. The effect of the chord Reynolds number  $Re_c$  on the leading edge celerity showed no clear trend. However, the trailing edge celerity was significantly reduced at higher Reynolds numbers, which was made even more evident when examining the trailing edge celerity with respect to the local Reynolds number  $Re_x$ .

Extracting the celerities from the hot-film measurements for all investigated test cases was not possible directly because of the requirement of needing to have many large isolated turbulent spots that spread over at least two consecutive hot-film sensors, leading to an ambiguity in the results. This again emphasises the advantages of the iTSP measurement technique for these flow conditions. However, an estimation for one condition with a high number of isolated turbulent spots showed good agreement between the leading and trailing edge celerities and those obtained with the iTSP measurements.

As with the spreading angle of turbulent wedges, the spreading angle  $\alpha$  of turbulent spots decreased with increasing Mach numbers. Additionally, although the opening angle  $\beta$  showed a large variation (typically between  $7^\circ$  and  $12^\circ$ ), a proportional relationship could nevertheless still be found between  $\alpha$  and  $\beta$ .

The merging behaviour of turbulent spots was also investigated. The leading edge celerities of trailing spots were found to be considerably slower if trailing within about one spot length from the calmed region of the up-front turbulent spot. In contrast, the spots grew independently of each other in the case of lateral merging. Furthermore, the growth of turbulent spots was unaffected when merging with turbulent wedges.

The spot propagation parameter  $\sigma$  was determined for selected cases and was found to decrease with increasing Mach numbers. This decrease was caused by the effect of Mach number on the turbulent spot celerities and spreading angle, as mentioned above.

The high temporal resolution of the iTSP measurements made it possible to determine the intermittency distribution directly, for which an acquisition frame rate of 20 kHz was shown to be sufficient for the investigated test cases. The intermittency distribution was found to correlate well with the Johnson intermittency model from the literature, derived from a theoretical standpoint. The transition location, defined at 50% intermittency, agreed well with the maximum temperature gradient, a measure often used to determine the transition location for a non-time-resolved measurement. However, the accuracy of this is dependent on the surface temperature history.

Using the intermittency determination, it was also possible to investigate turbulent wedges that likely arose from a surface inhomogeneity. A fully turbulent core and intermittent outer region could be identified for the case of a typical wedge. The spreading angles of turbulent spots were thereby found to be similar to those of the spreading angle of the wedge for an intermittency factor of  $\gamma = 0.1$ , demonstrating the similarity of spanwise growth for wedges and spots.

By determining the time-resolved heat flux distribution, it was possible to demonstrate that intermittent turbulent wedges comprise individual turbulent spots. Since they often closely follow one another, the leading edge celerity and the spot propagation parameter are reduced compared to isolated turbulent spots. In some cases, where several closely spaced turbulent spots merged, the resulting turbulent patches appeared as upstream pointing triangles. Due to the spatial growth of the turbulent spots, the intermittency factor steadily grew in the downstream direction.

The hot-film sensors were able to resolve T-S-waves up to a frequency of above 30 kHz. The detected frequencies agreed well with those found for the highest amplified T-S-waves as determined with the local linear stability solver LILO. The calculated wavenumber-frequency-diagram for the iTSP intensity map recorded at 100 kHz showed a distinct area of increased power spectrum density with frequencies close to those observed with hot-film sensors and LILO calculations for various flow conditions. The corresponding wavenumbers, however, were found to be about 4 times lower than expected by numerical calculations, implying phase velocities higher than the boundary layer edge velocity. This inconsistency could not be explained by artefacts introduced by the experimental setup, and raises a concern on the detection of T-S waves via iTSP, even though the frequency range was in quantitative agreement for various flow conditions. These aspects need to be further investigated in future work.

The presented results demonstrate the capabilities of fast-response iTSP to quantitatively resolve unsteady laminar-turbulent transition phenomena for the investigated flow cases. Apart from gaining a better understanding of turbulent spots and their growth behaviour, the results are also useful in various applications. Many transition models rely on empirical correlations of the effect of various flow conditions on the growth of turbulent spots [80]. Furthermore, the results can serve as validation measurements for numerical calculations, which has not been possible yet due to lack of experimental data. The advantage of the present measurements is that not only could the relevant parameters of turbulent spots - such as celerities and spreading and opening angles - be evaluated, but the heat flux distribution and development can be determined with high spatial resolution.

## 6.2 Outlook and further suggested work

In contrast to previous results where the influence of flow conditions on turbulent spots is often compared for various measurement techniques with an associated high degree of uncertainty, this study demonstrates the advantages of using one and the same measurement technique. Therefore, there is great value in continuing the work further to understand the role of turbulent spots in laminar-turbulent transition. Some questions remain from the current investigation which should be addressed in future:

- Why is the leading edge celerity determined here higher compared to the results from other works?
- Is it possible to have leading edge celerities higher than the boundary layer edge velocity, and under what circumstances and flow conditions?
- In what way does the overhang region at the leading edge influence the heat flux at the wall?
- What causes the decrease in leading-edge celerity for high subsonic Mach numbers, and is this reproducible also in other facilities and with other measurement techniques? Especially valuable would be an extension of the Mach number range for  $M > 0.8$  in the transonic region.
- Is the characteristic area of increased power spectrum density for the iTSP results and the factor 4 in wavelength difference compared to the calculated wavelength of T-S waves reproducible also for other flow conditions and wind tunnels?

To address these questions, improving the measurement technique further would be most desirable, especially to be able to improve the signal-to-noise ratios. The focus for this should be on the optimal screen layer thickness and enhanced illumination with more powerful light sources. Smaller and developing turbulent spots can be characterised by achieving a higher spatial resolution by either increasing magnification or camera resolution. Due to the limited optical access in KRG, a different facility may be more suitable in order to achieve these objectives. Additionally, using iTSP for an incompressible flow case and artificially generated turbulent spots is advisable to compare results with previous investigations. These experiments can be combined with other measurement techniques aimed at measuring properties in the boundary layer, like PIV/STB or hot-wire measurements, to simultaneously gain an understanding of the flow properties inside the boundary layer and at the wall. Extending the parameter range to supersonic conditions should help to address the effect of Mach number close to  $M = 1$ . Additionally, further numerical work is desirable. The combination of experimental and numerical simulations can gain further insights in the underlying physics of boundary layer transition processes and the effects observed in this work.

# Appendices



# Appendix A

## Remarks on Evaluation Techniques

### A.1 Further remarks on the heat flux calculations

This section deals with the heat flux as calculated numerically from the time-resolved surface temperature distribution in section 4.4. An alternative approach based on a semi-infinite base layer is presented here, and both methods are compared to each other. The semi-infinite approach is often used for quantitative heat flux determination with time-resolved thermographic imaging in short-duration wind tunnels [51, 90, 97, 112, 122, 135] and is presented below:

With the following assumptions

- semi-infinite coating thickness and thermal diffusivity  $\alpha$  constant (neither dependent on temperature nor location) and
- heat transfer into the model is one-dimensional, and
- the TSP layer is thin enough to be considered negligible

it is possible to obtain the time-varying surface heat-transfer rate through

$$q_w(t) = -\sqrt{\frac{\rho_b c_b k_b}{\pi}} \int_0^t \frac{dT/d\tau}{\sqrt{t-\tau}} d\tau \quad (\text{A.1.1})$$

with surface temperature  $T$  and the subscript  $b$  indicating the thermal properties of the TSP base layer [155]. Approximating a piece-wise linear-temperature profile the integration method proposed by Cook & Felderman [155] gives the heat flux

$$q_w(t_n) = -2\sqrt{\frac{\rho_b c_b k_b}{\pi}} \sum_{i=1}^n \frac{T(t_i) - T(t_{i-1})}{\sqrt{t_n - t_i} + \sqrt{t_n - t_{i-1}}} \quad (\text{A.1.2})$$

at every time step  $t_n$ . To estimate the validity of the semi-infinite approximation, Schultz & Jones [155] proposed the penetration depth  $x = 4\sqrt{\alpha t}$  where heat flux and temperature difference compared to infinite depth are below 1%. For a run time of 0.7 seconds the penetration depth is 1058  $\mu\text{m}$ , or 3347  $\mu\text{m}$  for a thermal diffusivity of  $\alpha = 1 \times 10^{-7} \text{ m}^2/\text{s}$

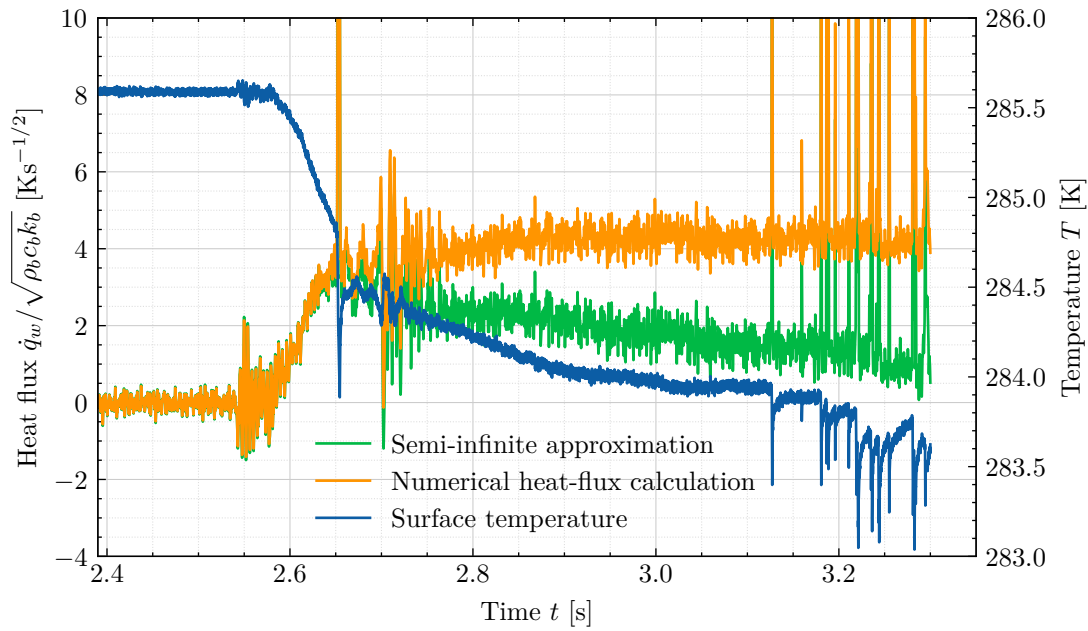


**Figure A.1.1:** Comparison of calculated heat flux with equation A.1.2 (semi-infinite approximation) and equation 4.4.7 (numerical calculation) as well as the temperature distribution at  $x = 0.1$  m,  $y = 0.167$  m for flow conditions  $Re_c = 6 \cdot 10^6$ ,  $M = 0.8$ , and  $\lambda_\theta = 19.0 \cdot 10^{-3}$ . Extension of figure 4.4.2.

and  $\alpha = 1 \times 10^{-6}$  m<sup>2</sup>/s which is much larger than the 100  $\mu$ m thickness of the base layer. Therefore equation A.1.2 cannot be used for a quantitative heat flux determination.

Figure A.1.1 shows the comparison of the calculated heat flux with that described in section 4.4 for a predominantly laminar boundary layer. Initially (at around 2.6 s to 2.7 s), both methods agree well with each other but for later times, the values for the semi-infinite approximation decline. This is unphysical as the general flow is expected to be relatively constant. The surface temperature at 3.0 s and with that the wall temperature ratio  $T_w/T_{aw}$  is close to constant, resulting in an expected constant heat flux. The observed decline is because the thermal diffusivity of primer and steel model is much higher than that of the base layer, the heat flux at the junction primer to base layer is underestimated, and therefore the apparent heat flux at the surface is too small.

In figure A.1.2, the heat flux of the turbulent spot discussed in figures 4.5.4 and 4.5.5 is presented. For the laminar boundary layer condition before and after the turbulent spot, the semi-infinite approximation yields a heat flux below the expected value. Normalising both calculations with the maximum heat flux level (during the passage of the turbulent spot) and an average laminar heat flux level as depicted in figure A.1.2(b), the differences are marginal. This is understandable as the thermal properties of primer and steel model are not relevant for this short time span of the turbulent spot passage. Therefore the qualitative behaviour is accurately modelled with the semi-infinite approximation when the investigated time-scale is small enough in respect to the base layer thickness. For a purely qualitative description it is therefore easier to refer to the semi-infinite approximation which can be computed much easier and faster.

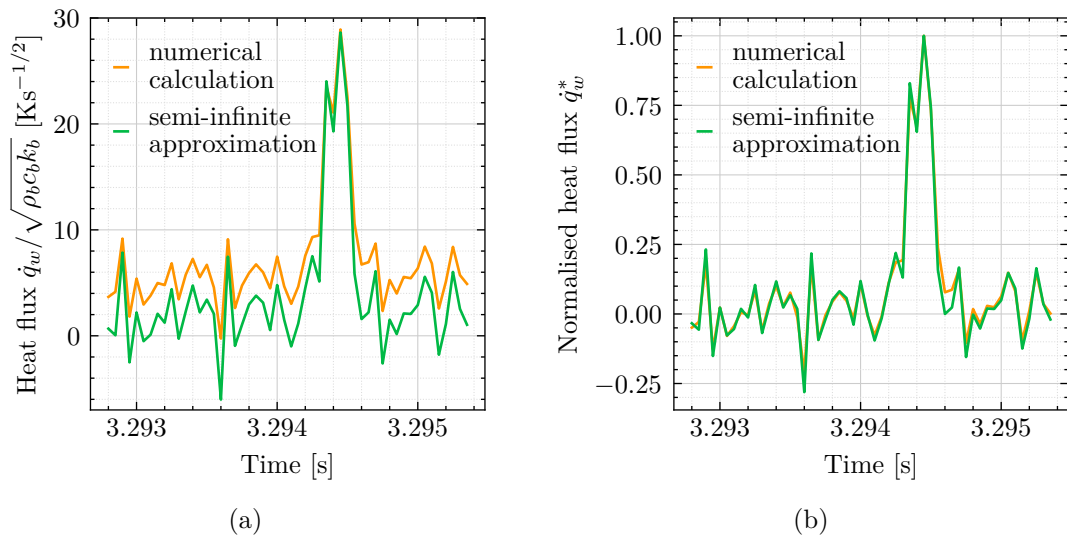


**Figure A.1.2:** Comparison of calculated heat flux with equation A.1.2 (semi-infinite approximation) and equation 4.4.7 (numerical calculation) for the turbulent spot presented in 4.5.4 and 4.5.5. Flow conditions are  $Re_c = 6 \cdot 10^6$ ,  $M = 0.8$ , and  $\lambda_\theta = 19.0 \cdot 10^{-3}$ .

## A.2 Other possible methods and comparisons determining celerities

This section describes further methods to determine the trailing and leading edge celerities, discussing their feasibility and comparing the different methods with each other.

Cross-correlating the intensity signal in a streamwise direction (i.e. for subsequent images) is not possible due to the inhomogeneous intensity and sensitivity distribution. Even a carefully executed calibration could not improve the distribution sufficiently. Furthermore, this would require a large amount of user input - for the spanwise position, appropriate points in time and exclusion of closely following spots to avoid false correlations.

The correlation of gradients in a streamwise direction is difficult because the leading edge interface does not necessarily correspond to the maximum gradient. The location is better described by the maximum of the second derivative, the highest change in heat transfer coefficient. The signal-to-noise ratio, however, was not good enough to identify this property with the required accuracy.

One possibility is to make use of triangles as the simplified geometric shape of turbulent spots in accelerated boundary layers. Time series of isolated turbulent spots can be approximated with triangles of increasing size through a suitable minimisation function. The geometry of the spot is determined by 6 independent parameters: Virtual spot initiation location in the spanwise and streamwise direction, time of initiation, spreading angle and leading and trailing edge celerity. An example of this is shown in figure A.2.1. A cost function is defined as the XOR of the triangles and the turbulent spot outline calculated as described in section 4.5.3 (red line) and minimised for the 10 image time series through the method of steepest descent. The resulting celerities are  $c_{le} = 1.01$  and  $c_{te} = 0.48$ . The spreading angle is  $\alpha = 9.2^\circ$ . With equation 2.3.1 the opening angle can be calculated to  $\beta = 8.3^\circ$ . Although this method seems reasonable it has some significant disadvantages: Firstly, the cost function as described above relies on the already detected turbulent spot outer edge and is therefore susceptible to the same limitations. It is possible to define a cost function based on the gradient alone but this relies on an arbitrarily set threshold and is not reliable due to the signal-to-noise ratio.

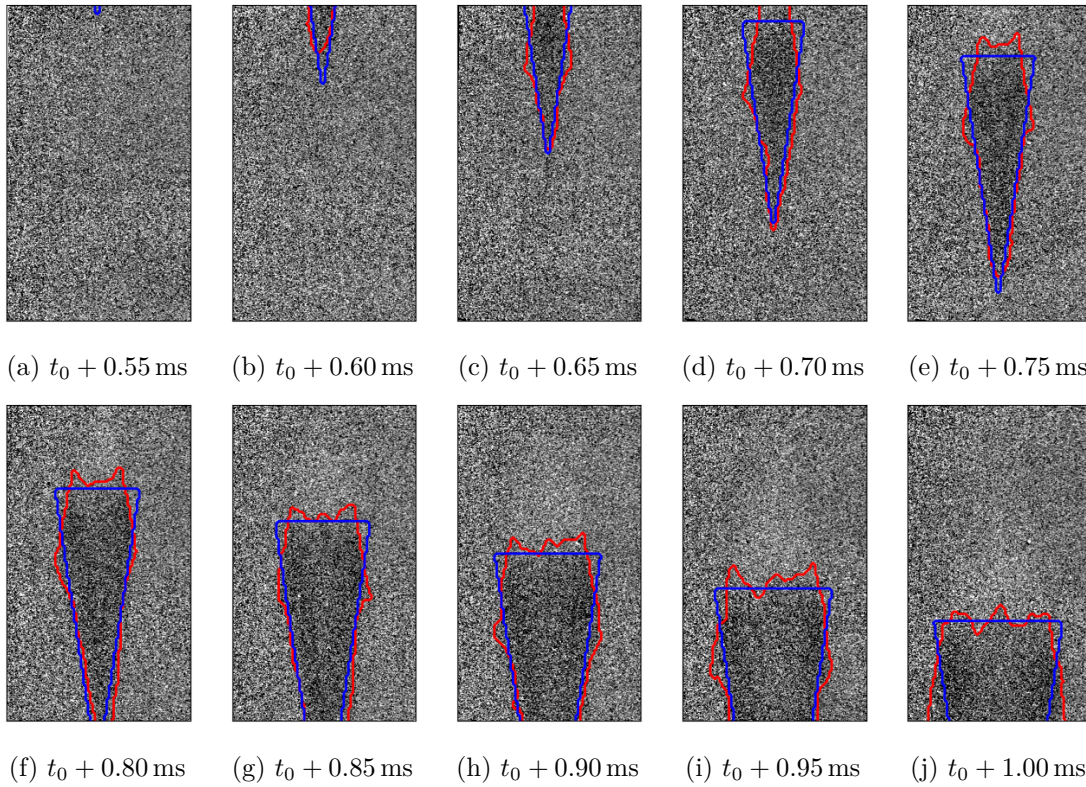


**Figure A.2.1:** Temporal intensity ratio gradient (colourmap as in figure 4.5.5) and triangular fit (blue) for the turbulent spot presented in 4.5.4 and 4.5.5 (red contours). Flow conditions are  $Re_c = 6 \cdot 10^6$ ,  $M = 0.8$ , and  $\lambda_\theta = 19.0 \cdot 10^{-3}$  at  $t_0 = 3.2936$  s.

Secondly, as mentioned above, the calculations require a lot of user input to determine suitable isolated turbulent spots - merging and closely following spots as well as spots that are only partially inside the area of interest are not suitable for this method, excluding a majority of turbulent spots detected in this investigation. Thirdly, the minimisation requires a very good first estimate due to the 6 degrees of freedom requiring even more manual user input. Lastly, as tempting as it is, the triangular shape is a major simplification of the shape and may not be suitable for all investigated flow conditions, especially for the trailing edge region, as was discussed in chapter 5.

### A.3 Remarks on the temperature correction procedure of hot-films

As stated in section 4.8, the quantitative measurements of the wall shear stress requires a correction of the measured raw voltage signals for a change in ambient temperature [70]. This can be approximated by [70]:

$$U_{corrected} = U_{measured} \sqrt{\frac{T_s - T_r}{T_s - T_a}} \quad (\text{A.3.1})$$

where,  $T_s$  is the sensor temperature,  $T_r$  is the temperature at calibration and determination of the overheat ratio OR (corresponds to the charge temperature  $T_c$  in KRG), and  $T_a$  is the ambient temperature in the test section during the measurement. This correction

is typically used for low-speed, continuously operated wind tunnels with a slow drift in ambient temperature and only valid for a small temperature range of several Kelvin [70]. It is uncertain that this correction applies to short-duration wind tunnels, as used in this investigation, and what an appropriate value of  $T_a$  would be. The driving temperature for heat flux at the wall (affecting the output signal of the hot-film sensors) is the (laminar) adiabatic wall temperature  $T_{aw}$  which is typically 10 K to 20 K below  $T_r$  in this investigation, depending on the flow conditions. The temperature correction stated above, however, also takes into account a temperature change of the leads, substrate and overall model temperature to which there is a significant heat flux and thus mainly responsible for the necessity of correction. The ambient temperature may therefore be best estimated with the wall temperature as measured with iTSP which is about 1 K to 3 K lower than  $T_r$ . The sensor temperature is calculated by

$$T_s = \frac{\text{OR} - 1}{\alpha_{TCR}} + T_r \quad (\text{A.3.2})$$

with temperature coefficient of resistance  $\alpha_{TCR}$ .  $\alpha_{TCR}$  is unknown in the current application and may vary from  $\alpha_{TCR} = 0.3 \text{ \%}/\text{K}$  [14] to  $\alpha_{TCR} = 0.69 \text{ \%}/\text{K}$  [12], the theoretical value for bulk nickel. Furthermore, the value is usually temperature-dependent and may vary considerably for higher temperatures. For a typical value used for hot-films of the current design and manufacturer,  $\alpha_{TCR} = 0.35 \text{ \%}/\text{K}$ , the sensor temperature is estimated at  $T_s \approx 388 \text{ K}$  but may be significantly higher depending on the true value of  $\alpha_{TCR}$  in this application. Assuming only a small change in effective ambient temperature, the correction factor is negligibly small for this sensor temperature.

For these reasons, no temperature correction was applied in the current investigation. The quasi wall shear stress is therefore assumed to be only a function of the local wall shear stress:  $\tau_q = h(\tau_w)$  with a monotonous function  $h$  that is at best linear.

## A.4 Error analysis for the laminar-turbulent transition measurements

This section covers the accuracy and reliability of directly determining the intermittency distribution with time-resolved temperature-sensitive paint discussed in section 5.2. They largely depend on two aspects: the TSP properties, especially the thickness and properties of the active layer, and the acquisition frame rate. The impact of both of these on the determination of the intermittency distribution for a compressible subsonic flow are discussed below.

**Active layer consideration** As outlined in section 3.4, the thickness of the active layer is estimated to be around  $0.8 \mu\text{m}$ . Based on the calculated temperature gradient close to the surface, this results in a temperature difference between top and bottom of the active layer of about 0.05 K for a typical case with a flow of  $M = 0.8$  and the stated thickness. This is valid if the thermal properties are the same for the active layer and for the base layer. Indeed, the thermal properties of the polyamide-based binder are comparable to each other and expected to be representative of the active layer (i.e. combined with the luminophore and after application to the model) [90]. Assuming the luminescent intensity recorded by the camera is homogenous throughout the active layer, a reasonable assumption considering the thin layer, this results in the surface temperature being underestimated by 0.025 K. This value is well below the absolute uncertainty of determined temperature

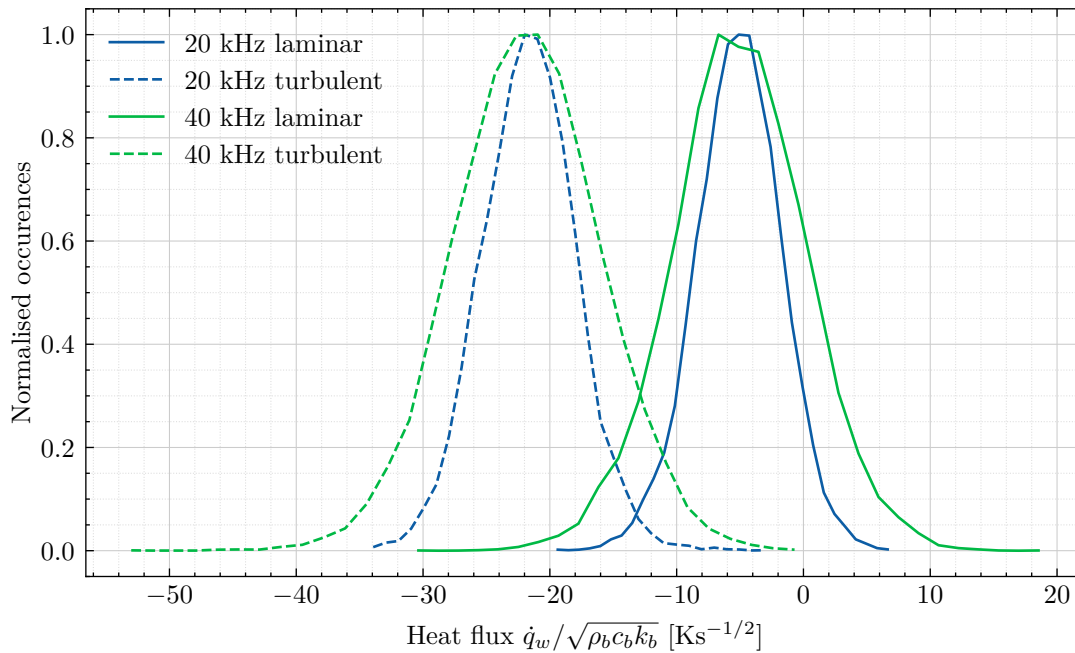


**Figure A.4.1:** Histograms for a fully laminar and turbulent boundary layer with acquisition frame rates 20 kHz and 40 kHz for  $3.0\text{ s} < t < 3.1\text{ s}$  with flow conditions  $Re_c = 7.5 \cdot 10^6$ ,  $M = 0.8$ , and  $\lambda_\theta = 12.9 \cdot 10^{-3}$ .

and much lower than the temperature difference between flow and surface. Although these estimations are based on a flow with Mach number 0.8, they are similar for lower Mach numbers since the lower temperature difference of flow to surface is compensated by a lower temperature gradient within the active layer. For this reason it is suitable to assume an infinitesimal thin active layer in the considerations of this work.

**Frame rate comparison** An important parameter for the direct determination of intermittency is the acquisition frame rate, and more specifically the exposure time. If it is too low, it is not possible to resolve small spatial areas of laminar and turbulent flow resulting in too steep of an intermittency distribution. A turbulent boundary layer would only be detected if a large portion of flow in the exposure time is turbulent and likewise for laminar parts in an otherwise turbulent boundary layer. Transition onset and end would therefore be detected too close together. If the frame rate is too high, on the other hand, the noise in the signal is generally increased, which in turn increases the false identifications. This can be seen in figure A.4.1 with the histograms of a laminar and turbulent boundary layer for acquisitions rates of 20 kHz and 40 kHz. While the overall position of the peaks are at the same location, the distribution is considerably wider for the 40 kHz case. Setting a simple threshold therefore leads to false detections as both peaks have a considerable overlap. The effect can be seen in figure A.4.2 in which the intermittency distribution for both frame rates are shown. To better compare the results, they are normalised by transition onset and length, based on the Johnson distribution. While there is a good agreement in the centre part of the transition process, the tail ends of the 40 kHz case never reach 0 and 1. Binning images in temporal directions allows investigation of which distributions could be expected if only lower framerates can be acquired. The intermittency distributions for the same run but different virtual acquisition frame rates are shown in figure A.4.3. As outlined above, lower frame rates lead to a steeper intermittency distribution

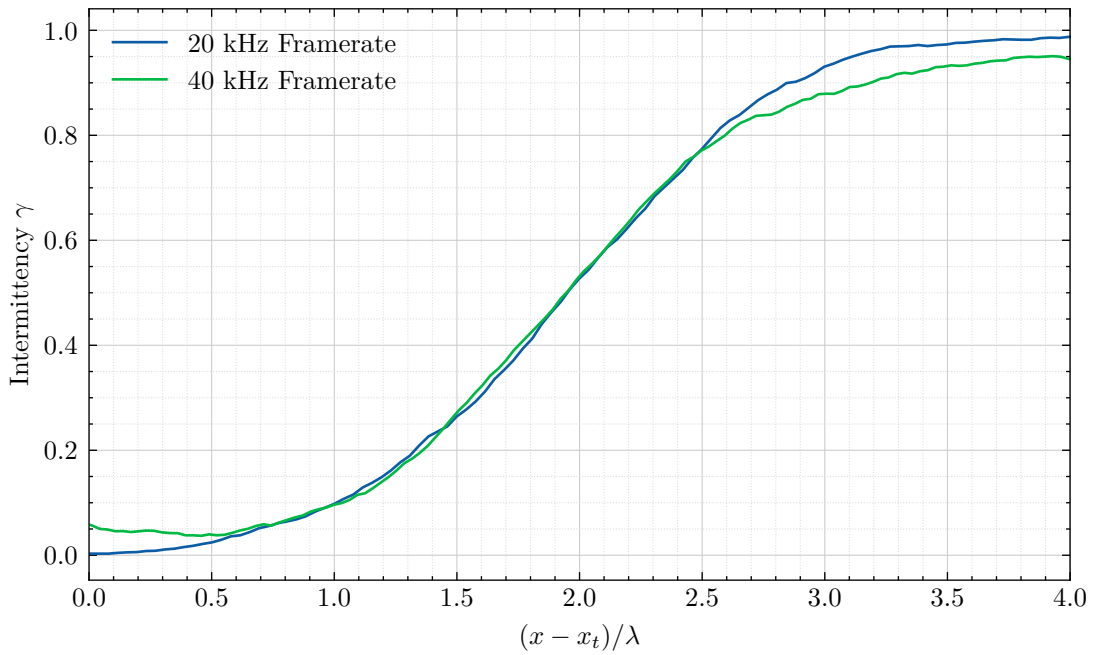


**Figure A.4.2:** Intermittency distribution for acquisition frame rates 20 kHz and 40 kHz for  $3.0\text{ s} < t < 3.1\text{ s}$  with flow conditions  $Re_c = 7.5 \cdot 10^6$ ,  $M = 0.8$ , and  $\lambda_\theta = 12.9 \cdot 10^{-3}$ .

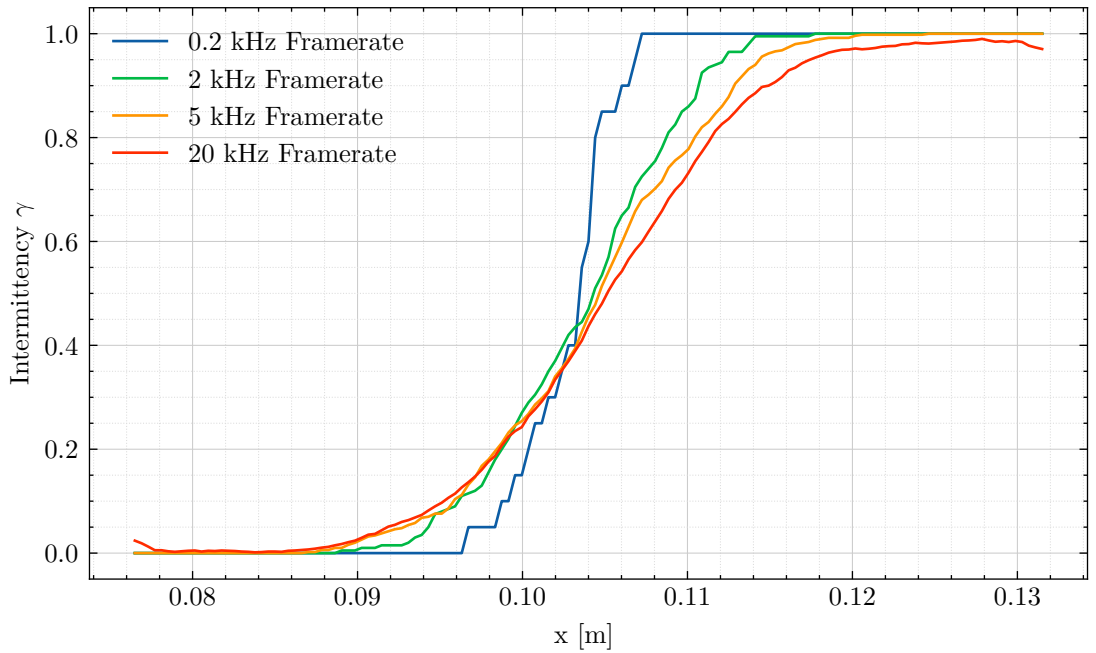


**Figure A.4.3:** Intermittency distribution for virtual frame rates for  $3.0\text{ s} < t < 3.1\text{ s}$  with flow conditions  $Re_c = 7.5 \cdot 10^6$ ,  $M = 0.8$ , and  $\lambda_\theta = 12.6 \cdot 10^{-3}$ .

as small laminar and turbulent patches cannot be resolved sufficiently. This is especially pronounced close to the end of transition.

## A.5 Remarks on visibility of markers in the result images

This section deals with the markers, which are still visible in figure 5.1.1, despite them nominally being cancelled out, i.e. even at the position of the markers, the correct surface temperature should be obtainable. Since the images were accurately aligned, this is mostly not an effect commonly seen when dividing images with slightly misaligned markers, in which the high contrast causes a dark-bright pattern in divided images. They are instead visible for a number of other reasons:

- The shallow focal depth means that some parts of the image are not totally in focus. These areas are dependent on the pressure in the facility. Since this varies depending on the flow conditions and from the pressure decreases from wind-off to wind-on condition (compare figure 3.1.2), the point of focus shifts and division of images does not completely cancel out the luminescent intensity variation.
- The black base absorbs more of the high power excitation light which causes the surface to warm up more than in areas with a screen layer. Part of the markers visible in the surface temperature images therefore physically have a higher temperature. This effect is estimated to be in the order of a tenth of a K.
- As can be seen in figure 4.1.4, the dark background causes a different loss of sensitivity over time.
- To retrieve quantitative temperature information, the intensity distribution of the excitation light and its decay must be accounted for. This was done with a low spatial resolution (lower than the typical marker size) and therefore the effect may not be accurately accounted for at the marker location.

This effect can only be seen because the colour map in figure 5.1.1 covers a narrow range of temperatures.

# Appendix B

## Additional results

This section provides additional results to those presented in section 5.1. In section B.1, further turbulent spot celerities are presented. Section B.2 discusses the aero-optical effects seen for high Mach numbers.

### B.1 Additional turbulent spot celerities

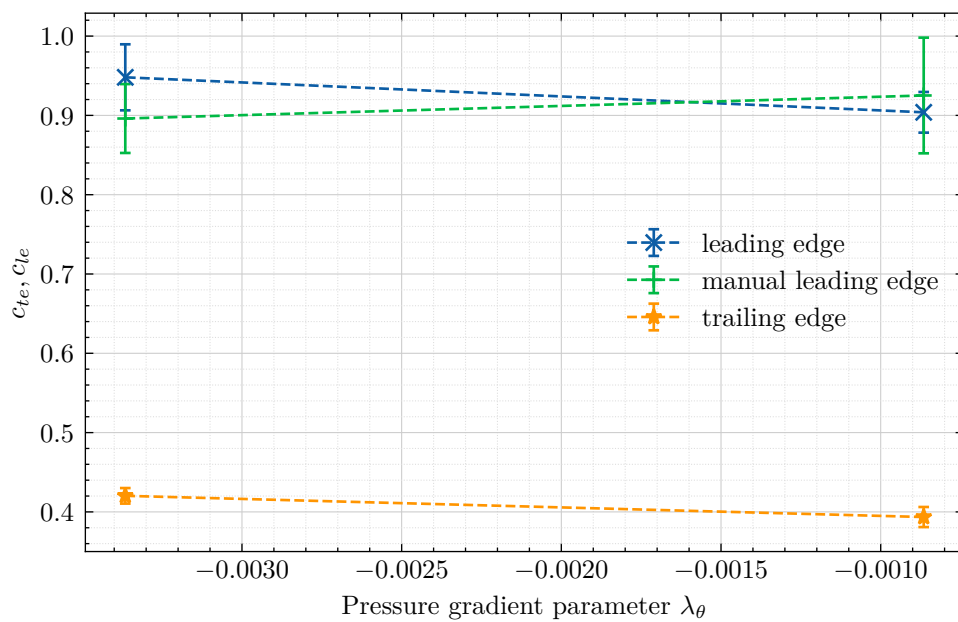


**Figure B.1.1:** Leading and trailing edge celerities for different pressure gradient parameters for  $Re_c = 3.5 \cdot 10^6$  and  $M = 0.35$ .

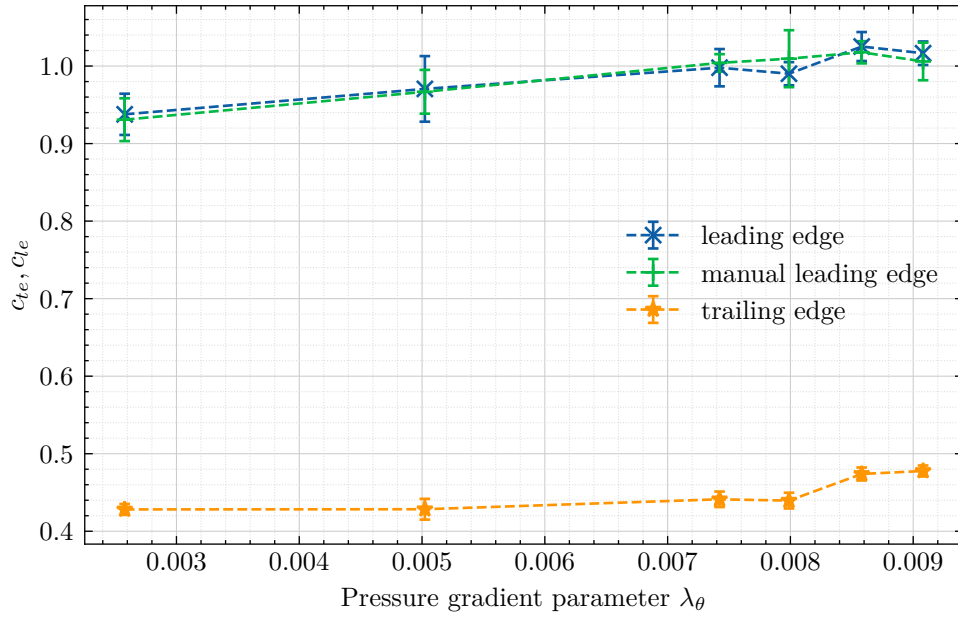


**Figure B.1.2:** Leading and trailing edge celerities for different pressure gradient parameters for  $Re_c = 6 \cdot 10^6$  and  $M = 0.4$ .

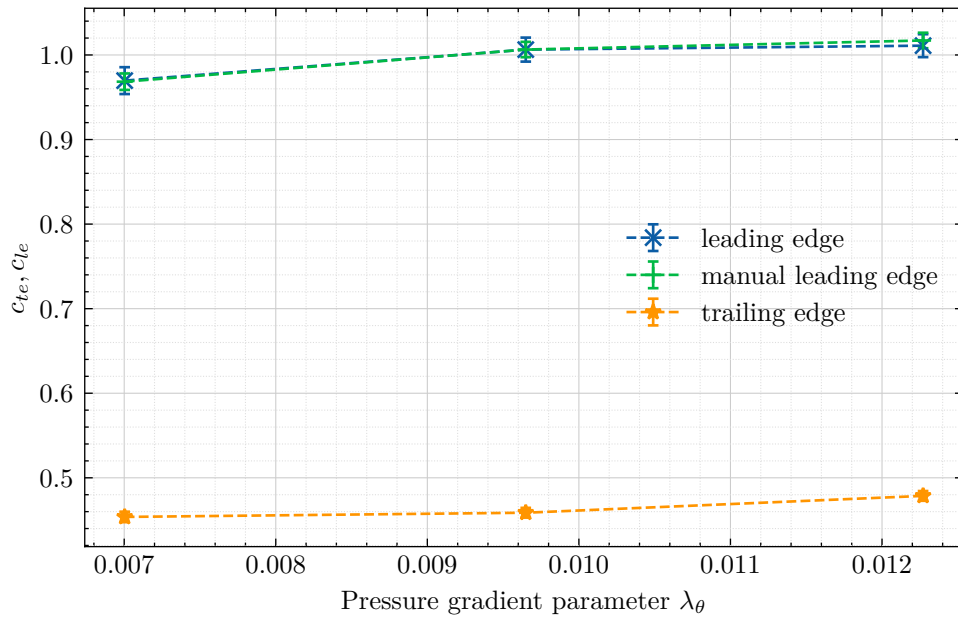


**Figure B.1.3:** Leading and trailing edge celerities for different pressure gradient parameters for  $Re_c = 6 \cdot 10^6$  and  $M = 0.6$ .

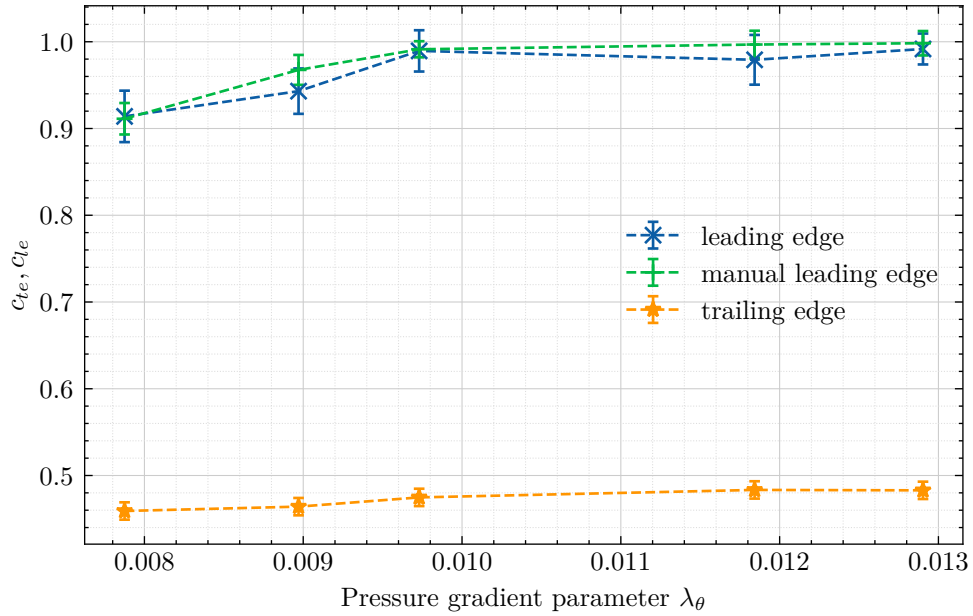


**Figure B.1.4:** Leading and trailing edge celerities for different pressure gradient parameters for  $Re_c = 6 \cdot 10^6$  and  $M = 0.7$ .

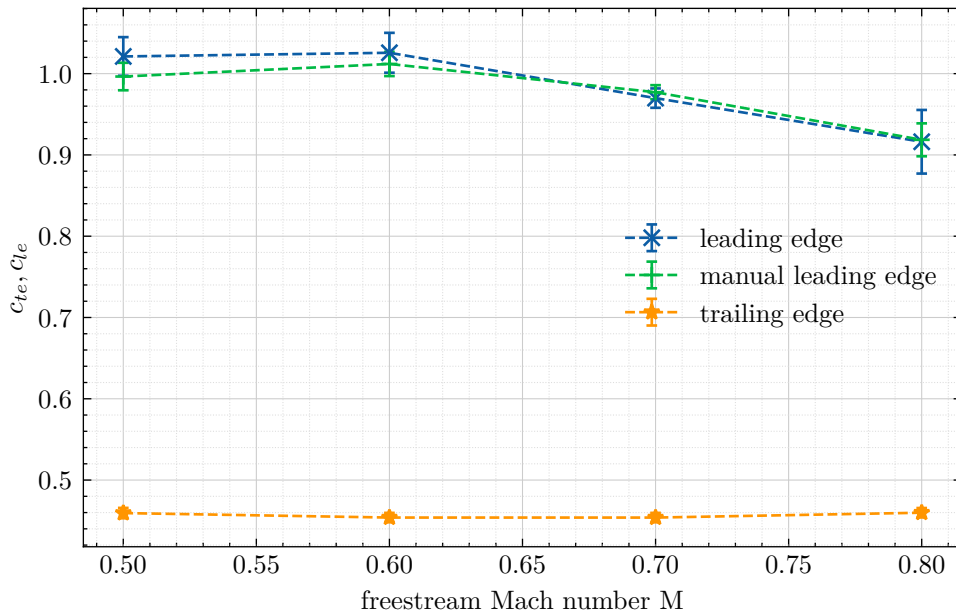


**Figure B.1.5:** Leading and trailing edge celerities for different Mach numbers for  $Re_c = 7.5 \cdot 10^6$  and  $\lambda_\theta = (11.1 - 14.5) \cdot 10^{-3}$ .

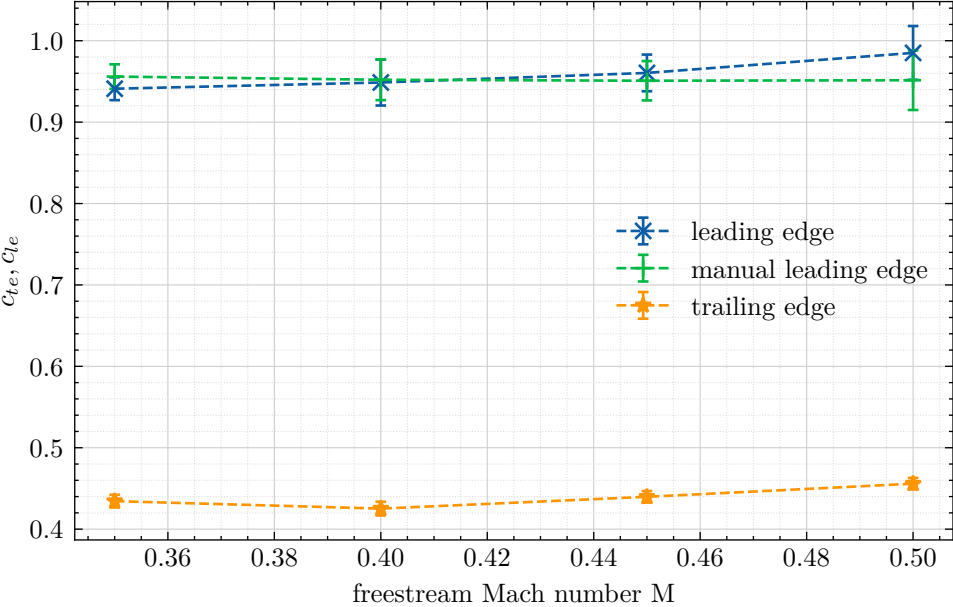


**Figure B.1.6:** Leading and trailing edge celerities for different Mach numbers for  $Re_c = 4.5 \cdot 10^6$  and  $\lambda_\theta = (0.5 - 1.0) \cdot 10^{-3}$ .

## B.2 Further remarks on the high Mach number cases

Figure 5.3.9 showed characteristic dark-light stripes, that are probably caused by an aero-optical effect of pressure waves travelling upstream. Based on the observed distance travelled by the prominent stripe in (e)-(h), the speed is about 80 m/s.

Figure B.2.1 shows the  $k - f$  wavenumber-frequency-diagram for the flow conditions (at  $M = 0.8$ ) presented in figure 5.3.9, but with a camera acquisition frequency of 40 kHz. In addition to the band of increased power spectrum density with positive wavenumbers, corresponding to downstream travelling fluctuations and also observed for the other cases presented in section 5.4.2, a further dominant band with negative wavenumbers can be seen. This corresponds to upstream travelling fluctuations and is probably caused by the same phenomenon that causes the dark-light stripes in figure 5.3.9. The phase velocity, based on equation 5.4.2, is about 80 m/s to 85 m/s. Both determined speeds agree reasonably well with difference in speed of sound to boundary layer edge velocity which equates to about 75 m/s in this case. This is the expected velocity of upstream travelling pressure fluctuations in wind tunnel coordinates. It is not clear what causes these pressure waves and if they are in or close to the boundary layer or further away from the model (in the freestream). The latter case would explain why the apparent measured velocities are slightly higher: the projected line of sight from camera to the model surface causes aero-optical effects in the line of sight to apparently travel more distance in the same time and therefore seem faster.

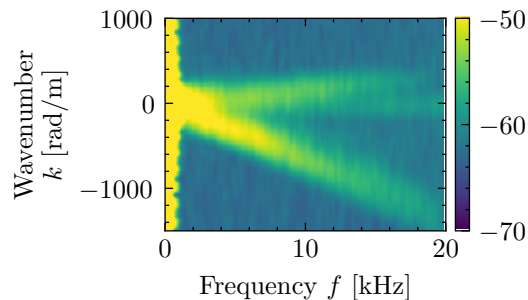


**Figure B.2.1:** Power spectrum  $k - f$ -diagram obtained from iTSP results. Intensity values are in dB scale. Flow conditions are  $Re_c = 8 \cdot 10^6$ ,  $M = 0.8$ , and  $\lambda_\theta = 19.4 \cdot 10^{-3}$ .



# Nomenclature

## Abbreviations

AoA	Angle of Attack
CAS	Chemical Abstract Service
CCD	Charge-Coupled Device
CMOS	Complementary Metal-Oxide-Semiconductor
CTA	Constant Temperature Anemometer
DLR	Deutsches Zentrum für Luft- und Raumfahrt e.V. (German Aerospace Center)
DNS	Direct Numerical Simulation
DPN	Data Point Number
FFT	Fast Fourier Transform
IR	Intensity Ratio
KRG	Cryogenic Ludwig-Tube Göttingen
LED	Light-Emitting Diode
LST	Linear Stability Theory
MHFS	Multiple Hot-Film Sensor array
NASP	National Aero-Space Plane
OR	Overheat Ratio
PaLASTra	flat Plate for the Analysis of the effect on LAmInar-turbulent transition of Surface imperfections, wall Temperature ratio and pressure gRADient
PIV	Particle Image Velocimetry
PSD	Power Spectral Density
PSP	Pressure-Sensitive Paint
RMS	Root Mean Square
Ru(phen)	Dichlorotris (1,10-phenanthroline) ruthenium (II) hydrate (98%)
STB	Shake-The-Box: Lagrangian particle tracking
T-S	Tollmien-Schlichting

## NOMENCLATURE

---

TLC	Thermochromic Liquid Crystals
ToPas	Three-dimensional Optical Pressure Analysis System
TSP/iTSP	(instationary) Temperature-Sensitive Paint

### Greek letters

$\alpha$	(half-)spreading angle of a turbulent spot or wedge [°], streamwise wavenumber [m <sup>-1</sup> ]
$\beta$	(half-)opening angle (apex angle) of a turbulent spot [°]
$\Delta$	difference
$\delta$	boundary layer thickness [m]
$\eta$	dimensionless distance to the location of transition onset $(x - x_s)/(x_e - x_s)$
$\gamma$	intermittency factor
$\kappa$	$\alpha_{max} \frac{\Delta t}{\Delta z^2}$
$\lambda_\theta$	pressure gradient parameter $\frac{\theta^2}{\nu} \frac{dU_e}{dx}$
$\mu$	dynamic viscosity [Pa · s]
$\Psi$	stream function [m <sup>2</sup> /s]
$\rho$	density [kg/m <sup>3</sup> ]
$\sigma$	spot propagation parameter
$\sigma_T$	standard deviation of surface temperature time signal
$\tau_q$	quasi wall shear stress
$\Theta$	transformation angle
$\varphi$	amplitude function of primary mode
$\xi$	dimensionless streamwise coordinate $\frac{x-x_t}{x_{75}-x_{25}}$

### Latin letters

$\dot{q}$	heat flux
$\dot{q}_w$	heat flux at the surface
$A$	amplitude
$b$	wing span [m]
$c$	chord length [m], specific heat capacity [J/(kg · K)]
$c_p$	pressure coefficient
$c_{te}$	leading edge celerity of turbulent spots normalised with boundary layer edge velocity $U_e$

$c_{OHR}$	celerity of the overhang region of turbulent spots normalised with boundary layer edge velocity $U_e$
$c_{te}$	trailing edge celerity of turbulent spots normalised with boundary layer edge velocity $U_e$
$E_{nr}$	activation energy for the non-radiating process
$f$	frequency [Hz]
$g$	spot production function
$I$	luminescent intensity
$k$	thermal conductivity [W/(m · K)]
$M$	freestream Mach number
$M_e$	Mach number at the boundary layer edge based on the local velocity
$N$	amplification factor
$P$	position at $x, y$ on the model surface
$p$	pressure [Pa]
$P_{el}$	electrical power
$R$	dependence volume (spot sweep volume), universal gas constant [J/(K · mol)]
$R_0$	resistance of hot-films at ambient temperature ( $T_c$ )
$R_s$	operating resistance of hot-films
$Re_c$	Reynolds number based on chord length, freestream velocity, and freestream kinematic viscosity
$Re_x$	Reynolds number based on streamwise location, freestream velocity, and freestream kinematic viscosity
$Re_\delta$	displacement thickness Reynolds number based on boundary layer displacement thickness, flow velocity and fluid kinematic viscosity at the boundary layer edge
$Re_\theta$	momentum thickness Reynolds number based on boundary layer momentum thickness, flow velocity and fluid kinematic viscosity at the boundary layer edge
$Re_{ind}$	indifference Reynolds number - minimum Reynolds number below which instability does not arise
$Re_{k,k}$	roughness Reynolds number based on the height of roughness $k$ and conditions at $k$ with an otherwise undisturbed laminar boundary layer
$S$	relative temperature sensitivity [%/K]
$s$	transformation scaling parameter
$T$	temperature [K]
$t$	time [s]
$T^*$	non-dimensional temperature $\frac{T - \overline{T_{lam}}}{\overline{T_{tur}} - \overline{T_{lam}}}$
$t_x, t_y$	transformation translation parameters in $x$ - and $y$ -direction

## NOMENCLATURE

---

$t_{le}$	passage time of the leading edge
$t_{te}$	passage time of the trailing edge
$Tu$	turbulence level
$U$	velocity in $x$ -direction [m/s]
$x$	chordwise coordinate, positive starting from the model leading edge to the model trailing edge [m]
$x_{25}$	streamwise location with intermittency $\gamma = 0.25$ [m]
$x_{75}$	streamwise location with intermittency $\gamma = 0.75$ [m]
$x_e$	locations of the end of the transition region [m]
$x_s$	locations of the start of the transition region [m]
$y$	spanwise coordinate, positive starting from the model port side to the model starboard side [m]
$z$	wall-normal coordinate, positive away from the wall [m]
$R_a$	average roughness [m]
$R_z$	mean peak-to-trough roughness [m]

## Subscripts

0	initial
$\infty$	freestream
$aw$	adiabatic wall
$c$	charge, calculated
$e$	boundary layer edge
$eval$	evaluation window
$FT$	fully turbulent
$I$	intermittent
$ind$	indifferent stability
$lam$	laminar
$ref$	reference
$t$	transition
$tur$	turbulent
$w$	wall
$x$	streamwise location

# Bibliography

- [1] Abu-Ghannam, B. J. and Shaw, R.: Natural transition of boundary layers—the effects of turbulence, pressure gradient, and flow history. *Journal of Mechanical Engineering Science* Vol. 22, 1980, pp. 213–228 (cit. on pp. 4, 19).
- [2] Amecke, J.: Direkte Berechnung von Wandinterferenzen und Wandadaptation bei zweidimensionaler Strömung in Windkanälen mit geschlossenen Wänden. DFVLR Institut für Experimentelle Strömungsmechanik, 1985 (cit. on p. 22).
- [3] Antonia, R. A., Chambers, A. J., Sokolov, M., and van Atta, C. W.: Simultaneous temperature and velocity measurements in the plane of symmetry of a transitional turbulent spot. *Journal of Fluid Mechanics* Vol. 108, 1981, pp. 317–343 (cit. on pp. 11, 78).
- [4] Ashill, P., Betts, C., and Gaudet, I.: A wind tunnel study of transition flows on a swept panel wing at high subsonic speeds. CEAS 2nd European forum on laminar flow technology. Vol. 10. 1996, pp. 1–17 (cit. on p. 95).
- [5] Bandyopadhyay, P. R.: Turbulence spot-like features of a boundary layer. *Annals of the New York Academy of Sciences* Vol. 404, 1983, pp. 393–395 (cit. on p. 11).
- [6] Beck, N., Landa, T., Seitz, A., Boermans, L., Liu, Y., and Radespiel, R.: Drag reduction by laminar flow control. *Energies* Vol. 11, 2018, p. 252 (cit. on p. 2).
- [7] Bellhouse, B. J. and Schultz, D. L.: Determination of mean and dynamic skin friction, separation and transition in low-speed flow with a thin-film heated element. *Journal of Fluid Mechanics* Vol. 24, 1966, pp. 379–400 (cit. on p. 63).
- [8] Bergero, C., Gosnell, G., Gielen, D., Kang, S., Bazilian, M., and Davis, S. J.: Pathways to net-zero emissions from aviation. *Nature Sustainability* Vol. 6, 2023, pp. 404–414 (cit. on p. 2).
- [9] Bergman, T. L., Lavine, A. S., Incropera, F. P., and Dewitt, D. P.: Fundamentals of Heat and Mass Transfer. Vol. 7. John Wiley & Sons, 2011 (cit. on p. 48).
- [10] Bertin, J. J. and Cummings, R. M.: Critical hypersonic aerothermodynamic phenomena. *Annual Review of Fluid Mechanics* Vol. 38, No. 1, 2006, pp. 129–157 (cit. on pp. 1, 2).
- [11] Bitter, M., Hilfer, M., Schubert, T., Klein, C., and Niehuis, R.: An ultra-fast TSP on a CNT heating layer for unsteady temperature and heat flux measurements in subsonic flows. *Sensors* Vol. 22, No. 2, 2022 (cit. on p. 29).
- [12] Braddom, S. R.: Design and characterization of robust hot film sensors for tactical aircraft inlets. Master’s thesis. Massachusetts Institute of Technology, 2002 (cit. on p. 125).

- [13] Braslow, A. L.: A history of suction-type laminar-flow control with emphasis on flight research. Monographs in Aerospace History No. 13, 1999 (cit. on p. 1).
- [14] Braune, M. and Koch, S.: Application of hot-film anemometry to resolve the unsteady boundary layer transition of a laminar airfoil experiencing limit cycle oscillations. *Experiments in Fluids* Vol. 61, No. 2, 2020, p. 68 (cit. on p. 125).
- [15] Brinkerhoff, J. R. and Yaras, M. I.: Numerical investigation of the generation and growth of coherent flow structures in a triggered turbulent spot. *Journal of Fluid Mechanics* Vol. 759, 2014, pp. 257–294 (cit. on p. 13).
- [16] Bushnell, D. M. and Tuttle, M. H.: Survey and bibliography on attainment of laminar flow control in air using pressure gradient and suction, Volume 1. *NASA RP 1035*, 1979 (cit. on p. 1).
- [17] Cantwell, B., Coles, D., and Dimotakis, P.: Structure and entrainment in the plane of symmetry of a turbulent spot. *Journal of Fluid Mechanics* Vol. 87, 1978, pp. 641–672 (cit. on pp. 2, 12, 77, 81).
- [18] Chaiworapuek, W. and Kittichaikarn, C.: Multi-plane visualization of an artificially initiated young turbulent spot using liquid crystals. *Experimental Thermal and Fluid Science* Vol. 77, 2016, pp. 179–187 (cit. on pp. 12, 15).
- [19] Chaiworapuek, W. and Kittichaikarn, C.: On the thermal and structural characteristics of an artificially generated young turbulent spot. *International Journal of Heat and Mass Transfer* Vol. 92, 2016, pp. 850–858 (cit. on pp. 15, 52, 61, 62).
- [20] Chaiworapuek, W., Nongnoi, S., and Kittichaikarn, C.: Visualization of thermal structure of turbulent spot under adverse pressure gradients using liquid crystals. *Agriculture and Natural Resources* Vol. 48, 2014, pp. 823–835 (cit. on pp. 3, 16, 79).
- [21] Chen, K. K. and Thyson, N. A.: Extension of Emmons’ spot theory to flows on blunt bodies. *AIAA Journal* Vol. 9, No. 5, 1971, pp. 821–825 (cit. on pp. 3, 4, 99).
- [22] Ching, C. Y. and LaGraff, J. E.: Measurement of turbulent spot convection rates in a transitional boundary layer. *Experimental Thermal and Fluid Science* Vol. 11, 1995, pp. 52–60 (cit. on pp. 17, 52, 80).
- [23] Chong, T. P. and Zhong, S.: On the three-dimensional structure of turbulent spots. *Journal of Turbomachinery* Vol. 127, 2005, pp. 545–551 (cit. on pp. 3, 12, 79, 81).
- [24] Chong, T. P. and Zhong, S.: On the momentum and thermal structures of turbulent spots in a favorable pressure gradient. *Journal of Turbomachinery* Vol. 128, No. 4, 2006 (cit. on pp. 11, 52).
- [25] Clark, J. P., Jones, T. V., and LaGraff, J. E.: On the propagation of naturally-occurring turbulent spots. *Journal of Engineering Mathematics* Vol. 28, 1994, pp. 1–19 (cit. on pp. 1, 4, 17, 28, 52, 79, 91).
- [26] Clark, J. P., Magari, P., Jones, T. V., and Lagraff, J. E.: Experimental studies of turbulent spot parameters using thin-film heat-transfer gauges. 31st Aerospace Sciences Meeting & Exhibit. 544. 1993 (cit. on pp. 3, 13, 52, 79, 81, 86, 91).
- [27] Clark, J. P., Magari, P. J., and Jones, T. V.: On the distribution of the heat transfer coefficient in turbulent and “transitional” wedges. *International Journal of Heat and Fluid Flow* Vol. 14, 1993, pp. 217–222 (cit. on pp. 9, 10, 103).
- [28] Clark, J. P.: A study of turbulent-spot propagation in turbine-representative flows. PhD thesis. St. Catherine’s College Oxford, 1993 (cit. on p. 87).

- 
- [29] Coles, D. and Barker, S. J.: Some Remarks on a Synthetic Turbulent Boundary Layer. *Turbulent Mixing in Nonreactive and Reactive Flows*. Boston, MA: Springer New York, 1975, pp. 285–293 (cit. on pp. 9, 10).
- [30] Costantini, M.: Experimental analysis of geometric, pressure gradient and surface temperature effects on boundary-layer transition in compressible high Reynolds number flows. PhD thesis. RWTH Aachen, 2016 (cit. on pp. 22, 25, 27, 33, 47, 48, 102).
- [31] Costantini, M., Fuchs, C., Henne, U., Klein, C., Ondrus, V., Bruse, M., Löhr, M., and Jacobs, M.: Experimental analysis of the performance of a wind-turbine airfoil using temperature-sensitive paint. *AIAA Journal* Vol. 59, No. 11, 2021, pp. 4449–4464 (cit. on p. 5).
- [32] Costantini, M., Hein, S., Henne, U., Klein, C., Koch, S., Schojda, L., Ondrus, V., and Schröder, W.: Pressure gradient and nonadiabatic surface effects on boundary layer transition. *AIAA Journal* Vol. 54, No. 11, 2016, pp. 3465–3480 (cit. on pp. 1, 48, 96).
- [33] Costantini, M., Henne, U., Risius, S., and Klein, C.: A robust method for reliable transition detection in temperature-sensitive paint data. *Aerospace Science and Technology* Vol. 113, 2021, p. 106702 (cit. on pp. 4, 5, 96).
- [34] Costantini, M., Risius, S., and Klein, C.: Experimental investigation of the effect of forward-facing steps on boundary layer transition. *Procedia IUTAM* Vol. 14, 2015, pp. 152–162 (cit. on pp. 9, 96).
- [35] Costantini, M., Risius, S., and Klein, C.: Step-induced transition in compressible high Reynolds number flow. *Flow* Vol. 2, 2022, E33 (cit. on pp. 25, 26).
- [36] Costantini, M., Risius, S., Klein, C., and Kühn, W.: Effect of forward-facing steps on boundary layer transition at a subsonic Mach number. *New Results in Numerical and Experimental Fluid Mechanics X: Contributions to the 19th STAB/DGLR Symposium Munich, Germany, 2014*. Springer. 2016, pp. 203–213 (cit. on p. 1).
- [37] Craik, A. D. D.: Non-linear resonant instability in boundary layers. *Journal of Fluid Mechanics* Vol. 50, 1971, pp. 393–413 (cit. on p. 8).
- [38] D’Ovidio, A., Harkins, J. A., and Gostelow, J. P.: Turbulent spots in strong adverse pressure gradients: Part 2—spot propagation and spreading rates. *Turbo Expo: Power for Land, Sea, and Air*. Vol. 78521. Citeseer. 2001, V003T01A085 (cit. on pp. 16, 47).
- [39] Dhawan, S. and Narasimha, R.: Some properties of boundary layer flow during the transition from laminar to turbulent motion. *Journal of Fluid Mechanics* Vol. 3, 1958, pp. 418–436 (cit. on pp. 18, 19, 93, 99).
- [40] Dimond, B.: Experimental investigation of the delay of step-induced transition by means of suction. Master’s thesis. Georg-August Universität Göttingen, 2018 (cit. on pp. 22, 25).
- [41] Dimond, B., Costantini, M., and Klein, C.: Experimental analysis of the effect of suction and step height on boundary-layer transition. *IUTAM Laminar-Turbulent Transition: 9th IUTAM Symposium, London, UK, September 2–6, 2019*. Springer. 2022, pp. 171–180 (cit. on pp. 5, 25, 47).
- [42] Dimond, B., Costantini, M., Koch, S., and Klein, C.: Combination of a time-and space-resolved measurement technique for laminar-turbulent transition detection. *20th Onera-DLR Aerospace Symposium ODAS*. 2020 (cit. on pp. 22, 110).

- [43] Dimond, B., Costantini, M., Risius, S., Fuchs, C., and Klein, C.: Experimental analysis of suction on step-induced boundary-layer transition. *Experimental Thermal and Fluid Science* Vol. 109, 2019, p. 109842 (cit. on pp. 5, 25, 47).
- [44] Doorley, D. J. and Smith, F. T.: Initial-value problems for spot disturbances in incompressible or compressible boundary layers. *Journal of Engineering Mathematics* Vol. 26, 1992, pp. 87–106 (cit. on p. 81).
- [45] Effects of novel coronavirus (COVID-19) on civil aviation: economic impact analysis. Economic Development of Air Transport Air Transport Bureau International Civil Aviation Organization (ICAO). 2023 (cit. on p. 2).
- [46] Egami, Y., Fey, U., Klein, C., Quest, J., Ondrus, V., and Beifuss, U.: Development of new two-component temperature-sensitive paint (tsp) for cryogenic testing. *Measurement Science and Technology* Vol. 23, 2012, p. 115301 (cit. on p. 30).
- [47] Egorov, I. V., Novikov, A. V., and Chuvakhov, P. V.: Numerical simulation of the evolution of turbulent spots in a supersonic boundary layer over a plate. *Mathematical Models and Computer Simulations* Vol. 15, 2023, pp. 118–124 (cit. on p. 77).
- [48] Elder, J. W.: An experimental investigation of turbulent spots and breakdown to turbulence. *Journal of Fluid Mechanics* Vol. 9, 1960, pp. 235–246 (cit. on pp. 8, 10, 11).
- [49] Emmons, H. W.: The laminar-turbulent transition in a boundary layer - Part I. *Journal of the Aeronautical Sciences* Vol. 18, 1951, pp. 490–498 (cit. on pp. 1, 4, 10, 18).
- [50] Fey, U., Egami, Y., and Engler, R.: High Reynolds number transition detection by means of temperature sensitive paint. 44th AIAA Aerospace Sciences Meeting and Exhibit. 2006 (cit. on pp. 23, 50).
- [51] Fiala, A., Hillier, R., and Estruch-Samper, D.: Roughness-induced turbulent wedges in a hypersonic blunt-body boundary layer. *Journal of Fluid Mechanics* Vol. 754, 2014, pp. 208–231 (cit. on pp. 10, 13, 103, 104, 108, 121).
- [52] Fiala, A., Hillier, R., Mallinson, S. G., and Wijesinghe, H. S.: Heat transfer measurement of turbulent spots in a hypersonic blunt-body boundary layer. *Journal of Fluid Mechanics* Vol. 555, 2006, pp. 81–111 (cit. on pp. 3, 14, 17, 51, 52, 79).
- [53] Fischer, M. C.: Spreading of a turbulent disturbance. *AIAA Journal* Vol. 10, No. 7, 1972, pp. 957–959 (cit. on pp. 4, 9, 28).
- [54] Fransson, J. H. M., Matsubara, M., and Alfredsson, P. H.: Transition induced by free-stream turbulence. *Journal of Fluid Mechanics* Vol. 527, 2005, pp. 1–25 (cit. on p. 19).
- [55] Fransson, J. H.: Turbulent spot evolution in spatially invariant boundary layers. *Physical Review E* Vol. 81, 2010, p. 035301 (cit. on pp. 16, 18).
- [56] Gad-El-Hak, M., Blackwelder, R. F., and Riley, J. J.: On the growth of turbulent regions in laminar boundary layers. *Journal of Fluid Mechanics* Vol. 110, 1981, pp. 73–95 (cit. on pp. 9–14, 16, 17, 78, 79, 81).
- [57] Glezer, A., Katz, Y., and Wygnanski, I.: On the breakdown of the wave packet trailing a turbulent spot in a laminar boundary layer. *Journal of Fluid Mechanics* Vol. 198, 1989, pp. 1–26 (cit. on p. 78).

- 
- [58] Goldstein, D., Chu, J., and Brown, G.: Lateral spreading mechanism of a turbulent spot and a turbulent wedge. *Flow, Turbulence and Combustion* Vol. 98, 2017, pp. 21–35 (cit. on pp. 4, 13, 103).
- [59] Gostelow, J. P. and Blunden, A. R.: Investigations of boundary layer transition in an adverse pressure gradient. *Journal of Turbomachinery* Vol. 111, No. 4, 1989, pp. 366–374 (cit. on p. 18).
- [60] Gostelow, J. P., Hong, G., Melwani, N., and Walker, G. J.: Turbulent spot development under a moderate adverse pressure gradient. Volume 3C: General. American Society of Mechanical Engineers, 1993 (cit. on pp. 12, 16).
- [61] Gostelow, J. P., Melwani, N., and Walker, G. J.: Effects of streamwise pressure gradient on turbulent spot development. *Journal of Turbomachinery* Vol. 118, 1996, pp. 737–743 (cit. on pp. 3, 16, 19, 52, 88, 92).
- [62] Gutmark, E. and Blackwelder, R. F.: On the structure of a turbulent spot in a heated laminar boundary layer. *Experiments in Fluids* Vol. 5, 1987, pp. 217–229 (cit. on pp. 3, 4, 9, 11, 16, 47, 52, 59, 77, 78, 81, 82, 88, 89, 92).
- [63] Harris, C. R. et al.: Array programming with NumPy. *Nature* Vol. 585, No. 7825, 2020, pp. 357–362 (cit. on p. 39).
- [64] Hein, S.: Nonlinear Nonlocal Transition Analysis. PhD thesis. DLR-Forschungsbericht, 2005 (cit. on p. 48).
- [65] Herbert, T.: Secondary instability of boundary layers. *Annual Review of Fluid Mechanics* Vol. 20, 1988, pp. 487–526 (cit. on pp. 8, 9).
- [66] Hodson, H. P., Huntsman, I., and Steele, A. B.: An investigation of boundary layer development in a multistage LP turbine. *Journal of Turbomachinery*, 1994 (cit. on p. 63).
- [67] Hogendoorn, C. J., de Lange, H. C., and van Steenhoven, A. A.: Design optimization for fast heat-transfer gauges. *Measurement Science and Technology* Vol. 9, 1998, pp. 428–434 (cit. on pp. 69, 83).
- [68] Hogendoorn, C. J.: Heat transfer measurements in subsonic transitional boundary layers. PhD thesis. Technische Universiteit Eindhoven, 1997 (cit. on pp. 52, 61, 80).
- [69] Hogendoorn, C. J., de Lange, H. C., and van Steenhoven, A. A.: Heat transfer measurements in transitional boundary layers. English. 2nd European thermal-sciences and 14th national heat transfer conference, 1996 : proceedings, Rome, Italy, 29-31 May, 1996. vol. 1. Edizioni ETS, 1996, pp. 593–600 (cit. on p. 61).
- [70] Hultmark, M. and Smits, A. J.: Temperature corrections for constant temperature and constant current hot-wire anemometers. *Measurement Science and Technology* Vol. 21, No. 10, 2010, p. 105404 (cit. on pp. 64, 124, 125).
- [71] IATA: Industry Statistics: Fact Sheet. 2023 (cit. on p. 2).
- [72] Jacobs, R. G. and Durbin, P. A.: Simulations of bypass transition. *Journal of Fluid Mechanics* Vol. 428, 2001, pp. 185–212 (cit. on p. 14).
- [73] James, C. S.: Observations of turbulent-burst geometry and growth in supersonic flow. Tech. rep. National Aeronautics and Space Administration Washington DC, 1958 (cit. on pp. 14, 17, 80).
- [74] Jewell, J. S., Leyva, I. A., and Shepherd, J. E.: Turbulent spots in hypervelocity flow. *Experiments in Fluids* Vol. 58, 2017, pp. 1–14 (cit. on pp. 15, 19, 61, 77).

- [75] Jewell, J. S., Parziale, N., Leyva, I., and Shepherd, J.: Turbulent spot observations within a hypervelocity boundary layer on a 5-degree half-angle cone. *Journal of Fluid Mechanics*, 2012 (cit. on pp. 3, 28).
- [76] Jocksch, A. and Kleiser, L.: Growth of turbulent spots in high-speed boundary layers on a flat plate. *International Journal of Heat and Fluid Flow* Vol. 29, 2008, pp. 1543–1557 (cit. on pp. 16, 88, 92).
- [77] Johnson, M. W.: Prediction of turbulent spot growth rates. Volume 3: Heat Transfer; Electric Power; Industrial and Cogeneration. American Society of Mechanical Engineers, 1999 (cit. on pp. 16, 17, 47, 79, 80, 87).
- [78] Johnson, M. W. and Fashifar, A.: Statistical properties of turbulent bursts in transitional boundary layers. *International Journal of Heat and Fluid Flow* Vol. 15, 1994, pp. 283–290 (cit. on pp. 19, 93, 98).
- [79] Joslin, R. D.: Overview of laminar flow control. Tech. rep. Langley Research Center, Hampton, Virginia, 1998 (cit. on pp. 1, 2).
- [80] Karsch, M., Van den Eynde, J., and Steelant, J.: Linearly combined transition model based on empirical spot growth correlations. *CEAS Space Journal*, 2023, pp. 1–12 (cit. on pp. 3, 4, 87, 117).
- [81] Katz, Y., Seifert, A., and Wygnanski, I.: On the evolution of the turbulent spot in a laminar boundary layer with a favourable pressure gradient. *Journal of Fluid Mechanics* Vol. 221, 1990, pp. 1–22 (cit. on pp. 3, 16).
- [82] Klebanoff, P. S., Tidstrom, K. D., and Sargent, L. M.: The three-dimensional nature of boundary-layer instability. *Journal of Fluid Mechanics* Vol. 12, 1962, pp. 1–34 (cit. on p. 8).
- [83] Klein, C., Engler, R., Henne, U., and Sachs, W.: Application of pressure-sensitive paint for determination of the pressure field and calculation of the forces and moments of models in a wind tunnel. *Experiments in Fluids* Vol. 39, 2005, pp. 475–483 (cit. on p. 44).
- [84] Klein, C., Henne, U., Sachs, W., Beifuss, U., Ondrus, V., Bruse, M., Lesjak, R., Löhr, M., Becher, A., and Zhai, J.: Combination of temperature sensitive paint and carbon nanotubes for transition detection. 53rd AIAA Aerospace Sciences Meeting. 2015, p. 1558 (cit. on p. 23).
- [85] Kline, S. J., Reynolds, W. C., Schraub, F. A., and Runstadler, P. W.: The structure of turbulent boundary layers. *Journal of Fluid Mechanics* Vol. 30, 1967, pp. 741–773 (cit. on p. 16).
- [86] Klothakis, A., Quintanilha Jr., H., Sawant, S. S., Protopapadakis, E., Theofilis, V., and Levin, D. A.: Linear stability analysis of hypersonic boundary layers computed by a kinetic approach: a semi-infinite flat plate at  $4.5 \leq M_\infty \leq 9$ . *Theoretical and Computational Fluid Dynamics* Vol. 36, No. 1, 2022, pp. 117–139 (cit. on p. 1).
- [87] Koch, S.: Zeitliche und räumliche Turbulenzentwicklung in einem Rohrwindkanal und deren Einfluss auf die Transition an Profilmodellen. PhD thesis. Institute of Aerodynamics and Flow Technology, DLR Goettingen, 2004 (cit. on pp. 21–23, 28, 63).
- [88] Krishnan, L. and Sandham, N. D.: Effect of Mach number on the structure of turbulent spots. *Journal of Fluid Mechanics* Vol. 566, 2006, pp. 225–234 (cit. on pp. 10–12, 17, 19, 69, 88, 92).

- 
- [89] Kubacki, S. and Dick, E.: An algebraic model for bypass transition in turbomachinery boundary layer flows. *International Journal of Heat and Fluid Flow* Vol. 58, 2016, pp. 68–83 (cit. on p. 1).
- [90] Laurence, S. J., Ozawa, H., Martinez Schramm, J., Butler, C. S., and Hannemann, K.: Heat-flux measurements on a hypersonic inlet ramp using fast-response temperature-sensitive paint. *Experiments in Fluids* Vol. 60, 2019, pp. 1–16 (cit. on pp. 48, 121, 125).
- [91] Lemarechal, J., Klein, C., Henne, U., Puckert, D. K., and Rist, U.: Spatially and temporally resolved visualization of turbulent spots in Blasius boundary layer transition. en. Proceedings 18th International Symposium on Flow Visualization. Zurich: ETH Zurich, 2018 (cit. on pp. 15, 62).
- [92] Levin, O. and Henningson, D. S.: Turbulent spots in the asymptotic suction boundary layer. *Journal of Fluid Mechanics* Vol. 584, 2007, pp. 397–413 (cit. on p. 18).
- [93] Lindberg, P.-A., Fahlgren, E. M., Alfredsson, P. H., and Johansson, A. V.: An experimental study of the structure and spreading of turbulent spots. *Laminar-Turbulent Transition*. Berlin, Heidelberg: Springer Berlin Heidelberg, 1984, pp. 617–624 (cit. on p. 78).
- [94] Liu, T., Sullivan, J. P., Asai, K., Klein, C., and Egami, Y.: Pressure and Temperature Sensitive Paints. 2nd ed. Experimental Fluid Mechanics. Springer, 2021 (cit. on pp. 5, 23, 24, 30).
- [95] Ludwig, H., Grauer-Carstensen, H., and Hottner, T.: Der Rohrwindkanal der Aerodynamischen Versuchsanstalt Göttingen. Deutsche Forschungs-und Versuchsanst. für Luft-und Raumfahrt, 1969 (cit. on p. 21).
- [96] Ludwig, H.: Der Rohrwindkanal. *Zeitschrift für Flugwissenschaften* Vol. 3, 1955, pp. 206–216 (cit. on p. 21).
- [97] Lunte, J. and Schuelein, E.: Heat transfer amplifications in transitional shock-wave/boundary-layer interactions. AIAA Aviation 2019 Forum. American Institute of Aeronautics and Astronautics, 2019 (cit. on p. 121).
- [98] Mack, L. M.: Boundary-layer linear stability theory. *Agard report* Vol. 709, No. 3, 1984 (cit. on p. 8).
- [99] Martinez Schramm, J. and Hilfer, M.: Time response calibration of ultra-fast temperature sensitive paints for the application in high temperature hypersonic flows. New Results in Numerical and Experimental Fluid Mechanics XII: Contributions to the 21st STAB/DGLR Symposium, Darmstadt, Germany, 2018. Springer. 2020, pp. 143–152 (cit. on p. 29).
- [100] Mautner, T. S. and Van Atta, C. W.: Wall shear stress measurements in the plane of symmetry of a turbulent spot. *Experiments in Fluids* Vol. 4, 1986, pp. 153–162 (cit. on p. 12).
- [101] Mayle, R. E. and Stripf, M.: “I-Spots” and Emmons’ spot production rate. *Journal of Turbomachinery* Vol. 143, 2021, p. 091019 (cit. on p. 69).
- [102] Mayle, R. E.: The 1991 IGTI scholar lecture: the role of laminar-turbulent transition in gas turbine engines. *Journal of Turbomachinery* Vol. 113, No. 4, 1991, pp. 509–536 (cit. on pp. 16, 19, 22, 79).
- [103] Mee, D. J. and Goyne, C. P.: Turbulent spots in boundary layers in a free-piston shock-tunnel flow. *Shock waves* Vol. 6, 1996, pp. 337–343 (cit. on pp. 14, 19).

## BIBLIOGRAPHY

---

- [104] Mee, D. J. and Tanguy, G.: Turbulent Spot Initiation Rates in Boundary Layers in a Shock Tunnel. 29th International Symposium on Shock Waves 1. Cham: Springer International Publishing, 2015, pp. 623–628 (cit. on p. 19).
- [105] Mee, D. J., Raghunath, S., and McGilvray, M.: Heat-transfer gauge arrays for identifying spot initiation in hypersonic transitional boundary layers. *Journal of Spacecraft and Rockets*, 2023, pp. 1–8 (cit. on p. 47).
- [106] Mee, D. J.: Boundary-layer transition measurements in hypervelocity flows in a shock tunnel. *AIAA Journal* Vol. 40, No. 8, 2002, pp. 1542–1548 (cit. on pp. 2, 14, 17, 79).
- [107] Mills, A.: Optical oxygen sensors utilising the luminescence of platinum metal complexes. *Platinum Metals Rev.* Vol. 41, 1997, pp. 115–127 (cit. on p. 29).
- [108] Miozzi, M., Capone, A., Costantini, M., Fratto, L., Klein, C., and Di Felice, F.: Skin friction and coherent structures within a laminar separation bubble. *Experiments in Fluids* Vol. 60, 2019, pp. 1–25 (cit. on pp. 47, 95).
- [109] Morkovin, M. V.: Bypass transition to turbulence and research desiderata. *NASA Lewis Research Center Transition in Turbines*, 1984 (cit. on p. 9).
- [110] Muhammad, C. and Chong, T. P.: Mitigation of turbulent noise sources by riblets. *Journal of Sound and Vibration* Vol. 541, 2022, p. 117302 (cit. on p. 16).
- [111] N. Vinod, R. G.: Pattern of breakdown of laminar flow into turbulent spots. *Physical Review Letters* Vol. 93, 2004, p. 114501 (cit. on p. 19).
- [112] Nagai, H., Ohmi, S., Asai, K., and Nakakita, K.: Effect of temperature-sensitive-paint thickness on global heat transfer measurement in hypersonic flow. *Journal of Thermophysics and Heat Transfer* Vol. 22, 2008, pp. 373–381 (cit. on p. 121).
- [113] Narasimha, R.: Recent advances in the dynamics of the transition zone. Proceedings of Tenth International Symposium on Air Breathing Engines, Nottingham, UK. Proceedings of Tenth International Symposium on Air Breathing Engines ... 1991, pp. 71–79 (cit. on p. 79).
- [114] Narasimha, R.: The laminar-turbulent transition zone in the boundary layer. *Progress in Aerospace Sciences* Vol. 22, 1985, pp. 29–80 (cit. on pp. 4, 13, 19, 93).
- [115] Narasimha, R.: Modelling the transitional boundary layer. Tech. rep. NASA, 1990 (cit. on pp. 19, 93).
- [116] Obremski, H. J., Morkovin, M. V., Landahl, M., Wazzan, A. R., Okamura, T. T., and Smith, A. M. O.: A portfolio of stability characteristics of incompressible boundary layers. North Atlantic Treaty Organization, Advisory Group for Aerospace Research and Development, 1969 (cit. on p. 9).
- [117] Ondrus, V., Meier, R. J., Klein, C., Henne, U., Schäferling, M., and Beifuss, U.: Europium 1,3-di(thienyl)propane-1,3-diones with outstanding properties for temperature sensing. *Sensors and Actuators A: Physical* Vol. 233, 2015, pp. 434–441 (cit. on p. 29).
- [118] Otsu, N.: A threshold selection method from gray-level histograms. *IEEE transactions on systems, man, and cybernetics* Vol. 9, 1979, pp. 62–66 (cit. on p. 62).
- [119] Owen, F. K.: Transition experiments on a flat plate at subsonic and supersonic speeds. *AIAA Journal* Vol. 8, No. 3, 1970, pp. 518–523 (cit. on p. 19).

- [120] Ozawa, H. and Laurence, S. J.: Experimental investigation of the shock-induced flow over a wall-mounted cylinder. *Journal of Fluid Mechanics* Vol. 849, 2018, pp. 1009–1042 (cit. on p. 29).
- [121] Ozawa, H.: Experimental study of unsteady aerothermodynamic phenomena on shock-tube wall using fast-response temperature-sensitive paints. *Physics of Fluids* Vol. 28, 2016 (cit. on p. 48).
- [122] Ozawa, H., Laurence, S. J., Martinez Schramm, J., Wagner, A., and Hannemann, K.: Fast-response temperature-sensitive-paint measurements on a hypersonic transition cone. *Experiments in Fluids* Vol. 56, 2015, p. 1853 (cit. on pp. 5, 48, 50, 51, 121).
- [123] Pandey, A., Casper, K. M., Flood, J. T., Bhakta, R., Spillers, R., and Beresh, S. J.: Tracking turbulent spots on a hypersonic cone at angle of attack using temperature-sensitive paint. AIAA Aviation 2021 Forum. 2021, p. 2889 (cit. on pp. 15, 52).
- [124] Perry, A. E., Lim, T. T., and Teh, E. W.: A visual study of turbulent spots. *Journal of Fluid Mechanics* Vol. 104, 1981, pp. 387–405 (cit. on pp. 11, 13).
- [125] Petersen, A. and Hilfer, M.: Boundary Layer Analysis of a Transonic High-Pressure Turbine Vane Using Ultra-Fast-Response Temperature-Sensitive Paint. Turbo Expo: Power for Land, Sea, and Air. Vol. 87110. American Society of Mechanical Engineers. 2023, V13DT36A007 (cit. on p. 29).
- [126] Prandtl, L.: Über Flüssigkeitsbewegung bei sehr kleiner Reibung. *Verhandlungen des III. Internationalen Mathematiker-Kongresses Heidelberg, Leipzig*, 1905 (cit. on p. 1).
- [127] Raghunath, S., Khoo, B. C., and Mee, D. J.: Characteristics of turbulent spots in a hypersonic transitional boundary layer inferred from dense arrays of thin-film heat transfer gauges. 32nd International Symposium on Shock Waves. 2019 (cit. on p. 15).
- [128] Raghunath, S., Mee, D., and Narasimha, R.: Estimating turbulent spot initiation rates from transition lengths in hypersonic boundary layers. *AIAA Journal* Vol. 55, No. 11, 2017, pp. 3640–3647 (cit. on pp. 2, 19).
- [129] Rakpakdee, W., Kittichaikarn, C., and Chaiworapuek, W.: Effect of boundary layer destabilization by a water jet on thermal and structural behavior of turbulent spot footprints. *International Journal of Heat and Mass Transfer* Vol. 135, 2019, pp. 491–510 (cit. on pp. 15, 52, 61).
- [130] Redford, J. A., Sandham, N. D., and Roberts, G. T.: Numerical simulations of turbulent spots in supersonic boundary layers: effects of Mach number and wall temperature. *Progress in Aerospace Sciences* Vol. 52, 2012, pp. 67–79 (cit. on pp. 16, 17, 69, 79).
- [131] Reed, H. L. and Saric, W. S.: Receptivity: the inspiration of Mark Morkovin. 45th AIAA Fluid Dynamics Conference. 2015, p. 2471 (cit. on p. 9).
- [132] Reynolds, O.: An experimental investigation of the circumstances which determine whether the motion of water shall be direct or sinuous, and of the law of resistance in parallel channels. *Philosophical Transactions of the Royal Society of London*, 1883, pp. 935–982 (cit. on p. 1).
- [133] Riley, J. J. and Gad-el-Hak, M.: The dynamics of turbulent spots. *Frontiers in Fluid Mechanics*. Berlin, Heidelberg: Springer Berlin Heidelberg, 1985, pp. 123–155 (cit. on p. 81).

- [134] Risius, S.: Development of a time-resolved quantitative surface-temperature measurement technique and its application in short-duration wind tunnel testing. PhD thesis. Georg-August-Universität Göttingen, 2018 (cit. on p. 36).
- [135] Risius, S., Beck, W. H., Klein, C., Henne, U., and Wagner, A.: Determination of heat transfer into a wedge model in a hypersonic flow using temperature-sensitive paint. *Experiments in Fluids* Vol. 58, 2017, pp. 1–13 (cit. on pp. 48, 50, 51, 121).
- [136] Risius, S., Costantini, M., Hein, S., Koch, S., and Klein, C.: Experimental investigation of Mach number and pressure gradient effects on boundary layer transition in two-dimensional flow. *New Results in Numerical and Experimental Fluid Mechanics XI*. Springer, 2018, pp. 305–314 (cit. on pp. 25, 36).
- [137] Risius, S., Costantini, M., Koch, S., Hein, S., and Klein, C.: Unit Reynolds number, Mach number and pressure gradient effects on laminar–turbulent transition in two-dimensional boundary layers. *Experiments in Fluids* Vol. 59, 2018, pp. 1–29 (cit. on pp. 25, 36, 47, 96).
- [138] Rosemann, H.: The Cryogenic Ludwieg-tube Tunnel at Gottingen. *AGARD-R-812*, 1996, 8–1 to 8–13 (cit. on p. 22).
- [139] Sabatino, D. R. and Smith, C. R.: Turbulent spot flow topology and mechanisms for surface heat transfer. *Journal of Fluid Mechanics* Vol. 612, 2008, pp. 81–105 (cit. on pp. 12, 15).
- [140] Sankaran, R. and Antonia, R. A.: Influence of a favorable pressure gradient on the growth of a turbulent spot. *AIAA journal* Vol. 26, No. 7, 1988, pp. 885–887 (cit. on pp. 16, 79, 87).
- [141] Sankaran, R., Sokolov, M., and Antonia, R. A.: Substructures in a turbulent spot. *Journal of Fluid Mechanics* Vol. 197, 1988, pp. 389–414 (cit. on p. 13).
- [142] Saric, W. S. and Thomas, A. S. W.: Experiments on the subharmonic route to turbulence in boundary layers. *Turbulence and chaotic phenomena in fluids*, 1984, pp. 117–122 (cit. on p. 8).
- [143] Savas, Ö. and Coles, D.: Coherence measurements in synthetic turbulent boundary layers. *Journal of Fluid Mechanics* Vol. 160, 1985, pp. 421–446 (cit. on p. 10).
- [144] Savitzky, A. and Golay, M. J. E.: Smoothing and differentiation of data by simplified least squares procedures. *Analytical chemistry* Vol. 36, 1964, pp. 1627–1639 (cit. on p. 47).
- [145] Schlichting, H.: Berechnung der Anfachung kleiner Störungen bei der Plattenströmung. *Zeitschrift für angewandte Mathematik und Mechanik* Vol. 13, 1933, pp. 171–174 (cit. on p. 8).
- [146] Schlichting, H. and Gersten, K.: *Boundary-layer theory*. 9th edition. Springer, Berlin, 2016 (cit. on pp. 1, 7, 79).
- [147] Schrauf, G.: COCO - a program to compute velocity and temperature profiles for local and nonlocal stability analysis of compressible, conical boundary layers with suction. *Zarm Technik report, Bremen, Germany*, 1998 (cit. on p. 47).
- [148] Schrauf, G.: LILO 2.1 users guide and tutorial. *GSSC Technical Report, Bremen, Germany* No. 6, 2006 (cit. on p. 48).
- [149] Schrauf, G.: Status and perspectives of laminar flow. *The Aeronautical Journal* Vol. 109, 2005, pp. 639–644 (cit. on p. 2).

- 
- [150] Schröder, A., Geisler, R., Elsinga, G. E., Scarano, F., and Dierksheide, U.: Investigation of a turbulent spot and a tripped turbulent boundary layer flow using time-resolved tomographic PIV. *Experiments in Fluids* Vol. 44, 2008, pp. 305–316 (cit. on p. 11).
- [151] Schröder, A. and Kompenhans, J.: Investigation of a turbulent spot using multi-plane stereo particle image velocimetry. *Experiments in Fluids* Vol. 36, 2004, pp. 82–90 (cit. on pp. 4, 11, 12).
- [152] Schubauer, G. B. and Klebanoff, P. S.: Contributions on the mechanics of boundary-layer transition. Tech. rep. 1289. National Advisory Committee for Aeronautics, 1956 (cit. on pp. 4, 9, 10, 12, 13, 18, 77, 80–82, 87, 103).
- [153] Schubauer, G. B. and Skramstad, H. K.: Laminar boundary-layer oscillations and stability of laminar flow. *Journal of the Aeronautical Sciences* Vol. 14, 1947, pp. 69–78 (cit. on p. 9).
- [154] Schülein, E.: Skin friction and heat flux measurements in shock/boundary layer interaction flows. *AIAA journal* Vol. 44, No. 8, 2006, pp. 1732–1741 (cit. on p. 48).
- [155] Schultz, D. L. and Jones, T. V.: Heat-transfer measurements in short-duration hypersonic facilities. AGARD AG-165. Agard. 1973 (cit. on pp. 33, 48, 51, 111, 121).
- [156] Shahinfar, S. and Fransson, J. H. M.: Effect of free-stream turbulence characteristics on boundary layer transition. *Journal of Physics: Conference Series*. Vol. 318. IOP Publishing. 2011, p. 032019 (cit. on p. 19).
- [157] Shehab, M., Moshhammer, K., Franke, M., and Zondervan, E.: Analysis of the potential of meeting the EU’s sustainable aviation fuel targets in 2030 and 2050. *Sustainability* Vol. 15, No. 9266, 2023 (cit. on p. 2).
- [158] Singer, B. A.: Characteristics of a young turbulent spot. *Physics of Fluids* Vol. 8, No. 2, 1996, pp. 509–521 (cit. on pp. 11, 18).
- [159] Smith, A. M. O. and Clutter, D. W.: The smallest height of roughness capable of affecting boundary-layer transition. *Journal of the Aerospace Sciences* Vol. 26, 1959, pp. 229–245 (cit. on pp. 26, 33, 100).
- [160] Sohn, K. H., O’Brien, J. E., and Reshotko, E.: Some characteristics of bypass transition in a heated boundary layer. *Turbulent Shear Flows 7*. Berlin, Heidelberg: Springer Berlin Heidelberg, 1991, pp. 137–153 (cit. on p. 11).
- [161] Solomon, W. J., Walker, G. J., and Gostelow, J. P.: Transition length prediction for flows with rapidly changing pressure gradients. *Journal of Turbomachinery* Vol. 118, 1996, pp. 744–751 (cit. on p. 19).
- [162] Sottong, R.: Private communication. 2015 (cit. on p. 50).
- [163] Srichan, S., Rakpakdee, W., Kiatsiriroat, T., and Chaiworapuek, W.: Thermal characterization of longitudinal merging of turbulent spots. *Experimental Heat Transfer* Vol. 32, 2019, pp. 488–508 (cit. on p. 15).
- [164] Steelant, J. and Dick, E.: Modeling of laminar-turbulent transition for high freestream turbulence. *Journal of Fluid Engineering* Vol. 123, No. 1, 2001, pp. 22–30 (cit. on p. 87).
- [165] Strand, J. S. and Goldstein, D. B.: Direct numerical simulations of riblets to constrain the growth of turbulent spots. *Journal of Fluid Mechanics* Vol. 668, 2011, pp. 267–292 (cit. on p. 16).

- [166] Theodorsen, T.: The structure of turbulence. *50 Jahre Grenzschichtforschung: Eine Festschrift in Originalbeiträgen*, 1955, pp. 55–62 (cit. on p. 11).
- [167] Tollmien, W.: Über die Entstehung der Turbulenz. *Vorträge aus dem Gebiete der Aerodynamik und verwandter Gebiete: Aachen 1929*, 1930, pp. 18–21 (cit. on p. 8).
- [168] Van den Eynde, J. and Steelant, J.: Compressibility and temperature effects on turbulent spot growth. *Proceedings of International Conference on High-Speed Vehicle Science Technology*, 2018 (cit. on p. 17).
- [169] Van der Walt, S., Schönberger, J. L., Nunez-Iglesias, J., Boulogne, F., Warner, J. D., Yager, N., Gouillart, E., and Yu, T.: Scikit-image: image processing in python. *PeerJ* Vol. 2, 2014, e453 (cit. on pp. 39, 62).
- [170] Van Hest, B. F. A., Passchier, D. M., and Ingen, J. L. van: The development of a turbulent spot in an adverse pressure gradient boundary layer. *Laminar-Turbulent Transition*. Berlin, Heidelberg: Springer Berlin Heidelberg, 1995, pp. 255–262 (cit. on pp. 16, 69).
- [171] Vasudevan, K. P., Dey, J., and Prabhu, A.: Spot propagation characteristics in laterally strained boundary layers. *Experiments in Fluids* Vol. 30, 2001, pp. 488–491 (cit. on p. 17).
- [172] Virtanen, P. et al.: SciPy 1.0: fundamental algorithms for scientific computing in python. *Nature Methods* Vol. 17, 2020, pp. 261–272 (cit. on p. 39).
- [173] Walker, G. J. and Gostelow, J. P.: Effects of adverse pressure gradients on the nature and length of boundary layer transition. *Journal of Turbomachinery* Vol. 112, No. 2, 1990, pp. 196–205 (cit. on pp. 4, 18).
- [174] Wang, Y. X., Choi, K.-S., Gaster, M., Atkin, C., Borodulin, V., and Kachanov, Y.: Early development of artificially initiated turbulent spots. *Journal of Fluid Mechanics* Vol. 916, 2021, A1 (cit. on p. 10).
- [175] Welch, P.: The use of fast fourier transform for the estimation of power spectra: a method based on time averaging over short, modified periodograms. *IEEE Transactions on Audio and Electroacoustics* Vol. 15, No. 2, 1967, pp. 70–73 (cit. on p. 109).
- [176] White, F. M. and Majdalani, J.: *Viscous fluid flow*. Vol. 3. McGraw-Hill New York, 2006 (cit. on pp. 7, 8).
- [177] Whitehead Jr., A.: NASP aerodynamics. National Aerospace Plane Conference. American Institute of Aeronautics and Astronautics, 1989 (cit. on pp. 2, 3).
- [178] Wu, X.: Inflow turbulence generation methods. *Annual Review of Fluid Mechanics* Vol. 49, 2017, pp. 23–49 (cit. on p. 13).
- [179] Wu, X.: New insights into turbulent spots. *Annual Review of Fluid Mechanics* Vol. 55, 2023 (cit. on pp. 3, 10, 11, 13, 16, 17).
- [180] Wu, X., Jacobs, R. G., Hunt, J. C., and Durbin, P. A.: Simulation of boundary layer transition induced by periodically passing wakes. *Journal of Fluid Mechanics* Vol. 398, 1999, pp. 109–153 (cit. on p. 14).
- [181] Wygnanski, I., Sokolov, M., and Friedman, D.: On a turbulent ‘spot’ in a laminar boundary layer. *Journal of Fluid Mechanics* Vol. 78, 1976, pp. 785–819 (cit. on pp. 3, 4, 9, 11–14, 47, 52, 59, 69, 78, 81, 82).

- [182] Wygnanski, I., Zilberman, M., and Haritonidis, J. H.: On the spreading of a turbulent spot in the absence of a pressure gradient. *Journal of Fluid Mechanics* Vol. 123, 1982, pp. 69–90 (cit. on pp. 17, 18, 78–81, 87).
- [183] Zanchetta, M. A. and Hillier, R.: Laminar turbulent transition at hypersonic speeds: the effects of nose blunting. Proceedings of the Second European Symposium on Aerothermodynamics for Space Vehicles. Vol. 367. 1995, p. 207 (cit. on p. 15).
- [184] Zhao, Y., Xiong, S., Yang, Y., and Chen, S.: Sinuous distortion of vortex surfaces in the lateral growth of turbulent spots. *Physical Review Fluids* Vol. 3, 7 2018, p. 074701 (cit. on p. 13).
- [185] Zhong, S., Chong, T. P., and Hodson, H. P.: A comparison of spreading angles of turbulent wedges in velocity and thermal boundary layers. *Journal of Fluids Engineering* Vol. 125, 2003, pp. 267–274 (cit. on pp. 9, 10).
- [186] Zhong, S., Kittichaikan, C., Hodson, H. P., and Ireland, P. T.: Visualisation of turbulent spots under the influence of adverse pressure gradients. *Experiments in Fluids* Vol. 28, 2000, pp. 385–393 (cit. on pp. 13, 16, 52, 61, 62).
- [187] Zilberman, M., Wygnanski, I., and Kaplan, R. E.: Transitional boundary layer spot in a fully turbulent environment. *The Physics of Fluids* Vol. 20, 1977, S258–S271 (cit. on p. 10).